DOTTORATO DI RICERCA IN

Scienze Biomolecolari e Farmaceutiche

CICLO

XXXVIII

Valorization of graphite-based industrial waste for the development and distribution of alternative energy vectors, primarily hydrogen.

Dipartimento di Farmacia

Settore Scientifico Disciplinare: CHEM-05/A

Dottorando

Dott. Stefano Di Giacomo

Coordinatore Prof.

Chiar.ma Prof.ssa Assunta Pandolfi

Tutor

Chiar.ma Prof.ssa Antonella Fontana

Anni Accademici 2022/2025

Sommario

1 Thesis Incipit 12
1.1 Critical Raw Materials (CRM) 12
1.2 State of Art 19
1.3 Thesis Aim 22
2.1 Introduction to analytical techniques 23
2.1.1 Raman spectroscopy 23
2.1.2 IR spectroscopy 26
2.1.3 XRD 27
2.1.4 TGA 31
2.1.5 Differential scanning calorimetry (DSC) 33
2.2 Carbon Brushes 36
2.3 Materials and Methods 37
2.3.2 DTA 37
2.3.3 SEM Analysis 38
2.4.1 Results 38
2.5 Waste characterization 40
3 Graphite 42
3.1 Top-Down methods 45
3.1.1 Liquid exfoliation 45
3.1.2 Electrochemical exfoliation 46
3.1.3 Oxidative chemical exfoliation 47
3.1.4 Reduction of graphene oxide into reduced graphene oxide 52
3.1.5 Arc Discharge technique 56
3.1.6 Mechanical exfoliation 57
3.2 Bottom-up Methods 58
3.2.1 The Epitaxial Growth of Graphene 58
3.2.2 Chemical vapour deposition 60
3.2.3 Laser-assisted procedures 67
3.2.4 Flash Graphene 69
4 Graphene applications 71
4.1 Detection of pollutants 71

4.2 Organic pollutants 73
4.3 Metal Ions 74
4.4 Photocatalysis 76
4.5 Electrocatalysis 78
5 Graphene Bioapplication 83
References 91
6 Graphene oxide accelerates TGFβ-mediated epithelial-mesenchymal transition and stimulates pro-inflammatory immune response in amniotic epithelial cells 115
6.1 Introduction 115
6.2 Materials and methods 117
6.2.1 Ethics statement 117
6.2.2 Preparation of GO suspension 117
6.2.3 Activation of substrates 117
6.2.4 Preparation of GO-functionalized substrates 118
6.2.5 AFM, FTIR and Raman spectroscopy characterization 118
6.2.6 AECs isolation and culture 119
6.2.7 Experimental plan 119
6.2.8 Gene analyses 120
6.2.9 Immunohistochemistry 120
6.2.10 ROS production and viability assay 120
6.2.11 TGFβ pathway assessment 123
6.2.12 Migration test 124
6.2.13 Cytokine and chemokine array 125
6.2.14 PBMCs proliferation assay 125
6.2.15 Analysis of hTHP1 IL6 secretion 125
6.2.16 Statistical analysis 126
6.3 Results 126
6.3.1. Characterization of GO aqueous dispersion 126
6.3.2 Surface characterization of GO-functionalized coverslips 126
6.3.3 GO induces EMT in AECs epithelial and mesenchymal markers 128
6.3.4 GO induces an increase of ROS production without affecting cell viability 129
6.3.5 GO induces EMT through the activation of TGFβ1/SMAD signaling pathway 130

6.3.6 GO stimulates a mesenchymal-type of collective migration 131
6.3.7 GO modulates AECs immune response by inducing release of either pro- and anti-inflammatory mediators.....132
6.3.8 GO affects the immunomodulatory properties of AECs 133
6.4 Discussion 133
6.5 Conclusion 138
References 140
7 Exploring Potential Impact of Graphene Oxide and Graphene Oxide-Polyethylenimine on Biological Behavior of Human Amniotic Fluid-Derived Stem Cells 148
7.1 Introduction 148
7.2. Materials and Methods 150
7.2.1 Characterization of GO and PEI Aqueous Solutions 150
7.2.2 GO and GO-PEI Preparation 150
7.2.3 AFM Characterization of Functionalized Coverslips.....151
7.2.4 ATR-FTIR, Raman Spectroscopy, and Raman Mapping of Functionalized Coverslips 151
7.2.5 Cell Culture 152
7.2.6 Mito Health Stain (HCS) 153
7.2.7 Cellular Attachment 153
7.2.8 Immunofluorescence Analysis of Ki67 Staining.....154
7.2.9 Western Blot (WB) 154
7.2.10 RNA Extraction from MVs 155
7.2.11 MicroRNA Expression Profiling.....155
7.2.12 Statistical Analysis 156
7.3 Results 156
7.3.1 GO and GO-PEI Precoated Coverslips Characterization 156
7.3.2 GO and GO-PEI Precoated Coverslips Influenced Cellular Adhesion and Proliferation 160
7.3.3 GO-PEI Restores Expression of Mitochondrial Respiratory Chain Proteins in hAFSCs 162
7.3.4 GO and GO-PEI Alter Secretion of miRNAs in hAFSCs 163
7.4 Discussion 165
7.5 Conclusions.....169

References 170
8 Nanosystems 177
The Evolution of Liposomal Science 178
8.1 Introduction 178
8.1.2 Classification 179
8.1.3 Conventional and Stealth Liposomes 180
8.1.4 Active Targeting 180
8.2 Methodologies of Liposomal Fabrication 180
8.2.1 The classic Thin-Film Hydration Method 181
8.2.2 Solvent Injection and Detergent Removal 181
8.2.3 Microfluidics and High-Pressure Homogenization 181
8.2.4 Mechanisms of Drug Encapsulation: Passive vs. Active Loading 182
8.3 Stability Challenges 182
8.3.1 Chemical Degradation: Oxidation and Hydrolysis 182
8.3.2 Physical Instability: Aggregation and Fusion 183
8.4 Smart Nanocarriers: The Mechanics of Triggered Release 183
8.4.1 pH-Sensitive Liposomes 183
8.4.2 Thermo-Responsive Liposomes 183
8.5 Purification and Separation Processes of the Unencapsulated Drug 184
8.5.1 Dialysis and Centrifugation 184
8.5.2 Size Exclusion Chromatography (SEC) 184
8.5.3 Determination of Encapsulation Efficiency 184
9.1 Exosomes 185
9.2 Biogenesis and Structural Complexity 186
9.3 Composition and Heterogeneous Cargo 186
9.4 Physiological Roles and Clinical Translation 187
10 Study of the interaction between Graphene Oxide and cholesterol using different artificial membrane models 188
10.1 Introduction 188
Experimental Section 192
10.2.1 Materials 192
10.2.2 Instruments 192

10.2.3 Preparation of GO suspension 193
10.2.4 Activation and functionalization of substrates with GO 194
10.2.5 Preparation of liposomal systems 194
10.2.6 GO treatment of liposomes 195
10.2.6 Dynamic Laser Light Scattering (DLS) analysis 195
10.2.7 Atomic Force Microscopy 196
10.2.8 CF dye release experiments 196
10.2.9 ^{1}H NMR cholesterol quantification 196
10.2.10 Raman experiments 197
10.2.11 Differential Scanning Calorimetry 198
10.2.12 Filipin III-cholesterol interaction study 198
10.2.13 Water permeability measurements 199
10.3 Results and Discussion 200
10.3.1 Characterization of GO 200
10.4 Morphological characterization of liposomal systems 202
10.4.1 Particle size and zeta potential 202
10.4.2 AFM analysis of liposomes 204
10.4.3 CF leakage experiments 205
10.4.5 Raman spectroscopy analysis 208
10.4.7 NMR quantification 215
10.4.8 DSC analysis 217
10.4.6 Cholesterol detection by Filipin III 220
10.4.7 Water Permeability measurements 223
10.5 Conclusion 226
References 228
11 Urineprint of high-altitude: Insights from analyses of urinary biomarkers and bio-physical-chemical features of extracellular vesicles 237
11.1 Introduction 237
11.2 Aims of the study 239
11.3 Methods 240
11.3.1 Study design 240
11.3.2 Participants 240

11.3.3 Urine sampling and management 240
11.3.4 Isolation of extracellular vesicles 242
11.3.5 Atomic force microscopy (AFM) investigation 243
11.3.6 Raman spectroscopy analysis 244
11.3.7 Statistical comparisons 244
11.4 Results 245
11.4.1 Urynalisis....245
11.4.2 OxInflammation 245
11.4.3 Atomic force microscopy 246
11.4.4 Raman spectroscopy....247
11.4.5 Summary report 249
11.5 Discussion 249
11.5.1 OxInflammation 251
11.5.2 Insights and technical considerations from AFM and Raman spectroscopy 253
11.5.3 Limitations....255
11.6 Conclusions....256
References....258
12 Phenolic terpenes in liposomal bilayers: Unraveling physicochemical interactions and membrane perturbation via biophysical and computational approaches....264
12.1 Introduction 264
12.2 Experimental....267
12.2.1 Chemicals and materials 267
12.2.2 Instruments 268
12.2.3 Computational details 269
12.2.4. Preparation of liposomal systems 269
12.2.5. Dynamic light scattering (DLS) analysis....270
12.2.6. Atomic force microscopy (AFM) analysis 270
12.2.7 Differential scanning calorimetry (DSC) experiments 271
12.2.8. Raman experiments....272
12.2.9. Fluorimetric measurements....272
12.3 Results and discussion 273
12.3.1. Computational analysis 273

Characterization of hybrid liposomal systems 275
12.3.2. Particle size and zeta potential 275
12.3.3 AFM analysis 277
12.3.4 Determining the microviscosity 277
12.3.5 DSC analysis 279
12.3.6 Raman analysis 283
12.3.7 Release experiments 286
12.3.8 Comparative discussion of the applied techniques 288
12.3.9 Conclusions 289
References 292
13 Reutilisation of the waste 299
14 Waste-Derived Nanoporous Graphene Oxide–TEPA Sorbents for High-Pressure CO_2 Capture 303
14.1 Introduction 303
14.2 Experimental 305
14.2.1 Materials 305
14.2.2 Synthesis procedures 306
14.2.3 Preparation of wGO 306
14.2.4 Preparation of porous GO 306
14.2.5 TEPA functionalization of porous GO 307
Characterization 307
14.2.6 Thermogravimetric analysis (TGA) 307
14.2.7 X-ray photoelectron spectroscopy (XPS) 307
14.2.8 Scanning electron microscopy (SEM) 307
Gas sorption experiments 308
14.2.9 Sample preparation 308
14.2.10 Experimental setup 308
14.2.11 Sorption procedure 308
14.2.12 Kinetics and validation 309
14.2.13 Raman spectroscopy 309
14.2.14 X-ray diffraction (XRD) 310
14.3 Results and Discussion 310

14.3.1 Gas sorption experiments 316
14.3.2 In pressure adsorption measurement 317
14.3.3 Structure-Performance Correlations 318
14.4 Conclusions 320
References 322
15 Nanocarb Project→ Photoelectrochemical O_2 evolution. 327
15.1 Substrate preparation 327
15.2 Graphene oxide synthesis 327
15.3 Graphene oxide electrophoretic deposition (EPD) 327
15.4 Thermal annealing 328
15.5 Raman Analysis 329
15.6 KuQuinone Spin Coating 329
15.7 Results and Discussion 329
15.8 Raman characterisation of spin-coated samples 333
15.9 X-ray diffraction 336
15.10 Photoelectrochemical measurements 337
15.11 Conclusions 338
16 Nanocarb Project→ CO_2 electroreduction 339
16.1 Introduction 339
16.2 Materials and methods 339
16.2.1 Electrode production 339
16.2.2 Electrochemical processes 339
16.2.3 Chronoamperometry 339
16.2.4 Product quantification by ^{1}H-NMR spectroscopy 340
16.3 Results and Discussion 341
16.4 Conclusion 343
17 Ullmann Reaction 344
17.1 Materials and Methods 344
17.2 Results and Discussion 345
17.3 Conclusions 351

1 Thesis Incipit

1.1 Critical Raw Materials (CRM)

Critical raw materials are essential components for technologies related to ecological transition. In fact, most of these technologies are closely linked to mining activities, highlighting the problems associated with their supply. One of the EU's main goals for the transition is to optimise the supply of CRMs, as Europe lacks this type of raw material. For this reason, reuse and recovery are key activities included in the CRMs Act[1]. This is mainly linked to the need to drastically reduce dependence on third countries, as demonstrated by the Russian-Ukrainian conflict, to avoid the same phenomenon that occurred with gas, as well as to improve the circularity and sustainability of processes.



Figure 1: *CRMs marked and relevant colour classification.*

In the CRMs Act, the European Union highlights and introduces benchmarks to be achieved by 2030, concerning the supply chain and diversification of supply:

- At least 10% of Europe's annual consumption of strategic materials must be covered by extraction within the EU. This means that at least 10% of Europe's needs must come from European mines;

- At least 40% of annual consumption must be covered by processing within the EU, i.e. by the European industry that transforms these raw materials into usable forms;
- At least 25% of annual consumption must come from recycling within the EU, thereby encouraging the circular economy and the recovery of materials from waste;
- No, more than 65% of the EU's annual consumption of a given strategic material may come from a single third country, to avoid excessive dependence on a single external supplier and reduce the risk of supply chain disruptions.

These benchmarks are set with the aim of increasing European autonomy, secur supply and sustainability throughout the strategic materials supply chain, from sourcing raw materials to processing and recycling, while reducing dependence on external countries. Through the CRMs Act, the EU has introduced the possibility of reducing the approval and regulatory timelines for the implementation of these types of technologies, related to both extraction processes, with times reduced to 27 months to acquire permits, and 15 months for the processing and manufacturing of raw materials, drastically streamlining the bureaucracy behind this supply chain.

Critical materials essential for green, digital, defence and aerospace technologies are listed. These include, among others, lithium, rare earths, cobalt, nickel, graphite and copper, all materials used primarily in batteries, wind turbines, electric vehicles and semiconductors. According to the Jacques Delors Centre, the increase in critical materials for a net zero transition will grow dramatically, with lithium in particular increasing up to 40 times for battery production, as well as a 3 to 7-fold increase in demand for rare earths. This is because technologies aimed at the ecological transition, such as wind turbines, require up to nine times more materials, and electric

vehicles can require up to six times more materials than their fossil fuel–based counterparts.



Figure 2*: Lithium reserves per country.*

As shown in Fig. 2, no EU country currently has significant lithium reserves. The EU should therefore increase its extraction percentage from the current 2% to 10%. It is also important to note that although Australia holds 47.8% of reserves, processing is dominated by China, an area in which the EU aims to hold 40% of internal processing[2].

But what are the applications and supply difficulties today? As shown in Fig. 3, applications are very often linked to industrial products with high added value; in fact, today the EU finds itself playing catch-up with powers such as the US and China, especially in terms of technologies related to the transition.

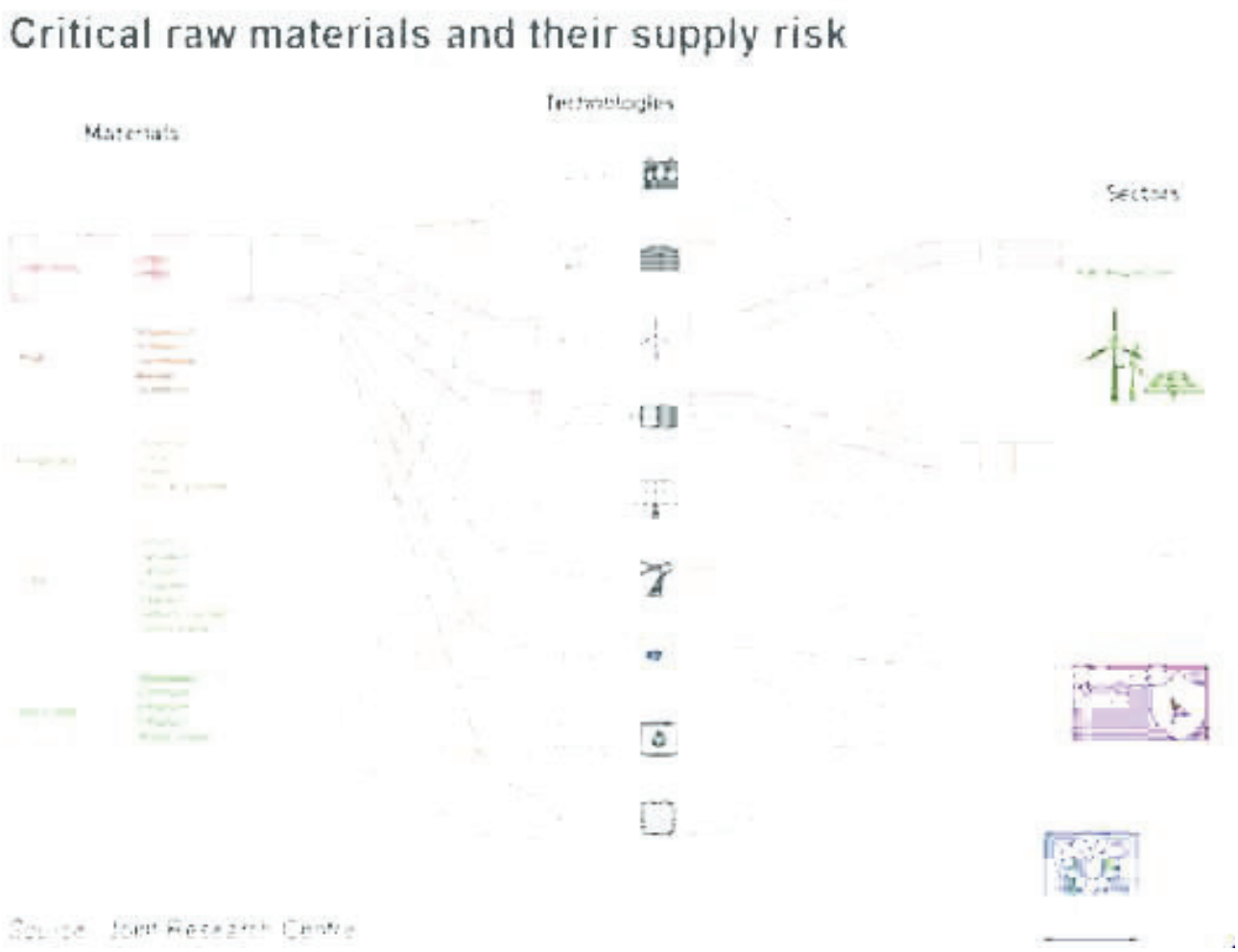

Figure 3*: Relationship between supply chain and application of each type of critical raw material.*

As shown in Fig. 3, rare earths and heavy metals are linked to the most critical sectors of the ecological transition. In fact, they are used both in energy production, such as in wind turbines and photovoltaic panels, and in magnets for electric mobility. The enormous costs associated with the need to import these raw materials, in addition to the increase in energy, have led to a drastic decline in European industry, which lags behind its international competitors in terms of technology, including in the automotive sector, where countries such as Germany used to excel. This is also closely related to the reduced cost of raw materials in China, which dominates the market for this type of technology. However, it is important to note from Fig. 4 that even if the risk associated with the supply of the material itself is low, its use can be ubiquitous, as in the case of copper and graphite,

which range from low to medium supply risk but are used in all the technologies shown in the figure. In fact, this risk is also relative.

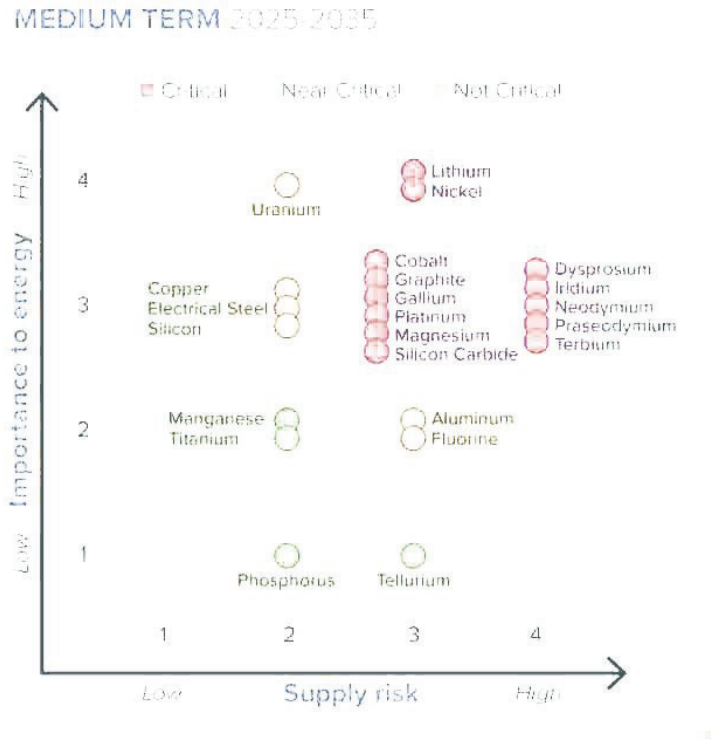

Figure 4: *Importance to energy and supply risk relationship in period between 2025-2035 for the US department of energy.*

As shown in Fig. 4, the EU CRMA, in addition to highlighting the importance of critical raw materials, is also emphasised by the US Department of Energy[3].

Supply risk, as defined by the "report on critical raw materials for the EU" drawn up in May 2014, is mainly a combination of three factors:

- High concentration of countries with poor governance;
- Substitutability;
- End-of-life recycling rates.

The first point refers to the risk of concentration in the supply of critical raw materials. More precisely, it is assessed using the Herfindahl-Hirschman Index, modified to take into account not only the

quantity produced by the various countries but also their quality of governance, as measured by the World Governance Index (WGI).

The second point, substitutability, is measured on a scale from 0 to 1, where 1, the maximum, indicates zero substitutability of the raw material.

Finally, the recycling rate refers to how much of the recycled content actually comes from discarded products, highlighting the circularity in the life cycle of metals.

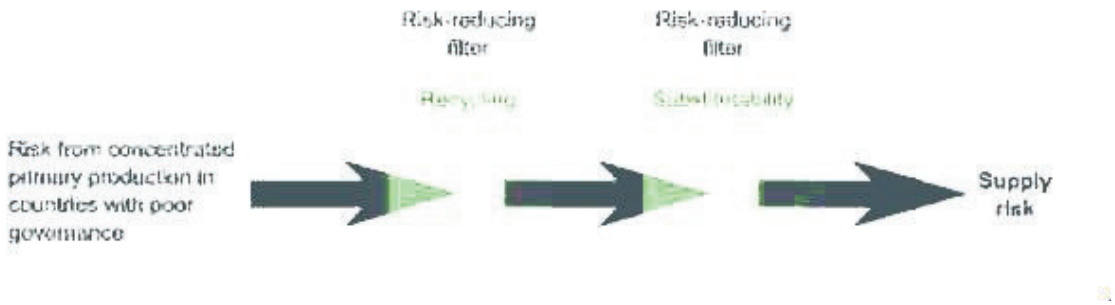

Figure 5*: Schematic illustration of factors that combined influences the supply risk of a material.*

But what is the situation in Italy? According to ISPRA[4], the Italian Institute for Environmental Protection and Research, there are 76 active mines, 22 of which are related to materials listed in the CRM Act and are mainly used for the extraction of feldspar, which is essential in the production of ceramics, and two of which are related to fluorite, which is used in the glass, steel, aluminium, electronics and refrigeration industries.

There is no extraction of metal ores in our country, so we are totally dependent on foreign supplies. However, recent mapping has revealed the presence of extractable lithium with low environmental impact in geothermal fluids in Tuscany, Lazio and Campania. More specifically:

- Copper: Metalliferous Hills, Ligurian-Emilian Apennines, Western Alps, Trentino, Carnia, Sardinia;
- Manganese: Liguria, Tuscany;
- Tungsten: Calabria (Cosenza, Reggio), eastern and northern Sardinia, central-eastern Alps (associated with lead-zinc);
- Cobalt: Sardinia, Piedmont (Punta Corna strategic);
- Magnesite: Tuscany;
- Magnesium salts: Veneto Pre-Alps;
- Titanium: Savona (open-cast mining not feasible due to environmental issues);
- Bauxite (for aluminium): Central Apennines (modest), Puglia, Nurra (Olmedo mine);
- Rare earths: contained in bauxite and fluorite deposits (Sardinia);
- Celestine (strontium): Sicilian sulphur mines, especially in the Nisseno area;
- Lithium: pegmatites on the islands of Elba, Giglio and Vipiteno; geothermal fluids in Tuscany, Lazio and Campania (very rich and with low environmental impact extraction);
- Barite: Bergamo, Brescia and Trentino;
- Graphite: Turin, Savona and Sila (Calabria).

The database, updated as part of the PNRR GeoSciencesIR project, represents the starting point for the development of the national mining programme, imposed by EU Regulation 1252/2024 (Critical Raw Materials Act) and entrusted to ISPRA by Decree Law 84/20243.

In recent years, there has been growing interest in the recovery of mining waste as a source of strategic raw materials.

In Italy, there are approximately 150 million cubic metres of waste from old mining activities, often in problematic deposits that cause heavy metal pollution. The new European regulation (CRM Act) proposes to consider this waste no longer just as an environmental problem to be remediated, but as a valuable resource to be recovered, reopening the debate on extraction and sustainability in Italy.

1.2 State of Art

For more than a third of critical raw materials, the main problem lies in recovery technologies. This is particularly true for high-tech waste, which is characterised by a very low concentration of light and heavy rare earths, consisting of just a few micrograms. For example, LEDs contain 29 µg of indium and 32 µg of gallium, as well as even smaller amounts of europium, yttrium, cerium and gadolinium. However, this contributes to a total of 62 million tonnes of waste in 2022. Finally, it must always be borne in mind that some recovery technologies for one type of metal are incompatible with another and this, especially in the case of this type of technology, which is characterised by multiple constituents, leads to a management problem that is difficult to solve[5].

To date, lithium recovery from lithium-ion batteries is possible, but very often not economically viable.

There are innovative technologies, such as bioleaching and hydrometallurgical processes. N-Methyl-Pyrrolidone (NMP) is generally used to detach the cathode material from the aluminium foil, often combined with ultrasonication at 80°C. The limitation lies in the impossibility of solubilising everything presents at the cathode, such as PVDF. An alternative is certainly metal leaching. In this method, inorganic acids such as HCl, H_2SO_4 or HNO_3 are among the most used. In the case of HCl, however, the development of Cl_2 leads to a serious environmental pollution problem, which results in increased costs.

$$2LiCoO_2 + 8HCl \rightarrow 2CoCl2 + Cl_2 + 2LiCl + 4H_2O$$

An alternative is the use of H_2SO_4 or HNO_3 combined with H_2O_2, which leads to very high recovery of metals at the cathode, Co and Li[6].

However, it is also important to recover graphite from the anode, as this is also a CRM. An electric vehicle with a Lithium-ion battery, LIB, contains a total of 50 kg of graphite, 10 kg of which is stored

in the battery[7]. The World Bank has predicted a demand of 4.5 million tonnes of graphite by 2050 to meet the demand linked to the econological transition, which is three times higher than global production in 2019. This leads to an estimate that the cost of graphite could reach a price 500% higher than the current one by 2050.

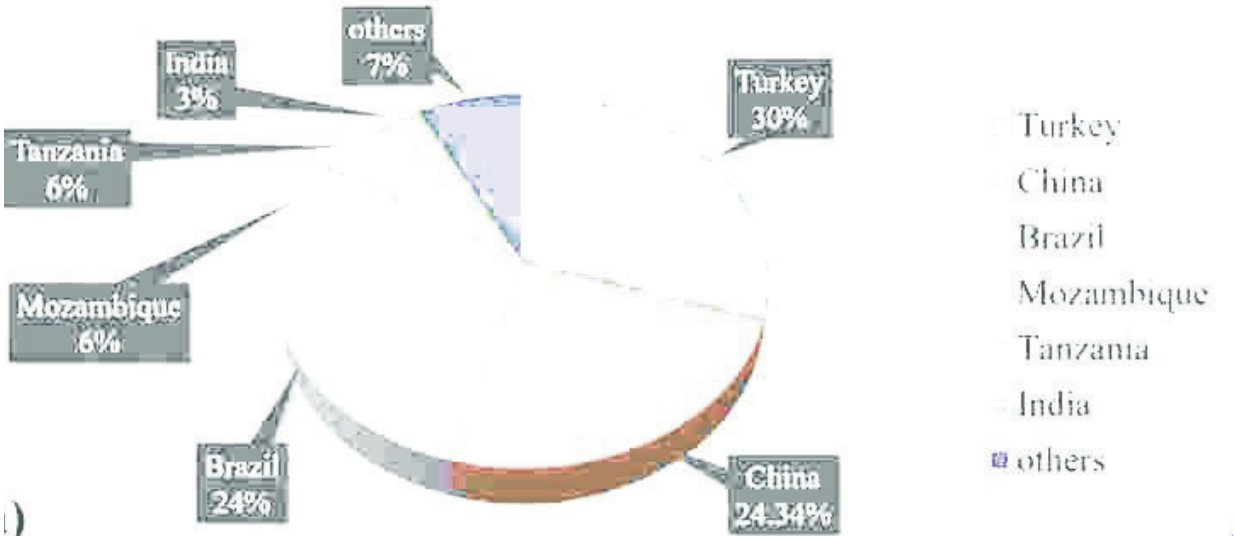

Figure 6*: world natural graphite reserves per country.*

A large percentage of graphite can be recovered, however, mainly from LIBs. To date, the process involves pre-treatment, often linked to safety, to prevent explosions and remove materials such as plastics.

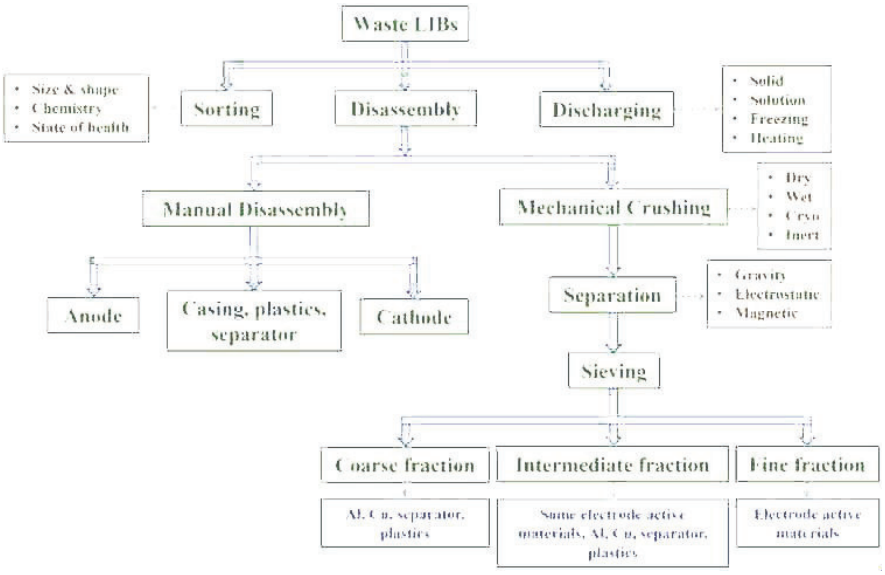

Figure 7*: Flowchart representing the recycling process of waste lithium-ion batteries, showing sorting, disassembly, crushing, separation, and sieving steps leading to coarse, intermediate, and fine material fractions.*

The sorting phase is essential for optimising the quality of the recovered material, as it allows separation based on chemical and physical characteristics. It can be either automated or manual, each with its own advantages and disadvantages. The advantage of manual sorting lies in its adaptability to different shapes and sizes, especially when the volume is large, while automated sorting is faster for a single type of battery, thanks to AI and software. Both of these steps, sorting and disassembly, which consists of breaking down the battery into pieces, go hand in hand with discharging the battery, either thermally or by completely discharging it through, for example, electrolysis[8].

Graphite is then obtained at the end, following the leaching processes described above, or through heat treatment, where the high temperature used, up to 3000°C in N_2, leads to a recovery of the crystalline structure of the graphite, through graphitisation processes of the discharged graphite[9].

In addition to batteries, a lot of graphite is used in other types of e-waste. Five million tonnes of e-waste are disposed of every year, for a total of 11.2 kg per person[10]. Among e-waste containing graphite, carbon brushes are certainly of considerable interest[11].

Carbon brushes are essential components of electric motors, used to transfer electricity between a fixed part and a rotating part such as commutators or slip rings. They are generally composed of graphite, metal powders (such as copper) and a binder that holds these components together. Graphite provides electrical conduction and self-lubrication, while metal additives improve strength and conductivity[12].

1.3 Thesis Aim

The thesis stems from the need to recycle brushes, following collaboration with Carbotech SrL, a company specialising in brushes for HVAC systems. More specifically, the waste consists of 100 tonnes, 40% of which is metallic copper, with the remainder being graphite and carbon. Carbon accounts for approximately 10% and derives from the process of baking the epoxy resin necessary for cross-linking.

This gave rise to the idea for this thesis, which aims to give a second life to the discarded material, which, as previously mentioned, amounts to around 100 tonnes. It was therefore essential to develop a recovery and separation method followed by various ideas for the application of graphite and copper, the two main components of the supply chain.

Graphite was used because of its potential for reuse in the form of graphene derivatives, whose applications range from the biomedical field, such as tissue engineering, to CO_2 capture and catalysis.

Copper, on the other hand, can easily be reused due to its strong catalytic activity.

2.1 Introduction to analytical techniques

For the purposes of this thesis, five characterisation techniques were mainly used.

2.1.1 Raman spectroscopy

Raman spectroscopy is a powerful tool for characterising carbonaceous materials. The Raman effect was first described by Chandrasekhara Venkata Raman, from whose description of the effect the technique derives its name and which earned him the Nobel Prize in Physics in 1930.

Raman scattering is a phenomenon in which a sample is irradiated by a monochromatic laser source and, following interaction with the electrons of the molecules, generates an oscillating electric dipole responsible for the diffusion process of the incident radiation. The radiation is thus analysed and consists almost entirely of the Rayleigh component, which is almost all of the energy. It is an elastic scattering process and does not cause any energy variation, having the same energy as the incident radiation, while the Stokes and anti-Stokes components have higher energies because they derive from inelastic scattering processes.

To best describe these effects, the phenomenon must be described from a quantum point of view. In fact, anti-Stokes lines are not predicted by classical theory, as they are extremely less intense than Stokes lines. Using a quantised energy scheme such as QK, it is possible to graph the different energy levels:

1. An incident photon with energy $\mathbf{h\nu_0}$ excites the molecule from a vibrational level of $\nu=0$ or $\nu=1$ to a virtual state;
2. From the virtual level, the molecule can relax in several ways:
    a) **Rayleigh scattering**: returns to the same initial vibrational state (from $\nu=0$ to $\nu=0$ or from $\nu= 1$ to $\nu=1$), so that the energy of the scattered photon is the same $\mathbf{h\nu_0}$;
    b) **Raman Stokes**: starts from $\nu=0$ and relax in $\nu=1$. So the photon's energy is $\mathbf{h\nu_0 - h\nu_1}$;
    c) **Raman anti-Stokes**: starts from $\nu=1$ and relaxes in $\nu=0$, so its energy is $\mathbf{h\nu_0+h\nu_1}$;

Generally, Stokes lines are more intense because at T_{room} is predominantly $v=0$[13].

As with infrared spectroscopy (IR), Raman spectroscopy provides information about the energy level of molecular vibrations. The result is expressed in terms of frequency from the relationship $E= h\nu$, which is specific to each molecular species, representing a sort of 'fingerprint' for each species and/or molecule. The chemical shift is shown on the x-axis. (cm^{-1}), which correspond to the energies of jumps between fundamental vibrational levels v=0 and v=1, while the y-axis shows the intensity, which is directly proportional to the number of Stokes photons collected during the acquisition process.

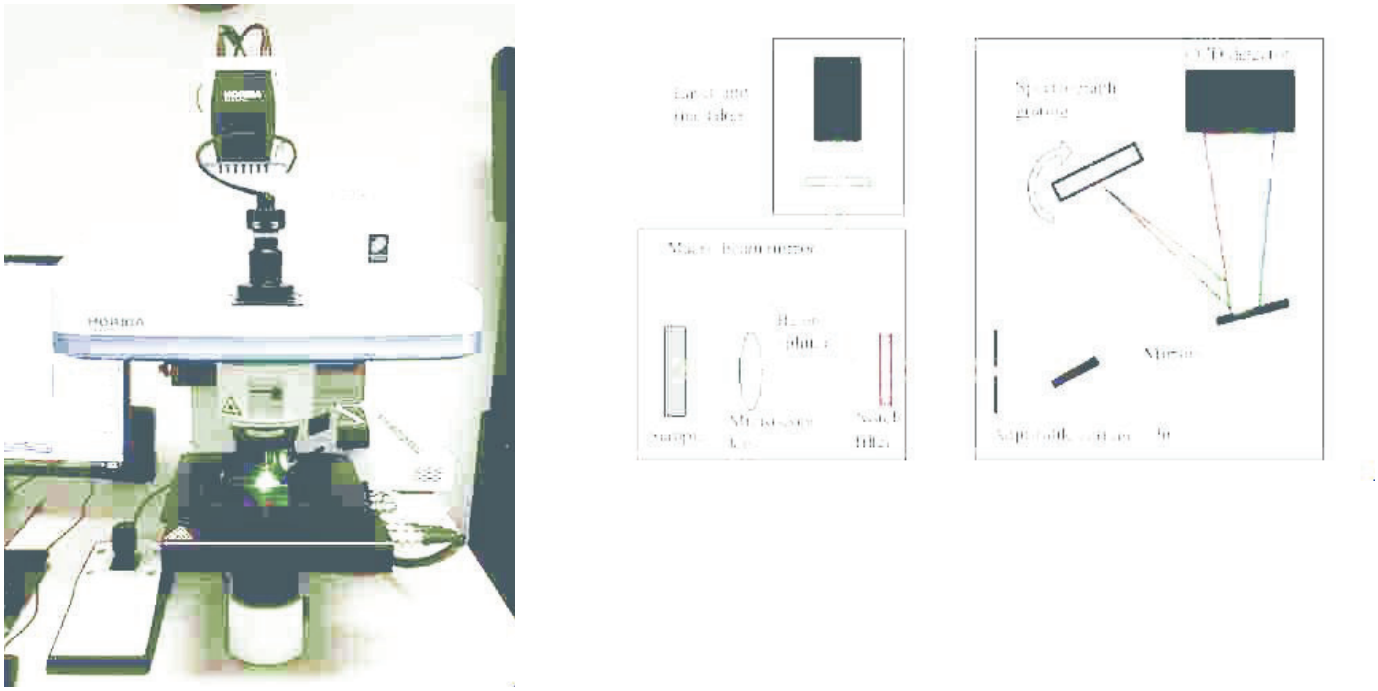

Figure 7*: Horiba XploRA Plus photo on the left and schematic representation of Raman instrumentation.*

Fig. 7, (on the right) shows the Raman spectroscopy system. The system uses:

- Monochromatic laser that excites the sample, producing elastic (Rayleigh) and inelastic (Raman) scattered light. A line filter filters the laser to transmit only the precise wavelength required, improving the selectivity and intensity of the excitation.

- The laser light is directed to the sample via a microscopic lens, often through a beam splitter that directs both the laser to the sample and the scattered light reflected to the collector system. The sample scatters the light via more intense Rayleigh scattering and less intense Raman scattering.
- The light scattered by interaction with the sample passes through a notch filter that blocks Rayleigh radiation but allows the shifted Raman bands (Stokes and anti-Stokes) to pass through, thus improving signal quality by eliminating background noise.
- The filtered Raman light then enters an adjustable slit that controls the spatial and spectral resolution of the system. It is then dispersed by a spectrograph with a diffraction grating that separates the light according to wavelength, distinguishing the different molecular vibrational modes. As the grating increases, and therefore the lines per millimeter increase (600, 1200, 1800, 2400 lines/mm for Horiba XploRA PLUS), the resolution increases;
- Finally, the scattered light is detected by a CCD (charge-coupled device) detector, which records the signal intensity as a function of wavelength and generates the characteristic Raman spectrum.

Raman spectroscopy is a technique particularly suited to the study of carbon-based materials, as it allows both long-range crystalline vibrations and short-range molecular vibrations of carbon species to be detected. These characteristics make it possible to obtain the distinctive “fingerprint” for each material.

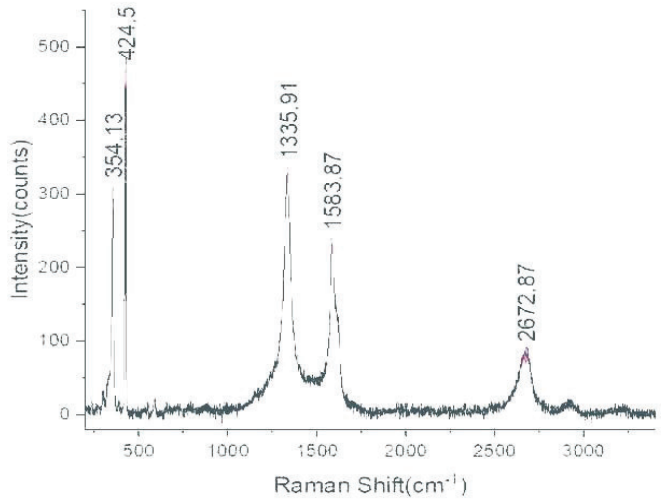

Figure 8: *Raman spectra of the waste recovered by Carbotech s.p.s. during brushes production. The interpretation will be discussed in the next Chapter.*

2.1.2 IR spectroscopy

When an infrared photon is absorbed by a molecule, it transitions from its fundamental vibrational state to an excited vibrational state. The molecule is then subjected to a series of stretching (stretching) of the chemical bond or deformation of the bond angle (bending). Stretching is a variation in the periodic interatomic distance and can be symmetrical or asymmetrical depending on whether the two atoms move closer together or further apart at the same time. Bending, on the other hand, occurs on the plane where the bond angle lies, so this deformation can be of the following types:

- **Scissoring**: symmetrical deformation of the plane (there is an opening or closing of the molecule like scissors);
- **Twisting**: if it is an asymmetrical deformation outside the plane;
- **Wagging**: symmetrical deformation out of plane;
- **Rocking**: symmetrical deformation on the plane;

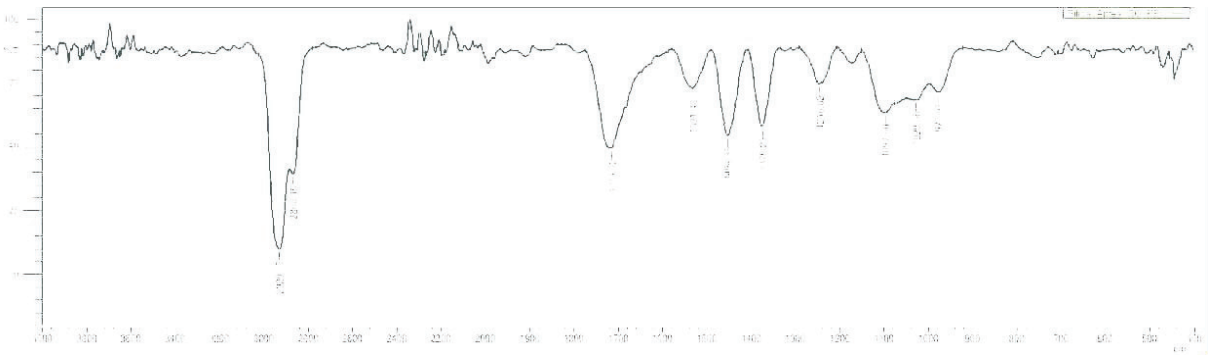

Figure 9: IR spectra of a silica-based composite with graphene oxide; this will be discussed in further chapters.

The wave number, ν, is shown on the x-axis, while the transmittance, which corresponds to the percentage of radiation transmitted, is shown on the y-axis. The area of an IR spectrum can be divided into three different regions:

- Region between 3600 and 1000 cm^{-1}: Due to vibrations of functional groups (-C=O, at around 1700 cm^{-1}, -C-O-C at around 1100 cm^{-1}, -C-O-H at around 1200 cm^{-1}, -C-C, -C=C-, etc.);
- Region between 1000 and 600 cm^{-1}: molecular fingerprint due to carbonaceous skeleton breathing, for instance;
- Region 200-600 cm^{-1}: Far IR due to vibration of heavy atoms and not-containing oxygen groups

The vibration frequency is described by the following equation:

$$\boldsymbol{\nu = 2\pi c\sqrt{(k/\mu)}}$$

where, $\boldsymbol{\nu}$ is the frequence, expressed in cm^{-1}, **c** is the speed of light constant, $\boldsymbol{\mu}$, is the reduced mass of the system, expressed as $m_1m_2/(m_1+m_2)$, while **k** is the bond strength constant (in N/m);

For example, from this equation, since -N-H has a different bond strength and a low reduced mass with respect to C-C bond it falls at 3300 cm^{-1} compared to *ca.* 1500 cm^{-1} of -C-C-[14].

2.1.3 XRD

X-ray diffraction is an analytical technique that allows the interaction between incident radiation and matter to be evaluated. The interaction of electromagnetic radiation with matter can lead to two different phenomena:

- Absorption: typical of XRD, incident electromagnetic radiation transfers part of its energy, increasing the temperature of the irradiated system or causing it to transition to an excited state, as in the case of X-rays, causing the system to eject electrons (photoelectric effect);
- Scattering: Incident radiation propagates within the analyte and there may or may not be an energy exchange between the material and the photon;

For this technique to work, coherent elastic scattering must irradiate the sample, passing through all lattice planes, and diffraction arises from the sum of the electromagnetic waves scattered by the atoms. Three different types of XRD exists:

- EDXD: energy dispersive X-ray diffraction, useful for liquids;
- XRPD: X-ray diffraction of powders;
- SC-XRD: single crystal XRD, although sample preparation is very complex, which makes this technique non-routine

It is possible to evaluate through XRD:

1. Lattice constant: unit of repetition of the crystal lattice. In short, it provides information on the characteristics of the crystal subunit in terms of size and shape, aimed at evaluating the cell parameters;
2. Spatial group of the substance: this is the combination of translational and point symmetries, evaluating all symmetry operations of the lattice on itself (difficult with XRPD, but feasible using Rietveld refinement);
3. Chemical connectivity of the asymmetric unit, the smallest portion of the structure, which cannot be superimposed on itself by any element of symmetry (very difficult to evaluate using XRPD, feasible with SC-XRD)
4. Evaluation of atomic displacement due to thermal vibrations, as atoms vibrate around their mean position.

Using X-ray crystallography, the most obvious data obtainable from the phenomenon of diffraction are undoubtedly the interplanar distance, the cell size and the strain.

The interplanar distance can be obtained from Bragg's law:

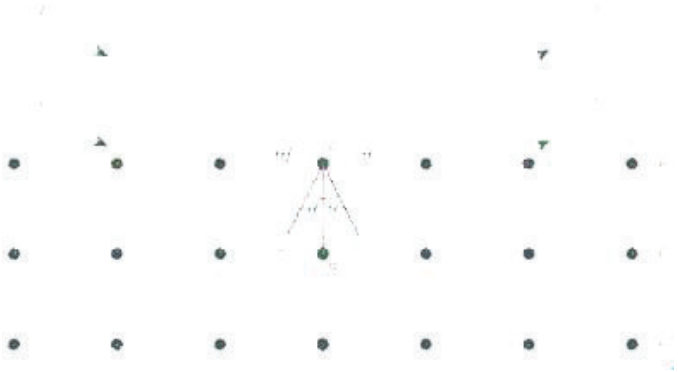

Scheme 1: Bragg's law interplanar distance.

When electromagnetic radiation strikes a crystal, it is subject to interference resulting from the reflection of waves by different crystal lattices. The extent of this interference can be calculated using Bragg's law:

$$n\lambda = 2d\sin(\theta)$$

In the formula, n is an integer, λ is the wavelength of the incident radiation (0.1542 nm in the case of the decay constant kα of copper), d is the distance between two adjacent planes, while θ is the angle formed with the crystal plane by the outgoing beam.

An XRD graph is characterised by intensity on the y-axis and θ on the x-axis.

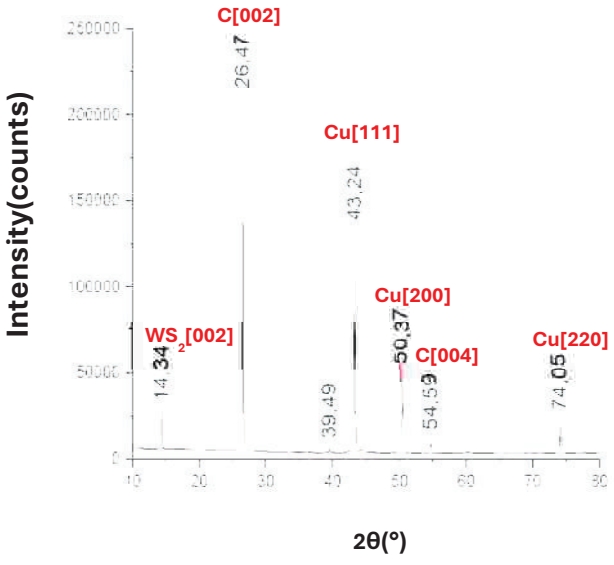

Figure 10: *Example of Carbotech's waste XRD diffractogram. The graph will be discussed in the next paragraph.*

As shown in Fig. 10, a particular index, called the Miller index, is shown in square brackets. It can be defined as a notation used in crystallography to describe planes and directions of a crystal lattice. It is defined by three integers, h, k and l, each of which represents a plane perpendicular to a specific direction in space. They are generally reported as the greatest common divisors of each index, and [hkl] represents a direction in the real physical space of the crystal. For example, indicating each index as a vector, in the case of an index [200], this will mean that the direction is twice the vector a_1, while a_2 and a_3 are characterised by the absence of a component.

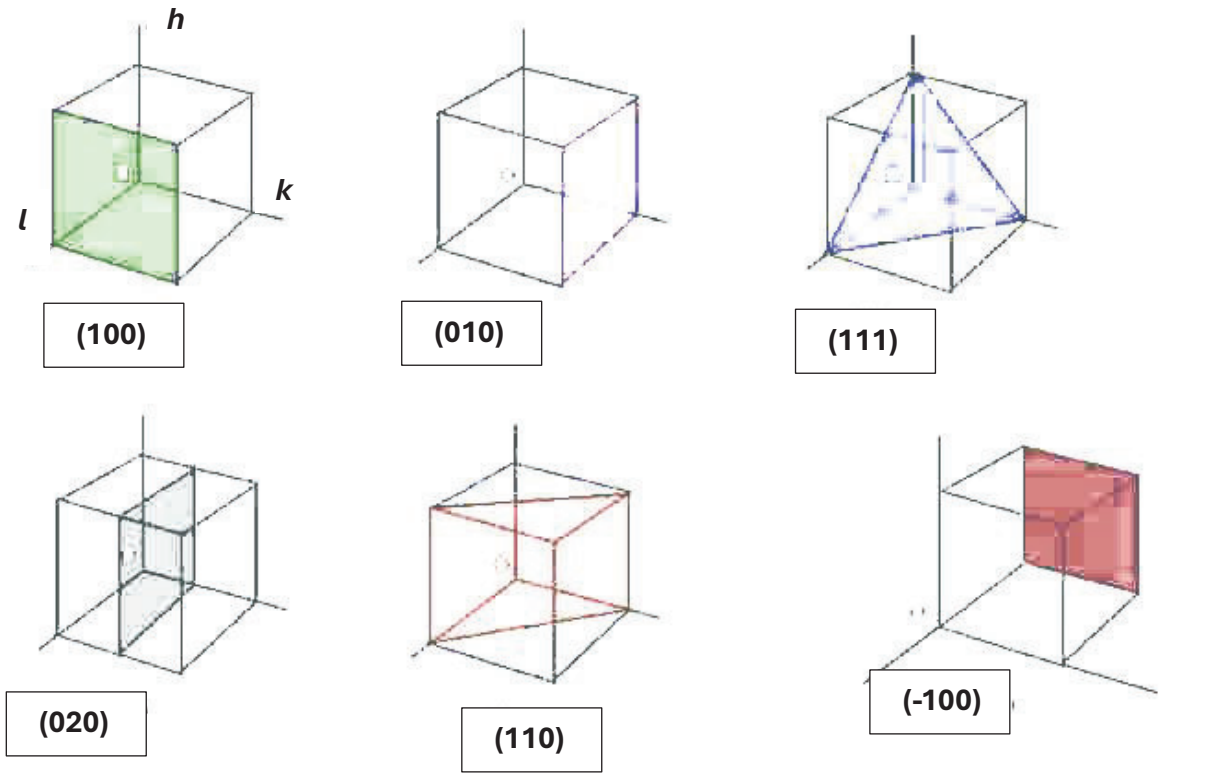

Figure 11: *Examples of miller index. The coloured region represents the different miller's index described below each image.*

It is very important to identify the Miller index as it provides information regarding purity and identification through 'fingerprinting', as well as the different reactivity of a given species to adsorption phenomena depending on the arrangement of atoms in the crystal subunit[15].

2.1.4 TGA

Thermogravimetry, or thermogravimetric analysis (TGA), is an experimental technique used to characterise materials and is part of the broader category of thermal analysis. In practice, it consists of continuously measuring how the mass of a sample varies over time or as the temperature changes, maintaining a controlled atmosphere that can be inert (Ar or N_2), oxidising (in air) or reducing (H_2 or forming gas).

During the experiment, the system records any weight loss or gain in the material as it is heated or cooled. The result obtained, called a thermogram or thermal decomposition curve, is a graph in which the change in mass (expressed as an absolute value or percentage) is plotted on the y-axis, as a function of temperature or time, which are plotted on the x-axis. The main components of a thermogravimetric analysis instrument are the thermal balance (or thermobalance), which measures the change in mass of the sample during heating or cooling with extreme precision; the furnace, usually made of refractory materials such as alumina or quartz, which allows very high temperatures to be reached; and the crucibles, i.e. the small containers in which the sample is placed, usually made of steel, platinum or alumina depending on the temperature.

There is also a temperature control system, which uses thermocouples to maintain and monitor the selected thermal programme (such as ramps or isotherms), and a gas ventilation and recirculation system that serves to control the atmosphere in the furnace and eliminate degradation gases.

Finally, the entire weight of the sample is recorded in real time, and the data is managed and processed by the computer connected to the instrument. Today, all these functions are integrated into a single device that also allows very small quantities of material to be analysed (from a few milligrams up to 1 g, depending on the size of the crucible), with a sensitivity in the order of micrograms, which is a thousand times more precise than the quantity analysed. When performing thermogravimetric analysis, it is essential to keep certain parameters constant, because even small variations can significantly affect the results and make them difficult to compare with each other.

The key factors to monitor are:

- The quantity of sample analysed: always the same when comparing multiple materials or multiple tests on the same material.
- The thermal programme: especially the heating rate, or ramp, which has a direct effect on the phenomena observed.
- The type of crucible: the material of the container also has its own thermal inertia, which can influence the behaviour of the sample at high temperatures.
- Gas flow in the furnace: this serves to ensure a controlled atmosphere but must be regulated to avoid turbulence or eddies that can distort the measurement, without forgetting the effect of buoyancy.
- Furnace cleaning: this is essential, whether done manually or through high-temperature cycles in an oxidising atmosphere, to avoid contamination or residues that could alter the data.

Furthermore, before starting the actual measurements, it is good practice to record a baseline with the empty instrument, which servekms both to check the condition of the machine and to correct any system drifts. Thermogravimetry is used in many fields, from scientific research to corporate quality control, including the analysis of water, agri-food products and more. The main applications include the study of the kinetics of degradation and reaction of materials, both in inert and oxidising atmospheres. This allows us to understand how a material behaves when heated, how stable it is, or to identify the different components in complex mixtures. The technique is also useful for studying liquids, analysing evaporation or absorption rates under controlled gas flows or different humidity levels. Another macroarea concerns analyses in an oxidative atmosphere, where the various kinetics of oxidation and absorption can be monitored, depending on the material and environmental conditions.

Then there is the application related to durability, i.e. predicting the useful life of a material based on thermal ageing: with TGA, the activation energy of a given process can be estimated, even with single analyses thanks to the most modern techniques. Finally, TGA can also be used to study the homogeneity of polymers with inorganic additives, identifying any sedimentation by observing the difference in residual mass between the different parts of the sample[16,17].

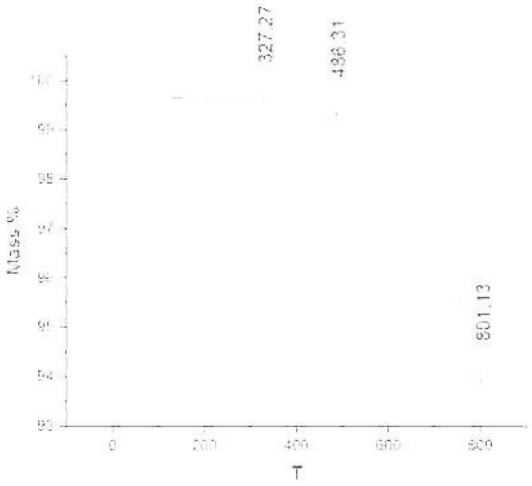

Figure 12: *Example of TGA thermogram of the waste. It will be discussed in the next paragraph.*

In summary, thermogravimetry (TGA) is used to analyse materials by accurately measuring the change in mass of a sample as the temperature varies or over time, in a controlled atmosphere. This allows the thermal stability, decomposition or oxidation kinetics, moisture content, additives or fillers to be studied, and the composition and behaviour of materials under specific thermal conditions to be evaluated. TGA is widely used in industry and research to characterise polymers, drugs, metals, inorganic materials and agri-food products, providing fundamental data for development, quality control and durability prediction.

2.1.5 Differential scanning calorimetry (DSC)

The differential scanning calorimeter (DSC) is a thermal analysis instrument that measures the difference in heat required to heat a sample and a reference, keeping them at almost identical

temperatures throughout the experiment. The technique uses a linear heating programme, in which the temperature of the sample increases progressively over time. To obtain reliable results, reference samples with a heat capacity comparable to that of the sample undergoing thermal analysis are used, and at the same time, it must be stable in that temperature range.

The method allows the analysis of transition events such as melting, crystallisation, or other phase transformations, accurately determining the associated energy changes. It is particularly useful in the study of materials, chemical reactions, and biomolecule properties, thanks to its high precision, which can reach up to ± 0.1°C. Modern DSC can also distinguish between enthalpic changes and kinetic phenomena, thus providing a detailed picture of the thermal properties of a sample. There are several types of differential scanning calorimetry (DSC), each with specific characteristics:

- Heat-flux DSC: in this system, the sample and reference are placed together on a support equipped with temperature sensors. The temperature difference between the two is monitored and integrated to calculate heat flow variations. This type of DSC offers a compact, lightweight structure with low thermal capacity, while maintaining the functionality of a traditional DSC furnace.
- Power differential DSC: in this case, the sample and reference are placed in separate, thermally insulated furnaces. The temperature of both is kept identical, and what is measured is the electrical power required to maintain this condition of thermal equilibrium between the two chambers.
- Fast-scan DSC: a more recent technique that uses micro-machined sensors, capable of reaching extremely high scanning speeds (up to 106 K/s) and very high sensitivity, ideal for rapid analysis of phase transitions and thermophysical properties of thermally sensitive compounds..

- Nanocalorimetry: applied for quantitative analysis of rapid phase transitions, especially in materials and physical chemistry research, such as melting, sublimation, and vaporisation pressures.
- Temperature Modulated DSC (TMDSC): here, a sinusoidal temperature variation is superimposed on linear heating. This allows for better separation of overlapping effects, distinguishing between changes in heat capacity (e.g. glass transition) and time-dependent processes such as cross-linking or drying.

Differential scanning calorimetry (DSC) is based on the principle that when a sample undergoes a physical transformation, such as a phase transition, the heat required to maintain the sample and a reference at the same temperature varies. If the transformation is endothermic, such as melting, the sample absorbs heat and therefore requires more heat than the reference to maintain a constant temperature. Conversely, in exothermic processes, such as crystallisation, the sample releases heat and therefore requires less heat to maintain the same temperature.

During the experiment, the sample and reference are placed in identical crucibles inside a temperature-controlled furnace. The difference in heat flow between the two is then measured, allowing the energy absorbed or released by the sample to be quantified. DSC also allows more subtle physical changes, such as glass transition, to be observed. Due to these characteristics, it is widely used in industry for quality control, assessing the purity of materials and studying processes such as polymer cross-linking[18,19].

2.2 Carbon Brushes

On average, depending on production during the period, the waste consists of 28% copper, over 50% graphite, less than 2% tungsten disulfide or molybdenum, WS_2 and MoS_2 respectively, while the remainder is phenolic and/or epoxy resin. The function of copper and graphite is undoubtedly the high conductivity and self-lubricating properties of the carbon material. More specifically, dendritic copper is used because of its high surface area compared to other types of copper. Bisulphides, on the other hand, have a lubricating function in the mixing process. Finally, polymeric resins are added in varying percentages to promote cross-linking.

More precisely, the brushes are sliding components mounted in contact with the commutator. The brushes receive energy from the motor and are in sliding contact with the rotating parts (commutator), transferring electrical energy by sliding. The exchange of electricity can give rise to sparks, as the electrical transfer occurs due to the friction between fixed parts (brushes) and rotating parts (commutator), but obviously this sparking must be controlled to give the system stability and consistency in power delivery, also extending the life of the brush. Therefore, the engineering of the brush is essential in extending its life, the motor will last longer, and all this depends on numerous factors related to the production process.

The production process involves four different steps:

1. Mixing graphite with epoxy resin, which is added in an ethanol solution;
2. Addition of copper and other metals with variable percentages depending on the application;
3. Pressing. In this phase, depending on the application, a specific mould is used. Generally, the pressure applied is equal to 3 tonnes/cm² using eccentric presses, thus obtaining the so-called ‘green’ material.
4. 4. Curing or sintering: Here, the process is mainly regulated by the timing involved in reaching the final temperature or ramp (where an isotherm is set), the duration of the isotherm, in an inert (N_2) or reducing environment.(Forming gas, N_2/H_2 95:5).

The ramp in turn affects two factors, which are the surface area of the copper and the cross-linking of the resin.

5. At the same time, the temperature reached is essential for modulating the phenomenon of resin carbonisation once it cross-links, which, by carbonising, loses its insulating properties, as well as being subject to an increase in surface area

2.3 Materials and Methods

2.3.2 DTA

The thermal behaviour and stability of the powder samples were investigated using a Differential Thermal Analysis (DTA) system (TA Instruments). The samples consisted of a homogeneous mixture of 75 wt% carbon-based material and 25 wt% additive, prepared by manual mixing in an agate mortar to ensure uniform dispersion of the components. Approximately 5 mg of each sample was loaded into an alumina crucible, while an empty alumina crucible was used as a reference to establish the baseline thermal response.

Two distinct thermal programs were applied to evaluate the influence of the heating rate on the thermal evolution of the material. In the first case, the sample was heated at a constant rate of 1 $°C \cdot min^{-1}$ up to 450 °C, followed by a 1-hour isothermal to allow for possible stabilization or structural rearrangement, as already routinary done in the factory.

In the second case, aimed to tune the process, the heating rate was increased to 10 $°C \cdot min^{-1}$, maintaining the same final temperature and isothermal step duration. Both analyses were conducted under an inert nitrogen atmosphere (100 $mL \cdot min^{-1}$) to prevent oxidative phenomena during heating. After completing each isothermal stage, the furnace was allowed to cool to room temperature.

Subsequently, both samples were subjected to a final heating ramp up to 800 °C at a rate of 1 °C/min to assess the high-temperature stability and resistance of the carbon-based composite to thermal degradation. The DTA curves obtained from these experiments were carefully analyzed to evaluate morphological transformations occurring within the material.

In addition to thermal analysis, the DTA apparatus was also employed as a controlled heating furnace to perform pre-treatment and surface conditioning of the samples. This approach allowed the evaluation of surface area variations and morphological changes as a function of the applied thermal profile, providing complementary information to the microstructural characterization performed by SEM.

2.3.3 SEM Analysis

The morphological characterization of the samples was carried out using a Phenom XL scanning electron microscope (Thermo Fisher Scientific) equipped with a backscattered electron detector (BSD Full). SEM images were acquired at an accelerating voltage of 10 kV and a chamber pressure of 0.10 Pa.

2.4.1 Results

Using a faster heating rate shows an increase in terms of thermal stability of the sample towards higher temperature as reported in Fig. 13. Indeed, the faster program shows a higher thermal stability that can reflect a higher resistance towards corrosion due to the sliding action of the carbon brush on the commutator, demonstrating indirectly how the curing program can tune it.

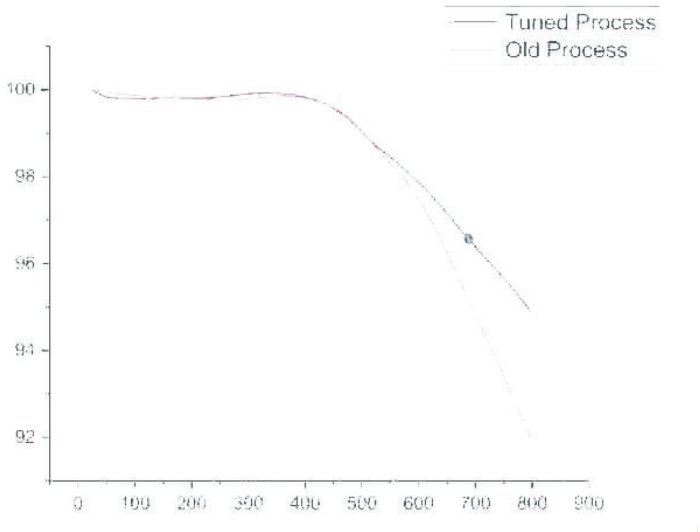

Figure 13: *TGA patterns of each sample at 1°C/min up to 800°C.*

The increase in resistance could be indirectly demonstrated trough the difference from a morphological point of view. Indeed, as shown in Fig. 14, the old process led to the fusion of copper dendrites, which doesn't occur with the tuned process.

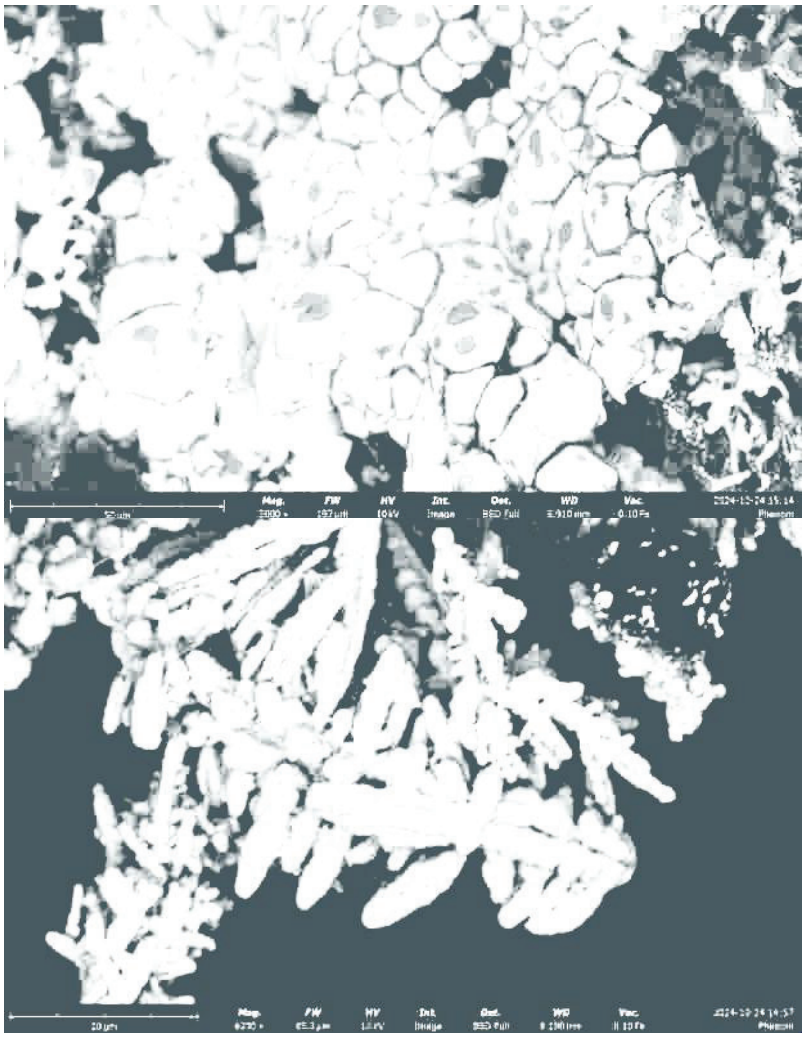

Figure 14: *A)1°C/min up to 450°C shows the fusion of dendrites. B) 10°C/min shows the preservation of dendritic structure*

2.5 Waste characterization

The waste consists mainly of graphite, polymer resin, and metals, primarily copper and/or tungsten and molybdenum disulphides.

Two different methods were used to separate the copper from the graphite.

Initially, an attempt was made to complex the copper, thus forming the tetramminodiacquarame complex using ammonia, $[Cu(NH_3)_4(H_2O)_2]^{2+}$.

Aqueous ammonia is added to the waste, promoting the following reaction:

$$Cu(OH)_{2\,(s)} + 4\ NH_4OH_{(aq)} \rightarrow [Cu\ (NH_3)_4(H_2O)_2]^{2+}{}_{(aq)} + 2\ H_2O + 2\ OH^-{}_{(aq)}$$

Since the waste copper is copper (0), oxidation and the consequent formation of hydroxide at basic pH are expected, which will then be complexed later.



Figure 15:photograph of blue ammonia-copper complex in water

Once the following separation has been carried out, the base body will consist of graphite, with copper content reduced from over 25% to a concentration of less than 1000 ppm, as confirmed by X-ray fluorescence analysis. To determine the copper concentration in the threated sample, we must account for the specific sample preparation used for the XRF analysis. Since the final volume was brought to

1 mL by adding an ammonia solution, the copper was stabilized as a tetraamminecopper(II) complex, which ensures a homogeneous liquid phase for a reliable reading.

Based on the XRF measurement of 772 ppm, the final concentration corresponds to 0.0772% p/p. This value represents the precise weight/weight percentage of copper within 1 mL of analyzed solution.

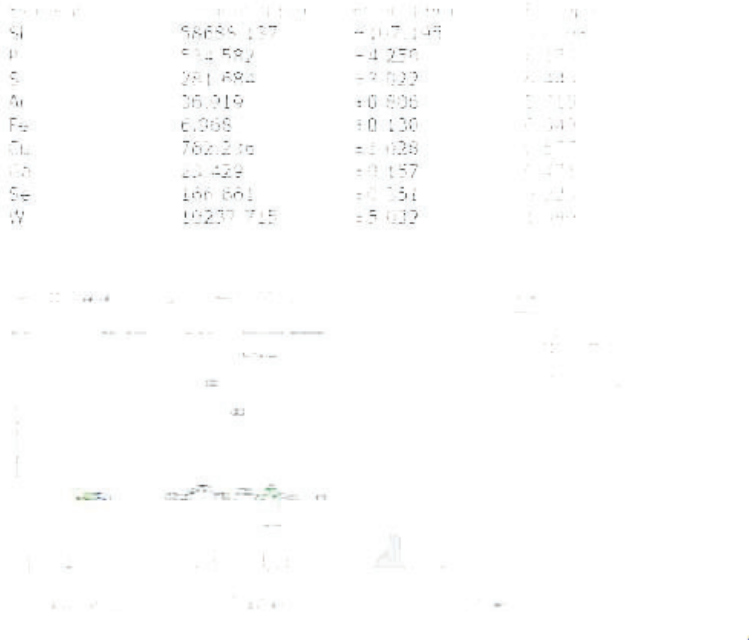

Figure 16:XRF report of quantification after the purification. DL: *Detection limit*.

The main problem with this method lies in the poor sustainability of the process, as ammonia is a toxic and highly irritating substance. Therefore, even if the aim were to recover it, however simple this may be, the risk of environmental pollution would be very high due to its high volatility.

For this reason, the flotation technique using heavy liquid medium was chosen.

Among the heavy liquids, sodium metatungstate was chosen. ($Na_6[H_2W_{12}O_{40}]$), a salt that dissolves in water, much safer than the classic iodoform, bromoform or mercury liquids.

In short, using an aqueous solution of sodium metatungstate, whose density varies with the concentration of the salt, the following can occur:

- A substance floats IF its density is lower than that of the medium;
- A substance sinks IF its density is greater than that of the medium;

Optimising the density of the solution so that it is intermediate between metallic copper (8.9 g/cm^3) and 2.2-2.4 g/cm^3 of graphite, it was possible to effectively separate the two components using a process that is:

a) Faster than separation with copper because processes can be accelerated by centrifugation;
b) Sustainable because it was possible to recover the medium for reuse.

3 Graphite

Graphite is a mineral consisting of carbon atoms, representing an allotropic form of carbon. In short, it is a structure consisting of more than hundreds of graphene sheets stacked on top of each other.

Graphite is found in nature, so it is subject to mining, or it is obtained artificially through the graphitisation process, where material such as coal is subjected to extreme temperatures (above 2000°C) which drastically reduces its defects, or through chemical vapour deposition of hydrocarbons.

It is the most stable allotrope of carbon under standard conditions, while at 4200°C it converts to diamond. Geologically, a slower conversion occurs in the upper mantle of the aarth at approximately 1500°C and pressures greater than 50,000 bar[20,21].

From a crystallographic point of view, it consists of sp^2 hybridised carbons with a trigonal planar geometry. The π electrons are delocalised above and below the plane and therefore contribute to Van

der Waals interactions between the individual layers, whose distance is 0.335 nm. The carbon atoms are arranged to form a honeycomb lattice with a bond distance of 0.142 nm.

There are two different allotropes, called alpha and beta, hexagonal and rhombohedral respectively, which differ in the type of stacking between graphene layers, whether these are ABA or ABC, with less stability for species characterised by ABC stacking.

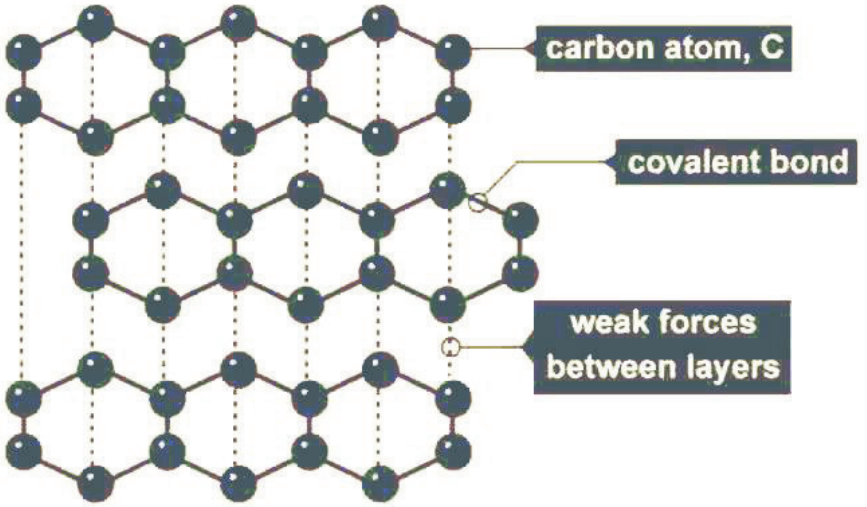

Figure 17:graphite structure that consists of many graphene layers stacked on each other.

Other allotropic forms of carbon are:

- Graphene;
- Carbon nanotubes;
- Fullerene;
- Diamond.

Among these, graphene is certainly of considerable interest. It was first isolated in 2004 by Geim and Noloselov, using a mechanical method called scotch tape, which involves applying tape to graphite powder and applying enough force to break the Van der Wasls between the layers, resulting in the isolation of a few layers.

The article in question, "Electric Field Effect in Atomically Thin Carbon Films", published in Science in 2004 describes the discovery and study of the electrical behaviour of thin atomic carbon films, i.e. graphene[22]. The authors show that it is possible to modulate the concentration of charge carriers in graphene by applying an electric field via a gate voltage, achieving charge densities of up to 10^{13} per cm^2 and mobility at room temperature of approximately 10,000 $cm^2/V \cdot s$. It is the fundamental work that led to the discovery of graphene, the two-dimensional material formed by a single atomic layer of carbon. This study was the basis for the awarding of the Nobel Prize in Physics in 2010 to Andre Geim and Konstantin Novoselov, who were honoured for their pioneering experiments on this unique material, isolated and characterised using extremely simple but innovative techniques, such as the use of adhesive tape to exfoliate graphite.

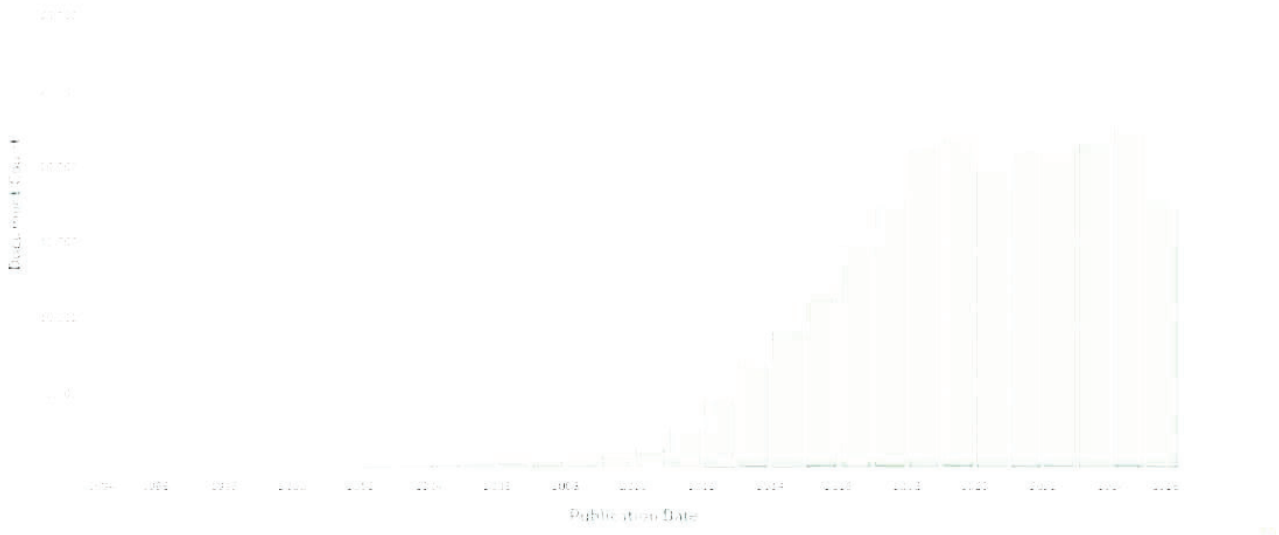

Figure 18: Patent application over time.

As shown in Fig. 18, patents related to graphene have begun to reach tens of thousands, with over 300,000 patents to date[23].

From a bibliographic production point of view, the numbers are very similar. In fact, Scopus shows more than 20,000 articles related to graphene per year. These results have been indicated to show the

significant impact of the material, first and foremost on the scientific community, and secondly, its industrial application, which is slowly gaining ground. The problem with this slowness is not due to the material properties, which are incredible in terms of mechanical strength, thermal conductivity, conductivity. In fact, it is characterized by incredible mechanical strength, thermal conductivity, conductivity having a hardness index (Mohs scale) equal to that of diamond, and at the same time, an extremely low weight, which makes it ideal for energy applications due to its high charge density, closely related to its large surface area. The only problem connected with its use is related with the difficulties related with the mass-scale production of this material.

3.1 Top-Down methods

3.1.1 Liquid exfoliation

The graphite is dispersed in organic solvents or water with surfactants and sonication, ball mills or shear mixing are applied in order to break the Van der Waals interactions between the graphite sheets, through mechanical energy generated, for example, during sonication by cavitation waves. Ball milling differs in that the powder is used as is, while the other two techniques are carried out in solution. The process can be optimised by intercalating ions such as Cs, K, iron, sulfate or hydrogensulfate and chloride. The limitation of this method lies in the heterogeneity of the material obtained, which varies in terms of flake size, low yield of exfoliation, and long exfoliation time and probable graphene oxidation.

The exfoliation methods are as follows:

> **Sonication:** the acoustic waves generated produce cavitation waves that lead to the generation of shockwaves stressing the material. These shockwaves propagate through the graphite, generating tensile stress. Due to the presence of multiple cavities, the resulting tensile stress causes the graphene layers to detach from each other.

The efficiency of the process and the amount of graphene produced depend heavily on the geometry of the vessel exposed to the sound energy and the dispersion volume. Graphene obtained by sonication has defects due to the high local pressures and temperatures generated by the cavitation phenomenon.

- **Shear mixing:** A rotor-stator system or rotating blade is used to agitate the graphite-containing suspension at high speed within a specific region, generating a shear force that allows the graphene layers to be exfoliated from the starting material. The solvents used can be NMP or water and surfactants.

3.1.2 Electrochemical exfoliation

A graphite rod is immersed in an electrolyte solution of ammonium sulphate, [$(NH_4)_2SO_4$] with a counterelectrode. When an electric current is applied, the electrolytes intercalate between the layers of the graphite rod, resulting in effective exfoliation of graphene sheets. The flakes are then collected by vacuum filtration and dispersed in solvents such as N-methyl-2-pyrrolidone (NMP). The adding of TEMPO (2,2,6,6-tetrametilpiperidin-1-il ossil) to the electrolyte can prevent the formation of ROS (produced by the electrolysis of water), that could damage the graphene. The as-obtained material is produced generally with high yields and can present low defects.

Electrochemical exfoliation of graphite generally occurs through ion intercalation, followed by expansion due to the gases produced. This process can be optimised by increasing the amount of ions intercalated during electrode pre-treatment.

Several studies have shown that preliminary treatment of graphite in concentrated sulphuric acid (H_2SO_4) significantly improves the yield and quality of graphene oxide (GO):

- Prolonged treatment in concentrated H_2SO_4 allows to increase GO yield from 10 to 50% by weight after 72 hours, with materials consisting of less than four layers and a C/O ratio of 5.
- Two-phase approach: the graphite is first charged to 2.2 V in H_2SO_4 95% for 10 minutes, producing intercalated graphite, then anodically exfoliated. The result is a high-yield GO. (>70%), high quality (>90% monolayer) and a low C/O ratio (3.2).
- Similar method of preintercalation consists of 50% H_2SO_4 at 1.6 V followed by 5 V anodic exfoliation. Changing the concentration of H_2SO_4 (40–60%), it is possible to control oxidation degree of GO, obtaining high oxidation degree (C/O < 2).
- Cathodic pre-treatment consists of applying −10 V for 30 s in 1 M H_2SO_4: H_3O^+ ions intercalate in graphite, making subsequent anodic exfoliation more efficient.

The anodic exfoliation is considered the most promising methodology for high exfoliation efficiency. It involves the intercalation of anions (negative species) in the graphite interlayers[24]. Applying a positive bias (positive current) to the graphite anode generates a positive charge that attracts bulky anion species (such as sulfate anions), which increase the gap between the sheets and assist their exfoliation. Various factors such as pH, voltage, and current density influence its quality[25]. Aqueous electrolytes such as H_2SO_4, HNO_3 and $HClO_4$ and their salts, are crucial for intercalation[26]

In summary, electrochemical pretreatments, both anodic and cathodic, increase the yield, quality and structural control of the GO produced[27].

3.1.3 Oxidative chemical exfoliation

The oxidative exfoliation of graphite is currently one of the most promising and widely adopted processes for preparing graphite oxide and its best-known derivative, graphene oxide (GO), which is now considered the raw material of choice for the large-scale production of advanced graphene

materials. In this approach, which is strongly driven by chemical oxidation, different oxygenated groups are progressively introduced into the carbon framework, distributing themselves heterogeneously on the surface of the basal planes. Their presence allows the intense van der Waals forces that keep the graphite sheets tightly stacked to be overcome, promoting extensive interlayer separation. The increase in interplanar distance is in fact a direct consequence of the insertion of these oxygenated functionalities, which alter the original structural order and give the solid a behavior profoundly different from that of the starting graphite. The chemical composition and structure of graphite oxide are strongly dependent on multiple factors, including the nature and strength of the oxidizing agents used, the characteristics of the graphitic precursor, and the operating conditions adopted.

Subsequently, by appropriate sonication treatment in suitable solvents the graphite oxide can be effectively exfoliated, giving rise to homogeneous suspensions containing single layer GO (SL-Graphene), few layers graphene (FLG), multilayer graphene (MLG).

Furthermore, GO can be converted to its reduced form, reduced graphene oxide (rGO), through a broad spectrum of reduction methods, each characterized by specificities, advantages, and limitations. Among these it is possible to find processes of thermal, chemical, electrochemical, hydrothermal nature, as well as innovative approaches based on microwave irradiations. Depending on the strategy, the final properties of the material can be tuned at will, giving rGO a central role in the development of advanced functional systems and emerging technologies.

Graphite oxidation can be achieved by following five well-established routes: the methods of Brodie, Staudenmaier, Hofmann, Hummers, and Tour. Over time, each of these approaches has been modified and optimized with the aim of achieving simpler, safer, and eco-driven procedures. In general, such methods are based on the reaction between a strong acidity (usually H_2SO_4, H_3PO_4 o HNO_3) and graphite, followed by the addition of an oxidizing agent like $KClO_3$, $KMnO_4$ o $NaNO_3$ capable of

oxidising the carbon surface andedges. This process facilitates the disintegration and expansion of graphitic planes[28].

Brodie's method

The first method for the oxidation of graphite was introduced by Benjamin Brodie in 1859. It involves the synthesis of multilayer GO by oxidation of graphite with $KClO_3$ and fuming HNO_3 at 60 °C for some days[29]. The as-obtained material (GO-BR) was dispersible in aqueous or alkaline media, but not in an acidic environment. After numerous oxidation, purification and drying steps, the final product showed a C, O and H content traceable to the general formula $C_{11}H_4O_5$ (C/O of around 2.2). During the litmus test, the material showed acidic behavior, prompting Brodie to coin the term "graphical acid". The main limitations of this procedure are the very long reaction time and the emission of toxic gases during the process.

Staudenmaier's Method

In 1898, L. Staudenmaier proposed a substantial improvement to Brodie's method by introducing an additional acid (H_2SO_4) and a slower and more controlled addition of the oxidant ($KClO_3$) [30].The innovations introduced consisted of adding small amounts of $KClO_3$ during the entire reaction, so as to reduce the risk of explosive products and excessive heat developments, and in increasing the acidity of the medium by concentrated H_2SO_4. The highly acidic environment allowed for the use of smaller quantities of fuming HNO_3, reducing the release of toxic gases such as NO_2 and N_2O_4 and making the approach relatively safer. The material obtained (GO-ST) presented properties similar to those of the GO-BR; however, the procedure remained long and dangerous, since the addition of $KClO_3$ took several days and the constant emission of ClO_2 had to be managed with inert gas.

Hofmann Method

In 1937, Hofmann proposed a slightly safer alternative based on the use of HNO_3 and $KClO_3$ to obtain a graphite oxide (GO-HO) with a lower oxygen content (C/O > 2.5)[31]. $KClO_3$, a strong oxidant, generates in situ highly reactive dioxygen species, while HNO_3 shows high reactivity towards aromatic carbonaceous surfaces such as graphite. However, even here the emission of toxic gases remains unavoidable.

In 1958, Hummers and Hofmann introduced the method that would mark a turning point in the chemical-oxidative exfoliation of graphite[32]. This approach proved to be the fastest and, overall, the safest of those available at the time to achieve GO (GO-HU), with a C/O ratio (2.25) very close to that of the GO-BR. The procedure uses excess of $KMnO_4$, H_2SO_4 and a small amount of $NaNO_3$. Initially graphite and $NaNO_3$ were dispersed in H_2SO_4 a 0 °C; $KMnO_4$ is then added slowly and the suspension kept at 35 °C. Afterwards, water is added and the system is brought to 98 °C for a short time. Eventually, H_2O_2 and water were added to eliminate residues of MnO_2, converting it into manganese sulfate and oxygen. The mixture is then purified by filtration, centrifugation and decantation to remove metal and acid residues. While safer than chlorate-based methods, the process still releases toxic nitrogen-based gases since $NaNO_3$ is transformed in situ in HNO_3. The GO obtained has sulphur residues (about 6%) and nitrogenous impurities due to the absorption or covalent presence of species from H_2SO_4 and HNO_3[30]. Although better balanced in terms of safety, speed and quality than previous methods, Hummers' method is still limited by toxic gas emissions and high temperatures[33], motivating numerous attempts to improve various operational aspects.

Tour method

In 2010, Tour[34] and collaborators further improved Hummers' method for obtaining GO with a high oxygen content. Instead of $NaNO_3$, a small amount of H_3PO_4 was used, an agent capable of promoting the etching and dispersion of graphite, in the presence of large quantities of $KMnO_4$ and H_2SO_4. The

materialis produced in high yields and is characterised by a high degree of oxidation and a more ordered and less defective structure than the products obtained through the previous methods (GO-BR, GO-HU and GO-ST). The formation of a more regular structure is attributed to the creation of five-membered cyclic phosphate groups between two vicinal diols in the basal plane. Compared to Hummers' method, this procedure generates a larger number of hydrophilic groups and does not release toxic gases, requiring only mild heating (50 °C). For these reasons, the improved method is considered safer, less toxic and particularly suitable for large-scale production[35].

To reduce the costs of industrial-scale production, attention is paid to processes conducted at room temperature or lower, as they limit thermal risks and generate less defective GO; however, these procedures are slower and less productive. The lateral dimensions of the flakes and the level of defects can be modulated by controlling various reaction parameters, such as amount of oxidant, type of graphite[36,37], dimensions of graphite flakes, graphite powders or microparticles[38], reaction time[38], temperature and intensity of mechanical agitation[38].

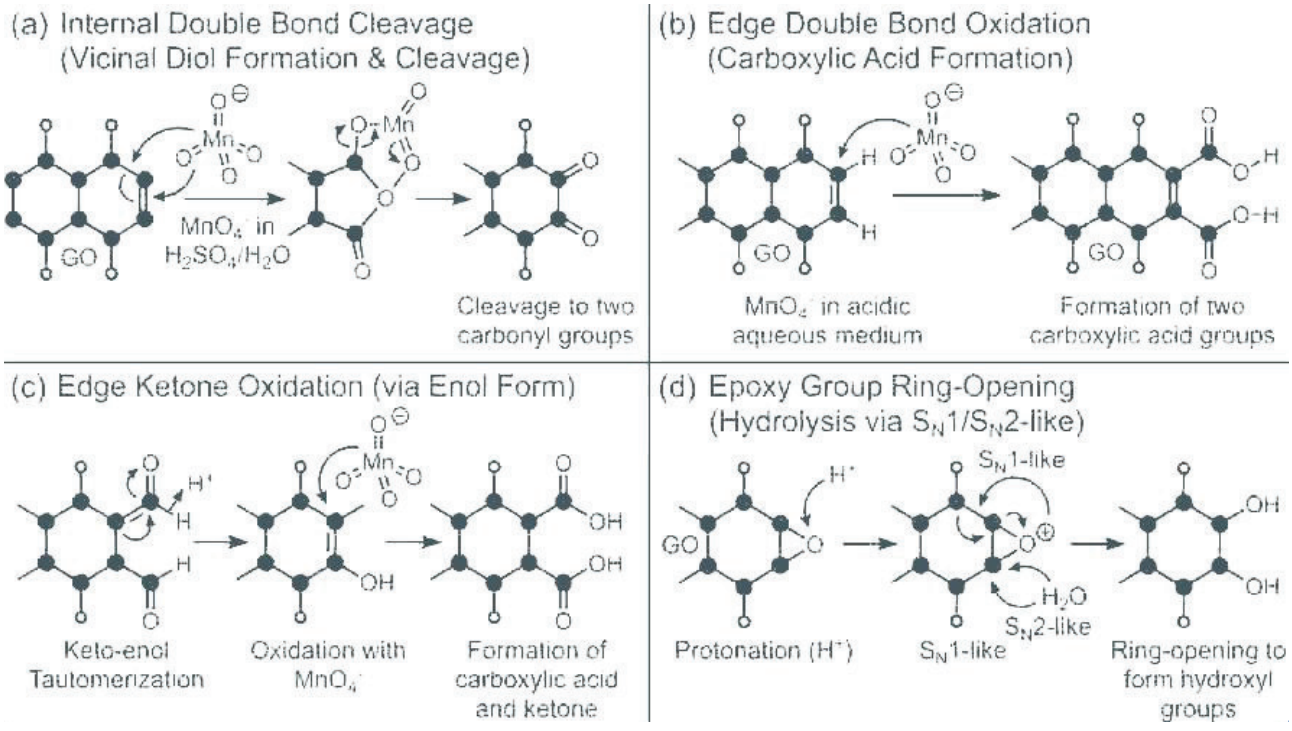

Figure 19:*Oxidation mechanism of graphite or graphite oxide through $KMnO_4$.*

3.1.4 Reduction of graphene oxide into reduced graphene oxide

rGO is a form of reduced GO with the aim of reducing the oxygen content and repairing defects present in the material, partially restoring the sp^2 graphenic structure. Several studies have reported that rGO possesses characteristics similar to those of pure graphene, especially with regard to surface, mechanical, thermal and electrical properties[39]. However, the product obtained after reduction is not identical to graphene, due to the presence of crystalline defects and oxygenated groups[40], which is why the material is more correctly called rGO. Despite surface defects, both GO and rGO have been widely used in numerous applications, including supercapacitors, batteries, water treatment, membrane separation, catalysis, biomedical, and smart textiles [41–43].

Among the most studied reduction methods are thermal reduction, microwave irradiation, photoreduction, hydrothermal reduction, electrochemical reduction, chemical reduction, and greener reduction pathways.

Thermal reduction

Thermal reduction of GO/graphite oxide by annealing represents one of the most widespread methods for the synthesis of graphene/rGO. During the process, GO is exfoliated into thinner sheets by rapid heating to high temperatures, in the absence or presence of an inert or slightly reducing atmosphere, or under vacuum. Heating causes the decomposition of oxygenated functional groups, which are released as gases; the expansion of these gases induces sheet separation. Part of the GO mass is lost during reduction in the form of CO_2, leaving structural damage and lattice defects.

The annealing temperature significantly affects the oxygen content, size and surface defects of the GO, in fact, high temperatures favour deoxygenation and defect care, which have repercussions on the conductivity[44] Negishi *et al.* demonstrated that reduction to temperature higher than 1000 °C in the presence of ethanol and H_2/Ar significantly restored the π-conjugated system[45].

Although a large plethora of studies have supported the hypothesis that reduction by heat treatment at high temperatures is extremely advantageous, there are nevertheless multiple and significant critical issues that limit the applicability of the thermal reduction method. Among these limitations stand out an onerous energy expenditure, attributable to prolonged heating to drastic temperatures, and the considerable expansion of process times, made necessary by an extremely slow heating rate to avoid the risk of catastrophic structural explosions. Furthermore, the essential need to assemble GO on substrates for various applications suggests that thermal reduction cannot be profitably applied to GO films deposited on substrates characterized by a low melting point (such as, for example, glass and polymeric materials[46].

Reduction by Microwave Irradiation (MWI)

Due to its intrinsic operational simplicity and excellent results achieved, microwave irradiation (MWI) has attracted increasing attention from the scientific community for the preparation of graphene by reducing GO, whether in the solid state, in solution, or by direct heating of intercalated graphite compounds. During the MWI process, direct energy transfer to the reagents ensures rapid and highly selective heating to extremely high temperatures, a condition which proves sufficient for a rapid reduction of GO[47].

Photoreduction

The photoreduction of GO is achieved through a photochemical process, a photothermal process, or a synergistic combination of the two. The most widely used method uses a photocatalyst to transfer electrons from sacrificial compounds to GO. While photothermal reduction is essentially based on thermal heating. In this process, the intrinsic energy of the photons is converted into thermal energy, which induces the reduction of GO[47].

Hydrothermal reduction

The hydrothermal method is routinely used to obtain controlled morphologies of different nanostructures under high pressure and high temperature conditions[48,49]. Recent studies have highlighted how the hydrothermal method can also be profitably applied for the reduction of GO in an aqueous environment. In hydrothermal reduction, a low-concentration aqueous GO solution is heated above the boiling point of water through an increase in applied pressure. Water heated above its boiling point generates a form of superheated/subcritical/supercritical water that can easily exceed the energy threshold required for GO reduction. Hydrothermal treatment of GO is pH dependent, reduces the number of oxygenated groups, and restores the sp^2 lattice in both acidic and basic media. It has also been shown that a solution at basic pH provides a better reduction of GO due to the absence of carbonyl groups[50]. Furthermore, rGO produced by hydrothermal treatment in basic media has fewer defects than that produced in acidic media, due to sufficient re-establishment of sp^2 domains as well as greatly improved C/O values.

Furthermore, the reduction time plays a crucial and determining role in the deoxygenation and restoration of GO defects during hydrothermal treatment. Therefore, during the hydrothermal treatment of GO, the reduction is governed by deoxygenation mechanics, while the restoration of the sp^2 lattice requires higher temperatures and longer times to improve the C/O ratio. However, there are disadvantages to maintaining a high temperature for a prolonged time: this reduces the size of the rGO flakes and produces a defective structure.

Electrochemical reduction

The electrochemical reduction of GO is a process that stands out for its simplicity and the fact that it can be conveniently carried out at room temperature. This is a not inconsiderable detail, which makes it inherently cheaper and greener. An aqueous buffer solution or a simple support electrolyte, preferably non-toxic, is used, which is a great advantage from an environmental point of view.

The key is GO itself. This material is first coated or deposited on a substrate that acts as a working electrode. These substrates can be of various types: sometimes they are conductors, such as carbon glass, indium tin oxide (ITO), or gold, other times, insulating supports are chosen, perhaps for flexibility reasons, such as ordinary glass or flexible plastics.

The mechanism is fundamentally driven by the electric current applied. It is this energy that triggers the reduction: in practice, we witness the elimination, or rather, the removal, of the clusters of oxygen-containing groups present on the GO structure. And while these oxygenated groups are removed, the rGO films are simultaneously formed and added to the surface of the working electrode.

It is interesting to note how the performance of this reduction can be "calibrated" by intervening on various parameters: the choice of electrolyte, the buffer solutions or the electrolysis parameters themselves. This gives considerable flexibility to the process[51].

This methd is particularly pappreciated because it is easy to perform, rapid, economically accessible and, as mentioned, environmentally friendly. It's one of the best ways to get high quality rGO.

Chemical Reduction

Chemical reduction is, undoubtedly, the most prominent method when aiming to obtain large quantities of graphene-like materials (rGO)[52]. The essence of this technique lies in immersing graphene oxide, previously deposited on a substrate in an aqueous solution or solvent, in a bath of chemical reducing agents. The great advantage of this process is its practicality and cost-effectiveness[53] being able to be made at room temperature or with mild heating, without the need for sophisticated instrumentation, thus making it ideal for full-scale production.

The choice of reducing agent is, in reality, the critical variable, a real compromise. If on the one hand we have extremely effective substances, such as hydrazine ,N_2H_4 and sodium borohydride $NaBH_4$, lithium aluminum hydride $LiAlH_4$ or hydrohalogenic acids (HI, HBr)[54]**,** on the other hand we cannot

ignore that many of these reductants are dangerous or toxic (hydrazine in particular)[55] Research is therefore pushing towards more eco-friendly alternatives such as ascorbic acid or plant extracts[56]. It is also important to consider that some reductants provide pure rGO, while others produce a functionalized rGO.

3.1.5 Arc Discharge technique

The use of electric arc discharge is a technique that has its roots in the chemistry of carbonaceous materials: it was way back in 1990, in fact, that Krastchmer and Hoffman demonstrated its effectiveness for the first time in preparing fullerenes C_{60}[57]. Today, this method is elegantly adapted for the production of graphene. The heart of the process is an arc discharge chamber (or furnace) which consists of a water-cooled steel vacuum chamber, inside which are housed the electrodes: a sacrificial graphite rod (the anode, which wears out) and a cathode, also made of graphite. To trigger synthesis, a constant (DC) or alternating (AC) current is passed through the electrodes as they come into contact. This generates a plasma and, crucially, causes vaporization of the anode. Graphene forms right inside this incandescent plasma and then deposits on the walls of the chamber in the form of black soot. The gaseous atmosphere inside the chamber plays a direct and determining role in the type of graphene that is generated, in particular its purity or doping. In time, numerous atmospheres were tested, including helium (He), hydrogen H_2, argon Ar, ammonia, NH_3 and carbon dioxide CO_2.[58–60].The arc discharge process is particularly appreciated because it lends itself to the production not only of pure graphene, but also of graphene doped with heteroatoms such as nitrogen, boron, and fluorine. Arc discharge is considered a potential technique for the production of doped graphene sheets.

However, the method is not without disadvantages that limit its widespread application:

1. .Lack of Control: there is a difficulty in controlling the formation of graphene.

2. Non-Optimal Doping: there are problems with unwanted doping and the low amount of controllable elemental doping.
3. Geometric difficulties: it is complex to make large electrodes.
4. Energy Costs: the energy-intensive nature of the process and the need for high-precision control hinder its full use for the industrial production of graphene.

3.1.6 Mechanical exfoliation

In mechanical exfoliation, graphite is exfoliated detaching its layers, using normal and lateral forces to overcome the weak van der Waals forces that bind the crystal planes, a mechanism that, unlike liquid-phase techniques, does not rely on cavitation.

Scotch-Tape method

This method, which deserved a Nobel Prize, is remarkably simple, based on the repeated application and removal of adhesive tape (scotch tape) on highly oriented graphite (HOPG) to peel through very thin layers. The flaws are its laborious nature and very low yield[61], limiting its use to the laboratory scale only.

Diamond-Wedge method

To seek greater scalability than the "scotch tape", Jayasena and Subbiah [437] introduced the single crystal diamond wedge method. An ultra-sharp wedge remains stationary as a HOPG pyramid slowly moves toward it, with the help of a high-frequency oscillation system. When the wedge touches the graphite, the surface layer is cut (cleavage) and collected, for example in a water bath[62]. Although it is capable of producing thin-layer graphene (FLG), it is not yet a method for large-scale production.

Ablation

Similar to the diamond wedge in that it uses mechanical erosion to thin graphite, in this method a rotating pencil lead moves toward a rotating disk of glass or quartz. The abrasive action (ablation) of the contact generates eroded graphite, which is then sonicated in solvents such as toluene or ethanol to extract the graphene[63]. The yield is remarkable (60-70%) and the product has an average thickness of 5-8 layers. The subsequent replacement of the mine with a graphite disk simplified the multi-step process[64].

Ball-Milling

Ball milling is another mechanical approach in which both normal and lateral forces are used[65]. However, excess normal forces from collisions can destroy the crystalline structure of graphene, causing fragmentation rather than exfoliation. For this reason, it is crucial to balance the forces, preferring shear forces (shear forces). For example, Zhao *et al.* have[66] used a low rotation speed of 300 rpm to promote flaking, obtaining after 30 hours a graphene with an average thickness of three layers. Efficiency can be increased by adding chemicals or surfactants, an approach known as wet ball milling, similar to liquid-phase exfoliation. *Lin et al.* used oxalic acid[67] for selective edge carboxylation, a process analogous to the Scotch tape method that improves delamination under shear forces.

3.2 Bottom-up Methods

3.2.1 The Epitaxial Growth of Graphene

Epitaxial growth is a highly refined deposition process, which, in its broadest sense, refers to the formation of a monocrystalline film on a substrate that is also monocrystalline. This produces an epitaxial film, characterized by a perfect atomic alignment or arrangement between the two layers. In

the specific context of Epitaxial Graphene (EG), the process results in the thermal synthesis of graphene sheets on a single-crystal Silicon Carbide (SiC) surface[68]. Although this method is renowned for producing graphene with extremely high crystallinity, it has two inherent and significant limitations: the use of exceptionally high temperatures and the inability to easily transfer graphene to other substrates for subsequent applications.

EG synthesis occurs when SiC crystals are heated to about 1300°C under ultra-high vacuum conditions. This heat causes the selective desorption of silicon atoms, leaving the carbon free to rearrange into graphene layers. The orientation of the SiC crystal is crucial and determines the nature of the growth. Advances in EG have been driven by studies aimed at controlling the thickness and size of the crystalline domain. Berger's group was among the first to synthesize ultra-thin graphite films (typically three graphene sheets) demonstrating that the thickness was predominantly temperature-controlled[69]. Rollings *et al.* further refined the technique by treating the samples in situ with silicon flux, managing to produce EGs with atomic thicknesses, up to 1-2 layers and microscopic dimensions[70].To overcome size and quality limitations, several research groups have developed ingenious variants to grow EG[71]. *Emtsev et al.* introduced ex situ graphitizationunder an Argon atmosphere at an elevated pressure of 900 mbar, as an alternative to the traditional high vacuum[72]. This approach allowed for better control of the Silicon sublimation rate, improving the surface morphology and obtaining monolayer films with wider 3x50 μm^2 domain sizes. Tromp and Hannon obtained comparable results but using a Si flow method (with disilane gas), managing to improve the quality of graphene through precise regulation of the Si vapor pressure[73]. These advanced approaches highlighted how manipulating the growth environment, in particular managing the Si partial pressure, is key to achieving the goal of a large-area EG with superior crystalline quality.

3.2.2 Chemical vapour deposition

The Chemical Vapor Phase Deposition (CVD) process represents one of the most established and versatile methodologies for the fabrication of high-quality solid films by the chemical vapor reaction of specific precursors on a solid substrate. This technique, for the synthesis of graphene, typically requires a well-defined tubular furnace system configuration, which necessarily includes three fundamental components: a gas delivery system (gas delivery system), a reactor and, finally, a gas and by-product evacuation system. The synthesis of graphene classically begins with the introduction into the reaction chamber of a gaseous mixture, composed of a carbon precursor (e.g., methane, CH_4), carrier gases such as Ar, and, in some cases, hydrogen H_2 which acts as the activation gas of the process. Subsequently, the thermal action of the furnace triggers the decomposition of the precursor, whose reactive species deposit carbon on the substrate, forming graphene on its surface. The most widely used substrates for this purpose have historically been Cu or Ni foils or films. The process ends with the expulsion of by-products and unreacted gases during the cooling phase[74].

It is crucial to emphasise that CVD-synthesised graphene grows on the surface of a metal catalyst, thus making a transfer process mandatory for metal removal and subsequent deposition of graphene on the final substrate intended for specific application. This transfer is often described as an aggressive step, which can induce deterioration and contamination of the nanomaterial surface.

Since its introduction for graphene synthesis, the CVD technique has undergone impressive diversification, with the introduction of numerous optimized variants. The use of different types of precursors, not limited to purified gases alone, but extended to solids, liquids, and even carbon-rich waste materials, has significantly broadened the spectrum of synthetic possibilities. In parallel, various materials for the substrates have been explored, among which nickel, copper, platinum, germanium and copper-nickel alloys stand out[75], although Cu and Ni remain the most studied and popular. Depending on the required parameters, different CVD system configurations were employed to improve the quality of graphene and maximize the amount produced, including atmospheric

pressure CVD (APCVD), low pressure CVD (LPCVD), ultra-high vacuum CVD (UHVCVD), and cold wall CVD.

The idea of applying CVD to graphene synthesis emerged in 2006, when Somani *et al.* proposed adapting this technique, already used for nanotube synthesis, using camphor as a precursor and Ni substrates. This first effort led to the obtaining of what was called "few-layer planar graphene", consisting of about 35 graphitic layers, paving the way for further refinements of the process[76].

In the following years, attention focused on obtaining higher-quality graphene and on larger areas.

In 2008, Yu and collaborators documented the formation of graphene on Ni foils using CH_4 as a carbon precursor, by a process known as surface segregation. They highlighted the crucial role of cooling rate and H_2 annealing of the substrate to improve its quality[77]. The following year, almost simultaneously, three separate research groups deepened APCVD synthesis on Ni films deposited via e-beams on Si/SiO_2 substrates. These pioneering studies not only demonstrated the possibility of fabricating devices such as FETs (Field Effect Transistors), but also highlighted how reducing the thickness of the Ni substrate and adopting shorter growth times could favor the predominance of mono- and bilayer graphene[78–80].

2009 marked a major breakthrough with the first documentation of a large-scale, high-quality, and uniform Cu synthesis. It was found that the growth of graphene on Cu acted through a self-limiting, surface-catalyzed mechanism, a phenomenon radically different from the precipitation/segregation process observed with Ni. It was hypothesized that this was related to the low solubility of carbon in copper, which prevents metal saturation and, consequently, limits growth once the surface is entirely covered[81].

It was confirmed, in the case of Ni, that carbon atoms initially diffuse and mix in the material and then segregate and precipitate on the surface, forming graphene. Conversely, on Cu, graphene is formed by a surface adsorption mechanism; once the entire surface is covered by the nanostructure,

growth stops due to the absence of additional Cu catalytic sites available for CH_4 decomposition. This crucial difference in carbon solubility in Cu has proven to be the key to the synthesis of graphene over a wide area[82].

In parallel, the investigation of a wide range of suitable metal substrates has developed. Kang and his team demonstrated that other metals with lower C solubility than Ni could be used, such as $Pt/SiO_2/Si$ films, obtaining single- and multi-layer graphene through careful control of the 1050°C-1250°Ce synthesis temperature of the surface morphology[83].

Gaseous precursor evolution

Since graphene is composed of only carbon atoms, in principle, any carbon source can be used as a precursor. Among the gaseous precursors, methane CH_4, ethylene C_2H_4 and acetylene C_2H_2 are the most typically used. The choice is crucial, as it impacts implementation difficulties and operating conditions, which is why different CVD configurations have been tested.

- Acetylene: Due to its higher reactivity than methane, acetylene allows for lower synthesis temperatures. In 2010, Nandamuri and his group reported APCVD synthesis on Ni films and foils, demonstrating that deposition could be achieved at temperatures below 600°C-700°C and that Ni thin films were more suitable for obtaining monolayer graphene[84].
- Ethylene: Ethylene is known to possess an intermediate reactivity between methane and acetylene[85], which gives an intermediate growth temperature but greater process controllability. As early as 2008, De Parga and co-authors had used it for the synthesis of corrugated monolayer graphene on Ru(111) through UHVCVD[86]. Subsequently, it was also successfully employed in an APCVD configuration on Cu at about 800°C[87]. Furthermore, the use of C_2H_4 has been recognized as a more ecologically sustainable procedure than CH_4[88].

The Use of Liquid and Solid Precursors

Although most CVD systems have been developed for gaseous precursors, the use of liquid- or solid-phase precursors has gained considerable interest, primarily for the purpose of reducing costs and reducing the risks associated with the use of more flammable gases such as CH_4, thus aiming for a larger industrial-scale synthesis. These states of matter require, however, alternative delivery systems. For liquids, bubblers or heating systems are used that evaporate them, then introduce the particles into the reaction zone via a carrier gas or H_2[89,90]. For solids, quartz boats or containers are used, heated near the metal substrate to decompose the carbon[91].

Liquid precursors

Numerous liquids, particularly alcohols and aromatic compounds, have been tested. In 2010, Miyata *et al.* documented the synthesis of high-quality monolayer graphene with large grain sizes on Ni foils in APCVD, implementing a "flash cooling" technique and using ethanol as a precursor[92]. In the same year, Srivastava and his group developed an LPCVD technique on Cu foils using hexane, obtaining continuous and large-scale graphene[93]. In the same year, Srivastava and his group developed an LPCVD technique on Cu foils using hexane, obtaining continuous and large-scale graphene[94].

A comparative analysis by *Gadipelli et al*. on a wide range of liquids (methanol, ethanol, benzene, hexane, toluene, acetic acid, and acetone) under the same operating conditions showed that benzene, and in particular methanol, produced the best quality graphene. Methanol was further distinguished by the absence of amorphous carbon and its ability to act simultaneously as a source of carbon and hydrogen[95]. Particularly surprising results were obtained by Li et al., who, using benzene on Cu in LPCVD, succeeded in obtaining high-quality monolayer graphene at exceptionally low temperatures of 300°C, demonstrating that strategic selection of precursor and CVD setup can dramatically reduce thermal requirements[89].

Attention has gone as far as the use of waste materials. Maarof et al. demonstrated that even refined cooking palm oil (a household waste) could be used to synthesize large-area monolayer graphene, thanks to an innovative spray-injector-assisted CVD system (SIA-CVD). This setup, with a nozzle and Cu substrate positioned at a controlled distance, optimized the decomposition kinetics, achieving optimal coverage of 97% at approximately 950°C[96]. Recenlty, Intaro *et al.* utilised a direct injection chemical vapor deposition (DLI-CVD), that is useful because it is possible to manage higher concentration of liquid without a bubbler. By using cyclohexane C_6H_{12} as precursor and N_2 as vector, process optimization was achieved at 950°C and 0.5 g/min[97,98].

Solid precursors

Solid precursors also offer significant advantages. Sun and colleagues demonstrated the possibility of synthesizing large-area, high-quality graphene using polymers, such as poly(methyl methacrylate) (PMMA). The polymer was deposited (spin-coated) on top of the Cu or Ni metal catalyst, and LPCVD synthesis could be achieved in just 10 minutes at temperatures approximately 800°C lower than previously reported values[99]. Subsequent studies of PMMA and polystyrene on Cu foils confirmed that, although graphene formation could begin as early as 400°C, the optimal large-scale quality was achieved at around 800°C.

Particular emphasis was given to the use of natural precursors. Ahmed et al. reported the synthesis of monolayers on Ni substrates in APCVD using camphor, at temperatures between 850 and 870°C[100]. A further line of research has focused on the use of solid waste materials. Ruan et al. demonstrated that nearly any type of carbon-containing waste, including chocolate, biscuits, grass, plastic, cockroaches, and dog feces, could be transformed into high-quality graphene pristines in LPCVD on Cu at approximately 1050°C[101].

The polycrystalline nature of CVD graphene represents a limitation for its electronic and mechanical properties. To overcome this limitation, research has focused on nucleation control in order to

synthesize single crystal domains of considerable size. The composition, geometry and arrangement of substrates within the CVD chamber were explored.

- The use of Catalytic Alloys. In 2011, Weatherup and colleagues demonstrated the effectiveness of Cu-Au alloys as LPCVD and APCVD substrates. The addition of Au significantly reduced the nucleation density of graphene, facilitating better control over uniformity and growth, and allowed monolayers (74%) to be obtained even at low temperatures 450°C[102]. Chen et al. explored Cu-Ni alloys by combining the advantages of both metals. They found that the thickness and quality of graphene could be controlled by modulating the temperature and, in particular, the cooling rate (optimals temperature values were 975°C and 100°C/s)[103]. Subsequently, Huang *et al.* obtained the rapid (5 min) growth of single crystal graphene on Cu/Ni(111) alloys[104].

- Substrate Geometry (Enclosures). A significant geometric innovation was introduced by Li and co-authors, who developed a technique using Cu foil envelopes or "pockets" for LPCVD synthesis. Graphene grown within these envelopes exhibited a dramatically lower core density, much larger crystalline domains, and a lower ad-layer density, phenomenon that was hypothesized to be due to the lower partial pressure of the precursor and unwanted species within the confined space[105]. Yang *et al.* confirmed and detailed the advantages of this approach: reduction of the precursor partial pressure (which decreases the nucleation density), high Cu partial pressure (better annealing) and lack of of SiO_2 residues [106]. Subsequently, Luo *et al.* demonstrated that the application of a sputtered outer layer of W and Mo to the Cu envelopes acted as a diffusion barrier and as a sink for excess carbon, suppressing nucleation and facilitating monolayers[107].

The large-scale synthesis of graphene, essential for its commercialisation and integration into industrial applications, has found a strategic response in the variant of CVD namely Roll-to-Roll Chemical Vapor Deposition (R2R CVD**)**. This methodology, which represents the adaptation of a

consolidated continuous production technique to the nanotechnology field, was proposed and tested for the first time in 2011 by *Hesjedal et al.*

The R2R CVD system is essentially configured as a traditional CVD setup integrated with a continuous tape substrate handling mechanism. This system is composed of a dispensing roller (pay-off roll) and a winding roller (winder roll system) which provide, respectively, for supplying the metal substrate sheet (typically Cu foils) and for collecting the final product.

With this pioneering methodology, Hesjedal demonstrated the feasibility of continuous growth of few-layer graphene on a 1-meter-long copper foil, operating under ambient pressure conditions and at temperatures close to 1000°C.[108]

This first result was crucial, as it unequivocally demonstrated that large-scale graphene synthesis was technically achievable, opening up concrete scenarios for industrial implementation.

However, the introduction of this technique made it necessary to consider new critical parameters closely related to the dynamic nature of the process, such as:

- The heating time and rolling speed of the tape.
- The interaction of reactive species (CH_4, in the case of Hesjedal) with the substrate during the heating phase.
- The cooling rate of the catalytic foil, which is directly dependent on the chosen rolling speed.

The large-scale synthesis of graphene, essential for its commercialisation and integration into industrial applications, has found a strategic response in the CVD variant known as Roll-to-Roll Chemical Vapor Deposition. [108].

In the years immediately following, several research groups devoted themselves to refining the setup to optimise the quality and length of the graphene produced.

Significant progress was achieved by Kobayashi *et al*., who reported the synthesis of a graphene ribbon as long as 100 meters. Their approach made use of a low-pressure variant, R2R LPCVD, using Cu as a substrate and implementing an efficient Joule heating system to reach 1000°C. The system was conceived inside a sealed stainless steel vacuum chamber with internal winders.

Operating at a rolling speed of 0.1 m/min, the entire growth process on the 100-meter substrate took 16 hours. The most important result was the demonstration that the use of lower pressures allowed to obtain better quality graphene, with a significant predominance of monolayer films[109].

3.2.3 Laser-assisted procedures

To address the growing need for graphene synthesis methodologies that are fast, clean and precisely localized, we have seen the development of techniques that exploit the concentrated energy of lasers as devices characterised by monochromaticity, coherence and directionality[110]. Laser-assisted procedures have emerged as powerful and versatile tools in a variety of application areas[111].

Laser-Induced Graphene (LIG)

Laser-Induced Graphene (LIG) is , characterized by a porous three-dimensional structure, obtained by selective irradiation of a carbon-based precursor with an infrared laser, although other types of laser sources have also been successfully employed[112,113].

This revolutionary technique offers the advantage of combining the preparation and modeling (patterning) of 3D graphene in a single step, eliminating the need for wet chemical steps[114]. The laser works by inducing a photochemical and photothermal transition in the substrate with a spatial precision that is difficult to match by traditional thermal techniques. The mechanism involves laser irradiation triggering the rearrangement of carbon atoms into a hexagonal lattice; subsequent

evolution and escape of gases from the precursor produces the characteristic porous, interconnected network of the LIG[116].

The LIG typically consists of a percolating network of porous multilayer graphene[115], which gives it excellent properties, including a high surface area (around 340 m^2/g) remarkable thermal stability (up to 900°C) and excellent conductivity.

The first report on this technique, in 2014, was the work of Tour's research group. They synthesised porous graphene by irradiating a commercial insulating polyimide film with a long-length infrared laser under ambient conditions.

As evidence of the versatility of the technique, the same group in 2018 developed an approach for the formation of porous 3D LIG not only on modified polyimide, but also on commonly used lignocellulosic materials such as wood, potatoes and bread. The results demonstrated the formation of LIGs with abundant folds, particularly when irradiation occurred in an inert or reducing atmosphere, using a defocused laser beam[115]. To address the application needs, two strategies for the roll-to-roll mass production of LIG were also proposed, integrating laser irradiation with the electrolytic deposition of catalysts for the creation of hybrid materials[116].

Laser ablation

A methodological alternative is represented by Laser Ablation, an approach that uses pulsed laser irradiation for the ablation of carbon targets, typically for the synthesis of carbon nanostructures, including graphene-based materials, under different environmental conditions (liquid, vacuum or gas). The main advantages of this procedure lie in its simplicity, reduced costs and the possibility of operating without the need for vacuum systems[117].

The first example of 2D graphene formation by ablation was reported by Qian *et al.* in 2011, through pulsed laser exfoliation of HOPG (Highly Oriented Pyrolytic Graphite). Using an Nd-YAG laser with

a wavelength of 532 nm and a pulse duration of 7 ns, carbon nanostructures were obtained, including few-layer graphene films with a thickness of a few nanometers and dimensions in the order of tens of micrometres[118].

Particularly noteworthy are studies using the liquid phase as an ablation medium, since the liquid acts as a temperature suppressor and facilitates the stabilization of exfoliated nanostructures. Kiran *et al.,* in 2017, synthesized FLG by femtosecond laser ablation of graphite powder suspended in ethanol at room temperature[119]. Subsequently, studies on nanosecond laser ablation in different liquid media (acetone, dimethylformamide and deionized water) also demonstrated that the use of acetone was particularly effective in producing high-quality graphene nanosheets with microfolded edges and thicknesses of less than ten layers.

In a variation of this technique reminiscent of liquid-source CVD, Huang *et al.* reported in 2020 a method for the rapid growth of graphene over a large area, using extra virgin olive oil as the liquid precursor[120].

3.2.4 Flash Graphene

In recent years, research has proposed solutions for graphene synthesis aimed at achieving not only high quality, but also a greater quantity of material more economically. The Grafene Flash fits into this perspective as an extremely promising option.

This technique, first reported in 2020 by Tour's group, uses the Joule Flash FJH Heating mechanism to rapidly convert any carbon source into what is called FG.

The methodology is based on the application of a high-intensity electrical discharge (coming from a capacitor bank) to an amorphous carbonaceous material placed between two electrodes inside a ceramic tube. The Joule action induces the achievement of extremely high temperatures 2700°C in a

very short time, less than 100 ms. This intense heat converts the precursor into a turbostratic through a bottom-up approach[121].

The crucial advantages of this technique are:

1. Precursor Versatility. Various solid carbon precursors can be used, including coal, petroleum coke, biochar, carbon black, discarded foods, rubber tires, and even mixed plastic waste.
2. Efficiency. No solvents or reactive gases required.
3. Quality. The obtained graphene has a low degree of defects, positioning itself among the best synthesized materials so far.

Tour's team also demonstrated the exceptional economic efficiency of the process: converting plastic waste into FG requires an estimated total energy cost of around $125/ton, an extremely cost-effective method for recycling waste into high-value-added materials[122]. Studies have also established that the process duration must be maintained between 30 and 100 ms to achieve optimal results; longer processes could lead to the formation of a material more similar to graphite[123].

4 Graphene applications

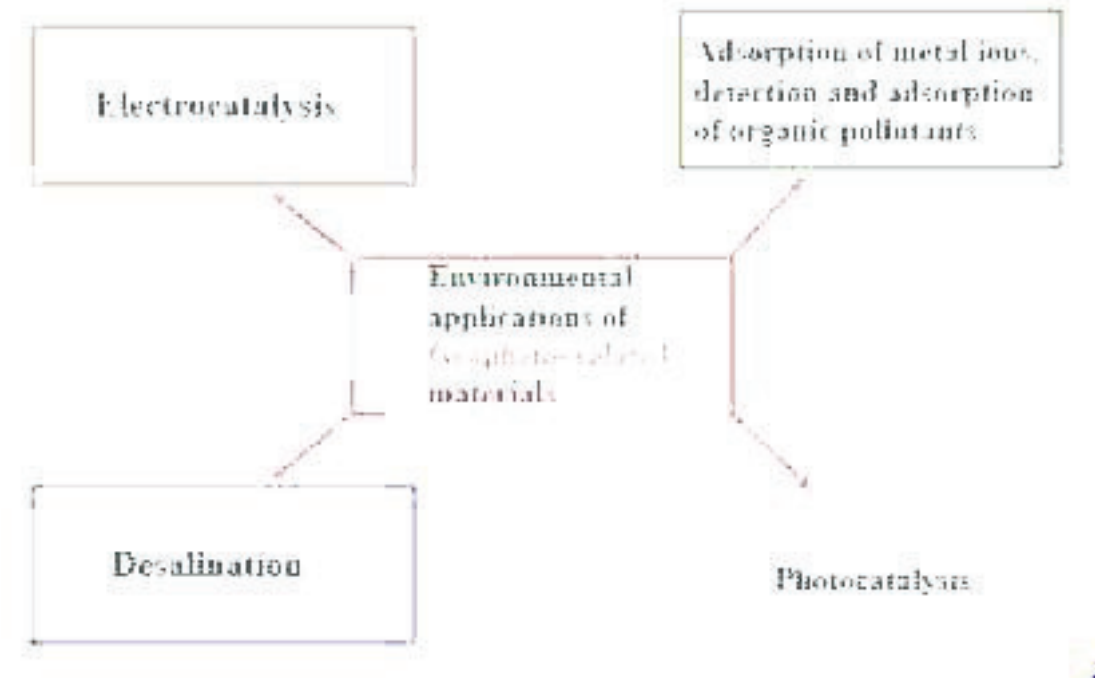

Figure 20: *Graphene environmental applications scheme.*

4.1 Detection of pollutants

Sensors based on graphene-based materials are emerging as extremely promising tools for detecting pollutants in wastewater. Their attractiveness stems mainly from two fundamental characteristics: on the one hand, the ability to miniaturize them down to nanometer dimensions, resulting in integration into portable or even wearable devices; on the other, their intrinsic high sensitivity to a wide range of chemical species, which allows for very low detection limits even in complex matrices.

However, despite these particularly favorable properties, the use of graphene and its derivatives as sensory platforms also presents some critical aspects. In particular, residual functional groups and side chains present on the surface of the material can interact non-selectively with unwanted molecules present in the sample. This leads to a strong dependence of sensor performance on environmental conditions, such as ionic strength, pH and temperature, and often results in spurious

or false positive responses[124]. Precisely to mitigate these unwanted effects, two main strategies have been developed: surface blocking and sample pretreatment.

Surface blocking typically involves the use of small molecules that saturate or shield the non-selective reactive sites present on graphene, thus reducing nonspecific adsorption. Sample pretreatment, on the other hand, is based on the preventive removal of interfering species in order to stabilize the matrix and ensure optimal conditions for analytical detection.

To achieve high selectivity towards the molecular target of interest, graphene-based sensors are further functionalized by anchoring highly specific biomolecules or ligands. These include antibodies, enzymes, selective polymers, and aptamers, each of which has chemical or biological affinities for a certain analyte.

The versatility of these sensors has favored their use in numerous application fields: the clinical sector, environmental monitoring and quality control in the food sector. In the environmental field, graphene-based sensors have proven particularly effective for the detection of heavy metals (such as Pb^{2+} and Cd^{2+}), pesticides and persistent organic compounds[125].

Another notable application is that developed by *Li et al.*[126], who realized a non-enzymatic electrochemical sensor consisting of graphene nanosheets combined with a gadolinium-based Prussian blue analogue (GdHCF), deposited on a glassy carbon electrode. This system allowed the detection of pesticides, with a quantification range between 0.008 and 10 μM and a detection limit of just 1 nM, once again demonstrating the effectiveness of the synergy between graphene and functional materials.

The usefulness of graphenic-based sensors, however, is not limited to chemical pollutants alone: pathogens can also be detected with high sensitivity. In fact, a field effect transistor (FET) based on micropatterned rGO and functionalized by rotavirus-specific antibodies, immobilized by a 1-pyrenbutyric N-hydroxysuccinimide ester, has been designed[127]. This device is able to detect

concentrations of the order of 10^2 pfu (Plaque Forming Units per milliliter), showing higher sensitivity than the conventional ELISA method.

Finally, recent developments have shown how integrating graphene with plasmon resonance phenomena in the terahertz domain (0.1–10 THz) can lead to further increases in sensitivity. A grounded graphene-based nanofluidic sensor, integrated between two additional graphene sheets, achieved a maximum sensitivity of 8470 nm/RIU (nanometers per Refractive Index Unit), marking one of the best performances reported in the literature for this class of devices[128].

The application of graphenic materials was then also extended to the removal of pesticides and drugs, both of which are frequently present in urban and industrial wastewater. For example, *Zhang et al.* used a cellulose-graphene oxide composite to adsorb the pesticide ametryn, achieving a maximum capacity of 8.53 mg g^{-1} at pH 9.0 and 298 K[129]. An even more marked improvement was observed by Boruah et al., who, by using a Fe_3O_4–GO hybrid material operating at pH 5, achieved approximately seven times higher adsorption capacity, highlighting the importance of integration between graphene and magnetic nanoparticles[130].

4.2 Organic pollutants

The strong abundance of π electrons in graphene also favors significant interactions with many pharmaceutical molecules, which often exhibit extended aromatic systems. This makes graphenic materials particularly suitable for the adsorption of pharmacologically active compounds. Lin et al. demonstrated the efficacy of an Fe_3O_4–GO composite for the removal of the antibiotic tetracycline: with an initial concentration of 50 mg L^{-1}, varying pH and stirring time, a maximum capacity of 39.10 mg g^{-1} was achieved. Organic dyes, often released by textile and tanning industries, can also be effectively removed using graphene-based magnetic composites. It also proved[131] that a graphene/Fe_3O_4 magnetic nanocomposite can increase the fuchsin dye removal efficiency from

82.2% up to 99.4%. When the material concentration exceeds 0.4 g L^{-1}, the adsorption equilibrium is reached, keeping the removal rate constant. The entire process follows pseudo-second-order kinetics, typical of chemical adsorption mechanisms. In addition to classical organic contaminants, a further environmental problem strongly linked to modern industrial activities is represented by the spills of oils and hydrocarbons into water bodies. To address this emergency, superhydrophobic materials characterized by high adsorption capacity and, above all, good reusability are being developed. A recent example is the one proposed by Khalilifard and Javadian[132], who made a magnetic superhydrophobic polyurethane sponge obtained through the connection of graphene oxide to a matrix functionalized with oleic acid and nanoparticles of Fe_3O_4. The material was able to be used for up to 15 adsorption cycles without showing any significant deterioration in oil removal capacity, demonstrating the potential of such systems for repeated environmental remediation operations.

4.3 Metal Ions

Heavy metals, such as arsenic, mercury, cadmium, chromium, and lead, are a major source of contamination in industrial wastewater. Their origin is often linked to activities such as electrodeposition, mining, the manufacture of batteries and microelectronic devices. The presence of these metal ions in the environment has harmful effects on human health, fauna, and flora, making it essential to adopt effective strategies for their removal from industrial wastewater. Among the various available techniques, adsorption using graphene-based materials has established itself as one of the most promising and effective methods[133].

The adsorption mechanism of heavy metals on graphenic materials, especially graphene oxide (GO), can be described through three main modes:

1. Electrostatic interaction. Functional species on the surface of graphene, often negatively charged, attract positive metal ions present in the liquid. This represents the simplest and most immediate mechanism for metal ion sequestration.

2. Ion exchange. Oxygenated groups such as –COOH and –OH present on the graphene surface interact with metal ions, promoting an ion exchange process in which metal ions are adsorbed while protons present in the functional groups are released into the solution. This mechanism increases the specificity and efficiency of adsorption[134].

3. Surface Complexation. In this case, metal ions bind directly to oxygenated functional groups present on the graphene surface forming stable complexes. Unlike ion exchange, proton release does not occur. This mechanism plays a predominant role in the adsorption of Pb(II) ions, ensuring a high selective affinity[135].

Studies report that the affinity of graphene oxide for different metal ions follows the order: Zn(II) < Cd(II) << Cu(II) < Pb(II), highlighting how lead is among the most easily adsorbable ions[135].

In recent years, attention has also shifted towards the recovery of rare earth metals, for which the use of nanomaterials has proven effective, although some post-adsorption structural modifications have limited applications. To address this problem, an innovative approach has been developed that integrates graphene materials with reusable supports, such as polyurethane sponges impregnated with titanium phosphate and graphene oxide, prepared by in situ precipitation. This strategy allows not only high adsorption capacity, but also the possibility of recycling and reusing the adsorbent material, making the process more sustainable and cost-effective.

4.4 Photocatalysis

Graphene oxide (GO) is configured as a functionalized derivative of graphene, whose two-dimensional atomic scaffold is enriched by a variety of oxygen-containing functional groups. The presence of such chemical moieties not only radically alters the surface properties of the material, giving it an intrinsic and marked hydrophilicity that promotes its colloidal stability in aqueous environments, but also profoundly modifies its electronic profile. In particular, the GO exhibits an energy bandgap approximately equal to 3.26 eV, a value that, according to what is reported in the literature[136], it is not static, but susceptible to fine modulation operable through strict control of the degree of oxidation of the carbon lattice.

The application potential of graphene oxide in heterogeneous photocatalysis has been extensively documented by several lines of research. In experimental settings aimed at reducing resazzurin to resorufin, nanostructured graphene oxide has demonstrated excellent efficiency: the reaction mechanism is triggered by the transition of electrons from the ground state following the absorption of photons in the ultraviolet (UV) spectrum, proceeding according to a pseudo-first-order kinetic model. In parallel, the efficacy of GO was tested in the degradation of persistent organic pollutants, such as 4-chlorophenol; the results obtained by Bustos-Ramírez et al. (2015) indicate an almost total degradative capacity (97%) over a time span of only 120 minutes, using a catalyst dosage of 0.8 g/L[137].The use of graphene oxide in solar-to-fuel processes, specifically in the conversion of CO_2 into liquid or gaseous fuels, also appears to be of particular scientific importance. Under visible irradiation, GO showed selectivity towards methanol production with a conversion rate of 0.172 μmol $g^{-1}h^{-1}$, outperforming traditional titanium dioxide TiO_2 catalysts by an order of magnitude, almost six times[138]. Finally, comparative analyses conducted by Kuang *et al.* on the photocatalytic reduction of CO_2 to carbon monoxide (CO) highlighted how lighting conditions drastically influence yields,

establishing an efficiency ratio of 2.7:2.1:1 between the use of simulated sunlight, UV radiation and baseline conditions, confirming the exceptional optical versatility of this nanomaterial[139].

Although semiconductors intrinsically possess the properties necessary to act as photocatalysts, thanks to their ability to generate charge separation and flexibility in modulating the band gap, their integration with graphene has become a predominant strategy to enhance its quantum efficiency. In such hybrid systems, graphene acts primarily as an electron acceptor, mitigating the phenomenon of charge-hole recombination. Numerous metal oxides[140], TiO_2, Cu_2O, ZnO as well as metal sulfides[141] like ZnS and CdS, have been extensively coupled to graphene to exploit these synergies.

A prime example is the nanohybrid composed of zinc oxide and graphene oxide, successfully used in the photodegradation of the dye Crystal Violet (CV). Similarly, self-assembled GO-TiO_2 nanorod composites have been investigated for the degradation of Methylene Blue under UV irradiation. The photocatalytic activity of ZnO-reduced graphene oxide (rGO) systems can be further optimised by acting on synthetic methodologies; the adoption of sonochemical procedures, for example, has been shown to significantly increase the efficiency in the degradation of Rhodamine B[142].

In addition to environmental remediation through pollutant degradation, graphene-based photocatalysts find crucial applications in clean energy production, specifically in H_2 generation and the conversion of CO_2 into solar fuels[143].

In more recent developments, research has turned towards even more complex ternary systems, such as rGO-TiO_2-ZnO and rGO-TiO_2-Cu_2O[144,145].

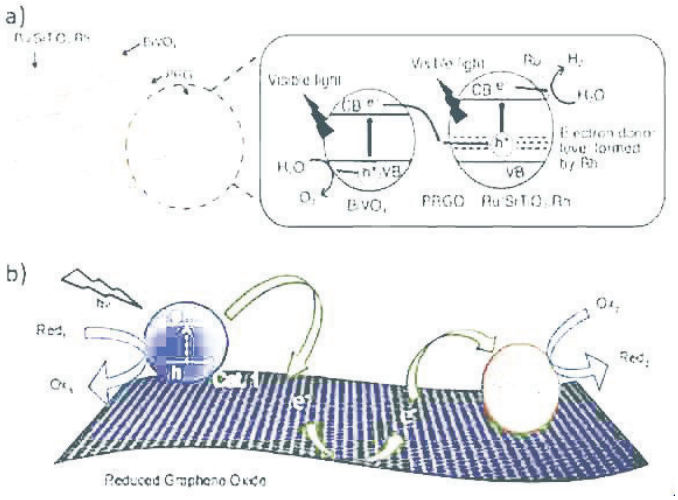

***Figure 21**: Schematic illustration of the photocatalytic system. (a) Proposed photoinduced charge-transfer mechanism in the Ru-based photosensitizer/semiconductor assembly under visible-light irradiation, showing electron excitation, interfacial electron injection, and proton-coupled reduction pathways. (b) Conceptual representation of reduced graphene oxide (rGO) acting as an electron-conducting platform connecting two catalytic sites (Cat. 1 and Cat. 2), where photogenerated electrons and holes are spatially separated to drive simultaneous oxidation and reduction reactions (e.g., CO_2 reduction) under illumination.*

4.5 Electrocatalysis

HER (Hydrogen evolution reaction)

The current paradigm of high-purity hydrogen production converges decisively towards electrocatalysis, surpassing photocatalysis processes in efficiency[146–148]. The technological heart of this transition is represented by electrolyzers, devices responsible for the molecular splitting of water (OWS), in which the hydrogen evolution reaction (HER) occurs at the cathode 0 V, while the oxygen evolution (OER) occurs at the anode + 1.23 V. However, the intrinsic kinetic slowness of HER and OER requires the use of catalysts to mitigate the high overpotentials that limit the industrial applicability of the process[149].

Although the noble metals (Pt, RuO_2, IrO_2) represent the performance standard, their scarcity and prohibitive cost[150], together with structural degradation phenomena such as carbon corrosion or aggregation of active sites[151], search for durable alternatives imperative. In this scenario,

nanostructured carbonaceous materials emerge as candidates of choice due to their excellent electrical conductivity and versatility of physicochemical properties[152,152].

Among the different allotropic forms of carbon (0D, 1D, 2D, 3D)[153,154], graphene stands out for a two-dimensional morphology with sp^2 hybridization which allows for unprecedented electronic modulation. Although pure graphene shows limited activity, its nanostructuring and chemical doping dramatically enhance its reactivity for HER[155]. Recent literature has extensively documented the potential of derivatives such as reduced oxide graphene (rGO) and quantum dots (GQD), highlighting how synergistic coupling with other materials can significantly lower energy barriers, including that of the complex oxygen reduction reaction (ORR), characterized by a high binding energy of 498 kJ/mol[156].

Despite the profusion of studies on collateral applications[157,158,159], it is interesting to fill the documentary gap regarding the progress made specifically in the field of graphene-based electrocatalysts for HER and OWS in the period 2018-2020. Mechanistically, in an acidic environment, hydrogen production is described through the sequential formation of Hads adsorbed intermediates following the Volmer, Tafel and Heyrovsky pathways:

- i) $H^+ + e^- \rightarrow {}^*H_{ads}$
- ii) $H_{ads} + H_{ads} \rightarrow H_2 + 2*$
- iii) $H_{ads} + H^+ + e^- \rightarrow H_2 + *$

Although the acidic environment favors rapid proton transfer kinetics, the use of noble metals such as platinum is limited by economic barriers, while more accessible metals, such as nickel, present critical issues in terms of structural stability. Therefore, the fundamental parameters for quantifying catalytic efficiency remain the exchange current density and the Tafel slope. In an alkaline environment, the mechanism evolves as follows, including the necessary dissociation of water:

- **i)** $H_2O + e^- + * \rightarrow H_{ads} + OH^-$

- **ii)** $H_{ads} + H_{ads} \rightarrow H_2 + 2*$
- **iii)** $H_{ads} + H_2O + e^- \rightarrow H_2 + OH^- + *$

Despite the metallic stability and ease of hydrogen diffusion in a basic environment, HER is intrinsically slower due to the high energy required for water molecule cleavage in the Volmer stage. Consequently, the selection of the ideal catalyst must necessarily balance the chemical stability and steric availability of the active sites.

In particular, strategies aimed at optimizing electrocatalytic properties are:

- Doping with heteroatoms (metallic and non-metallic);
- Synthesis of porous structures and surface functionalization;
- The design of nanostructured and three-dimensional (3D) morphologies.

The electrochemical and electronic properties of graphene-based materials can be modulated with extreme precision through various methodologies[160], among which doping with heteroatoms (both metallic and non-metallic), chemical functionalization and structural engineering stand out. The doping process can be carried out essentially according to two protocols: the carbonization of precursors enriched with heteroatoms in an inert atmosphere, or by post-synthetic treatments which, although requiring the use of toxic gases (like NH_3 for N-doping or SO_2 for S-doping), ensure strict control over the final composition. Recently, however, milder and safer precursors, such as melamine and urea, have been introduced, which allow homogeneous mixtures to be obtained through mechanical mixing processes followed by heat treatment.

A wide range of heteroatoms, including N, S, P, O, B, Cl, Br and I, have been investigated to enhance the electrocatalytic aptitudes of graphenic nanomaterials[161]. Structurally, the insertion of Boron (B), given its dimensional similarity to the carbon atom, does not induce drastic alterations in the lattice, limiting itself to generating a slight increase in bond lengths. In contrast, Nitrogen (N), due to its

electron-rich character and the ability to participate in both sp^2 and sp^3 hybridizations, induces a significant distortion in the planarity of graphene. Furthermore, the high electronegativity of nitrogen introduces a marked polarization effect within the carbon matrix. Phosphorus (P), although possessing a lower electronegativity, causes even more accentuated lattice distortions due to the larger atomic radius and the availability of d orbitals, which expand the possibilities of electronic interaction[162].

Nitrogen is the dopant that has catalyzed the greatest academic interest, manifesting itself mainly in three chemical configurations: N-pyridine, N-quaternary and N-pyrrole. Electronically, pyridine and pyrrole forms contribute to the π system of graphene through electron donation from π orbitals while quaternary nitrogen stably integrates within the basal plane, altering the density of electronic states and facilitating charge transfer during electrocatalytic processes.

Research has recently focused on the development of advanced graphenic materials doped simultaneously with metals and non-metals. Li et al. synthesised nitrogen-sulfur (N,S-G) co-doped graphene by one-pot calcination, achieving excellent performance for HER with an overpotential of only 0.29 V for a current density of 10 mA/cm^2 in 1M KOH[163].

The geometric control of the active sites takes on particular importance. It has been shown that the atomic dispersion of cobalt on basal planes of nitrogen-doped graphene allows the formation of coordinated Co-N and Co-S sites, which dramatically accelerate the Faradaic reaction kinetics at the interface. These systems showed reaction initiation potentials (onset potentials) of just 10 mV[164,164]. The use of Co-P cobalt phosphides supported on graphene sheets prevents the aggregation of nanostructures and facilitates electron transfer due to the mechanical stability of the carbon matrix[165]. Similarly, the integration of cobalt selenides ($Co_{0.85}$-Se) on rGO highlighted extremely small Tafel slopes (36.1 mV dec^{-1} in acid solution), confirming superior cyclic stability (beyond 1500 cycles).

A crucial strategy to prevent electrode degradation in corrosive environments is the encapsulation of metal nanoparticles within layers of graphene or carbon nanotubes[166]. Although encapsulation can partially shield the active sites, it positively modulates the electron spin density and charge distribution through electron transfer between the metal and the carbon shield[167].

Paradigmatic examples include bimetallic catalysts (Cu-Ni alloys) encapsulated in porous nitrogen-doped graphenic structures, where the coating thickness is tunable via the calcination temperature. These architectures demonstrated overpotentials of 122 mV on average with competitive Tafel slopes[168].

Given the onerousness of monolayer graphene on an industrial scale[169], reduced graphene oxide (rgo) is the most viable alternative. Composites based on rGO and transition metal dichalcogenides (TMDs), such as WS_2 and MoS_2[170,171], benefit from a synergistic effect in which graphene inhibits the agglomeration of TMDs and promotes charge transport. Ternary systems (es. $rGO/WS_2/WO_3$) showed superior HER kinetics with Tafel slopes of 37 mV/dec^{-1}.[172]

The most advanced frontier of electrocatalysis is represented by single-atom catalysts (Single-Atom Catalysts, SACs). The hexagonal structure of graphene sp^2 provides the ideal substrate for atomic dispersion, ensuring maximum exposure of catalytic centers and high mass loading[173]. Since isolated atoms cannot be doped directly into pristine graphene, defect or doped sites (N, B, O, S) are used as anchor points.

Recent studies by Xu et al. have highlighted how the activity of SACs depends closely on the coordination number and electronegativity of adjacent atoms. Exceptional results were obtained with Platinum, Pt, atoms dispersed on nitrogen-doped porous carbon, which required an overpotential of only 13 mV to reach 10 mA/cm^2 with a Tafel slope of 34 mV/dec^{-1}.[174]

5 Graphene Bioapplication

In the domain of biomaterials science, the essential requirement for any construct intended for biological integration is biocompatibility. Pioneering investigations into the cytophysics of graphene initially produced sometimes antithetical or inconclusive results[175], a drift attributable to the intrinsic novelty of the materials, the absence of a systematic taxonomy[176,177] and to the methodological complexities arising from the deeply interdisciplinary nature of nanobiotechnology[178].

The alleged antibacterial properties of graphenic materials represent a paradigmatic example of the controversies surrounding biocompatibility. Although initial studies had postulated universal bactericidal activity for such allotropes[179,180] a systematic evaluation carried out by a research consortium at the University of Manchester showed how the cytotoxic activity against *Escherichia coli* was actually determined by the presence of residual impurities from the synthesis process, such as sulphur, boron and sodium nitrate[181].

In subsequent years, it has been established that the cellular response is a function of a complex set of physicochemical parameters, including the synthesis protocol, the degree of purity, the number of layers, lateral dimensions, edge effects, defect density, doping (intentional or fortuitous) and surface functionalization[182,183]. Understanding these critical variables today allows for a rational bioengineering approach aimed at the synthesis of cell-friendly graphenic materials and the fabrication of biocompatible biointerfaces. In this sense, green chemistry methodologies are favored[184] and rigorous purification protocols aimed at eliminating cytotoxic contaminants. Furthermore, the use of substrates integrated with large-area graphene can mitigate the physical damage resulting from the sharp ends of nanoscale sheets, while the use of micrometer-sized flakes (> a few microns) or hybridization with polymer, polysaccharide or hydrogel matrices prevents endocytosis processes and the generation of parasitic redox species.

Currently, scientific consensus converges that appropriately engineered graphenic materials are not only biocompatible but often superior in providing a biomimetic microenvironment suitable for cell proliferation, differentiation, and development[185,186]

To assess graphene-induced cellular stress, several studies have monitored highly sensitive physiological indicators, such as autophagy levels, mitochondrial morphology, and membrane potential[187–189]. These investigations confirmed the absence of detectable adverse effects, suggesting instead that graphene positively modulates cell-substrate interactions, promoting cell adhesion through unique surface topography and adaptive surface chemistry.

The excellent biocompatibility was further validated in in vitro models of cardiac syncytium (e.g. neonatal rat ventricular cardiomyocytes, cardiomyocytes derived from mouse embryonic stem cells or human induced pluripotent stem cells) grown on planar rGO or graphene substrates by chemical vapor deposition (CVD). Finally, in vivo evidence from zebrafish embryos injected with graphene flakes (5–20 μm) showed baseline heart rates analogous to controls and full long-term viability, definitively corroborating the biological safety profile of the material[190].

The integration of graphene-based substrates represents a frontier of exceptional interest for cardiac tissue bioengineering, by virtue of their superlative biocompatibility with monolayer cultures of cardiomyocytes[191]. Such platforms emerge as a superior alternative to conventional supports such as Matrigel, commonly used in cardiomyocytic differentiation protocols starting from stem cells[192]. It has been widely documented that the incorporation of graphene into synthetic extracellular matrices significantly enhances the degree of maturation and electrophysiological properties of cardiomyocytes derived from human induced pluripotent stem cells (hiPSC-CMs), which, under standard culture conditions, tend to retain embryonic rather than adult-type phenotypes.

Recent experimental evidence conducted on hiPSC-CMs grown on single layers of graphene showed a markedly more mature phenotype, characterized by increased density and alignment of myofibrils,

overexpression of gap junction protein connexin 43 (Cx43) and an acceleration of the pulse conduction velocity, which evolves from values of 2.2 cm/s to 5.3 cm/s. In parallel, a refinement of calcium homeostasis is observed: the expression levels of ryanodine and pump receptors Ca^{2+}-ATPasi of the sarco-endoplasmic reticulum are increased, producing calcium transients with significantly larger amplitudes[188]. These phenomena suggest that the intrinsic conductivity of graphene is able to mimic the electrical microenvironment of the native myocardium, facilitating the propagation of electrical signals and driving cell maturation.

The versatility of graphene allows the creation of hybrid substrates that combine multifunctional biological and mechanical properties. A paradigmatic example is made up of collagen/graphene composite substrates, where the protein component provides the necessary biochemical support, while graphene modulates the elastic modulus (stiffness) and imparts an electrical conductivity similar to that of human cardiac tissues. Cardiomyocytes derived from murine embryonic stem cells cultured on such matrices exhibit improved alignment and morphological elongation associated with more defined cross-striated sarcomerate structures, unequivocal indicators of advanced structural maturation[193].

Similarly, the use of hybrid scaffolds made of reduced graphene oxide (rGO) and collagen induced, in only seven days, a substantial improvement in the mechanical and electrical properties of myocytes, with a concomitant upregulation of genes involved in electrical coupling (Cx43), muscle contraction (Troponin-T) and cytoskeletal organization (Actinin-4), regardless of the application of external electrical stimuli[194].

Further research indicates that graphene promotes the uptake and correct conformational presentation of matrix proteins such as vitronectin. Cardiomyocytes on vitronectin-coated graphene show enhanced expression of cardiomyogenic markers even in the absence of exogenous differentiation factors, suggesting that the material may induce mesodermal and endodermal lineage signaling pathways essential for cardiac development[195].

Finally, the engineering of nanopatterned anisotropic scaffolds, obtained by transferring graphene films onto topographic polymer substrates, has allowed the production of cardiomyocytes with excellent functional properties. These cells exhibit increased Z-band width, longer sarcomeres, and longer action potential duration, confirming how the combination of topographic stimuli and electrical conductivity is key to achieving a functional adult cardiac phenotype[196]. Considering that in vivo cardiac tissues exhibit an intrinsically three-dimensional morphology, the design of engineered cardiac tissues (*Engineered Heart Tissues, EHTs*) that replicate its geometric organization is imperative to ensure a correct recapitulation of intercellular coupling and complex physiological functions. The integration of graphene within 3D scaffolds gives the construct an anisotropic nanotopology and superior electroconductive properties, enabling not only structural support but also in situ electrophysiological stimulation and monitoring through the matrix itself.

In this perspective, graphene foams are configured as spongy scaffolds characterized by a network of interconnected pores, an extended surface area and a surface topography ranging from the nanometer to the micrometer scale. Compared to planar (2D) substrates, this architecture facilitates more efficient cellular communication and optimal transport of oxygen and nutrients. Neonatal rat cardiomyocytes integrated into graphene-enhanced nickel foams demonstrated high biocompatibility and overexpression of the Cx43 gene, which occurred even in the absence of direct electrical stimulation[196]. Furthermore, the development of electrically active graphene foams allowed the simultaneous recording of extracellular action potentials during cell culture[197].

An alternative strategy involves the direct incorporation of graphenic materials into 3D preparations. This approach has been observed to increase the differentiation rate of 3D embryoid bodies and improve their mechanical and electrophysiological properties[198]. Under electrical stimulation, these graphene-enhanced constructs exhibited more mature sarcomeric structures and superior physiological activity.

Clinically and therapeutically, Park et al. combined graphene oxide (GO) flakes with mesenchymal stem cells (MSCs), finding more effective engraftment of cells at sites of ischemic injury[199]. GO addition works by counteracting oxidative stress (ROS) typical of the ischemic environment and preventing anoikis (cell death induced by loss of adhesion), enhancing the therapeutic efficacy of cell transplantation. This study also highlighted how paracrine secretion of engrafted cells promotes angiogenesis and significantly reduces the infarcted area.

Finally, the biofabrication frontier explored the creation of complex multilayered cellular constructs. Through the sequential deposition of poly-L-lysine/GO nanofilms between homogeneous cardiomyocyte layers, it was possible to obtain three-dimensional structures with an elastic modulus of approximately 10 kPa[200]. These architectures showed increased expression of α-actinin and sustained vigorous spontaneous synchronous contraction 20-30 bpm, confirming the role of graphene as a pivotal element for the realisation of functional and biomimetic cardiac tissues.

The use of electrospinning (electrospinning) techniques for the production of three-dimensional scaffolds has allowed the development of nanofibrous matrices characterised by enhanced mechanical and electrical properties, ideal for interfacing with myocardial tissue[201]. The integration of graphenic materials within these polymer constructs not only acts as structural reinforcement, but enables active electrical stimulation of seeded cell populations.

Hitscherich *et al.* used electrospinning to create a 3 D polycaprolactone (PCL) scaffold enriched with homogeneously distributed graphene, observing marked enhancement of intercellular coupling and calcium homeostasis in cardiomyocytes derived from murine embryonic stem cells. This improvement is supported by overexpression of Connexin 43 (Cx43), superior sarcomeric organization, and a significant increase in the amplitude of calcium transients, increasing the fraction of calcium ion release per single beat[202].

Incorporation of reduced graphene oxide and silver (rGO-Ag) nanocomposites into polyurethane nanofibers demonstrated excellent biocompatibility and superior cell adhesion for human cardiac progenitor cells. In these systems, significant upregulation of key cardiospecific genes, such as GATA-4, Tbx18 and Troponin T, was detected[203].

Similarly, the integration of graphene (in concentrations ranging from 0.25% to 1% by weight) into nanofibrous scaffolds composed of polycaprolactone and polyglycerol sebacate (PCL/PGS) induced an increase in electrical conductivity, a balance of hydrophilicity and an increased surface roughness. These physical parameters positively influenced cellular kinetics, promoting adhesion, migration, proliferation and viability of human cardiomyocytes in a manner proportional to the fraction of graphene introduced[204].

Further advances have seen the use of electrospinning for the synthesis of hydrophilic scaffolds composed of PCL, chitosan, polypyrrole and graphene. This configuration has proven capable of emulating with extreme fidelity the elasticity and electrical conductivity of native myocardial tissue, supporting the biological and functional performance of mESC-derived cardiomyocytes[205].

The integration of rGO nanosheets into silk fibroin (SF) scaffolds allowed to optimize the nanotopology and electromechanical properties of the construct. When used for cardiac differentiation of hiPSCs transfected with the TBX18 gene, these scaffolds showed accelerated maturation and robust gene expression[206]. Alternatively, deposition of a single layer of rGO on the surface of electrospun fibroin substrates produced similar results, improving the electrophysiological maturity of neonatal rat cardiomyocytes through enhanced surface conductivity[207].

The evolution of microfabrication methodologies, such as microcontact printing, has allowed the creation of genipin-crosslinked gelatinous hydrogels containing graphene oxide (GO) with defined microstructured patterns. *Zhang et al.* demonstrated that neonatal rat ventricular cardiomyocytes, cultured on such substrates, exhibit parallel alignment to micropatterns and a substantial increase in

structural and functional maturity. This phenotypic evolution is supported by early cellular binucleation, more extensive sarcomeres, overexpression of key genes such as Actn and cTnT, and the establishment of synchronized uniaxial contractions within 48 hours, maintained for over three months[208].

The integration of reduced graphene oxide (rGO) into gelatin methacrylate hydrogel (GelMA) gives the material synergistic electromechanical properties. Comparative studies between GO, rGO and carbon nanotubes have highlighted how rGO-GelMA scaffolds, due to their superior conductivity, are more effective in promoting the rod-like morphology of cardiomyocytes and the expression of functional markers (Cx43, Troponin I). Furthermore, modulation of conductivity influences the electrophysiological phenotype: while GO-GelMA tends to induce atrial-like profiles, rGO-GelMA favors mixed atrioventricular phenotypes, while enhancing cellular mechanosensors (integrin, vinculin) for more robust contraction[209].

The use of decellularized extracellular matrices (dECMs) from porcine myocardium, combined with rGO, allowed the creation of scaffolds with tissue-specific protein profiles and tunable stiffness. These systems induced multifunctional improvements in calcium management, contraction force and conduction velocity[210]. Similarly, the use of polydopamine-based chitosan/GO composite hydrogels showed a 300% increase in bond strength and superior mechanical stability due to supramolecular interactions and hydrogen bonding, supporting higher spontaneous beat frequencies[211].

In the context of irreversible myocardial damage from infarction, the main challenge lies in the integration and survival of implanted cells (MSCs or cardiomyocytes) at the ischemic site. Graphene-enriched injectable hydrogels have proven to be excellent carriers for enhancing cell engraftment. For example, rGO-enhanced alginate hydrogels doubled the viability of MSCs compared to traditional supports and induced the upregulation of key genes such as TrpT-2 and Cx43 in the absence of exogenous stimuli[212].

Innovative solutions based on tropoelastin and GO nanoparticles have generated injectable scaffolds with high elasticity and toughness, minimizing the inflammatory response and allowing cellular depolarization at reduced excitation thresholds, indicative of advanced electrical integration[213]. To counteract the loss of vascularisation, *Paul et al*., employed GO-functionalized injectable hydrogels to deliver DNA plasmids for vascular endothelial growth factor (VEGF). In animal models of acute infarction, this strategy produced a reduction in scar area, mitigation of inflammation, and significant improvement in systolic ejection fraction[214].

Finally, the development of GO-functionalized heat inversion hydrogels (RTGs), capable of gelling at 37°C, confirmed the possibility of creating conductive 3D matrices capable of supporting long-term survival and functional maturation of cardiomyocytes directly in situ.

References

(1) Regulation (EU) 2024/1252 of the European Parliament and of the Council of 11 April 2024 Establishing a Framework for Ensuring a Secure and Sustainable Supply of Critical Raw Materials and Amending Regulations (EU) No 168/2013, (EU) 2018/858, (EU) 2018/1724 and (EU) 2019/1020 (Text with EEA Relevance); 2024. http://data.europa.eu/eli/reg/2024/1252/oj (accessed 2025-12-26).

(2) Mineral Commodity Summaries 2024.

(3) Notice of Final Determination on 2023 DOE Critical Materials List. Federal Register. https://www.federalregister.gov/documents/2023/08/04/2023-16611/notice-of-final-determination-on-2023-doe-critical-materials-list (accessed 2025-12-26).

(4) Carta mineraria. https://sinacloud.isprambiente.it/portal/apps/webappviewer/index.html?id=a3fa10ccab3840449847d27fad764152 (accessed 2025-12-26).

(5) van Gaalen, J. M.; Chris Slootweg, J. From Critical Raw Materials to Circular Raw Materials. ChemSusChem 2025, 18 (2), e202401170. https://doi.org/10.1002/cssc.202401170.

(6) Yao, Y.; Zhu, M.; Zhao, Z.; Tong, B.; Fan, Y.; Hua, Z. Hydrometallurgical Processes for Recycling Spent Lithium-Ion Batteries: A Critical Review. ACS Sustainable Chem. Eng. 2018, 6 (11), 13611–13627. https://doi.org/10.1021/acssuschemeng.8b03545.

(7) Lai, Y.; Zhu, X.; Li, J.; Gou, Q.; Li, M.; Xia, A.; Huang, Y.; Zhu, X.; Liao, Q. Recovery and Regeneration of Anode Graphite from Spent Lithium-Ion Batteries through Deep Eutectic Solvent Treatment: Structural Characteristics, Electrochemical Performance and Regeneration Mechanism. Chemical Engineering Journal 2023, 457, 141196. https://doi.org/10.1016/j.cej.2022.141196.

(8) Islam, M. S.; Kushwaha, A. K.; Misra, M. Review on the Recycling of Anode Graphite from Waste Lithium-Ion Batteries. J Mater Cycles Waste Manag 2024, 26 (6), 3341–3369. https://doi.org/10.1007/s10163-024-02093-4.

(9) Yu, H.; Dai, H.; Zhu, Y.; Hu, H.; Zhao, R.; Wu, B.; Chen, D. Mechanistic Insights into the Lattice Reconfiguration of the Anode Graphite Recycled from Spent High-Power Lithium-Ion Batteries. Journal of Power Sources 2021, 481, 229159. https://doi.org/10.1016/j.jpowsour.2020.229159.

(10) Waste Electrical and Electronic Equipment (WEEE): Flows, Quantities, and Management—A Global Scenario. In Electronic Waste Management and Treatment Technology; Butterworth-Heinemann, 2019; pp 1–34. https://doi.org/10.1016/B978-0-12-816190-6.00001-7.

(11) Zaman, A.; Ghosh, A.; Gangopadhyay, B.; Orasugh, J. T.; Santra, S.; Chakrobarty, J.; Karmakar, S.; Banerjee, P.; Ray, S. S.; Chattopadhyay, D. Sustainable Conversion of Waste Carbon Brush and Fly Ash into a Novel Nanocomposite for Selective Adsorption of Cationic Dyes. ACS Sustainable Resour. Manage. 2024, 1 (5), 978–993. https://doi.org/10.1021/acssusresmgt.4c00038.

(12) Che cos'è la spazzola di carbone nel motore? | Jinsun Carbon. https://jinsuncarbon.com/it/cose-la-spazzola-di-carbone-nel-motore/ (accessed 2025-12-26).

(13) Long, D. A. The Raman Effect: A Unified Treatment of the Theory of Raman Scattering by Molecules; Wiley: Chichester New York, 2002. https://doi.org/10.1002/0470845767.

(14) Atkins, P.; Paula, J. D.; Keeler, J. Atkins' Physical Chemistry, 12th ed.; Oxford University Press, 2022. https://doi.org/10.1093/hesc/9780198847816.001.0001.

(15) Giacovazzo, C.; Monaco, H. L.; Viterbo, D.; Scordari, F.; Gilli, G.; Zanotti, G.; Catti, M. Fundamentals of Crystallography.

(16) Gabbott, P. Principles and Applications of Thermal Analysis; Blackwell Pub: Oxford, 2008.

(17) Brown, M. E. Introduction to Thermal Analysis: Techniques and Applications; Springer Science & Business Media, 2006.

(18) Höhne, G. W. H.; Breuer, K.-H.; Eysel, W. Differential Scanning Calorimetry: Comparison of Power Compensated and Heat Flux Instruments. Thermochimica Acta 1983, 69 (1), 145–151. https://doi.org/10.1016/0040-6031(83)85073-4.

(19) Yurchenko, O.; Pernau, H.-F.; Engel, L.; Wöllenstein, J. Differential Thermal Analysis Techniques as a Tool for Preliminary Examination of Catalyst for Combustion. Sci Rep 2023, 13, 9792. https://doi.org/10.1038/s41598-023-36878-8.

(20) Warr, L. N. IMA–CNMNC Approved Mineral Symbols. Mineralogical Magazine 2021, 85 (3), 291–320. https://doi.org/10.1180/mgm.2021.43.

(21) Chung, D. D. L. Review Graphite. Journal of Materials Science 2002, 37 (8), 1475–1489. https://doi.org/10.1023/A:1014915307738.

(22) Novoselov, K. S.; Geim, A. K.; Morozov, S. V.; Jiang, D.; Zhang, Y.; Dubonos, S. V.; Grigorieva, I. V.; Firsov, A. A. Electric Field in Atomically Thin Carbon Films. Science 2004, 306 (5696), 666–669. https://doi.org/10.1126/science.1102896.

(23) Lens About – Search, Analyze and Manage Patent and Scholarly Data. Lens About. https://about.lens.org/ (accessed 2025-12-27).

(24) Yu, P.; Lowe, S. E.; Simon, G. P.; Zhong, Y. L. Electrochemical Exfoliation of Graphite and Production of Functional Graphene. Current Opinion in Colloid & Interface Science 2015, 20 (5), 329–338. https://doi.org/10.1016/j.cocis.2015.10.007.

(25) Wu, W.; Zhang, C.; Hou, S. Electrochemical Exfoliation of Graphene and Graphene-Analogous 2D Nanosheets. *J. Mater. Sci.* 2017, 52, 10649–10660. https://doi.org/10.1007/s10853-017-1289-x

(26) Liu, Z.; Wu, Z.-S.; Yang, S.; Dong, R.; Feng, X.; Müllen, K. Ultraflexible In-Plane Micro-Supercapacitors by Direct Printing of Solution-Processable Electrochemically Exfoliated Graphene. Advanced Materials 2016, 28 (11), 2217–2222. https://doi.org/10.1002/adma.201505304.

(27) Liu, F.; Wang, C.; Sui, X.; Riaz, M. A.; Xu, M.; Wei, L.; Chen, Y. Synthesis of Graphene Materials by Electrochemical Exfoliation: Recent Progress and Future Potential. *Carbon Energy* 2019, 1 (2), 173–199. https://doi.org/10.1002/cey2.14.

(28) Kumar, N.; Salehiyan, R.; Chauke, V.; Joseph Botlhoko, O.; Setshedi, K.; Scriba, M.; Masukume, M.; Sinha Ray, S. Top-down Synthesis of Graphene: A Comprehensive Review. FlatChem 2021, 27, 100224. https://doi.org/10.1016/j.flatc.2021.100224.

(29) Brodie, B. C. XIII. On the Atomic Weight of Graphite. Phil. Trans. R. Soc. 1859, No. 149, 249–259. https://doi.org/10.1098/rstl.1859.0013.

(30) Poh, H. L.; Šaněk, F.; Ambrosi, A.; Zhao, G.; Sofer, Z.; Pumera, M. Graphenes Prepared by Staudenmaier, Hofmann and Hummers Methods with Consequent Thermal Exfoliation Exhibit Very Different Electrochemical Properties. *Nanoscale* 2012, 4 (11), 3515–3522. https://doi.org/10.1039/c2nr30490b

(31) Hussain, A.; Weng, Y.; Huang, Y. Graphene and Graphene-Based Nanomaterials: Current Applications and Future Perspectives. In *Drug Delivery Using Nanomaterials*; Shahzad, Y., Rizvi, S. A. A., Yousaf, A. M., Hussain, T., Eds.; CRC Press/Taylor & Francis: Boca Raton, FL, 2022; pp. 209–228. https://doi.org/10.1201/9781003168584-9

(32) Hummers, W. S.; Offeman, R. E. Preparation of Graphitic Oxide. J. Am. Chem. Soc. 1958, 80 (6), 1339–1339. https://doi.org/10.1021/ja01539a017.

(33) Jilani, A.; Othman, M. H. D.; Ansari, M. O.; Hussain, S. Z.; Ismail, A. F.; Khan, I. U.; Inamuddin. Graphene and Its Derivatives: Synthesis, Modifications, and Applications in Wastewater Treatment. *Environmental Chemistry Letters* 2018, 16 (4), 1301–1323. https://doi.org/10.1007/s10311-018-0755-2

(34) Marcano, D. C.; Kosynkin, D. V.; Berlin, J. M.; Sinitskii, A.; Sun, Z.; Slesarev, A.; Alemany, L. B.; Lu, W.; Tour, J. M. Improved Synthesis of Graphene Oxide. *ACS Nano* 2010, 4 (8), 4806–4814. https://doi.org/10.1021/nn1006368

(35) Lavin-Lopez, M. del P.; Romero, A.; Garrido, J.; Sanchez-Silva, L.; Valverde, J. L. Influence of Different Improved Hummers Method Modifications on the Characteristics of Graphite Oxide in Order to Make a More Easily Scalable Method. Ind. Eng. Chem. Res. 2016, 55 (50), 12836–12847. https://doi.org/10.1021/acs.iecr.6b03533.

(36) Chen, J.; Yao, B.; Li, C.; Shi, G. An Improved Hummers Method for Eco-Friendly Synthesis of Graphene Oxide. Carbon 2013, 64, 225–229. https://doi.org/10.1016/j.carbon.2013.07.055.

(37) Wang, G.; Sun, X.; Liu, C.; Lian, J. Tailoring Oxidation Degrees of Graphene Oxide by Simple Chemical Reactions. *Appl. Phys. Lett.* 2011, 99 (5), 053114. https://doi.org/10.1063/1.3622637

(38) Shojaeenezhad, S. S.; Farbod, M.; Kazeminezhad, I. Effects of Initial Graphite Particle Size and Shape on Oxidation Time in Graphene Oxide Prepared by Hummers' Method. Journal of Science: Advanced Materials and Devices 2017, 2 (4), 470–475. https://doi.org/10.1016/j.jsamd.2017.09.003.

(39) Dreyer, D. R.; Park, S.; Bielawski, C. W.; Ruoff, R. S. The Chemistry of Graphene Oxide. Chem. Soc. Rev. 2009, 39 (1), 228–240. https://doi.org/10.1039/B917103G.

(40) Akhavan, O. The Effect of Heat Treatment on Formation of Graphene Thin Films from Graphene Oxide Nanosheets. Carbon 2010, 48 (2), 509–519. https://doi.org/10.1016/j.carbon.2009.09.069.

(41) Rubesh Ashok Kumar, S.; Vasvini Mary, D.; Suganya Josephine, G. A.; Riswan Ahamed, M. A. Graphene/GO/rGO Based Nanocomposites: Emerging Energy and Environmental Application– Review. Hybrid Advances 2024, 5, 100168. https://doi.org/10.1016/j.hybadv.2024.100168.

(42) Ghodake, V. S.; Koyale, P. A.; Delekar, S. D. rGO-Modified ZnO-TiO_2 Nanohybrids as Promising Antibacterial Agents for Biomedical Applications. *ChemistrySelect* 2025, 10 (5), Article e202405722. https://doi.org/10.1002/slct.202405722(43) Thankulkit, P.; Rojviroon, O.; Rajendran, R.; Alsawalha, M.; Arumugam, P.; Rojviroon, T.; Sirivithayapakorn, S. Development of AgFeO2/g-C3N4/RGO Nanocomposites with Superior Photocatalytic Activity and Antibacterial Properties for Wastewater

Treatment. Journal of Water Process Engineering 2025, 69, 106650. https://doi.org/10.1016/j.jwpe.2024.106650.

(44) De Silva, K. K. H.; Huang, H.-H.; Joshi, R.; Yoshimura, M. Restoration of the Graphitic Structure by Defect Repair during the Thermal Reduction of Graphene Oxide. Carbon 2020, 166, 74–90. https://doi.org/10.1016/j.carbon.2020.05.015.

(45) Band-like transport in highly crystalline graphene films from defective graphene oxides | Scientific Reports. https://www.nature.com/articles/srep28936 (accessed 2025-12-27).

(46) Pei, S.; Cheng, H.-M. The Reduction of Graphene Oxide. Carbon 2012, 50 (9), 3210–3228. https://doi.org/10.1016/j.carbon.2011.11.010.

(47) Kumar Singh, R.; Kumar, R.; Pratap Singh, D. Graphene Oxide: Strategies for Synthesis, Reduction and Frontier Applications. RSC Advances 2016, 6 (69), 64993–65011. https://doi.org/10.1039/C6RA07626B.

(48) Kumar, N.; Kumar, S.; Gusain, R.; Manyala, N.; Eslava, S.; Ray, S. S. Polypyrrole-Promoted rGO–MoS_2 Nanocomposites for Enhanced Photocatalytic Conversion of CO_2 and H_2O to CO, CH_4, and H_2 Products. *ACS Appl. Energy Mater.* 2020, 3 (10), 9897–9909. https://doi.org/10.1021/acsaem.0c01602

(49) Polshettiwar, V.; Varma, R. S. Continuous Hydrothermal Synthesis of Inorganic Nanoparticles: Applications and Future Directions. *Chem. Rev.* 2017, 117 (17), 11102–11153. https://doi.org/10.1021/acs.chemrev.6b00417

(50) Bosch-Navarro, C.; Coronado, E.; Martí-Gastaldo, C.; Sánchez-Royo, J. F.; Gómez, M. G. Influence of the pH on the Synthesis of Reduced Graphene Oxide under Hydrothermal Conditions. Nanoscale 2012, 4 (13), 3977–3982. https://doi.org/10.1039/C2NR30605K.

(51) Toh, S. Y.; Loh, K. S.; Kamarudin, S. K.; Daud, W. R. W. Graphene Production via Electrochemical Reduction of Graphene Oxide: Synthesis and Characterisation. Chemical Engineering Journal 2014, 251, 422–434. https://doi.org/10.1016/j.cej.2014.04.004.

(52) Dreyer, D. R.; Park, S.; Bielawski, C. W.; Ruoff, R. S. The Chemistry of Graphene Oxide. Chem. Soc. Rev. 2009, 39 (1), 228–240. https://doi.org/10.1039/B917103G.

(53) Pei, S.; Cheng, H.-M. The Reduction of Graphene Oxide. Carbon 2012, 50 (9), 3210–3228. https://doi.org/10.1016/j.carbon.2011.11.010.

(54) De Silva, K. K. H.; Huang, H.-H.; Joshi, R. K.; Yoshimura, M. Chemical Reduction of Graphene Oxide Using Green Reductants. Carbon 2017, 119, 190–199. https://doi.org/10.1016/j.carbon.2017.04.025.

(55) Khanra, P.; Kuila, T.; Kim, N. H.; Bae, S. H.; Yu, D.; Lee, J. H. Simultaneous Bio-Functionalization and Reduction of Graphene Oxide by Baker's Yeast. Chemical Engineering Journal 2012, 183, 526–533. https://doi.org/10.1016/j.cej.2011.12.075.

(56) Chua, C. K.; Pumera, M. Chemical Reduction of Graphene Oxide: A Synthetic Chemistry Viewpoint. Chem. Soc. Rev. 2013, 43 (1), 291–312. https://doi.org/10.1039/C3CS60303B.

(57) Solid C60: a new form of carbon | Nature. https://www.nature.com/articles/347354a0 (accessed 2025-12-27).

(58) Dallas, P.; Meysami, S. S.; Grobert, N.; Porfyrakis, K. Classification of Carbon Nanostructure Families Occurring in a Chemically Activated Arc Discharge Reaction. RSC Adv. 2016, 6 (30), 24912–24920. https://doi.org/10.1039/C5RA26325E.

(59) Subrahmanyam, K. S.; Panchakarla, L. S.; Govindaraj, A.; Rao, C. N. R. Simple Method of Preparing Graphene Flakes by an Arc-Discharge Method. *J. Phys. Chem. C* 2009, 113 (11), 4257–4259. https://doi.org/10.1021/jp900791y

(60) Wu, X.; Liu, Y.; Yang, H.; Shi, Z. Large-Scale Synthesis of High-Quality Graphene Sheets by an Improved Alternating Current Arc-Discharge Method. RSC Adv. 2016, 6 (95), 93119–93124. https://doi.org/10.1039/C6RA22273K.

(61) Yi, M.; Shen, Z. A Review on Mechanical Exfoliation for the Scalable Production of Graphene. J. Mater. Chem. A 2015, 3 (22), 11700–11715. https://doi.org/10.1039/C5TA00252D.

(62) Jayasena, B.; Subbiah, S. A Novel Mechanical Cleavage Method for Synthesizing Few-Layer Graphenes. *Nanoscale Res. Lett.* 2011, 6, 95. https://doi.org/10.1186/1556-276X-6-95.

(63) Janowska, I.; Vigneron, F.; Bégin, D.; Ersen, O.; Bernhardt, P.; Romero, T.; Ledoux, M. J.; Pham-Huu, C. Mechanical Thinning to Make Few-Layer Graphene from Pencil Lead. Carbon 2012, 50 (8), 3106–3110. https://doi.org/10.1016/j.carbon.2012.02.064.

(64) Pirzado, A. A.; Le Normand, F.; Romero, T.; Paszkiewicz, S.; Papaefthimiou, V.; Ihiawakrim, D.; Janowska, I. Few-Layer Graphene from Mechanical Exfoliation of Graphite-Based Materials: Structure-Dependent Characteristics. *ChemEngineering* 2019, 3 (2), 37. https://doi.org/10.3390/chemengineering3020037(65) Yi, M.; Shen, Z. A Review on Mechanical Exfoliation for the Scalable Production of Graphene. J. Mater. Chem. A 2015, 3 (22), 11700–11715. https://doi.org/10.1039/C5TA00252D.

(66) Zhao, W.; Fang, M.; Wu, F.; Wu, H.; Wang, L.; Chen, G. Preparation of Graphene by Exfoliation of Graphite Using Wet Ball Milling. J. Mater. Chem. 2010, 20 (28), 5817–5819. https://doi.org/10.1039/C0JM01354D.

(67) Lin, T.; Chen, J.; Bi, H.; Wan, D.; Huang, F.; Xie, X.; Jiang, M. Facile and Economical Exfoliation of Graphite for Mass Production of High-Quality Graphene Sheets. J. Mater. Chem. A 2012, 1 (3), 500–504. https://doi.org/10.1039/C2TA00518B.

(68) Bhuyan, M. S. A.; Uddin, M. N.; Islam, M. M.; Bipasha, F. A.; Hossain, S. S. Synthesis of Graphene. *Int. Nano Lett.* 2016, 6, 65–83. https://doi.org/10.1007/s40089-015-0176-1

(69) Berger, C.; Song, Z.; Li, T.; Li, X.; Ogbazghi, A. Y.; Feng, R.; Dai, Z.; Marchenkov, A. N.; Conrad, E. H.; First, P. N.; de Heer, W. A. Ultrathin Epitaxial Graphite: 2D Electron Gas Properties and a Route toward Graphene-Based Nanoelectronics. *J. Phys. Chem. B* 2004, 108 (52), 19912–19916. https://doi.org/10.1021/jp040650f.

(70) Rollings, E.; Gweon, G.-H.; Zhou, S. Y.; Mun, B. S.; McChesney, J. L.; Hussain, B. S.; Fedorov, A. V.; First, P. N.; de Heer, W. A.; Lanzara, A. Synthesis and Characterization of Atomically Thin Graphite Films on a Silicon Carbide Substrate. Journal of Physics and Chemistry of Solids 2006, 67 (9), 2172–2177. https://doi.org/10.1016/j.jpcs.2006.05.010.

(71) Virojanadara, C.; Yakimova, R.; Zakharov, A. A.; Johansson, L. I. Large Homogeneous Mono-/Bi-Layer Graphene on 6H–SiC(0 0 0 1) and Buffer Layer Elimination. J. Phys. D: Appl. Phys. 2010, 43 (37), 374010. https://doi.org/10.1088/0022-3727/43/37/374010.

(72) Emtsev, K. V.; Bostwick, A.; Horn, K.; Jobst, J.; Kellogg, G. L.; Ley, L.; McChesney, J. L.; Ohta, T.; Reshanov, S. A.; Röhrl, J.; Rotenberg, E.; Schmid, A. K.; Waldmann, D.; Weber, H. B.; Seyller, T. Towards Wafer-Size Graphene Layers by Atmospheric Pressure Graphitization of Silicon Carbide. Nature Mater 2009, 8 (3), 203–207. https://doi.org/10.1038/nmat2382.

(73) Tromp, R. M.; Hannon, J. B. Thermodynamics and Kinetics of Graphene Growth on SiC(0001). *Phys. Rev. Lett.* 2009, 102, 106104. https://doi.org/10.1103/PhysRevLett.102.106104

(74) Miao, C. CVD Synthesis of Graphene and Graphene Bipolar Junction Transistor. *Ph.D. Thesis*, University of California, Los Angeles, 2011. https://www.proquest.com/openview/44049b07d87df250e66566241845e4da/1?pq-origsite=gscholar&cbl=18750

(75) Xu, S.; Zhang, L.; Wang, B.; Ruoff, R. S. Chemical Vapor Deposition of Graphene on Thin-Metal Films. *Cell Rep. Phys. Sci.* 2021, 2, 100372. https://doi.org/10.1016/j.xcrp.2021.100372.

(76) Somani, P. R.; Somani, S. P.; Umeno, M. Planer Nano-Graphenes from Camphor by CVD. Chemical Physics Letters 2006, 430 (1), 56–59. https://doi.org/10.1016/j.cplett.2006.06.081.

(77) Yu, Q. K.; Lian, J.; Siriponglert, S.; Li, H.; Chen, Y. P.; Pei, S.-S. Graphene Segregated on Ni Surfaces and Transferred to Insulators. *Appl. Phys. Lett.* 2008, 93 (11), 113103. https://doi.org/10.1063/1.2982585

(78) Kim, K. S.; Zhao, Y.; Jang, H.; Lee, S. Y.; Kim, J. M.; Kim, K. S.; Ahn, J.-H.; Kim, P.; Choi, J.-Y.; Hong, B. H. Large-Scale Pattern Growth of Graphene Films for Stretchable Transparent Electrodes. Nature 2009, 457 (7230), 706–710. https://doi.org/10.1038/nature07719.

(79) Reina, A.; Jia, X.; Ho, J.; Nezich, D.; Son, H.; Bulovic, V.; Dresselhaus, M. S.; Kong, J. Large Area, Few-Layer Graphene Films on Arbitrary Substrates by Chemical Vapor Deposition. Nano Lett. 2009, 9 (1), 30–35. https://doi.org/10.1021/nl801827v.

(80) Gomez De Arco, L.; Zhang, Y.; Kumar, A.; Zhou, C. Synthesis, Transfer, and Devices of Single- and Few-Layer Graphene by Chemical Vapor Deposition. IEEE Transactions on Nanotechnology 2009, 8 (2), 135–138. https://doi.org/10.1109/TNANO.2009.2013620.

(81) Li, X.; Cai, W.; An, J.; Kim, S.; Nah, J.; Yang, D.; Piner, R.; Velamakanni, A.; Jung, I.; Tutuc, E.; Banerjee, S. K.; Colombo, L.; Ruoff, R. S. Large-Area Synthesis of High-Quality and Uniform Graphene Films on Copper Foils. *Science* 2009, 324 (5932), 1312–1314. https://doi.org/10.1126/science.1171245

(82) Yu, Q.; Jauregui, L. A.; Wu, W.; Colby, R.; Tian, J.; Su, Z.; Cao, H.; Liu, Z.; Paddle, J.; Chen, Y. P.; et al. Evolution of Graphene Growth on Ni and Cu by Carbon Isotope Labeling. *Nano Lett.* 2009, 9 (10), 3867–3872. https://doi.org/10.1021/nl902515k

(83) Kang, B. J.; Mun, J. H.; Hwang, C. Y.; Cho, B. J. Monolayer Graphene Growth on Sputtered Thin Film Platinum. J. Appl. Phys. 2009, 106 (10), 104309. https://doi.org/10.1063/1.3254193.

(84) Nandamuri, G.; Roumimov, S.; Solanki, R. Chemical Vapor Deposition of Graphene Films. *Nanotechnology* 2010, 21 (14), 145604.https://doi.org/10.1088/0957-4484/21/14/145604

(86) Vázquez de Parga, A. L.; Calleja, F.; Borca, B.; Passeggi, M. C. G., Jr.; Hinarejos, J. J.; Guinea, F.; Miranda, R. Periodically Rippled Graphene: Growth and Spatially Resolved Electronic Structure. *Phys. Rev. Lett.* 2008, 100, 056807. https://doi.org/10.1103/PhysRevLett.100.056807

(87) Celebi, K.; Cole, M. T.; Teo, K. B. K.; Park, H. G. Observations of Early Stage Graphene Growth on Copper. *Electrochem. Solid-State Lett.* 2012, 15 (1), K1–K4. https://doi.org/10.1149/2.005201esl

(88) Addou, R.; Dahal, A.; Sutter, P.; Batzill, M. Monolayer Graphene Growth on Ni(111) by Low Temperature Chemical Vapor Deposition. Appl. Phys. Lett. 2012, 100 (2), 021601. https://doi.org/10.1063/1.3675481.

(89) Li, Z.; Wu, P.; Wang, C.; Fan, X.; Zhang, W.; Zhai, X.; Zeng, C.; Li, Z.; Yang, J.; Hou, J. Low-Temperature Growth of Graphene by Chemical Vapor Deposition Using Solid and Liquid Carbon Sources. ACS Nano 2011, 5 (4), 3385–3390. https://doi.org/10.1021/nn200854p.

(90) Campos-Delgado, J.; Botello-Méndez, A. R.; Algara-Siller, G.; Hackens, B.; Pardoen, T.; Kaiser, U.; Dresselhaus, M. S.; Charlier, J.-C.; Raskin, J.-P. CVD Synthesis of Mono- and Few-Layer Graphene Using Alcohols at Low Hydrogen Concentration and Atmospheric Pressure. Chemical Physics Letters 2013, 584, 142–146. https://doi.org/10.1016/j.cplett.2013.08.031.

(91) Somani, P. R.; Somani, S. P.; Umeno, M. Planer Nano-Graphenes from Camphor by CVD. Chemical Physics Letters 2006, 430 (1), 56–59. https://doi.org/10.1016/j.cplett.2006.06.081.

(92) Miyata, Y.; Kamon, K.; Ohashi, K.; Kitaura, R.; Yoshimura, M.; Shinohara, H. A Simple Alcohol-Chemical Vapor Deposition Synthesis of Single-Layer Graphenes Using Flash Cooling. Appl. Phys. Lett. 2010, 96 (26), 263105. https://doi.org/10.1063/1.3458797.

(93) Srivastava, A.; Galande, C.; Ci, L.; Song, L.; Rai, C.; Jariwala, D.; Kelly, K. F.; Ajayan, P. M. Novel Liquid Precursor-Based Facile Synthesis of Large-Area Continuous, Single, and Few-Layer Graphene Films. *Chem. Mater.* 2010, 22 (11), 3457–3461. https://doi.org/10.1021/cm101027c

(94) Guermoune, A.; Chari, T.; Popescu, F.; Sabri, S. S.; Guillemette, J.; Skulason, H. S.; Szkopek, T.; Siaj, M. Chemical Vapor Deposition Synthesis of Graphene on Copper with Methanol, Ethanol, and Propanol Precursors. Carbon 2011, 49 (13), 4204–4210. https://doi.org/10.1016/j.carbon.2011.05.054.

(95) Gadipelli, S.; Calizo, I.; Ford, J.; Cheng, G.; Walker, A. R. H.; Yildirim, T. A Highly Practical Route for Large-Area, Single Layer Graphene from Liquid Carbon Sources Such as Benzene and Methanol. J. Mater. Chem. 2011, 21 (40), 16057–16065. https://doi.org/10.1039/C1JM12938D.

(96) Maarof, S.; Ali, A. A.; Hashim, A. M. Synthesis of Large-Area Single-Layer Graphene Using Refined Cooking Palm Oil on Copper Substrate by Spray Injector-Assisted CVD. *Nanoscale Res. Lett.* 2019, 14, 143. https://doi.org/10.1186/s11671-019-2976-0

(97) Li, Z.; Gordon, R. G.; Pallem, V.; Li, H.; Shenai, D. V. Direct-Liquid-Injection Chemical Vapor Deposition of Nickel Nitride Films and Their Reduction to Nickel Films. Chem. Mater. 2010, 22 (10), 3060–3066. https://doi.org/10.1021/cm903636j.

(98) Intaro, T.; Hodak, J.; Suwanyangyaun, P.; Botta, R.; Nuntawong, N.; Niki, M.; Kosuga, S.; Watanabe, T.; Koh, S.; Taychatanapat, T.; Sanorpim, S. Characterization of Graphene Grown by Direct-Liquid-Injection Chemical Vapor Deposition with Cyclohexane Precursor in N2 Ambient. Diamond and Related Materials 2020, 104, 107717. https://doi.org/10.1016/j.diamond.2020.107717.

(99) Sun, Z.; Yan, Z.; Yao, J.; Beitler, E.; Zhu, Y.; Tour, J. M. Growth of Graphene from Solid Carbon Sources. *Nature* 2009, 457, 706–710. https://doi.org/10.1038/nature09579..

(100) Graphene synthesis by thermal chemical vapor deposition using solid precursor. *J. Mater. Sci.: Mater. Electron.* 2013, 24, 4431–4435. https://doi.org/10.1007/s10854-013-1073-x.

(101) Liu, H.; Song, H.; Zhang, J.; Hu, Z.; Wang, X.; et al. Growth of Graphene from Food, Insects, and Waste. *ACS Nano* 2011, 5 (8), 7462–7468. https://doi.org/10.1021/nn202625c

(102) Weatherup, R. S.; Bayer, B. C.; Blume, R.; Ducati, C.; Baehtz, C.; Schlögl, R.; Hofmann, S. In Situ Characterization of Alloy Catalysts for Low-Temperature Graphene Growth. *Nano Lett.* 2011, 11 (10), 3846–3850. https://doi.org/10.1021/nl202036y

(103) Chen, S.; Cai, W.; Piner, R. D.; Suk, J. W.; Wu, Y.; Ren, Y.; Kang, J.; Ruoff, R. S. Synthesis and Characterization of Large-Area Graphene and Graphite Films on Commercial Cu–Ni Alloy Foils. *Nano Lett.* 2011, 11 (9), 4148–4152. https://doi.org/10.1021/nl201699j

(104) Huang, M.; Biswal, M.; Park, H. J.; Jin, S.; Qu, D.; Hong, S.; Zhu, Z.; Qiu, L.; Luo, D.; Liu, X.; Yang, Z.; Liu, Z.; Huang, Y.; Lim, H.; Yoo, W. J.; Ding, F.; Wang, Y.; Lee, Z.; Ruoff, R. S. Highly Oriented Monolayer Graphene Grown on a Cu/Ni(111) Alloy Foil. ACS Nano 2018, 12 (6), 6117–6127. https://doi.org/10.1021/acsnano.8b02444.

(105) Li, X.; Magnuson, C. W.; Venugopal, A.; Tromp, R. M.; Hannon, J. B.; Vogel, E. M.; Colombo, L.; Ruoff, R. S. Large-Area Graphene Single Crystals Grown by Low-Pressure Chemical Vapor Deposition of Methane on Copper. *J. Am. Chem. Soc.* 2011, 133 (9), 2816–2819. https://doi.org/10.1021/ja109793s(106) Yang, M.; Sasaki, S.; Ohnishi, M.; Suzuki, K.; Miura, H. Electronic Properties and Strain Sensitivity of CVD-Grown Graphene with Acetylene. Jpn. J. Appl. Phys. 2016, 55 (4S), 04EP05. https://doi.org/10.7567/JJAP.55.04EP05.

(107) Luo, B.; Caridad, J. M.; Whelan, P. R.; Thomsen, J. D.; Mackenzie, D. M. A.; Grubišić Čabo, A.; Mahatha, S. K.; Bianchi, M.; Hofmann, P.; Jepsen, P. U.; Bøggild, P.; Booth, T. J. Sputtering an Exterior Metal Coating on Copper Enclosure for Large-Scale Growth of Single-Crystalline Graphene. 2D Mater. 2017, 4 (4), 045017. https://doi.org/10.1088/2053-1583/aa85d5.

(108) Hesjedal, T. Continuous Roll-to-Roll Growth of Graphene Films by Chemical Vapor Deposition. *Appl. Phys. Lett.* 2011, 98 (13), 133106. https://doi.org/10.1063/1.3573866.

(109) Kobayashi, T.; Bando, M.; Kimura, N.; Shimizu, K.; Kadono, K.; Umezu, N.; Miyahara, K.; Hayazaki, S.; Nagai, S.; Mizuguchi, Y.; Murakami, Y.; Hobara, D. Production of a 100-m-Long High-Quality Graphene Transparent Conductive Film by Roll-to-Roll Chemical Vapor Deposition and Transfer Process. Appl. Phys. Lett. 2013, 102 (2), 023112. https://doi.org/10.1063/1.4776707.

(110) Jalili, M.; Ghanbari, H.; Moemen Bellah, S.; Malekfar, R. High-Quality Liquid Phase-Pulsed Laser Ablation Graphene Synthesis by Flexible Graphite Exfoliation. Journal of Materials Science & Technology 2019, 35 (3), 292–299. https://doi.org/10.1016/j.jmst.2018.09.048.

(111) Ye, R.; James, D. K.; Tour, J. M. Laser-Induced Graphene: From Discovery to Translation. Advanced Materials 2019, 31 (1), 1803621. https://doi.org/10.1002/adma.201803621.

(112) Stanford, M. G.; Zhang, C.; Fowlkes, J. D.; Hoffman, A.; Ivanov, I. N.; Rack, P. D.; Tour, J. M. High-Resolution Laser-Induced Graphene. Flexible Electronics beyond the Visible Limit. ACS Appl. Mater. Interfaces 2020, 12 (9), 10902–10907. https://doi.org/10.1021/acsami.0c01377.

(113) Beckham, J. L.; Li, J. T.; Stanford, M. G.; Chen, W.; McHugh, E. A.; Advincula, P. A.; Wyss, K. M.; Chyan, Y.; Boldman, W. L.; Rack, P. D.; Tour, J. M. High-Resolution Laser-Induced Graphene from Photoresist. ACS Nano 2021, 15 (5), 8976–8983. https://doi.org/10.1021/acsnano.1c01843.

(114) Ye, R.; James, D. K.; Tour, J. M. Laser-Induced Graphene: From Discovery to Translation. *Adv. Mater.* 2019, 31 (1), 1803621. https://doi.org/10.1002/adma.201803621

(115) Ye, R.; James, D. K.; Tour, J. M. Laser-Induced Graphene. Acc. Chem. Res. 2018, 51 (7), 1609–1620. https://doi.org/10.1021/acs.accounts.8b00084.

(116) Lin, J.; Peng, Z.; Liu, Y.; Ruiz-Zepeda, F.; Ye, R.; Samuel, E. L. G.; Yacaman, M. J.; Yakobson, B. I.; Tour, J. M. Laser-Induced Porous Graphene Films from Commercial Polymers. Nat Commun 2014, 5 (1), 5714. https://doi.org/10.1038/ncomms6714.

(117) Hameed, R.; Khashan, K. S.; Sulaiman, G. M. Preparation and Characterization of Graphene Sheet Prepared by Laser Ablation in Liquid. Materials Today: Proceedings 2020, 20, 535–539. https://doi.org/10.1016/j.matpr.2019.09.185.

(118) Qian, M.; Zhou, Y. S.; Gao, Y.; Park, J. B.; Feng, T.; Huang, S. M.; Sun, Z.; Jiang, L.; Lu, Y. F. Formation of Graphene Sheets through Laser Exfoliation of Highly Ordered Pyrolytic Graphite. *Appl. Phys. Lett.* 2011, 98 (17), 173108. https://doi.org/10.1063/1.3584021

(119) Kiran, G. R.; Chandu, B.; Acharyya, S. G.; Rao, S. V.; Srikanth, V. V. S. S. One-Step Synthesis of Bulk Quantities of Graphene from Graphite by Femtosecond Laser Ablation under Ambient Conditions. *Philos. Mag. Lett.* 2017, 97 (6), 229–234. https://doi.org/10.1080/09500839.2017.1320437

(120) Huang, Y.; Sepioni, M.; Whitehead, D.; Liu, Z.; Guo, W.; Zhong, X.; Gu, H.; Li, L. Rapid Growth of Large Area Graphene on Glass from Olive Oil by Laser Irradiation. Nanotechnology 2020, 31 (24), 245601. https://doi.org/10.1088/1361-6528/ab7ef6.

(121) Luong, D. X.; Bets, K. V.; Algozeeb, W. A.; Stanford, M. G.; Kittrell, C.; Chen, W.; Salvatierra, R. V.; Ren, M.; McHugh, E. A.; Advincula, P. A.; Wang, Z.; Bhatt, M.; Guo, H.; Mancevski, V.; Shahsavari, R.; Yakobson, B. I.; Tour, J. M. Gram-Scale Bottom-up Flash Graphene Synthesis. Nature 2020, 577 (7792), 647–651. https://doi.org/10.1038/s41586-020-1938-0.

(122) Algozeeb, W. A.; Savas, P. E.; Luong, D. X.; Chen, W.; Kittrell, C.; Bhat, M.; Shahsavari, R.; Tour, J. M. Flash Graphene from Plastic Waste. *ACS Nano* 2021, 15 (2), 1765–1779. https://doi.org/10.1021/acsnano.0c06328

(123) Stanford, M. G.; Bets, K. V.; Hoffman, A. N.; Epshteyn, A.; Kumar, A.; Sae Hong, J.; Chabal, Y. J.; Kumbur, E. C.; Das, S.; Yushin, G.; Yakobson, B. I.; Tour, J. M. Flash Graphene Morphologies. ACS Nano 2020, 14 (10), 13691–13699. https://doi.org/10.1021/acsnano.0c05900.

(124) Lian, W.; Liu, S.; Yu, J.; Xing, X.; Li, J.; Cui, M.; Huang, J. Electrochemical Sensor Based on Gold Nanoparticles Fabricated Molecularly Imprinted Polymer Film at Chitosan-Platinum Nanoparticles/Graphene-Gold Nanoparticles Double Nanocomposites Modified Electrode for Detection of Erythromycin. Biosens Bioelectron 2012, 38 (1), 163–169. https://doi.org/10.1016/j.bios.2012.05.017.

(125) Yang, L.; Wang, G.; Liu, Y.; Wang, M. Development of a Biosensor Based on Immobilization of Acetylcholinesterase on NiO Nanoparticles–Carboxylic Graphene–Nafion Modified Electrode for Detection of Pesticides. Talanta 2013, 113, 135–141. https://doi.org/10.1016/j.talanta.2013.03.025.

(126) Li, Y.; Xu, M.; Li, P.; Dong, J.; Ai, S. Nonenzymatic Sensing of Methyl Parathion Based on Graphene/Gadolinium Prussian Blue Analogue Nanocomposite Modified Glassy Carbon Electrode. Anal. Methods 2014, 6 (7), 2157–2162. https://doi.org/10.1039/C3AY41820K.

(127) Liu, F.; Kim, Y. H.; Cheon, D. S.; Seo, T. S. Micropatterned Reduced Graphene Oxide Based Field-Effect Transistor for Real-Time Virus Detection. Sensors and Actuators B: Chemical 2013, 186, 252–257. https://doi.org/10.1016/j.snb.2013.05.097.

(128) Esfandiari, M.; Jarchi, S.; Nasiri-Shehni, P.; Ghaffari-Miab, M. Enhancing the sensitivity of a transmissive graphene-based plasmonic biosensor. Applied Optics 2021, 60 (5), 1201–1208. https://opg.optica.org/ao/abstract.cfm?uri=ao-60-5-1201.

(129) Zhang, C.; Zhang, R.; Ma, Y.; Guan, W.; Wu, X.; Liu, X.; Li, H.; Du, Y.; Pan, C. Preparation of Cellulose/Graphene Composite and Its Applications for Triazine Pesticides Adsorption from Water. ACS Sustainable Chemistry & Engineering 2015, 3, 396–405. https://doi.org/10.1021/sc500738k

(130) Boruah, P. K.; Sharma, B.; Hussain, N.; Das, M. R. Magnetically Recoverable Fe3O4/Graphene Nanocomposite towards Efficient Removal of Triazine Pesticides from Aqueous Solution: Investigation of the Adsorption Phenomenon and Specific Ion Effect. Chemosphere 2017, 168, 1058–1067. https://doi.org/10.1016/j.chemosphere.2016.10.103.

(131) Wang, C.; Feng, C.; Gao, Y.; Ma, X.; Wu, Q.; Wang, Z. Preparation of a Graphene-Based Magnetic Nanocomposite for the Removal of an Organic Dye from Aqueous Solution. Chemical Engineering Journal 2011, 173 (1), 92–97. https://doi.org/10.1016/j.cej.2011.07.041.

(132) Khalilifard, M.; Javadian, S. Magnetic superhydrophobic polyurethane sponge loaded with Fe3O4@oleic acid@graphene oxide as high performance adsorbent oil from water. Chemical Engineering Journal 2021, 408, 127369. https://www.sciencedirect.com/science/article/abs/pii/S1385894720334938

(133) Sadeghi, M. H.; Tofighy, M. A.; Mohammadi, T. One-Dimensional Graphene for Efficient Aqueous Heavy Metal Adsorption: Rapid Removal of Arsenic and Mercury Ions by Graphene Oxide Nanoribbons (GONRs). Chemosphere 2020, 253, 126647. https://doi.org/10.1016/j.chemosphere.2020.126647.

(134) Ali, I.; Basheer, A. A.; Mbianda, X. Y.; Burakov, A.; Galunin, E.; Burakova, I.; Mkrtchyan, E.; Tkachev, A.; Grachev, V. Graphene Based Adsorbents for Remediation of Noxious Pollutants from Wastewater. Environment International 2019, 127, 160–180. https://doi.org/10.1016/j.envint.2019.03.029.

(135) Hur, J.; Shin, J.; Yoo, J.; Seo, Y.-S. Competitive Adsorption of Metals onto Magnetic Graphene Oxide: Comparison with Other Carbonaceous Adsorbents. The Scientific World Journal 2015, 2015, 836287. https://doi.org/10.1155/2015/836287

(136) Yeh, T.-F.; Syu, J.-M.; Cheng, C.; Chang, T.-H.; Teng, H. Graphite Oxide as a Photocatalyst for Hydrogen Production from Water. Advanced Functional Materials 2010, 20 (14), 2255–2262. https://doi.org/10.1002/adfm.201000274

(137) Bustos-Ramírez, K.; Barrera-Díaz, C. E.; De Icaza-Herrera, M.; Martínez-Hernández, A. L.; Natividad, R. 4-chlorophenol removal from water using graphite and graphene oxides as photocatalysts. Journal of Environmental Health Science and Engineering 2015, 13, 33. https://doi.org/10.1186/s40201-015-0184-0

(138) Hsu, H.-C.; Shown, I.; Wei, H.-Y.; Chang, Y.-C.; Du, H.-Y.; Lin, Y.-G.; Tseng, C.-A.; Wang, C.-H.; Chen, L.-C.; Lin, Y.-C.; Chen, K.-H. Graphene oxide as a promising photocatalyst for CO2 to methanol conversion. Nanoscale 2013, 5 (1), 262–268. https://doi.org/10.1039/C2NR31718D

(139) Kuang, Y.; Shang, J.; Zhu, T. Photoactivated Graphene Oxide to Enhance Photocatalytic Reduction of CO2. ACS Applied Materials & Interfaces 2020, 12 (3), 3580–3591. https://doi.org/10.1021/acsami.9b18899

(140) Gao, P.; Li, A.; Sun, D. D.; Ng, W. J. Effects of Various TiO2 Nanostructures and Graphene Oxide on Photocatalytic Activity of TiO2. Journal of Hazardous Materials 2014, 279, 96–104. https://doi.org/10.1016/j.jhazmat.2014.06.061.

(141) Zou, J.-P.; Wang, L.-C.; Luo, J.; Nie, Y.-C.; Xing, Q.-J.; Luo, X.-B.; Du, H.-M.; Luo, S.-L.; Suib, S. L. Synthesis and Efficient Visible Light Photocatalytic H2 Evolution of a Metal-Free g-C3N4/Graphene Quantum Dots Hybrid Photocatalyst. Applied Catalysis B: Environmental 2016, 193, 103–109. https://doi.org/10.1016/j.apcatb.2016.04.017.

(142) Yein, W. T.; Wang, Q.; Feng, X.; Li, Y.; Wu, X. Enhancement of Photocatalytic Performance in Sonochemical Synthesized ZnO–rGO Nanocomposites Owing to Effective Interfacial Interaction. Environ Chem Lett 2018, 16 (1), 251–264. https://doi.org/10.1007/s10311-017-0651-1.

(143) Cowan, A. J.; Durrant, J. R. Long-Lived Charge Separated States in Nanostructured Semiconductor Photoelectrodes for the Production of Solar Fuels. Chem. Soc. Rev. 2013, 42 (6), 2281–2293. https://doi.org/10.1039/C2CS35305A.

(144) Almeida, B. M.; Melo Jr, M. A.; Bettini, J.; Benedetti, J. E.; Nogueira, A. F. A Novel Nanocomposite Based on TiO_2/Cu_2O/Reduced Graphene Oxide with Enhanced Solar-Light-Driven Photocatalytic Activity. Applied Surface Science 2015, 324, 419–431. https://doi.org/10.1016/j.apsusc.2014.10.105.

(145) Raghavan, N.; Thangavel, S.; Venugopal, G. Enhanced Photocatalytic Degradation of Methylene Blue by Reduced Graphene-Oxide/Titanium Dioxide/Zinc Oxide Ternary Nanocomposites. Materials Science in Semiconductor Processing 2015, 30, 321–329. https://doi.org/10.1016/j.mssp.2014.09.019.

(146) Islam, A.; Teo, S. H.; Awual, Md. R.; Taufiq-Yap, Y. H. Assessment of Clean H_2 Energy Production from Water Using Novel Silicon Photocatalyst. Journal of Cleaner Production 2020, 244, 118805. https://doi.org/10.1016/j.jclepro.2019.118805.

(147) Jing, X.; Peng, X.; Cao, Y.; Wang, W.; Wang, S. Enhanced Photocarriers Separation of Novel CdS/Pt/Mo_2C Heterostructure for Visible-Light-Driven Hydrogen Evolution. RSC Adv. 2018, 8 (59), 33993–33999. https://doi.org/10.1039/C8RA05473H.

(148) Islam, A.; Teo, S. H.; Awual, M. R.; Taufiq-Yap, Y. H. Improving the Hydrogen Production from Water over MgO Promoted Ni–Si/CNTs Photocatalyst. Journal of Cleaner Production 2019, 238, 117887. https://doi.org/10.1016/j.jclepro.2019.117887.

(149) Shah, S. S. A.; Najam, T.; Aslam, M. K.; Ashfaq, M.; Rahman, M. M.; Wang, K.; Tsiakaras, P.; Song, S.; Wang, Y. Recent Advances on Oxygen Reduction Electrocatalysis: Correlating the Characteristic Properties of Metal Organic Frameworks and the Derived Nanomaterials. Applied Catalysis B: Environment and Energy 2020, 268, 118570. https://doi.org/10.1016/j.apcatb.2019.118570.

(150) Lai, W. H.; Zhang, L.; Hua, W.; Indris, S.; Yan, Z.; Hu, Z.; Zhang, B.; Liu, Y.; Wang, L.; Liu, M.; Wang, Y.; Liu, J. General π-Electron-Assisted Strategy for Ir, Pt, Ru, Pd, Fe, Ni Single-Atom Electrocatalysts with Bifunctional Active Sites for Highly Efficient Water Splitting. Angewandte Chemie International Edition 2019, 58 (34), 11868–11873. https://doi.org/10.1002/anie.201904614

(151) Liu, M.; Zhang, C.; Chen, W. Novel Nanomaterials as Electrocatalysts for Fuel Cells. In Nanomaterials for Green Energy; Elsevier, 2018; pp 169–204. https://doi.org/10.1016/B978-0-12-813731-4.00006-0.

(152) Nemiwal, M.; Kumar, D. Recent Progress on Electrochemical Sensing Strategies as Comprehensive Point-Care Method. Monatsh Chem 2021, 152 (1), 1–18. https://doi.org/10.1007/s00706-020-02732-0.

(153) Huang, H.; Yan, M.; Yang, C.; He, H.; Jiang, Q.; Yang, L.; Lu, Z.; Sun, Z.; Xu, X.; Bando, Y.; Yamauchi, Y. Graphene Nanoarchitectonics: Recent Advances in Graphene-Based Electrocatalysts for Hydrogen

Evolution Reaction. Advanced Materials 2019, 31 (48), 1903415. https://doi.org/10.1002/adma.201903415.

(154) Zhu, J.; Hu, L.; Zhao, P.; Lee, L. Y. S.; Wong, K.-Y. Recent Advances in Electrocatalytic Hydrogen Evolution Using Nanoparticles. Chem. Rev. 2020, 120 (2), 851–918. https://doi.org/10.1021/acs.chemrev.9b00248.

(155) Jiang, K.; Siahrostami, S.; Zheng, T.; Hu, Y.; Hwang, S.; Stavitski, E.; Peng, Y.; Dynes, J.; Gangisetty, M.; Su, D.; Attenkofer, K.; Wang, H. Isolated Ni Single Atoms in Graphene Nanosheets for High-Performance CO2 Reduction. Energy Environ. Sci. 2018, 11 (4), 893–903. https://doi.org/10.1039/C7EE03245E.

(156) Ma, R.; Lin, G.; Zhou, Y.; Liu, Q.; Zhang, T.; Shan, G.; Yang, M.; Wang, J. A review of oxygen reduction mechanisms for metal-free carbon-based electrocatalysts. npj Computational Materials 2019, 5, 78. https://doi.org/10.1038/s41524-019-0210-3

(157) Shao, Y.; Jiang, Z.; Zhang, Q.; Guan, J. Progress in Nonmetal-Doped Graphene Electrocatalysts for the Oxygen Reduction Reaction. ChemSusChem 2019, 12 (10), 2133–2146. https://doi.org/10.1002/cssc.201900060.

(158) Yu, T.; Breslin, C. B. Review—2D Graphene and Graphene-Like Materials and Their Promising Applications in the Generation of Hydrogen Peroxide. J. Electrochem. Soc. 2020, 167 (12), 126502. https://doi.org/10.1149/1945-7111/abad6f.

(159) Ali, A.; Shen, P. K. Recent Progress in Graphene-Based Nanostructured Electrocatalysts for Overall Water Splitting. Electrochemical Energy Reviews 2020, 3 (2), 370–394. https://doi.org/10.1007/s41918-020-00066-3

(160) Xu, H.; Cheng, D.; Cao, D.; et al. RETRACTED ARTICLE: A universal principle for a rational design of single-atom electrocatalysts. Nature Catalysis 2018. https://doi.org/10.1038/s41929-018-0063-z

(161) Wang, X.-R.; Liu, J.-Y.; Liu, Z.-W.; Wang, W.-C.; Luo, J.; Han, X.-P.; Du, X.-W.; Qiao, S.-Z.; Yang, J. Identifying the Key Role of Pyridinic-N–Co Bonding in Synergistic Electrocatalysis for Reversible ORR/OER. Advanced Materials 2018, 30, 1800005. https://doi.org/10.1002/adma.201800005

(162) Kumar, R.; Sahoo, S.; Joanni, E.; Singh, R. K.; Maegawa, K.; Tan, W. K.; Kawamura, G.; Kar, K. K.; Matsuda, A. Heteroatom Doped Graphene Engineering for Energy Storage and Conversion. Materials Today 2020, 39, 47–65. https://doi.org/10.1016/j.mattod.2020.04.010.

(163) Li, X.; Duan, X.; Han, C.; Fan, X.; Li, Y.; Zhang, F.; Zhang, G.; Peng, W.; Wang, S. Chemical Activation of Nitrogen and Sulfur Co-Doped Graphene as Defect-Rich Carbocatalyst for Electrochemical Water Splitting. Carbon 2019, 148, 540–549. https://doi.org/10.1016/j.carbon.2019.04.021.

(164) Zhang, Y.; Li, W.; Lu, L.; Song, W.; Wang, C.; Zhou, L.; Liu, J.; Chen, Y.; Jin, H.; Zhang, Y. Tuning Active Sites on Cobalt/Nitrogen Doped Graphene for Electrocatalytic Hydrogen and Oxygen Evolution. Electrochimica Acta 2018, 265, 497–506. https://doi.org/10.1016/j.electacta.2018.01.203.

(165) Zheng, L.; Hu, W.; Shu, X.; Zheng, H.; Fang, X. Ultrafine CoPx Nanoparticles Anchored on Nitrogen Doped Reduced Graphene Oxides for Superior Hydrogenation in Alkaline Media. Advanced Materials Interfaces 2018, 5 (15), 1800515. https://doi.org/10.1002/admi.201800515.

(166) Jeong, S.; Hu, K.; Ohto, T.; Nagata, Y.; Masuda, H.; Fujita, J.-I.; Ito, Y. Effect of Graphene Encapsulation of NiMo Alloys on Oxygen Evolution Reaction. ACS Catalysis 2020, 10 (1), 792–799. https://doi.org/10.1021/acscatal.9b04134 (accessed 2025-12-28(167) Zheng, X.; Yao, Y.; Wang, Y.; Liu, Y. Tuning the Electronic Structure of Transition Metals Embedded in Nitrogen-Doped Graphene for Electrocatalytic Nitrogen Reduction: A First-Principles Study. Nanoscale 2020, 12 (17), 9696–9707. https://doi.org/10.1039/D0NR00072H.

(168) Liu, B.; Peng, H.-Q.; Cheng, J.; Zhang, K.; Chen, D.; Shen, D.; Wu, S.; Jiao, T.; Kong, X.; Gao, Q.; Bu, S.; Lee, C.-S.; Zhang, W. Nitrogen-Doped Graphene-Encapsulated Nickel–Copper Alloy Nanoflower for Highly Efficient Electrochemical Hydrogen Evolution Reaction. Small 2019, 15 (48), 1901545. https://doi.org/10.1002/smll.201901545.

(169) Jin, H.; Guo, C.; Liu, X.; Liu, J.; Vasileff, A.; Jiao, Y.; Zheng, Y.; Qiao, S.-Z. Emerging Two-Dimensional Nanomaterials for Electrocatalysis. Chemical Reviews 2018, 118 (13), 6337–6408. https://doi.org/10.1021/acs.chemrev.7b00689.

(170) Han, X.; Tong, X.; Liu, X.; Chen, A.; Wen, X.; Yang, N.; Guo, X.-Y. Hydrogen Evolution Reaction on Hybrid Catalysts of Vertical MoS2 Nanosheets and Hydrogenated Graphene. ACS Catal. 2018, 8 (3), 1828–1836. https://doi.org/10.1021/acscatal.7b03316.

(171) Yao, Y.; Jin, Z.; Chen, Y.; Gao, Z.; Yan, J.; Liu, H.; Wang, J.; Li, Y.; Liu, S. (Frank). Graphdiyne-WS2 2D-Nanohybrid Electrocatalysts for High-Performance Hydrogen Evolution Reaction. Carbon 2018, 129, 228–235. https://doi.org/10.1016/j.carbon.2017.12.024.

(172) Chen, Y.; Ren, R.; Wen, Z.; Ci, S.; Chang, J.; Mao, S.; Chen, J. Superior Electrocatalysis for Hydrogen Evolution with Crumpled Graphene/Tungsten Disulfide/Tungsten Trioxide Ternary Nanohybrids. Nano Energy 2018, 47, 66–73. https://doi.org/10.1016/j.nanoen.2018.02.023.

(173) Fei, H.; Dong, J.; Chen, D.; Hu, T.; Duan, X.; Shakir, I.; Huang, Y.; Duan, X. Single atom electrocatalysts supported on graphene or graphene-like carbons. Chemical Society Reviews 2019, 48 (20), 5207–5241. https://doi.org/10.1039/C9CS00422J

(174) Ye, S.; Luo, F.; Zhang, Q.; Zhang, P.; Xu, T.; Wang, Q.; He, D.; Guo, L.; Zhang, Y.; He, C.; Ouyang, X.; Gu, M.; Liu, J.; Sun, X. Highly Stable Single Pt Atomic Sites Anchored on Aniline-Stacked Graphene for Hydrogen Evolution Reaction. Energy Environ. Sci. 2019, 12 (3), 1000–1007. https://doi.org/10.1039/C8EE02888E.

(175) Pinto, A. M.; Gonçalves, I. C.; Magalhães, F. D. Graphene-Based Materials Biocompatibility: A Review. Colloids and Surfaces B: Biointerfaces 2013, 111, 188–202. https://doi.org/10.1016/j.colsurfb.2013.05.022.

(176) Wick, P.; Louw-Gaume, A. E.; Kucki, M.; Krug, H. F.; Kostarelos, K.; Fadeel, B.; Dawson, K. A.; Salvati, A.; Vázquez, E.; Ballerini, L.; Tretiach, M.; Benfenati, F.; Flahaut, E.; Gauthier, L.; Prato, M.; Bianco, A. Classification Framework for Graphene-Based Materials. Angew Chem Int Ed 2014, 53 (30), 7714–7718. https://doi.org/10.1002/anie.201403335.

(177) Park, M. V. D. Z.; Bleeker, E. A. J.; Brand, W.; Cassee, F. R.; van Elk, M.; Gosens, I.; de Jong, W. H.; Meesters, J. A. J.; Peijnenburg, W. J. G. M.; Quik, J. T. K.; van de Sandt, J. J. M.; Sips, A. J. A. M.; Wijnhoven, S. W. P. Considerations for Safe Innovation: The Case of Graphene. ACS Nano 2017, 11 (10), 95749593. https://doi.org/10.1021/acsnano.7b04120.

(178) Reina, G.; González-Domínguez, J. M.; Criado, A.; Vázquez, E.; Bianco, A.; Prato, M. Promises, Facts and Challenges for Graphene in Biomedical Applications. Chem. Soc. Rev. 2017, 46 (15), 4400–4416. https://doi.org/10.1039/C7CS00363C.

(179) Akhavan, O.; Ghaderi, E. Toxicity of Graphene and Graphene Oxide Nanowalls against Bacteria. ACS Nano 2010, 4 (10), 5731–5736. https://doi.org/10.1021/nn101390x.

(180) Hu, W.; Peng, C.; Luo, W.; Lv, M.; Li, X.; Li, D.; Huang, Q.; Fan, C. Graphene-Based Antibacterial Paper. ACS Nano 2010, 4 (7), 4317–4323. https://doi.org/10.1021/nn101097v.

(181) Barbolina, I.; Woods, C. R.; Lozano, N.; Kostarelos, K.; Novoselov, K. S.; Roberts, I. S. Purity of graphene oxide determines its antibacterial activity. 2D Materials 2016, 3 (2),

025025. https://cnanotechmed.com/publications/purity-of-graphene-oxide-determines-its-antibacterial-activity/

(182) Seifi, T.; Kamali, A. R. Anti-Pathogenic Activity of Graphene Nanomaterials: A Review. Colloids and Surfaces B: Biointerfaces 2021, 199, 111509. https://doi.org/10.1016/j.colsurfb.2020.111509.

(183) Pang, L.; Dai, C.; Bi, L.; Guo, Z.; Fan, J. Biosafety and Antibacterial Ability of Graphene and Graphene Oxide In Vitro and In Vivo. Nanoscale Res Lett 2017, 12 (1), 564. https://doi.org/10.1186/s11671-017-2317-0.

(184) Fernández-Merino, M. J.; Guardia, L.; Paredes, J. I.; Villar-Rodil, S.; Solís-Fernández, P.; Martínez-Alonso, A.; Tascón, J. M. D. Vitamin C Is an Ideal Substitute for Hydrazine in the Reduction of Graphene Oxide Suspensions. The Journal of Physical Chemistry C 2010, 114 (14), 6426–6432. https://doi.org/10.1021/jp100603h.

(185) Wang, J.; Cui, C.; Nan, H.; Yu, Y.; Xiao, Y.; Poon, E.; Yang, G.; Wang, X.; Wang, C.; Li, L.; Boheler, K. R.; Ma, X.; Cheng, X.; Ni, Z.; Chen, M. Graphene Sheet-Induced Global Maturation of Cardiomyocytes Derived from Human Induced Pluripotent Stem Cells. ACS Appl. Mater. Interfaces 2017, 9 (31), 25929–25940. https://doi.org/10.1021/acsami.7b08777.

(186) Kenry; Lee, W. C.; Loh, K. P.; Lim, C. T. When Stem Cells Meet Graphene: Opportunities and Challenges in Regenerative Medicine. Biomaterials 2018, 155, 236–250. https://doi.org/10.1016/j.biomaterials.2017.10.004.

(187) Rastogi, S. K.; Bliley, J.; Matino, L.; Garg, R.; Santoro, F.; Feinberg, A. W.; Cohen-Karni, T. Three-Dimensional Fuzzy Graphene Ultra-Microelectrodes for Subcellular Electrical Recordings. Nano Res. 2020, 13 (5), 1444–1452. https://doi.org/10.1007/s12274-020-2695-y.

(188) Rastogi, S. K.; Raghavan, G.; Yang, G.; Cohen-Karni, T. Effect of Graphene on Nonneuronal and Neuronal Cell Viability and Stress. Nano Lett. 2017, 17 (5), 3297–3301. https://doi.org/10.1021/acs.nanolett.7b01215.

(189) Lasocka, I.; Szulc-Dąbrowska, L.; Skibniewski, M.; Skibniewska, E.; Gregorczyk-Zboroch, K.; Pasternak, I.; Hubalek Kalbacova, M. Cytocompatibility of Graphene Monolayer and Its Impact on Focal Cell Adhesion, Mitochondrial Morphology and Activity in BALB/3T3 Fibroblasts. Materials 2021, 14 (3), 643. https://doi.org/10.3390/ma14030643.

(190) Savchenko, A.; Cherkas, V.; Liu, C.; Braun, G. B.; Krumov, A.; Meffin, H.; Sheets, E. D.; Okun, M. S.; Dalal, R.; Papoian, V.; Shafique, S.; Eliceiri, K. W.; Zaitsev, A. V.; Sokolov, I.; Moll, J.; Khraiche, M. L.; Mikheev, A. M. Graphene biointerfaces for optical stimulation of cells. Science Advances 2018, 4 (5), eaat0351. https://doi.org/10.1126/sciadv.aat0351.

(191) Kim, T.; Kahng, Y. H.; Lee, T.; Lee, K.; Kim, D. H. Graphene Films Show Stable Cell Attachment and Biocompatibility with Electrogenic Primary Cardiac Cells. Molecules and Cells 2013, 36 (6), 577–582. https://doi.org/10.1007/s10059-013-0277-5.

(192) Hitscherich, P.; Aphale, A.; Gordan, R.; Whitaker, R.; Singh, P.; Xie, L.-H.; Patra, P.; Lee, E. J. Electroactive graphene composite scaffolds for cardiac tissue engineering. Journal of Biomedical Materials Research Part A 2018, 106 (11), 2923–2933. https://doi.org/10.1002/jbm.a.36481.

(193) Ryan, A. J.; Kearney, C. J.; Shen, N.; Khan, U.; Kelly, A. G.; Probst, C.; Brauchle, E.; Biccai, S.; Garciarena, C. D.; Vega-Mayoral, V.; Loskill, P.; Kerrigan, S. W.; Kelly, D. J.; Schenke-Layland, K.; Coleman, J. N.; O'Brien, F. J. Electroconductive Biohybrid Collagen/Pristine Graphene Composite Biomaterials with Enhanced Biological Activity. Advanced Materials 2018, 30 (15), 1706442. https://doi.org/10.1002/adma.201706442

(194) Norahan, M. H.; Pourmokhtari, M.; Saeb, M. R.; Bakhshi, B.; Soufi Zomorrod, M.; Baheiraei, N. Electroactive Cardiac Patch Containing Reduced Graphene Oxide with Potential Antibacterial Properties. Materials Science and Engineering: C 2019, 104, 109921. https://doi.org/10.1016/j.msec.2019.109921.

(195) Lee, T.-J.; Park, S.; Bhang, S. H.; Yoon, J.-K.; Jo, I.; Jeong, G.-J.; Hong, B. H.; Kim, B.-S. Graphene Enhances the Cardiomyogenic Differentiation of Human Embryonic Stem Cells. Biochemical and Biophysical Research Communications 2014, 452 (1), 174–180. https://doi.org/10.1016/j.bbrc.2014.08.062.

(196) Smith, A. S. T.; Yoo, H.; Yi, H.; Ahn, E. H.; Lee, J. H.; Shao, G.; Nagornyak, E.; Laflamme, M. A.; Murry, C. E.; Kim, D.-H. Micro- and Nano-Patterned Conductive Graphene–PEG Hybrid Scaffolds for Cardiac Tissue Engineering. Chem. Commun. 2017, 53 (53), 7412–7415. https://doi.org/10.1039/C7CC01988B.

(197) Ameri, S. K.; Singh, P. K.; D'Angelo, R.; Stoppel, W.; Black, L.; Sonkusale, S. R. Three dimensional graphene scaffold for cardiac tissue engineering and in-situ electrical recording. Annu. Int. Conf. IEEE Eng. Med. Biol. Soc. (EMBC) 2016, 2016, 4201–4203. https://doi.org/10.1109/EMBC.2016.7591653

(198) Ahadian, S.; Zhou, Y.; Yamada, S.; Estili, M.; Liang, X.; Nakajima, K.; Shiku, H.; Matsue, T. Graphene Induces Spontaneous Cardiac Differentiation in Embryoid Bodies. Nanoscale 2016, 8 (13), 7075–7084. https://doi.org/10.1039/C5NR07059G.

(199) Park, J.; Kim, B.-S.; et al. Graphene Oxide Flakes as a Cellular Adhesive: Prevention of Reactive Oxygen Species Mediated Death of Implanted Cells for Cardiac Repair. ACS Nano 2015, 9 (5), 4987–4999. https://doi.org/10.1021/nn507149w

(200) Shin, S. R.; Zihlmann, C.; Akbari, M.; et al. Reduced Graphene Oxide-GelMA Hybrid Hydrogels as Scaffolds for Cardiac Tissue Engineering. Small 2016, 12 (27), 3677–3689. https://doi.org/10.1002/smll.201600178

(201) Zhao, L. A novel graphene oxide polymer gel platform for cardiac tissue engineering application. 3 Biotech 2019, 9 (11), 401. https://doi.org/10.1007/s13205-019-1912-4

(202) Hitscherich, P.; Aphale, A.; Gordan, R.; Whitaker, R.; Singh, P.; Xie, L.; Patra, P.; Lee, E. J. Electroactive Graphene Composite Scaffolds for Cardiac Tissue Engineering. Journal of Biomedical Materials Research Part A 2018, 106 (11), 2923–2933. https://doi.org/10.1002/jbm.a.36481.

(203) Nazari, H.; Azadi, S.; Hatamie, S.; Zomorrod, M. S.; Ashtari, K.; Soleimani, M.; Hosseinzadeh, S. Fabrication of Graphene-Silver/Polyurethane Nanofibrous Scaffolds for Cardiac Tissue Engineering. Polymers for Advanced Technologies 2019, 30 (8), 2086–2099. https://doi.org/10.1002/pat.4641.

(204) Fakhrali, A.; Nasari, M.; Poursharifi, N.; Semnani, D.; Salehi, H.; Ghane, M.; Mohammadi, S. Biocompatible Graphene-Embedded PCL/PGS-Based Nanofibrous Scaffolds: A Potential Application for Cardiac Tissue Regeneration. Journal of Applied Polymer Science 2021, 138 (40), 51177. https://doi.org/10.1002/app.51177.

(205) Electroconductive Graphene-Containing Polymeric Patch: A Promising Platform for Future Cardiac Repair | ACS Biomaterials Science & Engineering. https://pubs.acs.org/doi/10.1021/acsbiomaterials.0c00266 (accessed 2025-12-28).

(206) Nazari, H.; Heirani-Tabasi, A.; Hajiabbas, M.; Khalili, M.; Shahsavari Alavijeh, M.; Hatamie, S.; Mahdavi Gorabi, A.; Esmaeili, E.; Ahmadi Tafti, S. H. Incorporation of Two-Dimensional Nanomaterials into Silk Fibroin Nanofibers for Cardiac Tissue Engineering. Polymers for Advanced Technologies 2020, 31 (2), 248–259. https://doi.org/10.1002/pat.4765.

(207) Zhao, G.; Qing, H.; Huang, G.; Genin, G. M.; Lu, T. J.; Xu, F. Reduced graphene oxide functionalized nanofibrous silk fibroin matrices for engineering excitable tissues. NPG Asia Materials 2018, 10, 982–994. https://doi.org/10.1038/s41427-018-0092-8

(208) Zhang, F.; Meng, H.-X.; Liu, H.-X.; Lu, Y.-Q.; Liu, C.-M.; Zhang, Z.-M.; Qu, K.-Y. Easy Applied Gelatin-Based Hydrogel System for Long-Term Functional Cardiomyocyte Culture and Myocardium Formation. ACS Biomaterials Science & Engineering 2019, 5 (7), 3324–3335. https://doi.org/10.1021/acsbiomaterials.9b00515

(209) Lee, J.; Manoharan, V.; Cheung, L.; et al. Nanoparticle-Based Hybrid Scaffolds for Deciphering the Role of Multimodal Cues in Cardiac Tissue Engineering. ACS Nano 2019, 13 (11), 12525–12539. https://doi.org/10.1021/acsnano.9b03050

(210) Tsui, J. H.; Leonard, A.; Camp, N. D.; Long, J. T.; Nawas, Z. Y.; Chavanachat, R.; Smith, A. S. T.; Choi, J. S.; Dong, Z.; Ahn, E. H.; Wolf-Yadlin, A.; Murry, C. E.; Sniadecki, N. J.; Kim, D.-H. Tunable Electroconductive Decellularized Extracellular Matrix Hydrogels for Engineering Human Cardiac Microphysiological Systems. Biomaterials 2021, 272, 120764. https://doi.org/10.1016/j.biomaterials.2021.120764.

(211) Jing, X.; Mi, H.-Y.; Napiwocki, B. N.; Peng, X.-F.; Turng, L.-S. Mussel-Inspired Electroactive Chitosan/Graphene Oxide Composite Hydrogel with Rapid Self-Healing and Recovery Behavior for Tissue Engineering. Carbon 2017, 125, 557–570. https://doi.org/10.1016/j.carbon.2017.09.071.

(212) Karimi Hajishoreh, N.; Baheiraei, N.; Naderi, N.; Salehnia, M. Reduced Graphene Oxide Facilitates Biocompatibility of Alginate for Cardiac Repair. Journal of Bioactive and Compatible Polymers 2020, 35 (4–5), 363–377. https://doi.org/10.1177/0883911520933913.

(213) Annabi, N.; Shin, S. R.; Tamayol, A.; Miscuglio, M.; Bakooshli, M. A.; Assmann, A.; Mostafalu, P.; Sun, J.-Y.; Mithieux, S.; Cheung, L.; Tang, X. (Shirley); Weiss, A. S.; Khademhosseini, A. Highly Elastic and Conductive Human-Based Protein Hybrid Hydrogels. Advanced Materials 2016, 28 (1), 40–49. https://doi.org/10.1002/adma.201503255.

(214) Paul, A.; Hasan, A.; Kindi, H. A. Al; Gaharwar, A. K.; Rao, V. T. S.; Nikkhah, M.; Shin, S. R.; Krafft, D.; Dokmeci, M. R.; Shum-Tim, D.; Khademhosseini, A. Injectable Graphene Oxide/Hydrogel-Based Angiogenic Gene Delivery System for Vasculogenesis and Cardiac Repair. ACS Nano 2014, 8 (8), 8050–8062. https://doi.org/10.1021/nn5020787

(215) Bangham, A. D. A Correlation between Surface Charge and Coagulant Action of Phospholipids. Nature 1961, 192 (4808), 1197–1198. https://doi.org/10.1038/1921197a0.

(216) Bangham, A. D.; Hill, M. W.; Miller, N. G. A. Preparation and Use of Liposomes as Models of Biological Membranes. In Methods in Membrane Biology: Volume 1; Korn, E. D., Ed.; Springer US: Boston, MA, 1974; pp 1–68. https://doi.org/10.1007/978-1-4615-7422-4_1.

(217) Gregoriadis, G.; Neerunjun, D. E. Control of the Rate of Hepatic Uptake and Catabolism of Liposome-Entrapped Proteins Injected into Rats. Possible Therapeutic Applications. European Journal of Biochemistry 1974, 47 (1), 179–185. https://doi.org/10.1111/j.1432-1033.1974.tb03681.x.

(218) Akbarzadeh, A.; Rezaei-Sadabady, R.; Davaran, S.; Joo, S. W.; Zarghami, N.; Hanifehpour, Y.; Samiei, M.; Kouhi, M.; Nejati-Koshki, K. Liposome: Classification, Preparation, and Applications. Nanoscale Res Lett 2013, 8 (1), 102. https://doi.org/10.1186/1556-276X-8-102.

(219) Jiskoot, W.; Teerlink, T.; Beuvery, E. C.; Crommelin, D. J. A. Preparation of Liposomes via Detergent Removal from Mixed Micelles by Dilution. Pharmaceutisch Weekblad Scientific Edition 1986, 8 (5), 259–265. https://doi.org/10.1007/BF01960070.

(220) Kaddah, S.; Khreich, N.; Kaddah, F.; Charcosset, C.; Greige-Gerges, H. Cholesterol Modulates the Liposome Membrane Fluidity and Permeability for a Hydrophilic Molecule. Food and Chemical Toxicology 2018, 113, 40–48. https://doi.org/10.1016/j.fct.2018.01.017.

(221) Allen, T. M. The Use of Glycolipids and Hydrophilic Polymers in Avoiding Rapid Uptake of Liposomes by the Mononuclear Phagocyte System. Advanced Drug Delivery Reviews 1994, 13 (3), 285–309. https://doi.org/10.1016/0169-409X(94)90016-7.

(222) Nsairat, H.; Khater, D.; Sayed, U.; Odeh, F.; Al Bawab, A.; Alshaer, W. Liposomes: structure, composition, types, and clinical applications. Heliyon 2022, 8 (5), e09394. https://www.cell.com/heliyon/fulltext/S2405-8440(22)00682-X

(223) Torchilin, V. P. Recent advances with liposomes as pharmaceutical carriers. Nature Reviews Drug Discovery 2005, 4 (2), 145–160. https://doi.org/10.1038/nrd1632

(224) Barenholz, Y. (Chezy). Doxil® — The First FDA-Approved Nano-Drug: Lessons Learned. Journal of Controlled Release 2012, 160 (2), 117–134. https://doi.org/10.1016/j.jconrel.2012.03.020.

(225) Alshaer, W.; Hillaireau, H.; Fattal, E. Aptamer-Guided Nanomedicines for Anticancer Drug Delivery. Advanced Drug Delivery Reviews 2018, 134, 122–137. https://doi.org/10.1016/j.addr.2018.09.011.

(226) Batzri, S.; Korn, E. D. Single Bilayer Liposomes Prepared without Sonication. Biochimica et Biophysica Acta (BBA) - Biomembranes 1973, 298 (4), 1015–1019. https://doi.org/10.1016/0005-2736(73)90408-2.

(227) Wagner, A.; Vorauer-Uhl, K.; Kreismayr, G.; Katinger, H. The crossflow injection technique: an improvement of the ethanol injection method. Journal of Liposome Research 2002, 12 (3), 259–270. https://doi.org/10.1081/LPR-120014761.

(228) Bolotin, E. M.; Cohen, R.; Bar, L. K.; Emanuel, N.; Ninio, S.; Barenholz, Y.; Lasic, D. D. Ammonium Sulfate Gradients for Efficient and Stable Remote Loading of Amphipathic Weak Bases into Liposomes and Ligandoliposomes. Journal of Liposome Research 1994, 4 (1), 455–479. https://doi.org/10.3109/08982109409037057

(229) Crowe, J. H.; Crowe, L. M.; Carpenter, J. F.; Rudolph, A. S.; Wistrom, C. A.; Spargo, B. J.; Anchordoguy, T. J. Interactions of Sugars with Membranes. Biochimica et Biophysica Acta (BBA) - Reviews on Biomembranes 1988, 947 (2), 367–384. https://doi.org/10.1016/0304-4157(88)90015-9.

(230) Mura, S.; Nicolas, J.; Couvreur, P. Stimuli-Responsive Nanocarriers for Drug Delivery. Nature Mater 2013, 12 (11), 991–1003. https://doi.org/10.1038/nmat3776.

(231) Needham, D.; Park, J.-Y.; Wright, A. M.; Tong, J. Materials characterization of the low temperature sensitive liposome (LTSL): effects of the lipid composition (lysolipid and DSPE–PEG2000) on the thermal transition and release of doxorubicin. Faraday Discussions 2013, 161, 515–534. https://doi.org/10.1039/C2FD20111A

(232) Bozzuto, G.; Molinari, A. Liposomes as nanomedical devices. International Journal of Nanomedicine 2015, 10, 975–999. https://doi.org/10.2147/IJN.S68861

(233) Mathieu, M.; Martin-Jaular, L.; Lavieu, G.; Théry, C. Specificities of secretion and uptake of exosomes and other extracellular vesicles for cell-to-cell communication. Nature Cell Biology 2019, 21 (1), 9–17. https://doi.org/10.1038/s41556-018-0250-9

(234) van Niel, G.; D'Angelo, G.; Raposo, G. Shedding Light on the Cell Biology of Extracellular Vesicles. Nat Rev Mol Cell Biol 2018, 19 (4), 213–228. https://doi.org/10.1038/nrm.2017.125.

6 Graphene oxide accelerates TGFβ-mediated epithelial-mesenchymal transition and stimulates pro-inflammatory immune response in amniotic epithelial cells

DOI: https://doi.org/10.1016/j.mtbio.2023.100758

6.1 Introduction

Amniotic-derived stem cells isolated from placenta have been pro posed as promising candidates in developing therapeutic treatments in regenerative medicine[1–4]. Amniotic epithelial cells (AECs) which are among the most studied amniotic-derived cells to date, along with the large availability, also offer many advantages such as no ethical con cerns, high plasticity without any tumor derives as well as both basal and induced immunomodulatory properties[1,5]. In particular, the increasing clinical interests on AECs are mainly related to their great plasticity that had been attributed to their early embryological stage origin and to the presence of a variable subpopu lation of cells expressing pluripotent markers[6–9]. The preclinical settings started to define insights the AECs pro-regenerative mechanisms expressed by combining trans-differentiation with paracrine activities[10]. To this regard, AECs are able to differentiate into tendon-like cells in experimental injured Achille tendons[4,11,12]. Likewise, other evi dences demonstrated a similar trans-differentiation ability of AECs to wards cardiomyocyte-like and hepatocyte-like cells[13,14]. AECs immune paracrine activity had been well documented to date in different systems to accelerate healing by promoting the transition from the inflammatory to the proliferative phase[15,16] and by developing an anti-fibrotic action[17,18]. AECs express a basal release of immunomodulatory bioactive factors aimed physiologically to generate the immune tolerance at the barrier between the two semi-allogenic organism mother and fetus[19,20]. However, the immunomodulatory properties of AECs are also amplified in response to inflammatory stimulus[21,22] and when the cells have been inserted in injured tissues[4]. Additionally, also tissue engineering strategies have also been proposed to potentiate the AECs immune action by seeding them on immune inductive scaffolds[23].

Alternatively, graphene oxide (GO) has been proposed as an immune mimetic material largely used for eliciting stem cell-based regenerative therapies[24,25] even though this strategy has never been tempted up to now on AECs. Indeed, GO possess exceptional properties with respect to other additives or nanomaterials. It is a one atom thick molecule and therefore its surface is widely extended with respect to its weight allowing to adsorbe/interact with a heavy amount of proteins, drugs, ligands and cell membranes. Moreover, the low cost and the ease of functionalization and therefore the possibility to tune at will properties such as water affinity, adsorption capacity towards different molecules, surface charge, to name a few, makes GO a very attractive alternative. To this regard, it has been proven that GO constructs used for cardiac regeneration were able to reduce inflammation by interacting with macrophages and decreasing the release of reactive oxygen species[26]. At the same time, evidences collected *in vitro* demonstrated that GO nanoparticles (GONPs) were able to inhibit LPS-induced interleukin 6 (IL-6) release and to stimulate IL-10 synthesis in blood cell cultures[27]. Similarly, GO enriched polypropylene suture threads buttons decreased the expression of inflammatory markers in primary human gingival fibroblasts exposed to LPS[28].

Noteworthy, GO-based treatments may regulate stem cells immune response by modulating their phenotype, in particular, by inducing the epithelial-mesenchymal transition (EMT) as demonstrated on human retinal pigment epithelial cells and lung carcinoma epithelial cells[29–31]. In presence of GO, epithelial cells demonstrated to down-regulate E-Cadherin and β-Cadherin epithelial markers while mesenchymal markers like Vimentin, N-Cadherin, α-SMA and matrix metalloproteinases (MMP-2 and MMP-9) were upregulated. Taking advantage of such a mechanism, GO was able to enhance the migration potential of epithelial stem cells, which could be crucial for accelerating wound healing [30,31]. Despite GO-based materials are revealed as great promises for biomedical applications by receiving increasing attractiveness[32–35], there is lack of information available on their effect on AECs, an emerging source of stem cell broadly proposed for the regeneration of several biological systems[36] as well as for developing stem cell based- and -free protocols for autoimmune diseases. To this aim,

the present research has been designed to assess the effects of GO-loaded glass surfaces on AECs phenotype, to study the intracellular pathway involved and, finally, to verify the impact on stem-cell immune paracrine activity.

6.2 Materials and methods

6.2.1 Ethics statement

No ethic statement is required for the present research since: 1. ovine AECs and PMBS isolation have been both isolated from waste biological samples collected at the abattoir from animals slaughtered for food purposes; 2. human leukemia monocytic cell line (hTHP1) were purchased from ATCC (Manassas, Virginia, USA).

6.2.2 Preparation of GO suspension

An aqueous solution of 4 g/L of graphene oxide (Graphenea, Donostia San Sebastian, Spain) was added to Ultrapure MilliQ water (electric resistance >18.2 MΩ/cm), from a Millipore Corp. model Direct- Q 3 system, to reach the concentration of 20 μg/mL and bath ultrasonicated for 30 min (37 kHz, 180 W; Elmasonic P60H; Elma). The concentration of GO was checked spectrophotometrically at λ_{max} of 230 nm by using a Varian Cary 100 BIO UV–vis spectrophotometer. GO flake dimensions and ζ-potential were determined by using dynamic laser light scattering (DLS) (90plus/BI-MAS ZetaPlus multiangle particle size analyzer, Brookhaven Instrument Corp.).

6.2.3 Activation of substrates

The reactions were carried out by using two different supports, i.e., 16 mm and 5 mm round glass coverslips, previously washed and ultrasonicated in isopropanol and acetone. Each side of the substrates was activated with an UV-ozone lamp (PSD-UV4 Novascan UV Ozone System Base model, Novascan Technologies, Boone; NC) for 30 min to increase the hydrophilicity of the surface and to improve the covalent binding of molecules. After the activation, the substrates were incubated with a 3- (aminopropyl)triethoxysilane (APTES) (Sigma-Aldrich, ST. Louis, MO) solution 1 M in

ethanol for 1 h to form the silanized derivatives and then rinsed with ethanol to remove the excess of APTES.

6.2.4 Preparation of GO-functionalized substrates

The GO-functionalized substrates were prepared as previously described[33]. In detail, the APTES-activated coverslips were dipped in 20 μg/mL aqueous solution of GO for 5 h. In this way, GO flakes were covalently bound to APTES amino groups, exposed on activated substrates surfaces, through epoxy ring opening reaction or amide formation with edge carboxylic groups. After the incubation, the coverslips were rinsed with Milli-Q water to get rid of any excess of GO and subsequently sterilized under UV lamp for 2 h.

6.2.5 AFM, FTIR and Raman spectroscopy characterization

The surface topography of GO-functionalized coverslips was investigated with AFM by using the Multimode 8 AFM microscope (Bruker, Billerica, Massachusetts) equipped with a Nanoscope V controller in Tapping in air mode. Commercial silicon cantilever RTESPA-300 (cantilever resonance frequency 300 kHz and nominal elastic constant 40 N/m) with a nominal tip radius of 8 nm was used to analyze properties such as topography across a scan size of 20 μm × 20 μm. The images were analyzed by Nanoscope Analysis 1.8 software and the bearing analysis tool was used to calculate the percentage of surface covered by GO flakes, in the form of both single layers and overlapped GO.

IR spectra were obtained using a Shimadzu IRAffinity-1S FTIR spectrophotometer (Shimadzu Italia S.r.l., Milan, Italy) equipped with a sealed and desiccated interferometer, a DLATGS (Deuterated Triglycine Sulphate Doped with L-Alanine) detector and a single reflection diamond ATR crystal (QATR 10, Shimadzu Italia S.r.l., Milan, Italy). All FTIR spectra were recorded in the range from 500 to 3500 cm^{-1} co-adding 45 interferograms at a resolution of 4 cm^{-1} with Happ–Genzel apodization. The ATR crystal was carefully cleaned before each analysis, a background was recorded for each sample and the measurements were performed in triplicate. Spectra manipulation was carried out with the software LabSolution IR version 2.27 (Shimadzu Italia S.r.l., Milan, Italy). The Raman

spectra of GO-functionalized substrates were obtained by confocal and high-performance Raman microscope (XploRA PLUS, HORIBA, Japan) with deep-cooled CCD detector technology. LabSpec (Horiba, Japan) was employed to control the Raman spectroscopic system and for the optimization and processing of the acquired data. All Raman spectroscopic measurements were performed in the range of 900–1900 cm^{-1} and with a 1800-line/mm grating. A single spectrum of the sample has been detected with a 532 nm laser, with a time of 8 s and 20 accumulations. For the Raman mapping of the G band intensity, an area of 400 μm^2 was chosen by using a 100 × objective and scanned with an excitation laser of 532 nm. Raman spectra are the overlaid spectra obtained by multivariate analysis (LabSpec 6's Multivariate Analysis module) recorded in an area of 400 μm^2, using step between the points of 400 nm through SWIFT modality with a time of 1 s of acquisition and 1 accumulation. Furthermore, a pinhole of 100 μm and a 50 μm slit were used.

6.2.6 AECs isolation and culture

Ovine AECs were collected from the amniotic membrane (AM) of fetuses at middle stage of gestation. AECs were collected following a previously validated protocol [37]. Freshly isolated AECs were seeded at a density of 10.000 cells/well in a 12 well/plate on commercial glass coverslip as a control (AECs) or on GO-functionalized ones (AECs + GO).

6.2.7 Experimental plan

The different stem cell conditions and analysis performed are summarized in Fig. 1. Briefly, freshly isolated AECs were cultured in standard condition as control (AECs on uncoated coverslip) or on GO-coated coverslip (AECs + GO) until 70–80% of confluence. Then, the culture media (CM) was replaced with serum-free medium supplemented with or without 1 μg/mL LPS for 1 h. The cultural medium was replaced again with fresh serum-free medium and the cells were cultured for further for 24 h. At the end, AECs were collected as well as the serum-free CMs by centrifuging them at 300 g for 10 min to remove cell debris. AECs were analyzed for epithelial and mesenchymal gene and protein markers, assessed for TGFβ pathway and, finally, tested for migration. CM were used for

assessing cytokines and chemokines release and for performing immune biological assays on ovine PBMC and human leukemia monocytic cell line hTHP138.

6.2.8 Gene analyses

The EMT gene markers were analyzed by Real-time qPCR and normalized to GAPDH (Table 1). The relative expression was calculated by the comparative Ct (ΔCt) [39] and expressed as fold change over freshly isolated AECs (T_0) = 1. The reaction of RT-PCR was performed in triplicate for each experimental replicate of each different biological sample (n = 3).

Table 1

Primers details used for RT-qPCR analysis (also reported in Russo V et al., 2022[40]).

Gene	Forward	Reverse
VIM	5'-GACCAGCTCACCAACGACA-3'	5'-CTCCTCCTGCAACTTCTCCC-3'
CYTO8	5'-CTCAAAGGCCAGAGGGCTTC-3'	5'-CTTGGCCTGAGCATCCTTGA-3
SNAIL	5'-GTCGTGGGTGGAGAGCTTTG– 3'	5'-TGCTGGAAAGTGAGCTCTGG– 3'
TWIST	5'-GCCGGAGACCTAGATGTCATTG-3'	5'-CCACGCCCTGTTTCTTTGAAT-3'
ZEB	5'-TGGCAAAAGAAAACCCATGGAAA-3'	5'-AAAGTGACCAGGGCTCACAG-3'
GAPDH	5'-CCTGCACCACCAACTGCTTG-3'	5'-TTGAGCTCAGGGATGACCTTG-3'

6.2.9 Immunohistochemistry

AECs phenotype was defined by analyzing the epithelial (E-Cadherin and CYTO8) and mesenchymal (VIM) protein expression and localization by immunocytochemistry (ICC) as previously reported [21]. Nuclear counterstaining was obtained with DAPI (Vectastain) at the final dilution of 1:2000 in PBS. The omission of primary antibodies (Abs) was used as negative control. Details on Abs and dilutions are specified in Table 2. The reaction was carried out in triplicate on each biological replicate (n = 3) for each experimental condition.

6.2.10 ROS production and viability assay

The effects of GO on cell viability were investigated in AECs and AECs + GO by assessing ROS production and cell proliferation using, respectively, DCFDA (Cellular ROS Detection Kit:Abcam)

and MTS proliferation assay (G3582, Promega). ROS detection was performed by using the fluorogenic agent 2′,7′-dichlorofluorescein diacetate (DCFDA), which is able to diffuse into the cells and be deacetylated by cellular esterases to a nonfluorescent compound, following later oxidization by ROS to 2′, 7′- dichlorofluorescein (DCF). For this purpose, both AECs and AECs + GO were plated into 96-multiwell plates at cell densities of 10,000 cells/well. Twenty-four hours later, the cells were washed with PBS and incubated with 10 μM DCFDA diluted in phenol red–free medium (DMEM F12, Corning) for 40 min at 37 ˚C in the dark, according to the provider's instructions. After an additional wash with PBS, fluorescence was evaluated at excitation of 495 nm and emission of 529 nm for 80 min by using EnSpire® Multimode Plate Reader (PerkinElmer, Waltham, MA, USA). For data analysis, blank readings were subtracted to every single measurement. On the other hand, AECs and AECs + GO cell proliferation was assessed by using CellTiter96 Aqueous One Solution Cell Proliferation Assay following manufacturer's instruction (G3582, Promega).

Table 2

Primary and secondary antibodies used for ICC and WB. (Ref(a)[21]; Ref(b)[40]).

Gene	Forward	Reverse
VIM	5'-GACCAGCTCACCAACGACA-3'	5'-CTCCTCCTGCAACTTCTCCC-3'
CYTO8	5'-CTCAAAGGCCAGAGGGCTTC-3'	5'-CTTGGCCTGAGCATCCTTGA-3
SNAIL	5'-GTCGTGGGTGGAGAGCTTTG– 3'	5'-TGCTGGAAAGTGAGCTCTGG– 3'
TWIST	5'-GCCGGAGACCTAGATGTCATTG-3'	5'-CCACGCCCTGTTTCTTTGAAT-3'
ZEB	5'-TGGCAAAAGAAAACCCATGGAAA-3'	5'-AAAGTGACCAGGGCTCACAG-3'
GAPDH	5'-CCTGCACCACCAACTGCTTG-3'	5'-TTGAGCTCAGGGATGACCTTG-3'

Investigation	Primary Antibody	Dilution	Secondary Antibody	Dilution
ICC	E-Cadherin[a] (LS Bio, Massachusetts, USA)	1:100	Anti-rabbit Alexa Fluor (Sigma-Aldrich, St. Louis, MO, USA)	1:200
	CYTO8[a,b] (Abcam, Cambridge, UK)	1:200	Anti-mouse Alexa Fluor (Sigma-Aldrich, St. Louis, MO, USA)	1:500
	VIM[a,b] (Agilent Technologies, California, USA)	1:200	Anti-mouse Cy3 (Sigma-Aldrich, St. Louis, MO, USA)	1:750
WB	Rabbit pSMAD2[a] (3108 Cell Signalling)	1:500	Anti-rabbit HRP conjugated (31461, Pierce™ Antibody)	1:2000
	Rabbit SMAD2/3[a] (3102 Cell Signalling)	1:500	Anti-rabbit HRP conjugated (31461, Pierce™ Antibody)	1:2000
	Mouse α-TUBULIN[a] (SIGMA T5168)	1:1000	Anti-mouse HRP conjugated (Santa Cruz sc 516102)	1:10000

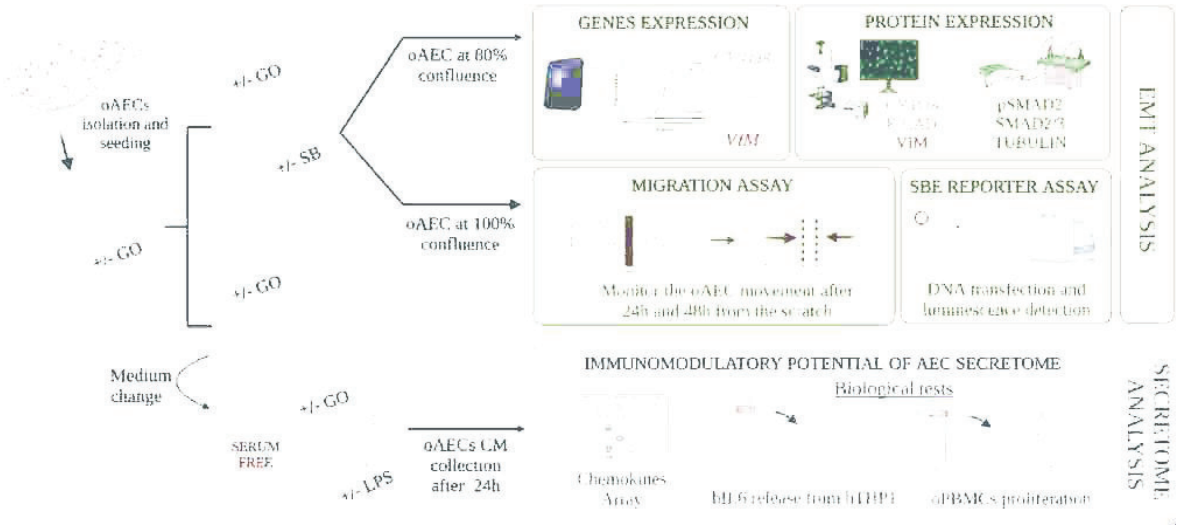

Fig. 1. Experimental design of AECs seeded on GO-coated glass coverslips. GO-induced EMT was studied by analyzing the gene expression of the CYTO8 (epithelial marker), SNAL, TWIST, ZEB (transcription factors of the EMT) and VIM (mesenchymal marker), the protein expression of CYTO8 and E-CAD (epithelial markers), VIM (mesenchymal marker) and p SMAD2, SMAD2/3 (downstream markers of TGFβ signaling pathway), the migration assay at 24 and 48 h, and the SBE reporter assay.

GO-induced immunomodulatoty properties of AECs secretome was studied by analyzing the chemokine expression with a Human Inflammation Antibody Array membrane, and the biological effect on hTHP-1 and oPBMCs.

6.2.11 TGFβ pathway assessment

TGFβ and SMAD 2/3 activation was assessed by using SBE reporter. For WB analysis the total protein was extracted from each sample in lysis buffer (50 mM Tris HCl pH 8, 250 mM NaCl, 5 mM EDTA, 0.1% Triton X- 100 10%) with Phosphatase Inhibitor (P5726, Sigma) and Protease Inhibitor Cocktails (P8340, Sigma) diluted according to manufacturing instruction. Samples were put on ice for 30 min, and then centrifuged at 12,000×*g* for 12 min at 4 ˚C. The supernatant was collected, and 5 µL of the supernatant were used to determine protein concentration with Quick Start™ Bradford 1x Dye Reagent (BioRad). Afterwards, 30 µg of total protein was separated by 10% SDS-PAGE, and

then transferred to nitrocellulose membranes (BIORAD) with TURBO Transfers (BioRad). Membranes were subsequently incubated with Every blot blocking solution (Biorad) for 5 min. Primary antibodies (Table 2) were incubated overnight at 4 ˚C whereas specific secondary HRP conjugated IgG antibodies for 1 h, at room temperature. ClarityMax ECL reagents (LiteAblot PLUS Euroclone EMP011005) were used to detect signals with Azure Byosystem. Densitometric analysis was performed using ImageJ.

The SBE Reporter kit (Cat#: 60654, BPSBioscience) was used for monitoring the activity of TGFβ/SMAD signaling pathway in the EMT of AECs seeded on normal or GO-coated coverslips, following manufacturer's instructions. Briefly, after the cells reached 50–60% confluence, the DNA transfection was performed by using lipofectamine with the provided vectors from the kit. After 24 h of transfection, the medium was changed to serum-free medium with the activator TGFβ1 (final concentration 10 ng/mL) or the inhibitor SB-505124 (final concentration 2 μM). After 18 h of stimulation, luciferase activity was evaluated by dual-luciferase (Firefly-Renilla) reporter assay system (BPS Bioscience, 60683–1, USA) with a luminometer following manufacturer's protocol. The normalized luciferase activity of the SBE reporter was obtained by subtracting the background and the non-inducible firefly luminescence before representing the ratio of Firefly luminescence from Notch Firefly luciferase to Renilla luminescence from control Renilla luciferase.

6.2.12 Migration test

AECs or AECs + GO were tested for their migration properties by seeding them on 500 μm cell culture inserts (Ibidi, 80209) placed on top of normal (AEC) and GO-coated (AEC + GO) coverslips. After reaching full confluence, cells were starved for a period of 5 h in serum-free media. Then, the cell culture inserts were removed and the incubation was continued and monitored for 24 and 48 h in fresh serum-free media. The wound closure of each well was photographed using a digital camera.

The percentage of wound healing and the velocity of migration was quantified by + Imagej migration plugin software[41].

6.2.13 Cytokine and chemokine array

Multiple pro-and anti-inflammatory cytokines released in the AECs and AECs + GO, with or without LPS exposure, were detected by using a specific Human Inflammation Antibody Array (Abcam, ab134003) carried out according to the manufacturer's instructions and previously validated on ovine AEC model[42,43].

6.2.14 PBMCs proliferation assay

The immunomodulatory activities of AECs were analyzed on peripheral blood mononuclear cells (PBMCs) by testing their proliferation. Briefly, ovine PBMCs were obtained by density gradient centrifugation with Ficoll-Paque PLUS (Amersham Bisciences, catalogue 18-1152-69) of 16 mL peripheral blood following manufacturer's instruction. PBMCs were then activated by adding phytohemagglutinin (PHA; Sigma) at a final concentration of 2.5 µg/mL. A total of 2×10^5 of PHA stimulated PBMCs were plated and cultured for 72 h with CM derived from immune-activated AECs (LPS stimulus) seeded on normal or GO- coated coverslips. PBMCs proliferation was assessed by using CellTiter96 Aqueous One Solution Cell Proliferation Assay following manufacturer's instructions (Promega-G3582).

6.2.15 Analysis of hTHP1 IL6 secretion

CM biological effect on activated human macrophages was performed by assessing the IL-6 release through an ELISA assay. In detail, the human THP-1 cells were maintained in RPMI 1640 medium containing glutamine and supplemented with 10% FBS and 1 mM sodium pyruvate (Gibco; Thermo Fisher Scientific, Inc., Waltham, MA, USA). Afterwards, monocytes were differentiated into macrophages, as previously described[38]. THP-1-derived macrophages were treated with the CM diluted 1:1, with complete RPMI medium for 24 h. Thereafter, the supernatants were collected, centrifugated at 3000×*g* for 10 min at 4 ˚C, filtered using a 0.2 µm Ministart sterile filter (Sartorius,

Varedo, Italy), and stored at − 80 °C until further use. These cellular supernatants were used to quantify the concentrations of released IL-6 using the Human IL-6 Uncoated Invitrogen ELISA Kit assay (ThermoFisher, San Diego, CA, USA) according to the manufacturer's directions. The plates were read at 450 nm and the sensitivity of the ELISA assay was in the range 2–200 pg/mL.

6.2.16 Statistical analysis

The quantitative data were obtained by analyzing each sample in triplicate for each experimental condition performed at least in triplicate. The results were firstly assessed for distribution using Shapiro Wilks test and analyzed by *t*-test or One-way Anova test followed by Tuckey post hoc test. (GraphPad Prism 9, GraphPad Software, San Diego, CA, USA). Significant was set at $p < 0.05$.

6.3 Results

6.3.1. Characterization of GO aqueous dispersion

The concentration of the GO dispersed in Milli-Q water was checked spectrophotometrically. The UV–vis spectra showed a characteristic absorption peak at λ 230 nm (Fig. 2A), which can be attributed to the π- π* transitions for aromatic C–C bonds and a shoulder at λ 290–300 nm being the fingerprint of n- π* transitions of carbonyl groups. Preliminary DLS and ζ-potential experiments evidenced that GO dispersions comprised large-sized (average diameter of 777.1 ± 123.8 nm) and negatively charged (− 25.02 ± 1.65 mV) flakes, with a polydispersity index of 0.33 ± 0.02, indicating the modest homogeneity in size of the material.

6.3.2 Surface characterization of GO-functionalized coverslips

AFM analysis was used to characterize the surface of the GO- functionalized supports. The analysis revealed the presence of individual GO sheets with not uniform lateral dimensions, in agreement with DLS measurements. The ultrasound vibrations of the bath sonicator, used to promote the GO dispersion, favored the breaking of the sheets into smaller and not homogeneous flakes. Isolated GO sheets were well visualized onto the surface of GO-functionalized samples. In addition, the

topographical AFM analysis was employed to investigate the thickness of the GO flakes present onto coverslips surface. The AFM images were analyzed by Nanoscope Analysis 1.8 Software, tracing several topographical cross sections on the GO-functionalized area and recording the vertical distance values. The height profiles confirmed the presence of single layers of GO sheets with a thickness of few nanometers (Fig. 3A). In the same samples it was also possible to notice brighter ripples with a thickness that reached tens of nanometers, due to the random reaction of GO flakes with the APTES-activated surface and the consequent GO sheets overlapping. Moreover, the bearing analysis of AFM software performed on three different 400 μm^2 regions (Fig. 3B–D), and the relevant (Fig. 3B1-D1), revealed that GO flakes were uniformly distributed on the coverslips surface, covering the 70.4 (±5.5) % of the surface.

The chemical conjugation of GO to the coverslips was confirmed by FT-IR spectroscopy. The FTIR spectrum of GO-functionalized glass was compared to that of the glass in Fig. 2B. The presence of GO in the GO- functionalized glass was confirmed by the peak around 3300 cm^{-1} referring to the O–H stretching of GO; the peak at 1724 cm^{-1} due to the C=O stretching of carbonylic and carboxylic groups of GO and the bands between 1550 cm^{-1} and 1650 cm^{-1} highlighting the presence of the olefinic and aromatic C–=C sp^2 of the hydrocarbon lattice. The band at 1250 cm^{-1} corresponding to C–N stretching confirmed the binding of GO to the silanized glass. Moreover, the two C–H stretching bands around 2900 cm^{-1} were indicative of the presence of saturated carbon in the GO structure. Eventually, the huge band of the glass around 1050 cm^{-1} due to Si–O asymmetric stretching became broader and split into two peaks, due the presence of C–O stretching in the1000-1300 cm^{-1} region.

To further confirm the distribution of GO flakes on the coverslips surface, Raman spectroscopy analysis was performed. Firstly, the single spectrum of the GO-functionalized substrate confirmed the presence of the D and G fingerprints peaks of GO centered at ~1350 and ~1600 cm^{-1} (Fig. 2C), respectively: the G band related to sp^2 hybridized carbon atoms forming the honeycomb structure, and the D peak indicative of the defects of the aromatic lattice and therefore due to edges, sp^3 carbons

and bonds of carbon with oxygen atoms. Lastly, the cumulative Raman spectra obtained for a 400 μm^2 area (Fig. 2D) and the relevant Raman mapping of G band intensities on the same region (Fig. 2E) were reported. The intensity color scale of the mapping varies from dark brown, for zones without GO, to bright yellow for regions with the maximum concentration of GO. Despite the presence of dark regions, Raman spectroscopy confirmed the relatively homogeneous coverage of the analyzed surface by GO flakes, in agreement with AFM measurements.

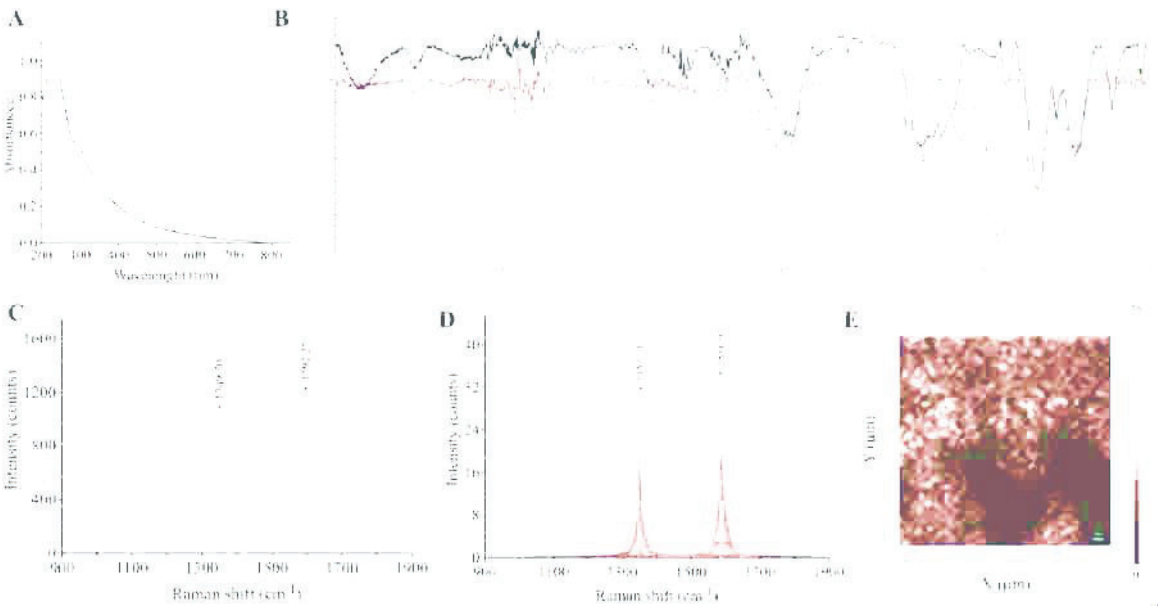

Fig. 2. (A) UV–vis spectra of 20 μg/mL GO dispersion. (B) FTIR spectra of glass coverslip (red spectrum) and GO-functionalized coverslip (black spectrum). (C) Raman spectra of GO-functionalized coverslip. (D) Cumulative Raman spectra for a 400 μm^2 area of GO-coverslip. (E) Relevant Raman mapping of D and G bands intensity on the same 400 μm^2 region. (For interpretation of the references to color in this figure legend, the reader is referred to the Web version of this article.) **Fig. 3.** (A) AFM image of surface topography and corresponding height cross-sectional profiles of GO-functionalized coverslips. (B–D) Three different AFM images of 400 μm^2 surface of GO-functionalized coverslips. (B1-D1) Images, corresponding to the surfaces depicted in B-D, in which the blue regions represent the areas covered by GO flakes, including single-layer nanosheets and overlapped GO sheets. (For interpretation of the references to color in this figure legend, the reader is referred to the Web version of this article.)

6.3.3 GO induces EMT in AECs epithelial and mesenchymal markers

To assess the EMT process in AECs, the expression of downregulation of the epithelial marker CYTO8 ($p < 0.05$) and upregulation of transcription factors SNAIL ($p < 0.05$), TWIST ($p < 0.01$),

ZEB ($p < 0.05$) and late mesenchymal marker VIM ($p < 0.01$) in the samples AECs + GO compared to control AECs (Fig. 4A). Immunofluorescence results confirmed the molecular data showing greater positivity to VIM marker and a very weak presence of CYTO8 in AECs + GO samples respect to AECs that display high positivity to CYTO8 and only some cells positive to VIM (Fig. 4B). Accordingly, the cell morphology changes according to the culture conditions (data not showed).

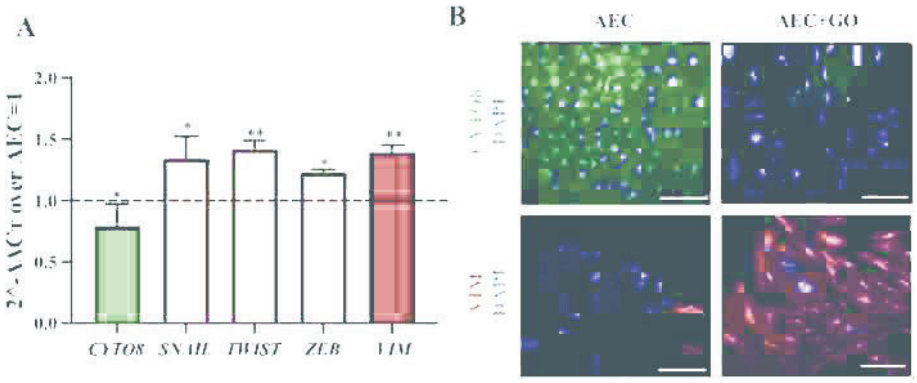

Fig. 4. (A) Genes expression analyses of EMT related markers. The graph shows the gene expression of *CYTO8, SNAIL, TWIST, ZEB* and *VIM* in the AECs + GO samples normalized on AECs = 1 (dashed line). Significance is relative to comparison with AECs obtained by *t*-test analysis and is denoted by the super-

script $*p < 0.05$ and $**p < 0.01$ *vs* AECs. (B) Representative images of AECs and AECs + GO for CYTO8 (green) and VIM (red). The nuclei were colored with DAPI (blue). Magnification at 10×. Scale bar 100 μm. Values were considered significant for p

< 0.05, with the indicated superscripts $**p < 0.01$ *vs* AECs. (For interpretation of the references to color in this figure legend, the reader is referred to the Web version of this article.)

6.3.4 GO induces an increase of ROS production without affecting cell viability

According to recent evidences, GO may influence cell viability due to its ability to induce an increase in ROS production[44,45]. Therefore, ROS production was measured in both AECs and AECs + GO by using DCFDA method for 80 min (Fig. 5A). Intriguingly, both AECs cultured on normal (AECs) and GO-coated coverslips (AECs + GO) showed a time-depended increase of ROS production (Fig. 5A).

However, a significant difference in ROS generation was recorded from 45 to 80 min in AECs + GO compared to AECs (Fig. 5A).

In order to explore whether this increase of ROS production affected cell viability, AECs and AECs + GO were subjected to MTS-based cell proliferation assay (Fig. 5B). Notably, AECs + GO showed similar proliferation rate compared to AECs, thus suggesting that AECs viability was not affected by the GO-induced increasing of ROS production.

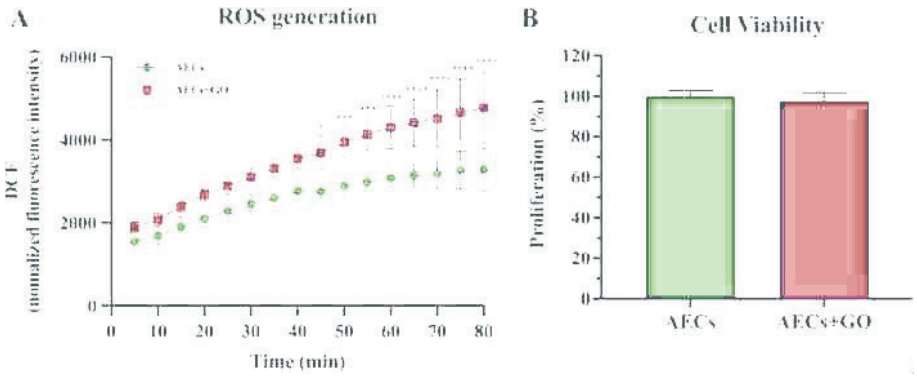

Fig. 5. *AEC's viability and cytotoxicity under GO-coated coverslips exposition. (A) Reactive oxygen species (ROS) generation measured by DCFDA Cellular ROS Detection Kit on AECs seeded in normal or GO-coated coverslips. (B) Cell viability studies performed with MTS proliferation assay. Significance indicated with the superscript *p < 0.05, ***p < 0.001 and ****p < 0.0001 vs AECs.*

6.3.5 GO induces EMT through the activation of TGFβ1/SMAD signaling pathway

In order to study the signaling pathway involved in the GO-induced EMT on AECs it was firstly evaluated SMAD protein phosphorylation. The WB results showed an upregulation of the ratio pSMAD/SMAD on the AECs + GO in comparison to the control (Fig. 6A). Moreover, SB505124 treatment (AECs + GO + SB) was able to reduce the pSMAD/ SMAD to the basal levels. On the contrary, no differences were observed on AECs and AECs + SB. To confirm the involvement of the TGFβ1/ SMAD signaling pathway activation, SBE luciferase assay was used. While no luciferase activity was observed on the control, TGFβ1 stimulation (AECs + TGFβ1) markedly increased SMAD phosphorylation. (Fig. 6B). Notably, GO induced an increased luciferase activity similar to

the positive control (AECs + TGFβ1), whilst the phosphorylation of SMAD induced by GO was inhibited when the cells were treated with SB505124 (AECs + GO + SB) (Fig. 6B).

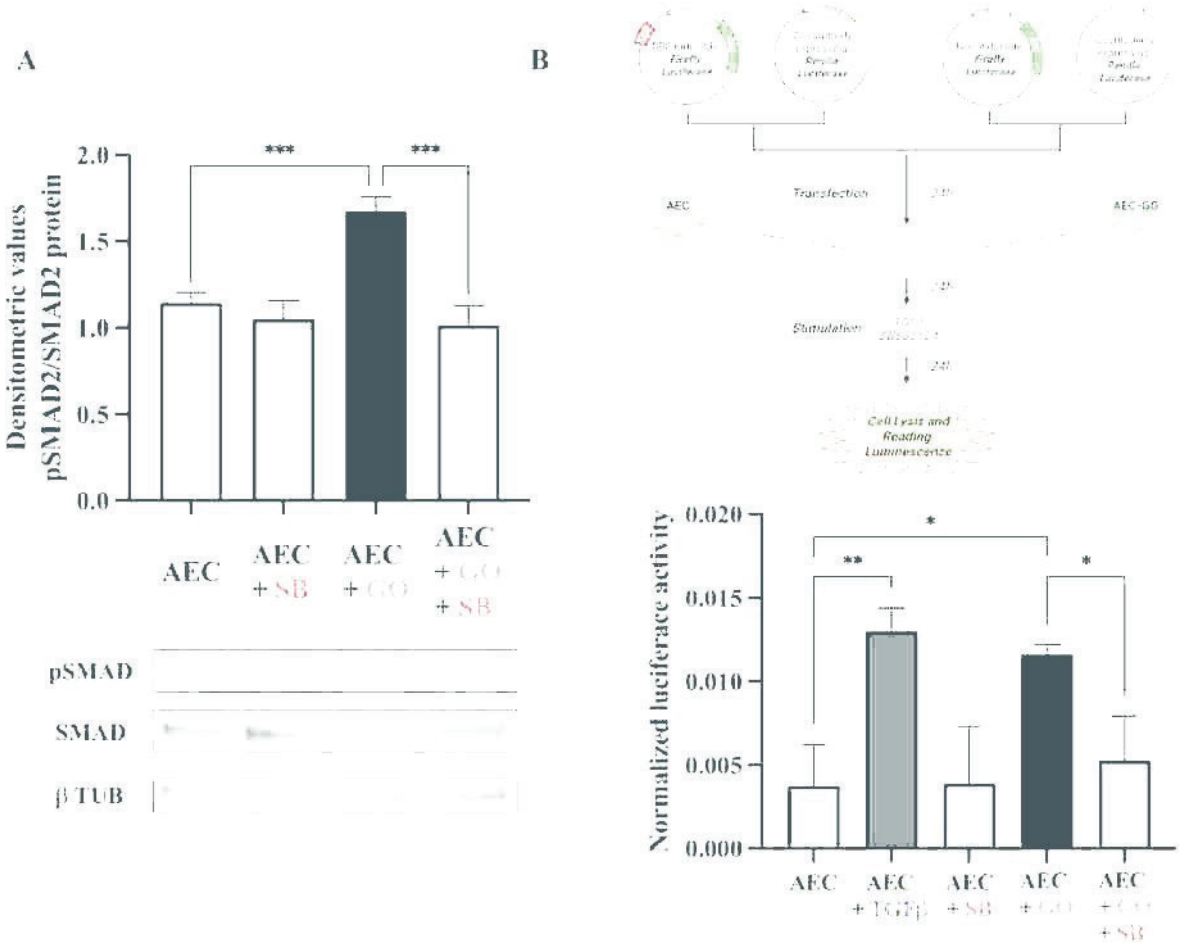

Fig. 6. *TGFβ signaling pathway analysis on GO-induced EMT.(A) Western blot of SMAD2/3 and pSMAD2/3 in A549 and H460 GO with or without SB505124.*

*(B) Graphical representationSE blockade leads in order to reverse TGFβ signaling pathway activation. Significance is represented with the asterisks * $p < 0.05$, ** $p < 0.01$ and *** $p < 0.001$.**

6.3.6 GO stimulates a mesenchymal-type of collective migration

The early activation of EMT is often associated with an increase of cell migration. In this regard, the wound healing assay was performed to evaluate the effects of GO on AECs lateral migration.

The results showed a similar cells clonal movement, but a faster wound closure was already evident in AECs + GO after 48 h compared to control AECs that do not show a complete closure of the wound at the same time point (Fig. 7A). This data was supported by the analyses of the percentage of closure in which was evident how AECs + GO were able to reach already the 50% of closure at 24 h compared to AECs ($p < 0.01$) (Fig. 7B). The speed analyses showed how AECs + GO displayed an increased speed of migration at 24 h and 48 h respect to control AECs ($p < 0.005$) even though at 48 h they diminished their rate ($p < 0.01$) (Fig. 7C). On the contrary, AECs moved homogeneously and at the same speed with no significance differences recorded between 24 h and 48 h (Fig. 7C). Finally, the double immunohistochemistry for E-Cadherin and Vimentin performed during cell migration indicated that either AECs and AECs + GO showed collective type of migration (Fig. 7D). However, AECs showed mainly membrane expression of E-Cadherin and relatively low expression of Vimentin, suggesting an epithelial type of collective migration (Fig. 7D); conversely, AECs + GO greatly increased Vimentin expression and reduced or showed cytoplasmic expression of E-Cadherin, further suggesting that these cells migrate according to a mesenchymal-type of collective migration (Fig. 7D)[46].

6.3.7 GO modulates AECs immune response by inducing release of either pro- and anti-inflammatory mediators

In order to determine whether GO under an inflammatory condition affects the secretion of different cytokines or chemokines, a specific Human Inflammation Antibody Array was used to test conditioned medium (CM) derived from either AECs and AECs + GO stimulated with LPS in order to recapitulate an inflammatory insult (Fig. 8). To this aim cells were treated with 1 μg/mL LPS for 1 h and then the stimulus was removed from the CM that was collected after other 24 h.

This test allowed to analyze not only anti- and pro-inflammatory cytokines but also angiogenetic factors. To this regard, it has been demonstrated how GO induced the increase of several

inflammatory cytokines (such as IL3, IL16, TNF-α, TNF-β, EOTAXIN, EOTAXIN-2, MIG, IFN-γ, IL-12 p70, MIP-1δ) compared with AECs cultured under control conditions (Rantes, MIP-1β, IL-1α) when stimulated with LPS (Fig. 8). Conversely, AECs without GO up-regulated the secretion of anti-inflammatory molecules (IL-13, TGFβ1, IL-10, IL-11, I-309, IL-12 p40) respect to AECs + GO (PDGF-BB) (Fig. 8). Intriguingly, different soluble factors with angiogenetic potential were induced by the two conditions. In particular, GO increased the secretion of IL-17, sTNF RI, sTNF RII whereas AECs alone preferentially induced IL-7, M-CSF (Fig. 8).

6.3.8 GO affects the immunomodulatory properties of AECs

In order to test the paracrine activity of CM collected from AECs and AECs + GO, proliferation of peripheral blood mononuclear cells (PBMCs) and IL-6 secretion from hTHP-1-derived macrophages has been analyzed. Proliferation of PBMCs was assessed as an index of AECs inhibitory abilities, while IL-6 secretion on THP-1-derived macrophages was assessed as an index of immune cell activation.

As result, CM derived from both AECs and AECs + GO suppressed PHA-stimulated PBMCs proliferation of 75% and 60%, respectively. Moreover, LPS stimulation further increased the reduction of PBMCs proliferation in AECs (Fig. 9). Conversely, AECs + GO stimulated with LPS showed a significant reduction in the PBMCs inhibition (Fig. 9A). In addition, CM derived from both AECs and AECs + GO stimulated with LPS induced a marked release of IL-6 with a significant increase recorded in AECs + GO (Fig. 9B).

6.4 Discussion

In summary, the present study demonstrated that GO coated on glass surfaces is able to accelerate EMT on ovine AECs through the TGFβ/ SMAD-dependent pathway activation. In particular, this is the first instance where the immunomodulatory impact of GO has been examined emphasizing the

potential of utilizing the EMT induced by this biomimetic material to target stem cell regenerative capabilities.

These results were obtained by using an *in vitro* model taking advantage of glass coverslips functionalized with micrometric GO flakes, as confirmed by FTIR analyses. Both AFM measurements and Raman spectroscopy highlighted the homogeneous and prevailingly single layer distribution of GO over the slides despite a few ripples of overlapping GO sheets were monitored by AFM. The uniform distribution of micrometric GO over the coverslips ensured that cells, seeded on the functionalized substrates, were always in contact with GO flakes thus exploiting its features. In particular, AECs could take advantages of the significant morphological and structural changes of the cellular membrane induced by GO on different cells[33] as well as its tendency to adsorb and therefore concentrate proteins on its surface[47].

Of note, no evidences of toxicity were recorded in AECs, thus indicating the safety of this support for cell culture despite that fact that GO was able to increase ROS production as similarly reported in other cell source[44,45]. However, the most impressive influence exerted by GO on AEC was the activation of signaling mechanisms inducing a massive EMT. The EMT-MET processes have been documented in AECs, a subset of epithelial stem cells, either under physiological condition during labor (by fostering the weakening of the amniotic membrane and the delivery) or under applicative biomedical procedures. More in detail, AECs may be induced towards EMT during *in vitro* expansion[37,48] or *in vivo* after transplantation into mesenchymal-derived tissues[40].

To the *in vitro* regard, AECs once isolated from amniotic membrane (AM) undergo EMT as an adaptive response to the 2D incubation within three cultural passages if not properly expanded[21,49]. Interestingly, AECs when seeded onto GO-coated coverslips show a faster EMT onset compared to CTR cells, thus suggesting the GO modulation of the mechanisms phenotype.

The EMT-inductive action of GO has been previously demonstrated in other cell models even if the mechanisms involved remain contradictory. Liao and colleagues[29] demonstrated that reduced-GO (rGO) was able to trigger EMT activation in A549 epithelial cells within 48 h through the uptake either of nanosheets or particle aggregates of rGO via endocytosis. Consistently, Park and co-workers also reported that nano-GO (a granular material) quickly induces EMT in retinal pigment epithelium cells by activating phospholipase D (PLD) pathway[31]. Alternatively, GO-mediated EMT induction has been demonstrated to be stimulated by interactions between plasmatic membrane and GO[30] or through its passive diffusion[50]. Conversely, in the present study GO induced EMT acting at membrane level since any GO particle internalization was hooked to the coverslip thanks to covalent bounds[33].

Under similar experimental conditions, the nano-topography characteristics of the biomaterial surfaces have been proposed as drivers of *in vitro* cell behavior. Fiedler et al. demonstrated how topographically patterned interfaces with dimensions ≥10 nm influences the adhesion and proliferation of multipotent mesenchymal stromal cells and human osteoblasts[51]. Furthermore, it has been evidenced that GO-coated glass offers nanoscale topographical cues for stem cell attachment, proliferation, and differentiation[52]. In this context, several studies have observed how the surface topography of functionalized scaffolds can induce EMT by upregulating TGFβ secretion[53–56]. Indeed, TGFβ pathway is a key mechanism in promoting EMT by transcriptionally controlling a number of downstream genes[57]. The intracellular signaling is activated by TGFβR complex's receptor and operates on SMADs (SMAD2/3) effectors by inducing the serine phosphorylation upon ligand binding[58]. Similarly, the results obtained in this study seem to confirm the nano-topographical hypothesis, as GO-coated surface is able to induce EMT by activating, analogously, TGFβ-dependent mechanisms. In detail, GO induces the real time TGFβ-mediated SMAD2/3 phosphorylation promoting the shift towards mesenchymal phenotype of GO-exposed AECs.

In agreement with previous findings, GO-induced EMT enhanced AECs migration[29,31]. Of note, in this study more information on cell mobility was collected. Indeed, it has been demonstrated that GO

promoted a collective cell movement thus activating a typology of migration very effective in promoting wound closure. Notably, depending on the nature of the interactions amongst cells it is possible to distinguish between two types of collective migration: (1) slow migration of tight fasten epithelial cells and (2) faster migration of mesenchymal cells bearing weak heterophilic interactions[46]. In particular GO-coated surface induced in cultured AECs a mesenchymal-like collective migration highlighted by the prevalence of Vimentin positive cells on the border of the experimentally induced wound, instead of the E-cadherin positive ones recorded in control conditions, controlling an epithelial-like collective migration.

The GO-induced EMT significantly impacted also the immunomodulatory properties of AECs, both in their basal state and under inductive (LPS) conditions. The immunomodulation is exerted mainly through the paracrine/autocrine actions of the released cytokines and chemokines.

Indeed, those molecules are essential in modulating the dialogue between stem cells and cells populating the damaged tissue, foremost amongst them the immune cells. Reasonably, GO-mediated immune behavior is modified in response to AECs induced mesenchymal phenotype shift, as previously reported under different experimental conditions[21,40]. For instance, GO nanosheets seem to play a role in activating M1 pro-inflammatory macrophages in a way that is strictly dependent on their size[59,60]. Furthermore, in presence of an inflammatory stimulus, GO uptake rather than inducing a strict M1-polarization, promotes the control of M1/M2 balance, thus ensuring a facilitated innate immune response[61]. To this regard, the present results demonstrated that GO-AECs exposed to LPS enhance their pro-inflammatory interleukins production, thus inducing a more efficient activation of THP1 in releasing IL-6 and, at the same time, by reducing their inhibitory action on PBMC proliferation.

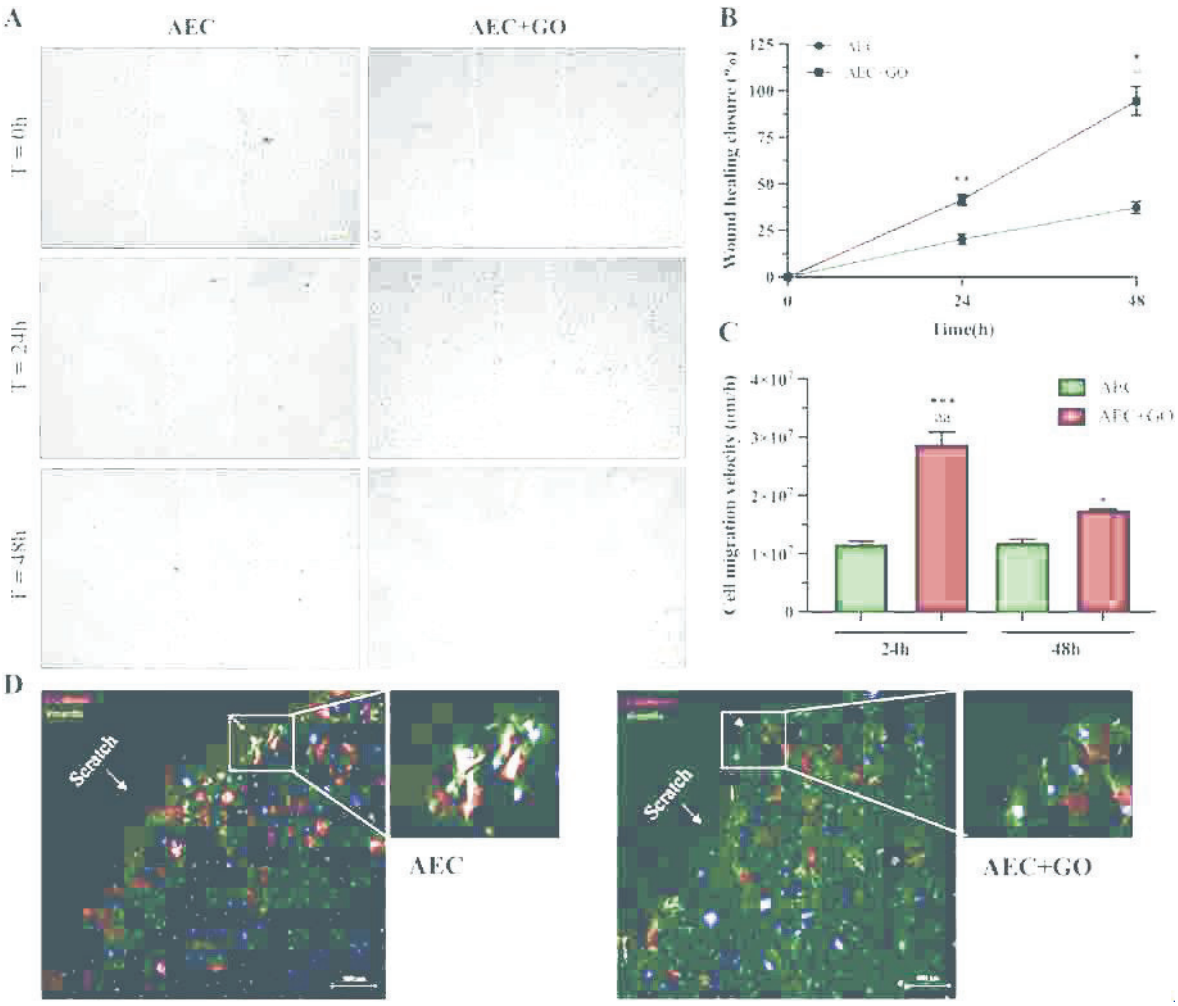

Fig. 7. Migratory potential of AECs under GO exposition. (A) Representative images of the cells migration ability under control condition (AECs) and under GO stimulation (AECs + GO) at 24 and 48 h (Scale 100 μm) (B) Representation of the percentage of wound healing closure where 0 represent the empty scratch and 100 the closed scratch. Significance is represented with the superscript $*p < 0.05$ (AECs + GO *vs* AECs 48 h), $**p < 0.05$ (AECs + GO *vs* AECs 24 h) and $^{aa}p<0.01$ (AECs + GO 48 h *vs* AECs + GO 24 h). (C) Graphical representation of the rate of closure (μm/h). Significance is represented with the superscript $***p < 0.005$ (AECs + GO *vs* AECs 24 h), $*p < 0.05$ (AECs + GO *vs* AECs 48 h) and $^{aa}p<0.01$ (AECs + GO 24 h *vs* AECs + GO 48 h). (D) Immunocytochemistry of E-Cadherin (red) and Vimentin (green) on AECs (left) and AECs + GO (right) during migration. Magnification in 10×. (For interpretation of the references to color in this figure legend, the reader is referred to the Web version of this article.)

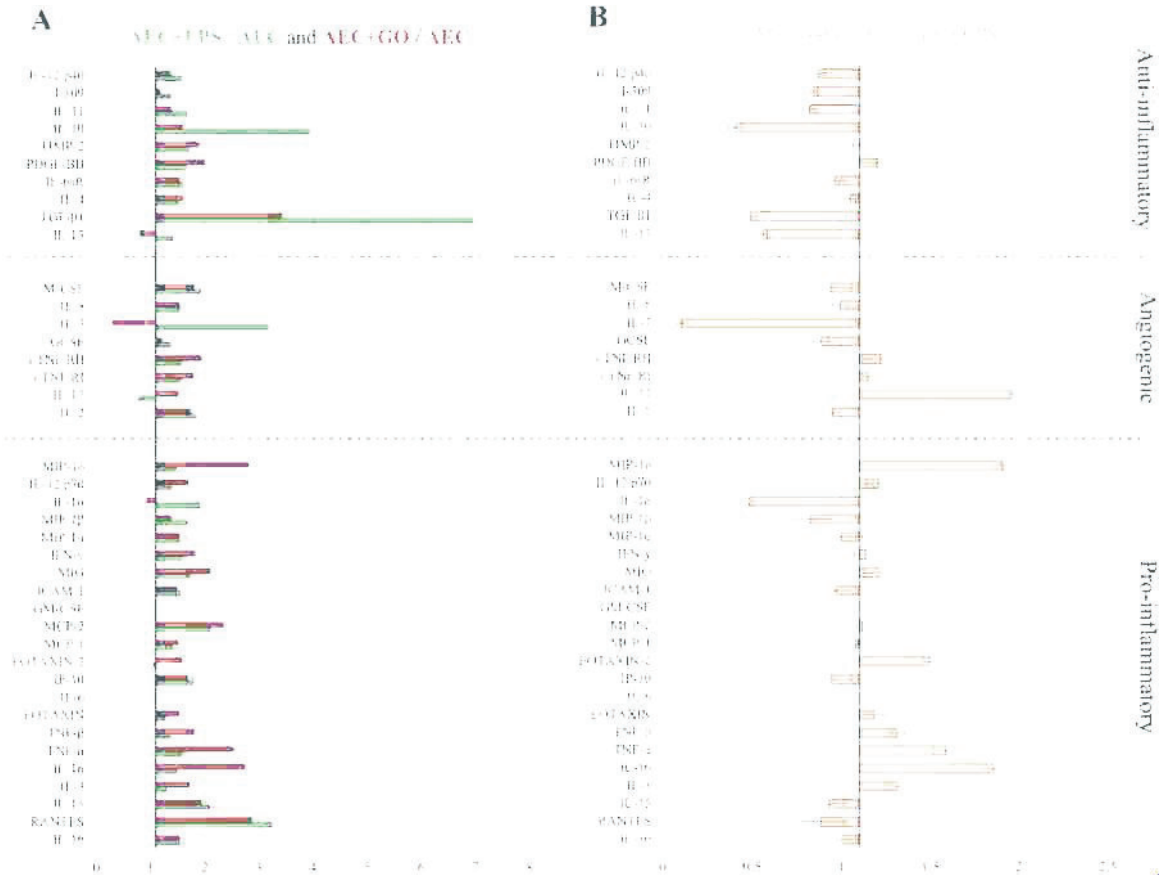

Fig. 8. Cytokines factors profile expression. (A) The layout of the array and representative images of chemokines detection. (B) Quantification by densitometric analysis of antibodies array of untreated AECs and treated samples (AECs + LPS and AECs + GO + LPS), collected after 24 h from the LPS stimulation.

6.5 Conclusion

In conclusion, the adhesion of epithelial stem cells on a GO- functionalized surface might overall constitute a tailored microenvironment useful to face the inflammatory phase of the regenerative process. Indeed, GO promoting the shift of AECs towards the mesenchymal phenotype potentiates both their anti-fibrotic[62–64] and pro-regenerative actions[4,36,40,65]. In fact, AECs due to EMT enhance cell migration and the secretion of inflammatory mediators, thereby increasing the recruitment of other immune cells. Moreover, such behavior provides a favorable local condition to promote matrix remodeling[40] and endogenous progenitor activation which are both essential to speed up the wound

repair by moving the inflammatory stage toward the more advanced proliferative and regenerative phases.

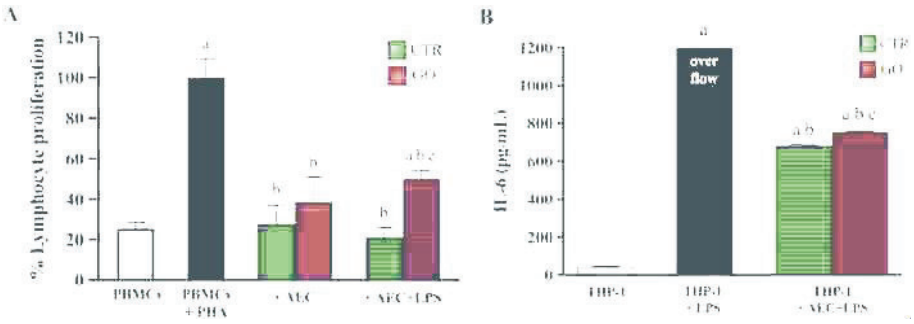

Fig. **9.** Biological effect of AECs derived secretome on immune cells. (A) PBMCs proliferation assay after PHA induction and CM-AECs exposition ± GO and ± LPS. Significance is represented with the superscript; [a]$p < 0.01$ (*vs* PBMCs); [b]$p < 0.01$ (*vs* PBMCs + PHA); [c]$p < 0.01$ (*vs* PBMCs + PHA + CM-AECs + LPS). (B) IL-6 secretion of hTHP-1-derived macrophages after CM-AECs + LPS exposition ± GO. Significance is represented with the superscript; [a]$p < 0.01$ (*vs* THP- 1); [b]$p < 0.01$ (*vs* THP-1 + LPS); [c]$p < 0.01$ (*vs* THP- 1 + CM-AECs + LPS).

References

(1) C.L. Insausti, M. Blanquer, A.M. García-Hernandez, G. Castellanos, J.M. Moraleda, ´ Amniotic membrane-derived stem cells: immunomodulatory properties and potential clinical application, Stem Cells Cloning, Adv. Appl. 7 (2014) 53–63, https://doi.org/10.2147/SCCAA.S58696.

(2) Q. Liang, Z. Liu, C. Zhu, B. Wang, X. Liu, Y. Yang, X. Lv, H. Mu, K. Wang, Intrahepatic T-cell receptor β immune repertoire is essential for liver regeneration, Hepatology (2018), https://doi.org/10.1002/hep.30067.

(3) T. Miki, Amnion-derived stem cells: in quest of clinical applications, Stem Cell Res. Ther. 2 (2011) 25, https://doi.org/10.1186/scrt66.

(4) B. Barboni, V. Russo, V. Gatta, N. Bernabo, P. Berardinelli, A. Mauro, A. Martelli, `
L. Valbonetti, A. Muttini, O. Di Giacinto, M. Turriani, A. Silini, G. Calabrese, M. Abate, O. Parolini, L. Stuppia, M. Mattioli, Therapeutic potential of hAECs for early Achilles tendon defect repair through regeneration, J. Tissue Eng. Regen. Med. 12 (2018), e1594, https://doi.org/10.1002/term.2584. –e1608.

(5) T. Miki, Stem cell characteristics and the therapeutic potential of amniotic epithelial cells, Am. J. Reprod. Immunol. 80 (2018), e13003, https://doi.org/ 10.1111/aji.13003.

(6) I.L. García-Castro, G. García-Lopez, D. ´ Avila-Gonz´ alez, H. Flores-Herrera, ´ A. Molina-Hernandez, W. Portillo, E. Ramón-Gallegos, N.F. Díaz, Markers of ´ pluripotency in human amniotic epithelial cells and their differentiation to progenitor of cortical neurons, PLoS One 10 (2015), e0146082, https://doi.org/10.1371/journal.pone.0146082.

(7) T. Miki, T. Lehmann, H. Cai, D.B. Stolz, S.C. Strom, Stem cell characteristics of amniotic epithelial cells, Stem Cell. 23 (2005) 1549–1559, https://doi.org/ 10.1634/stemcells.2004-0357.

(8) B. Barboni, V. Russo, V. Curini, A. Martelli, P. Berardinelli, A. Mauro, M. Mattioli, M. Marchisio, P. Bonassi Signoroni, O. Parolini, A. Colosimo, Gestational stage affects amniotic epithelial cells phenotype, methylation status, immunomodulatory and stemness properties, Stem Cell Rev. Reports 10 (2014) 725–741, https://doi.org/10.1007/s12015-014-9519-y.

(9) E. Resca, M. Zavatti, T. Maraldi, L. Bertoni, F. Beretti, M. Guida, G.B. La Sala, P. V. Guillot, A.L. David, N.J. Sebire, A. De Pol, P. De Coppi, Enrichment in c-Kit improved differentiation potential of amniotic membrane progenitor/stem cells, Placenta 36 (2015) 18–26, https://doi.org/10.1016/j.placenta.2014.11.002.

(10) B. Barboni, V. Russo, P. Berardinelli, A. Mauro, L. Valbonetti, H. Sanyal, A. Canciello, L. Greco, A. Muttini, V. Gatta, L. Stuppia, M. Mattioli, Placental stem cells from domestic animals: translational potential and clinical relevance, Cell Transplant. (2018), https://doi.org/10.1177/0963689717724797.

(11) B. Barboni, V. Curini, V. Russo, A. Mauro, O. Di Giacinto, M. Marchisio, M. Alfonsi, M. Mattioli, Indirect Co-culture with tendons or tenocytes can program amniotic epithelial cells towards stepwise tenogenic differentiation, PLoS One 7 (2012), e30974, https://doi.org/10.1371/journal.pone.0030974.

(12) B. Barboni, V. Russo, V. Curini, A. Mauro, A. Martelli, A. Muttini, N. Bernabo, ` L. Valbonetti, M. Marchisio, O. Di Giacinto, P. Berardinelli, M. Mattioli, Achilles tendon regeneration can be improved by amniotic epithelial cell allotransplantation, Cell Transplant. 21 (2012) 2377–2395, https://doi.org/ 10.3727/096368912X638892.

(13) F. Marongiu, R. Gramignoli, K. Dorko, T. Miki, A.R. Ranade, M. Paola Serra,
S. Doratiotto, M. Sini, S. Sharma, K. Mitamura, T.L. Sellaro, V. Tahan, K.J. Skvorak, E.C.S. Ellis, S.F. Badylak, J.C. Davila, R. Hines, E. Laconi, S.C. Strom, Hepatic differentiation of amniotic epithelial cells, Hepatology 53 (2011) 1719–1729, https://doi.org/10.1002/hep.24255.

(14) C.-H. Fang, J. Jin, J.-H. Joe, Y.-S. Song, B.-I. So, S.M. Lim, G.J. Cheon, S.-K. Woo, J.-C. Ra, Y.-Y. Lee, K.-S. Kim, In vivo differentiation of human amniotic epithelial cells into cardiomyocyte-like cells and cell transplantation effect on myocardial infarction in rats: comparison with cord blood and adipose tissue-derived mesenchymal stem cells, Cell Transplant. 21 (2012) 1687–1696, https://doi.org/ 10.3727/096368912X653039.

(15) A. Mauro, V. Russo, L. Di Marcantonio, P. Berardinelli, A. Martelli, A. Muttini, M. Mattioli, B. Barboni, M1 and M2 macrophage recruitment during tendon regeneration induced by amniotic epithelial cell allotransplantation in ovine, Res. Vet. Sci. 105 (2016) 92–102, https://doi.org/10.1016/j.rvsc.2016.01.014.

(16) G. Pietrosi, A. Fernandez-Iglesias, M. Pampalone, M. Ortega-Ribera, J.J. Lozano, H. García-Caldero, L. Abad-Jorda, P.G. Conaldi, O. Parolini, G. Vizzini, A. Luca, ` J. Bosch, J. Gracia-Sancho, Human amniotic stem cells improve hepatic microvascular dysfunction and portal hypertension in cirrhotic rats, Liver Int. 40 (2020) 2500–2514, https://doi.org/10.1111/liv.14610.

(17) H. Li, J.Y. Niederkorn, S. Neelam, E. Mayhew, R.A. Word, J.P. McCulley, H. Alizadeh, Immunosuppressive factors secreted by human amniotic epithelial cells, Investig. Ophthalmol. Vis. Sci. 46 (2005) 900–907, https://doi.org/10.1167/ iovs.04-0495.

(18) T.Z. Ramuta, M.E. Kreft, Human amniotic membrane and amniotic ˘ membrane–derived cells: how far are we from their use in regenerative and reconstructive urology? Cell Transplant. (2018) https://doi.org/10.1177/ 0963689717725528.

(19) A.B. Hamilton, A.G. Betz, Gimme Shelter - the Immune System during Pregnancy (Munoz-Suano 2011) (Impressao Ok), vol. 241, pdf, 2011, pp. 20–38.

(20) J.M. Ilarregui, D.O. Croci, G. a Bianco, M. a Toscano, M. Salatino, M.E. Vermeulen, J.R. Geffner, G. a Rabinovich, Tolerogenic signals delivered by dendritic cells to T cells through a galectin-1-driven immunoregulatory circuit involving interleukin 27 and interleukin 10, Nat. Immunol. 10 (2009) 981–991, https://doi.org/ 10.1038/ni.1772.

(21) A. Canciello, V. Russo, P. Berardinelli, N. Bernabo, A. Muttini, M. Mattioli, ` B. Barboni, Progesterone prevents epithelial-mesenchymal transition of ovine amniotic epithelial cells and enhances their immunomodulatory properties, Sci. Rep. 7 (2017) 3761, https://doi.org/10.1038/s41598-017-03908-1.

(22) A. Canciello, G. Teti, E. Mazzotti, M. Falconi, V. Russo, A. Giordano, B. Barboni, Progesterone prolongs viability and anti-inflammatory functions of explanted preterm ovine amniotic membrane, Front. Bioeng. Biotechnol. (2020), https://doi. org/10.3389/fbioe.2020.00135.

(23) V. Russo, M. El Khatib, G. Prencipe, A. Cervero-Varona, M.R. Citeroni, A. Mauro, ´P. Berardinelli, M. Faydaver, A.A. Haidar-Montes, M. Turriani, O. Di Giacinto, M. Raspa, F. Scavizzi, F. Bonaventura, L. Liverani, A.R. Boccaccini, B. Barboni, Scaffold-mediated immunoengineering as innovative strategy for tendon regeneration, Cells 11 (2022) 266, https://doi.org/10.3390/cells11020266.

(24) M. Maleki, R. Zarezadeh, M. Nouri, A.R. Sadigh, F. Pouremamali, Z. Asemi, H. S. Kafil, F. Alemi, B. Yousefi, Graphene oxide: a promising material for regenerative medicine and tissue engineering, Biomol. Concepts 11 (2020) 182–200, https://doi.org/10.1515/bmc-2020-0017.

(25) J. Saleem, L. Wang, C. Chen, Immunological effects of graphene family nanomaterials, NanoImpact 5 (2017) 109–118, https://doi.org/10.1016/j. impact.2017.01.005.

(26) J. Han, Y.S. Kim, M.-Y. Lim, H.Y. Kim, S. Kong, M. Kang, Y.W. Choo, J.H. Jun, S. Ryu, H. Jeong, J. Park, G.-J. Jeong, J.-C. Lee, G.H. Eom, Y. Ahn, B.-S. Kim, Dual roles of graphene oxide to attenuate inflammation and elicit timely polarization of macrophage phenotypes for cardiac repair, ACS Nano 12 (2018) 1959, https://doi. org/10.1021/acsnano.7b09107. –1977.

(27) K. Lategan, H. Alghadi, M. Bayati, M. de Cortalezzi, E. Pool, Effects of graphene oxide nanoparticles on the immune system biomarkers produced by RAW 264.7 and human whole blood cell cultures, Nanomaterials 8 (2018) 125, https://doi. org/10.3390/nano8020125.

(28) L. Fonticoli, F. Diomede, A. Nanci, A. Fontana, Y. Della Rocca, D. Guadarrama Bello, S. Pilato, O. Trubiani, J. Pizzicannella, G.D. Marconi, Enriched graphene oxide-polypropylene suture threads buttons modulate the inflammatory pathway induced by Escherichia coli lipopolysaccharide, Int. J. Mol. Sci. 24 (2023) 6622, https://doi.org/10.3390/ijms24076622.

(29) Y. Liao, W. Wang, X. Huang, Y. Sun, S. Tian, P. Cai, Reduced graphene oxide triggered epithelial-mesenchymal transition in A549 cells, Sci. Rep. 8 (2018), 15188, https://doi.org/10.1038/s41598-018-33414-x.

(30) J. Zhu, B. Li, M. Xu, R. Liu, T. Xia, Z. Zhang, Y. Xu, S. Liu, Graphene oxide promotes cancer metastasis through associating with plasma membrane to promote TGF-β signaling-dependent epithelial–mesenchymal transition, ACS Nano 14 (2020) 818–827, https://doi.org/10.1021/acsnano.9b07891.

(31) S.Y. Park, W.C. Song, B. Kim, J.-W. Oh, G. Park, Nano-graphene oxide-promoted epithelial–mesenchymal transition of human retinal pigment epithelial cells through regulation of phospholipase D signaling, Nanomaterials 11 (2021) 2546, https://doi.org/10.3390/nano11102546.

(32) R. Di Carlo, A. Di Crescenzo, S. Pilato, A. Ventrella, A. Piattelli, L. Recinella, Chiavaroli, S. Giordani, M. Baldrighi, A. Camisasca, B. Zavan, M. Falconi, A. Cataldi, A. Fontana, S. Zara, Osteoblastic differentiation on graphene oxide- functionalized titanium surfaces: an in vitro study, Nanomaterials 10 (2020) 654, https://doi.org/10.3390/nano10040654.

(33) S. Pilato, S. Moffa, G. Siani, F. Diomede, O. Trubiani, J. Pizzicannella, D. Capista, M. Passacantando, P. Samorì, A. Fontana, 3D graphene oxide-polyethylenimine scaffolds for cardiac tissue engineering, ACS Appl. Mater. Interfaces (2023), https://doi.org/10.1021/acsami.3c00216.

(34) M. Di Giulio, R. Zappacosta, S. Di Lodovico, E. Di Campli, G. Siani, A. Fontana, L. Cellini, Antimicrobial and antibiofilm efficacy of graphene oxide against chronic wound microorganisms, Antimicrob. Agents Chemother. 62 (2018), https://doi. org/10.1128/AAC.00547-18.

(35) M. Radunovic, M. De Colli, P. De Marco, C. Di Nisio, A. Fontana, A. Piattelli, Cataldi, S. Zara, Graphene oxide enrichment of collagen membranes improves DPSCs differentiation and controls inflammation occurrence, J. Biomed. Mater. Res., Part A 105 (2017) 2312–2320, https://doi.org/10.1002/jbm.a.36085.

(36) A.R. Silini, O. Parolini, Placental cells and derivatives, Cell Transplant. 27 (2018) 1–2, https://doi.org/10.1177/0963689717745332.

(37) A. Canciello, L. Greco, V. Russo, B. Barboni, Amniotic epithelial cell culture, Methods Mol. Biol. (2018), https://doi.org/10.1007/978-1-4939-8600-2_7.

(38) B. Dufrusine, A. Di Francesco, S. Oddi, L. Scipioni, C.B. Angelucci, C. D'Addario, M. Serafini, A.-K. Hafner, D. Steinhilber, M. Maccarrone, E. Dainese, Iron- ¨ dependent trafficking of 5-lipoxygenase and impact on human macrophage activation, Front. Immunol. 10 (2019), https://doi.org/10.3389/ fimmu.2019.01347.

(39) K.J. Livak, T.D. Schmittgen, Analysis of relative gene expression data using real- time quantitative PCR and the $2^{-\Delta\Delta}$CT method, Methods 25 (2001) 402–408, https://doi.org/10.1006/meth.2001.1262.

(40) V. Russo, A. Mauro, A. Peserico, O. Di Giacinto, M. El Khatib, M.R. Citeroni, E. Rossi, A. Canciello, E. Mazzotti, B. Barboni, Tendon healing response is dependent on epithelial–mesenchymal–tendon transition state of amniotic epithelial stem cells, Biomedicines 10 (2022) 1177, https://doi.org/10.3390/ biomedicines10051177.

(41) I. del Molino del Barrio, G. Wilkins, A. Meeson, S. Ali, J. Kirby, Breast Cancer, An examination of the potential of ACKR3 to modify the response of CXCR4 to CXCL12, Int. J. Mol. Sci. 19 (2018) 3592, https://doi.org/10.3390/ijms19113592.

(42) V. Russo, M. El Khatib, G. Prencipe, A. Mauro, O. Di Giacinto, A.A. Haidar-Montes, F. Pulcini, B. Dufrusine, A. Cervero-Varona, M. Faydaver, C. Di Berardino, ´ E. Dainese, P. Berardinelli, M. Schnabelrauch, B. Barboni, Tendon 3D scaffolds establish a tailored microenvironment instructing paracrine mediated regenerative amniotic epithelial stem cells potential, Biomedicines 10 (2022) 2578, https://doi. org/10.3390/biomedicines10102578.

(43) M. Di Mattia, A. Mauro, S. Delle Monache, F. Pulcini, V. Russo, P. Berardinelli, M. R. Citeroni, M. Turriani, A. Peserico, B. Barboni, Hypoxia-mimetic CoCl2 agent enhances pro-angiogenic activities in ovine amniotic epithelial cells-derived conditioned medium, Cells 11 (2022) 461, https://doi.org/10.3390/ cells11030461.

(44) M. Pelin, L. Fusco, C. Martín, S. Sosa, J. Frontin˜an-Rubio, J.M. Gonz´ alez- ´ Domínguez, M. Duran-Prado, E. V´ azquez, M. Prato, A. Tubaro, Graphene and ´ graphene oxide induce ROS production in human HaCaT skin keratinocytes: the role of xanthine oxidase and NADH dehydrogenase, Nanoscale 10 (2018) 11820–11830, https://doi.org/10.1039/C8NR02933D.

(45) J. Shen, J. Dong, F. Shao, J. Zhao, L. Gong, H. Wang, W. Chen, Y. Zhang, Y. Cai, Graphene oxide induces autophagy and apoptosis via the ROS-dependent AMPK/ mTOR/ULK-1 pathway in colorectal cancer cells, Nanomedicine 17 (2022) 591–605, https://doi.org/10.2217/nnm-2022-0030.

(46) A. Canciello, A. Cervero-Varona, A. Peserico, A. Mauro, V. Russo, A. Morrione, ´ A. Giordano, B. Barboni, “In medio stat virtus”: insights into hybrid E/M phenotype attitudes, Front. Cell Dev. Biol. 10 (2022), https://doi.org/10.3389/ fcell.2022.1038841.

(47) H. Li, K. Fierens, Z. Zhang, N. Vanparijs, M.J. Schuijs, K. Van Steendam, N. Feiner Gracia, R. De Rycke, T. De Beer, A. De Beuckelaer, S. De Koker, D. Deforce, L. Albertazzi, J. Grooten, B.N. Lambrecht, B.G. De Geest, Spontaneous protein adsorption on graphene oxide nanosheets allowing efficient intracellular vaccine protein delivery, ACS Appl. Mater. Interfaces 8 (2016) 1147–1155, https://doi. org/10.1021/acsami.5b08963.

(48) L.S. Richardson, R.N. Taylor, R. Menon, Reversible EMT and MET mediate amnion remodeling during pregnancy and labor, Sci. Signal. 13 (2020) 139–148, https:// doi.org/10.1126/scisignal.aay1486.

(49) A. Alcaraz, A. Mrowiec, C.L. Insausti, E.M. García-Vizcaíno, C. Ruiz-Canada, M. C. Lopez-Martínez, J.M. Moraleda, F.J. Nicol´ as, Autocrine TGF-´ β induces epithelial to mesenchymal transition in human amniotic epithelial cells, Cell Transplant. 22 (2013) 1351–1367, https://doi.org/10.3727/096368912X657387.

(50) T. Lammel, P. Boisseaux, M.-L. Fernandez-Cruz, J.M. Navas, Internalization and ´ cytotoxicity of graphene oxide and carboxyl graphene nanoplatelets in the human hepatocellular carcinoma cell line Hep G2, Part, Fibre Toxicol 10 (2013) 27, https://doi.org/10.1186/1743-8977-10-27.

(51) J. Fiedler, B. Ozdemir, J. Bartholom¨ a, A. Plettl, R.E. Brenner, P. Ziemann, The ¨ effect of substrate surface nanotopography on the behavior of multipotnent mesenchymal stromal cells and osteoblasts, Biomaterials 34 (2013) 8851–8859, https://doi.org/10.1016/j.biomaterials.2013.08.010.

(52) A. Savchenko, R.T. Yin, D. Kireev, I.R. Efimov, E. Molokanova, Graphene-based scaffolds: fundamentals and applications for cardiovascular tissue engineering, Front. Bioeng. Biotechnol. 9 (2021), https://doi.org/10.3389/fbioe.2021.797340.

(53) C. Zhang, H. Yuan, H. Liu, X. Chen, P. Lu, T. Zhu, L. Yang, Z. Yin, B.C. Heng, Y. Zhang, H. Ouyang, Well-aligned chitosan-based ultrafine fibers committed teno- lineage differentiation of human induced pluripotent stem cells for Achilles tendon regeneration, Biomaterials 53 (2015) 716–730, https://doi.org/10.1016/j. biomaterials.2015.02.051.

(54) X. Xu, L. Ma, Y. Wu, L. Tang, Micropillar-based culture platform induces epithelial- mesenchymal transition in the alveolar epithelial cell line, J. Biomed. Mater. Res., Part A 106 (2018) 3165–3174, https://doi.org/10.1002/jbm.a.36511.

(55) Y.K. Girard, C. Wang, S. Ravi, M.C. Howell, J. Mallela, M. Alibrahim, R. Green, G. Hellermann, S.S. Mohapatra, S. Mohapatra, A 3D fibrous scaffold inducing tumoroids: a platform for anticancer drug development, PLoS One 8 (2013), e75345, https://doi.org/10.1371/journal.pone.0075345.

(56) F.F.R. Damanik, T.C. Rothuizen, C. van Blitterswijk, J.I. Rotmans, L. Moroni, Towards an in vitro model mimicking the foreign body response: tailoring the surface properties of biomaterials to modulate extracellular matrix, Sci. Rep. 4 (2014) 6325, https://doi.org/10.1038/srep06325.

(57) Y. Tsubakihara, A. Moustakas, Epithelial-mesenchymal transition and metastasis under the control of transforming growth factor β, Int. J. Mol. Sci. 19 (2018) 3672, https://doi.org/10.3390/ijms19113672.

(58) F. Xie, L. Ling, H. Van Dam, F. Zhou, L. Zhang, TGF-& beta; signaling in cancer metastasis, Acta Biochim. Biophys. Sin. 50 (2018) 121–132, https://doi.org/ 10.1093/abbs/gmx123.

(59) J. Ma, R. Liu, X. Wang, Q. Liu, Y. Chen, R.P. Valle, Y.Y. Zuo, T. Xia, S. Liu, Crucial role of lateral size for graphene oxide in activating macrophages and stimulating pro-inflammatory responses in cells and animals, ACS Nano 9 (2015) 10498–10515, https://doi.org/10.1021/acsnano.5b04751.

(60) R. Diez-Orejas, M.J. Feito, M. Cicu´endez, L. Casarrubios, J.M. Rojo, M.T. Portoles, ´ Graphene oxide nanosheets increase Candida albicans killing by pro-inflammatory and reparative peritoneal macrophages, Colloids Surf. B Biointerfaces 171 (2018) 250–259, https://doi.org/10.1016/j.colsurfb.2018.07.027.

(61) M.J. Feito, R. Diez-Orejas, M. Cicu´endez, L. Casarrubios, J.M. Rojo, M.T. Portoles, ´ Characterization of M1 and M2 polarization phenotypes in peritoneal macrophages after treatment with graphene oxide nanosheets, Colloids Surf. B Biointerfaces 176 (2019) 96–105, https://doi.org/10.1016/j.colsurfb.2018.12.063.

(62) A. Silini, O. Parolini, B. Huppertz, I. Lang, Soluble factors of amnion-derived cells in treatment of inflammatory and fibrotic pathologies, Curr. Stem Cell Res. Ther. 8 (2013) 6–14, https://doi.org/10.2174/1574888X11308010003.

(63) N. Andrewartha, G. Yeoh, Human amnion epithelial cell therapy for chronic liver disease, Stem Cell. Int. (2019) (2019) 1–10, https://doi.org/10.1155/2019/ 8106482.

(64) H. Wang, Y. Tian, X. Li, M. Yang, Y. Yan, Amniotic mesenchymal stem cells derived hepatocyte-like cells attenuated liver fibrosis more efficiently by mixed-cell transplantation, Int. J. Physiol. Pathophysiol. Pharmacol. 12 (2020) 11–24. http ://www.ncbi.nlm.nih.gov/pubmed/32211118.

(65) A.R. Silini, A. Cargnoni, M. Magatti, S. Pianta, O. Parolini, The long path of human placenta, and its derivatives, in regenerative medicine, Front. Bioeng. Biotechnol. 3 (2015), https://doi.org/10.3389/fbioe.2015.00162.

7 Exploring Potential Impact of Graphene Oxide and Graphene Oxide-Polyethylenimine on Biological Behavior of Human Amniotic Fluid-Derived Stem Cells

DOI:https://doi.org/10.3390/ijms252413598

7.1 Introduction

Regenerative medicine and tissue engineering are pioneering fields in life sciences, aiming to restore or replace lost or impaired organs and tissues through cell transplantation supported by scaffolds[1]. Recently, scientists have focused on developing new biomaterials that can provide optimized support for cellular attachment, migration, proliferation, and differentiation, helping to replace, regrow, or repair tissues[1,2]. Nanomedicines, which exploit nanomaterials ranging from 10 to 200 nm in size, offer significant multifunctionality due to the high surface-to-volume ratio and peculiar surface and chemical properties of nanoobjects. Various nanoscale structures, such as dendrimers, liposomes, polymer-based nanoparticles, micelles, carbon nanotubes, and graphene derivatives, were created for this purpose. In this scenario, graphene oxide (GO), produced by oxidizing graphene, has emerged as a versatile nanomaterial with extensive applications in biomedicine, particularly in the realm of regenerative medicine and tissue engineering. It supports the possibility to create a niche for stem cell growth that is crucial for stem cell biology since the microenvironment and substrate play a pivotal role in direct stem cell fate[3]. In addition, since it is a flexible substrate and can be easily transformed in an electrically conductive nanomaterial, it could be used to create a 3D scaffold for cardiac and muscle engineering or as a nerve guidance conduit for peripheral nerve regeneration[1,4]. It is generally preferred over graphene for creating homogeneous aqueous suspensions due to the oxygen-containing functional groups on its basal plane (hydroxyl and epoxide groups) and edges (carboxyl groups).

The interaction between GO and stem cells was the subject of numerous studies, revealing both promising results and notable challenges[5]. On one hand, GO has been shown to support stem cell adhesion, proliferation, and differentiation into various lineages such as osteogenic, neural, and adipogenic pathways. Its biocompatibility and the demonstrated[6] ability of small GO nanoflakes to interact with the cell membrane, mimicking extracellular mechanical signaling and promoting the release of microvesicles, further enhance its appeal as a biomaterial scaffold. However, the application of GO is not without limitations. Concerns regarding its cytotoxicity, long-term stability, and potential inflammatory responses highlight the need for a thorough understanding of its interactions with biological systems[7]. Additionally, variations in the synthesis and functionalization of GO can lead to inconsistent outcomes, complicating the reproducibility and reliability of experimental results[7]. A derivative of GO, Graphene Oxide-Polyethylenimine (GO-PEI) was created through the covalent functionalization of GO with linear polyethylenimine (PEI) macromolecules. Previous studies have shown that, although cross-linking between GO and PEI results in the formation of structurally defined tridimensional structures with controlled porosity, the most effective sample able to promote cell growth was the one layer of GO functionalized with PEI[8].

Human amniotic fluid stem cells (hAFSCs) are a population of stem cells that can be isolated from amniotic fluid during amniocentesis[9]. They were always considered multipotent and committed through the mesodermal lineage[2,10,11]. Despite that, recent studies have demonstrated that they share some epigenetic and genetic features with human-induced pluripotent stem cells (hiPSCs)[12] and can give rise to ectodermal lineages such as motor neurons[13]. These properties make hAFSCs very good candidates in the field of regenerative medicine, since they can be easily isolated during medical routine procedures without any ethical issues, have neither immunogenic nor tumorigenic potential, are less expensive, and are easier to culture than hiPSCs[12]. Anyway, to avoid altering the differentiation capacity of the cells, hAFSCs growing on scaffolds should retain

all their biological and genetic features, including miRNA expression, since it was demonstrated that these non-coding RNAs are deeply implicated in the control of the developmental process and cellular differentiation[14].

This study aimed to investigate for the first time the effect of GO and GO-PEI on the adhesion, proliferation, and metabolic features of hAFSCs in order to identify the most suitable scaffold for regenerative medicine.

7.2. Materials and Methods

7.2.1 Characterization of GO and PEI Aqueous Solutions

The commercial aqueous solution of 4 g/L of graphene oxide from Graphenea (Donostia San Sebastian, Spain) was diluted with Ultrapure Milli-Q water (electric resistance> 18.2 MΩ/cm, Millipore Corp. model Direct-Q 3 system, Merck Millipore, Darmstadt, Germany) to reach the elected concentration of GO and bath-ultrasonicated for 30 min (37 kHz, 180 W; Elmasonic P60H; Elma Schmidbauer GmbH, Singen, Germany). The concentration of GO was spectrophotometrically checked at λmax of 230 nm by using a Varian Cary 100 BIO UV–vis spectrophotometer (Varian, Victoria, Australia). A linear polyethylenimine (PEI) aqueous solution was obtained by the solubilization of 8 mg of powder (average Mn 4000, PDI ≥ 1.3; MerkGaA, Darmstadt, Germany) in HCl-acidified Milli-Q water. The solution was stirred until clearing, neutralized with sodium hydroxide, and added to Milli-Q water to obtain a final concentration of 0.16 mg/mL.

7.2.2 GO and GO-PEI Preparation

Round glass coverslips were silanized by dipping the UV-ozone activated coverslips in 1 M 3-(aminopropyl)triethoxysilane (APTES) solution in ethanol (MerckGaA, Darmstadt, Germany). The silanized coverslips were then dipped in aqueous solutions of GO 20 µg/mL or sequentially

in GO and PEI aqueous dispersions (in order to obtain GO or GO-PEI substrates, respectively)[8]. After incubation, the coverslips were rinsed with water and sterilized by UV irradiation. The surface topography and the distribution of GO flakes on the functionalized substrates were investigated by AFM and Raman spectroscopy mapping (Figure 2) analyses and then the substrates were used as support for amniotic fluid stem cell culture.

7.2.3 AFM Characterization of Functionalized Coverslips

The surface topography of the GO and GO-PEI functionalized coverslips was investigated with Atomic Force Microscopy (AFM) by using the MultiMode 8 AFM microscope (Bruker, Billerica, MA, USA) equipped with a Nanoscope V controller in Tapping Mode in air. A commercial silicon cantilever RTESPA-300 (rectangular geometry, resonance frequency 300 kHz and nominal spring constant 40 N/m) with a nominal tip radius of 8 nm was used to analyze the topography across a scan size of 20 μm × 20 μm. The images were analyzed by Nanoscope Analysis 1.8 software (Bruker, Billerica, MA, USA) and the bearing analysis tool was used to calculate the percentage of surface covered by GO flakes, in the form of both single layers and overlapped GO, and by the GO-PEI network.

7.2.4 ATR-FTIR, Raman Spectroscopy, and Raman Mapping of Functionalized Coverslips

IR spectra were collected using a Shimadzu IRAffinity-1S FTIR spectrophotometer (Shimadzu Italia S.r.l., Milan, Italy) equipped with an interferometer, a DLATGS (Deuterated Triglycine Sulfate Doped with l-Alanine) detector, and a single reflection diamond ATR crystal (QATR 10, Shimadzu Italia S.r.l., Milan, Italy). All FTIR spectra were recorded from 500 to 3500 cm^{-1}

through the co-addition of 450 interferograms at a resolution of 4 cm^{-1} with Happ-Genzel apodization. The ATR crystal was carefully cleaned with acetone and ethanol before each analysis, a background was recorded for each sample using the glass coverslip, and the measurements were performed in triplicate. Spectra manipulation was performed with LabSolution IR version 2.27 (Shimadzu Italia S.r.l., Milan, Italy).

The Raman mapping of the GO-coated glass coverslips and the GO–PEI-coated glass coverslips (Figure 2) were obtained by confocal and a high-performance Raman microscope (XploRA PLUS, HORIBA, Kyoto, Japan) with deep-cooled CCD detector technology. LabSpec (HORIBA, Kyoto, Japan) was employed to control the Raman spectroscopic system and optimize and process the acquired data, to carry out Lorentzian deconvolution of the peaks. All Raman spectroscopic measurements were performed in the 600–2000 cm^{-1} range and with a 1800-line/mm grating. The samples were detected with a 532 nm laser, with a time of 1 s and 7 accumulations. Moderate power irradiation at the sample surface (~10 mW) was used, focusing on the surface with a 100× objective to avoid laser-induced heating.

7.2.5 Cell Culture

Amniotic fluid samples were obtained after written informed consent in accordance with the Declaration of Helsinki. All samples had normal diploid karyotypes. The study was approved by the ethics committees and all experiments were performed in accordance with the relevant guidelines and regulations. The hAFSCs were isolated as previously described[14] from women undergoing amniocentesis for prenatal diagnosis at 16–17 weeks of pregnancy; the cells were cultured in Iscove's modified Dulbecco's medium (IMDM) (Thermo Fisher Scientific Waltham, MA, USA), supplemented with 20% fetal bovine serum (FBS, Corning New York, NY, USA), 1%

penicillin/streptomycin, 2 mM l-glutamine, and 5 ng/mL basic fibroblast growth factor (bFGF, Thermo Fisher Scientific Waltham, MA, USA). The cells were cultured at 37 °C 5% CO_2.

7.2.6 Mito Health Stain (HCS)

The mitochondrial functionality was analyzed by HCS Mitochondrial Health Kit (Thermo Fisher Scientific Waltham, MA, USA) following the manufacturer's procedures. Briefly, hAFSCs were seeded at 1×10^5 cell/well on the standard support (CTRL) or coverslip coated with GO and GO-PEI. After 48 h, the hAFSCs were incubated with MitoStain for 30 min at 37 °C and then fixed in 4% paraformaldehyde for 10 min. Nuclei were counterstained by Hoechst 33342. To quantify the fluorescence, 8 different fields for each sample were acquired by EVOS M7000 (Thermo Fisher Scientific Waltham, MA, USA) and analyzed by Celleste Image Analysis Software v5.0 (Thermo Fisher Scientific Waltham, MA, USA). The mean fluorescence intensity of each field was normalized on the number of the nuclei.

7.2.7 Cellular Attachment

Cellular attachment was determined by counting the number of nuclei. The hAFSCs were seeded at 1×10^5 cell/well on the standard support (CTRL) or coverslip coated with GO and GO-PEI for 24 h. The cells were fixed in 4% paraformaldehyde for 10 min and the nuclei were counterstained by Hoechst 33342. The nuclei were automatically counted in 16 random fields for each condition by ImageJ v1.54k. The tool Watershed was used to discriminate singular nuclei within nuclear aggregates.

7.2.8 Immunofluorescence Analysis of Ki67 Staining

The hAFSCs were seeded at 1 × 10^5 cell/well on the standard support (CTRL) or coverslip coated with GO and GO-PEI. After 48 h, immunofluorescence analysis was performed as previously described[68,69]. Briefly, the cells were fixed in 4% paraformaldehyde for 10 min and permeabilized by Triton 0.5% for 15 min. After blocking with 5% bovine serum albumin (BSA) for 30 min, the cells were stained with 1:100 anti-Ki67 Alexa fluor 488 conjugated antibody (Thermo Fisher Scientific Waltham, MA, USA) overnight at 4 ˚C.

The nuclei were counterstained with 1:1000 DAPI (Thermo Fisher Scientific Waltham, MA, USA). Eight fields for each well were acquired by EVOS M7000 (Thermo Fisher Scientific Waltham, MA, USA) and analyzed by Celleste Image Analysis Software v5.0 (Thermo Fisher Scientific Waltham, MA, USA).

7.2.9 Western Blot (WB)

The hAFSCs were seeded at 1 × 10^5 cell/well on the standard support (CTRL) or coverslip coated with GO and GO-PEI. After 48 h, the cells were lysed in RIPA Buffer (Thermo Fisher Scientific Waltham, MA, USA) supplemented with protease/phosphatase inhibitors (cOmplete/PhosSTOP™, Roche, Basilea, Switzerland). Protein quantification was determined in triplicate using the Rapid Gold BCA Protein Assay Kit (Thermo Fisher Scientific, Waltham, MA, USA) following the manufacturer's instructions. For WB, 10 µg of the protein were loaded on 4–12% gradient precast gel (Biorad, Hercules, CA, USA). The proteins were then separated according to their molecular weight by SDS-PAGE and semi-dry transferred to a PVDF membrane (Millipore A/S, Copenhagen, Denmark) for 1 h. The membranes were blocked for 1 h in 5% BSA in tris-buffered saline (TBS) containing 0.1% Tween20 (TBST) and incubated in 1:1000 anti-OXPHOS (Abcam, Cambridge, MA,

USA) at 4 ˚C overnight. The subsequent incubation in 1:1000 secondary antibody goat anti-mouse (Thermo Fisher Scientific, Waltham, MA, USA) was performed at room temperature for 1 h. The bands were visualized using Super Signal ECL (Thermo Fisher Scientific, Waltham, MA, USA) and acquired using iBright (Thermo Fisher Scientific, Waltham, MA, USA). Finally, the bands were quantified using ImageJ v1.54k and normalized as the total stain intensity obtained using the No-Stain™ Protein Labeling Reagent (Thermo Fisher Scientific, Waltham, MA, USA) following the manufacturer's procedure

.

7.2.10 RNA Extraction from MVs

Total RNA, including miRNAs, was isolated from all MVs by the Total Exosome RNA and Protein Isolation kit (Invitrogen, Thermo Fisher Scientific, Waltham, MA, USA). The quantity and quality of the total RNAs were assessed by the microvolume UV–vis spectrophotometer NanoPhotometer (Implen, GmbH, Munich, Germany).

7.2.11 MicroRNA Expression Profiling

MicroRNA expression analysis in MVs from the hAFSC culture on GO and GO +PEI substrates was carried out by the TaqMan™ Array Human MicroRNA A Cards v2.0 (Applied Biosystems, Foster City, CA, USA). A reverse transcription reaction was performed using the Megaplex RT primer Pool A and TaqMan MicroRNA Reverse Transcription kits (Applied Biosystems, Waltham, MA, USA). A preamplification reaction of complementary DNAs (cDNAs) was executed by the TaqMan PreAmp Master Mix 2X and Megaplex PreAmp Primers pool A (Applied Biosystems, Waltham, MA, USA). The preamplified products were diluted with 0,1X TE at a pH = 8.0 and mixed with the TaqMan™

Universal Master Mix II, no UNG (Applied Biosystems, Waltham, MA, USA), and nuclease-free water. They were then loaded into the TaqMan™ Array Human MicroRNA A plates following the manufacturer's instructions and processed by qRT-PCR, using a QuantStudioTM 7 Pro Real-Time PCR detection system (Life Technologies, Carlsbad, CA, USA). Only miRNAs showing a maximum Ct = 35 and no outlier replicates were included in the analysis. In the TaqMan™ Array Human MicroRNA A Cards, three TaqMan MicroRNA Assay endogenous controls were included to aid in data normalization and one TaqMan MicroRNA Assay not related to human was included as a negative control.

7.2.12 Statistical Analysis

All data are presented as the mean ± SD of 3 independent experiments. The statistical analysis was performed by Prism 9 (GraphPad, San Diego, CA, USA) using the one-way ANOVA followed by Tukey's post hoc. The level of significance was set at $p < 0.05$.

7.3 Results

7.3.1 GO and GO-PEI Precoated Coverslips Characterization

GO scaffolds were obtained by covalently linking GO to glass coverslips by exploiting the nucleophilic attack of 3-(aminopropyl)triethoxysilane (APTES) amine groups linked to the glass coverslips to the reactive epoxides on the GO flakes. Analogously, PEI was linked to GO scaffolds by nucleophilic attack of its free amine moieties with reactive groups in GO (Figure 1). The obtained glass coverslips coated with GO and GO-PEI were characterized by using Atomic Force Microscopy (AFM) and Raman and IR spectroscopy. The AFM analysis revealed the presence of individual GO sheets well visualized onto the surface of the GO and GO-PEI functionalized

coverslips. In both samples, it was possible to notice bright ripples due to the random reaction of the GO flakes with the APTES-activated surface The obtained glass coverslips coated with GO and GO-PEI were characterized by using Atomic Force Microscopy (AFM) and Raman and IR spectroscopy. The AFM analysis revealed the presence of individual GO sheets well visualized onto the surface of the GO and GO-PEI functionalized coverslips.

In both samples, it was possible to notice bright ripples due to the random reaction of the GO flakes with the APTES-activated surface and the consequent GO sheets overlapping. In addition, the bearing analysis tool of AFM software (Nanoscope Analysis 1.8, Bruker, Billerica, MA, USA) demonstrated a GO surface coverage of 44.3 (±1.4) % over a total surface area of 400 μm^2, whereas the addition of PEI increases the coverage to 59.3 (±0.6)%, corresponding to 237.2 μm^2 (Figure 2A, C). and the consequent GO sheets overlapping. In addition, the bearing analysis tool of AFM software (Nanoscope Analysis 1.8, Bruker, Billerica, MA, USA) demonstrated a GO surface coverage of 44.3 (±1.4) % over a total surface area of 400 μm^2, whereas the addition of PEI increases the coverage to 59.3 (±0.6) %, corresponding to 237.2 μm^2 (Figure 2A,C). To further confirm the distribution of the GO flakes on the coverslips surface, Raman spectroscopy analysis wasperformed. TheRamanspectraoftheGO-functionalizedandGO PEI-functionalized glass coverslips are reported in Figure 2E,F as overlayed deconvoluted spectra of a 400 μm2 area. The G peak (band at 1600 cm−1) is related to the graphitic derived material breathing mode of C-C sp2, while the D peak (band at ≈1350 cm−1) refers to the defected graphene structure. To further confirm the distribution of the GO flakes on the coverslips surface, Raman spectroscopy analysis was performed. The Raman spectra of the GO-functionalized and GO-PEI-functionalized glass coverslips are reported in Figure 2E,F as overlayed deconvoluted spectra of a 400 μm2 area. The G peak (band at 1600 cm−1) is related to the graphitic-derived material breathing mode of C-C sp^2, while the D peak (band at ≈1350 cm−1) refers to the defected graphene structure. The Raman mappings, created by using the Raman peak intensity of GO deposited on the selected area, yield

images of GO distribution and concentration. They are false color images in which each pixel is shaded according to the following: (i) the relative intensities of the graphene G band to evaluate the GO distribution (see Figure 2B,D); and (ii) the D bandwidth to identify the oxidation degree of the graphene oxide deposited on the The Raman mappings, created by using the Raman peak intensity of GO deposited on the selected area, yield images of GO distribution and concentration. They are false color images in which each pixel is shaded according to the following: (i) the relative intensities of the graphene G band to evaluate the GO distribution (see Figure 2B,D); and (ii) the D bandwidth to identify the oxidation degree of the graphene oxide deposited on the glass coverslip (see Figure S1 in the Supplementary Materials). As shown in Figure 2B,D, Raman mappings demonstrated a complete coverage of GO on both samples despite the concentration of GO varying in the mapped area, with the concentration of GO increasing from the black regions to the yellow regions. glass coverslip (see Figure S1 in the Supplementary Materials). As shown in Figure 2B,D, Ramanmappings demonstrated a complete coverage of GO on both samples despite the concentration of GO varying in the mapped area, with the concentration of GO increasing from the black regions to the yellow regions. Raman spectroscopy is also used to evaluate the degree of GO functionalization with PEI. As is widely reported in the literature[15,16], the oxidation degree of GO, inversely proportional to the GO functionalization[8], is evaluated by analyzing the D peak width, Raman spectroscopy is also used to evaluate the degree of GO functionalization with PEI. As is widely reported in the literature[15,16], the oxidation degree of GO, inversely proportional to the GO functionalization[8], is evaluated by analyzing the D peak width, with higher bandwidth indicating a more oxidized GO. In the GO-PEI functionalized substrate, a reduction in the oxidation degree, probably due to the covalent binding of PEI amine groups to graphene oxide epoxy moieties, can be inferred by comparing the D peak width of the GO samples before and after functionalization with PEI (compare Figure S1A,B in the Supplementary Materials, respectively). with higher bandwidth indicating a more oxidized GO. In the GO-PEI functionalized substrate, a reduction in the oxidation degree, probably due to the covalent binding of PEI amine groups to graphene oxide

epoxy moieties, can be inferred by comparing the Dpeak width of the GO samples before and after functionalization with PEI (compare Figure S1A,B in the Supplementary Materials, respectively). As reported in Figure 2G, Figures S2 and S3 in the Supplementary Materials, IR spec tra confirmed the occurred chemical functionalization of the glass coverslips.

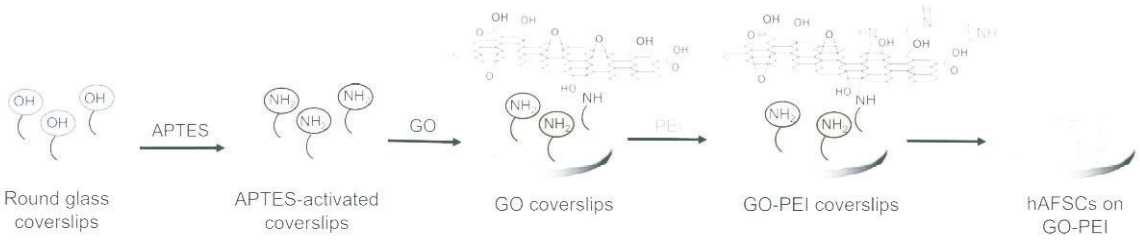

Figure 1. Representation of functionalization route of glass coverslips with GO and PEI and hAFSCs culture on GO-PEI substrates.

Firstly, the presence of graphene oxide in the GO-functionalized coverslips was highlighted by the peaks at around 1500–1600 cm^{-1} related to C=C in-plane vibrations and by the band above 1700 cm^{-1} due to the C=O stretching, as widely reported in the literature[17,18]. Furthermore, peaks at around 2800–3000 cm^{-1} were registered and related to the combination of C-H symmetric and asymmetric stretching vibrations of APTES and GO[19,20]. After the incubation of the GO coverslips into the PEI solution, the IR spectra showed differences in the 2900 cm^{-1} region, with an increased intensity of the C-H stretching bands due to the contribution of PEI carbonaceous skeletal chains[21]. The covalent functionalization between GO and PEI is confirmed by the new band at 1246 cm^{-1} due to C–N vibrations (bonded to an aromatic ring)[22] and the simultaneous decrease in the band at 1087 cm^{-1}, which is attributable to C-O stretching vibration of the epoxide groups[22].

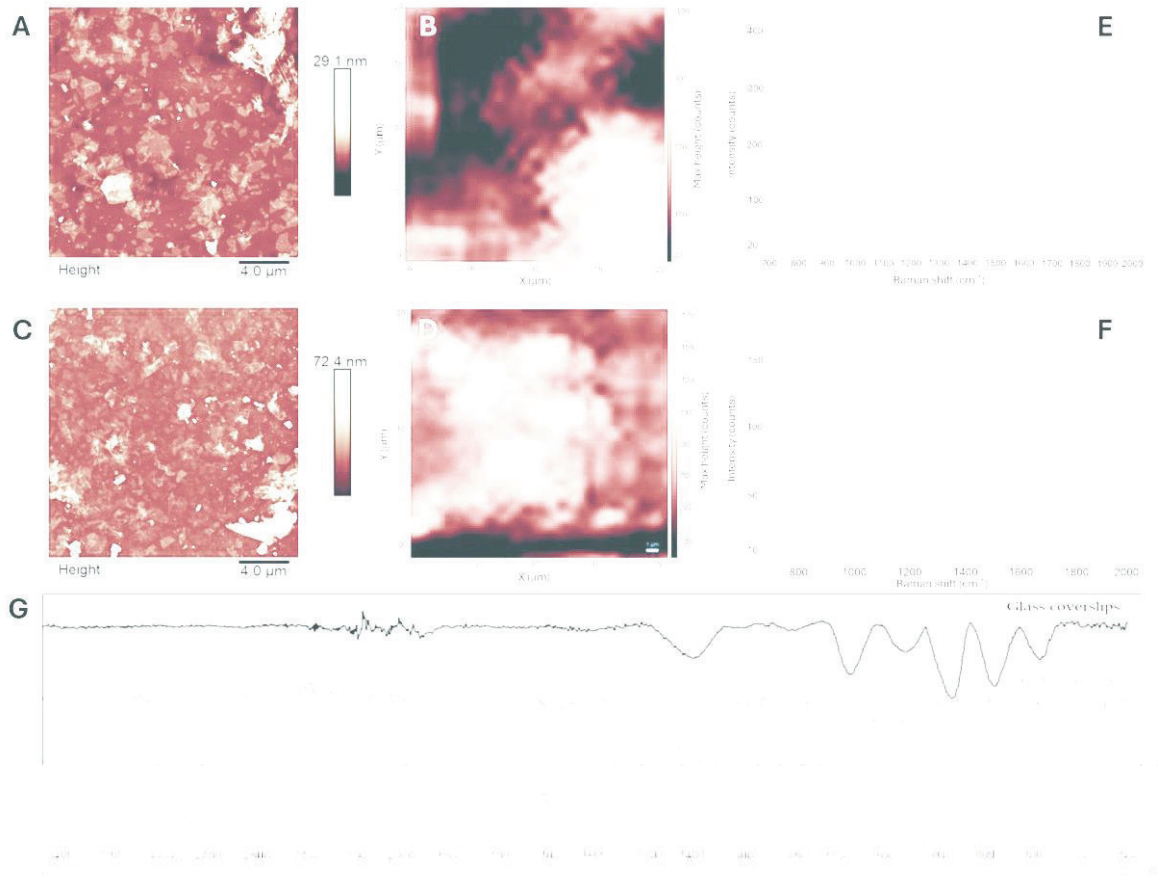

Figure 2. AFM images of surface topography and Raman mapping of (**A**,**B**) GO functionalized coverslip and (**C**,**D**) GO-PEI functionalized coverslip; (**E**) overlayed Raman spectra of 400 µm^2 area of GO-coated glass coverslip; and (**F**) overlayed Raman spectra of 400 µm^2 area of GO-PEI-coated glass coverslip. In AFM micrographs, color represents the height of deposited materials with height increasing from brown dots to white dots. In Raman mapping, intensity of G peak, corresponding to GO concentration, increases when passing from black to yellow regions. (**G**) FTIR spectra of glass coverslip (black line), GO-functionalized coverslip (red line), and GO-PEI coverslip (green line).

7.3.2 GO and GO-PEI Precoated Coverslips Influenced Cellular Adhesion and Proliferation

In order to assess whether the GO and/or GO-PEI altered the cellular adhesion, hAFSCs were stained 24 h after seeding on different coated supports with Hoechst 33342. The cell count demonstrated a reduction in the attached cells on the GO and GO-PEI supports (Figure 3A), suggesting that these two derivatives of graphene interfere with cellular attachment. Despite that, when the cellular proliferation rate was analyzed by Ki67 expression, hAFSCs on GO-PEI supports displayed a proliferation rate comparable to the CTRL condition, whereas the GO condition showed a reduced percentage of Ki67$^+$ cells, both at 48 h and 120 h (Figure 3B, C).

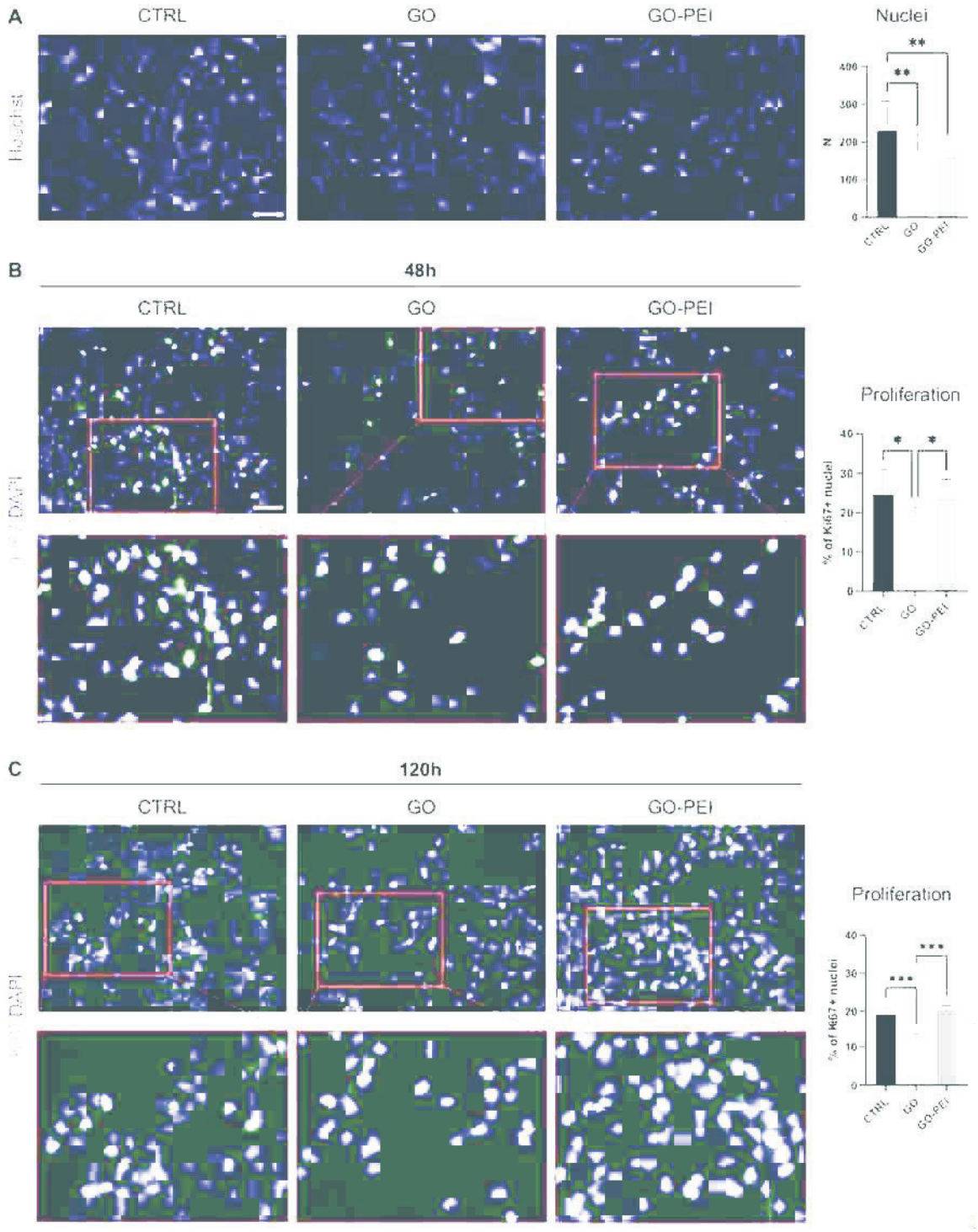

Figure 3. Effect of GO and GO-PEI on cellular adhesion and proliferation. (**A**) Cellular attachment on different types of supports, as indicated, was evaluated 24 h after seeding. Cells were fixed and nuclei were counterstained with Hoechst 33342 (blue). Magnification 20×, scale bar 100 µm. Histogram showed number of nuclei counted for each condition. Data expressed as mean ± SD. (**B**,**C**) Immunohistochemical detection of Ki67 (green fluorescence) at 48 h and 120 h after seeding, as indicated. Nuclei were counterstained with DAPI (blue). Magnification 20×, scale bar 100 µm. Histogram indicates % of $Ki67^+$ nuclei in different experimental conditions, as indicated. Data expressed as mean ± SD. * $p < 0.05$, ** $p < 0.01$, *** $p < 0.001$.

Then, MitoHealth, a specific red fluorescent probe that accumulates in healthy mitochondria in a proportional manner with mitochondrial membrane potential (MMP), was used to investigate whether BPs and PFs can harm mitochondrial activity. Data reported in Figure 4 showed that neither GO nor GO-PEI altered the MMP in hAFSCs.

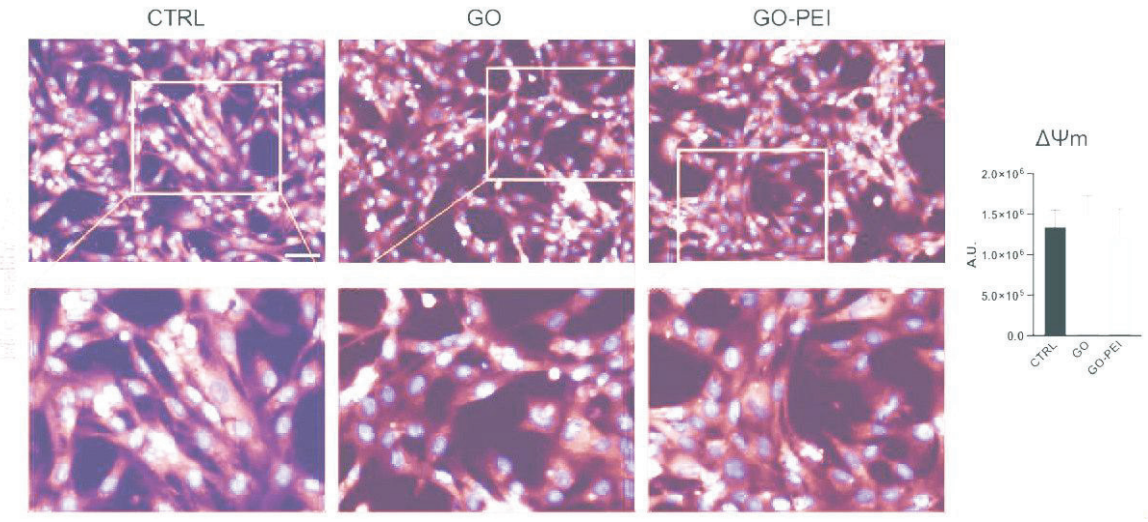

Figure 4. Effect of GO and GO-PEI on MMP. Detection of MMP (red fluorescence) 48 h after seeding for each condition. Nuclei were counterstained with DAPI (blue). Original magnification: 20×, scale bar 100 µm. Histogram indicates fluorescent intensity normalized by number of nuclei in each field. Data expressed as mean ± SD.

7.3.3 GO-PEI Restores Expression of Mitochondrial Respiratory Chain Proteins in hAFSCs

Mitochondria plays a pivotal role in regulating cell biology cycle and proliferation[23]. Since the alterations of the cellular proliferation rate were detected in the cells growing on coverslips coated with GO, but unexpectedly no MMP modifications were reported, a deeper analysis of the expression protein complexes belonging to the mitochondrial oxidative phosphorylation system (OXPHOS) was performed.

Data reported in Figure 5 showed that the hAFSCs growing for 48 h on GO-coated coverslips expressed lower levels of Complex II-Succinate dehydrogenase (CII-SDHB) and Complex V-ATP synthase (CV-ATP5A), while the protein expression of these two complexes was comparable in CTRL and GO-PEI samples, suggesting that this coating does not alter the mitochondrial

functionality of stem cells. The difference in protein expression observed in the GO condition was also reflected in the mean complex expression (Figure 5B).

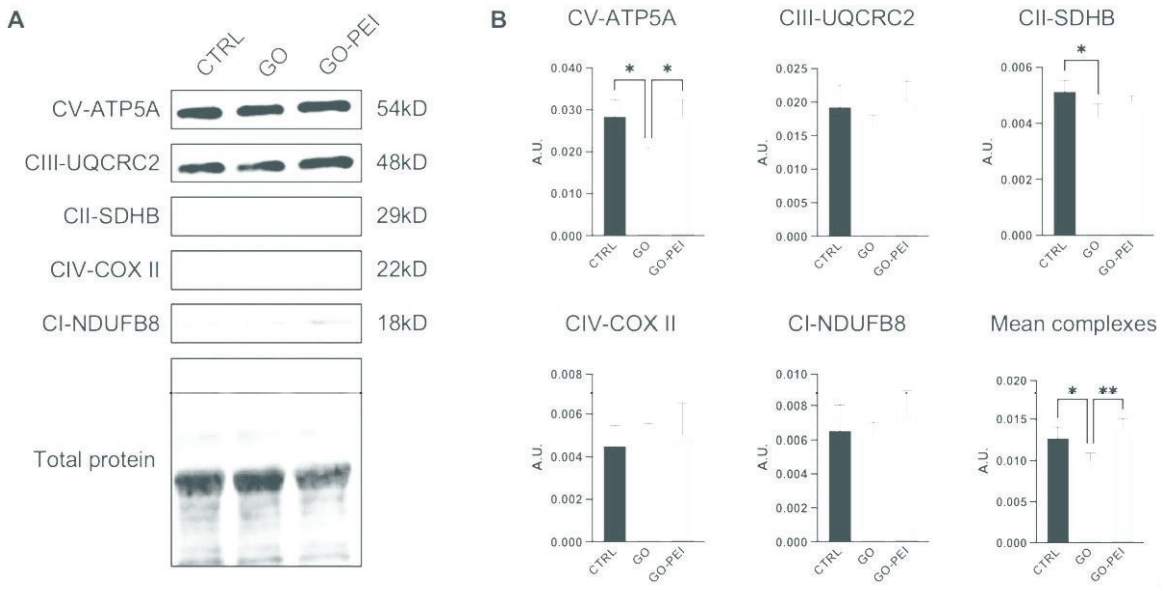

Figure 5. Protein expression of mitochondrial respiratory chain complexes. (**A**) Representative Western blot showing changes in expression of (OXPHOS) proteins 48 h from seeding in different conditions, as indicated. (**B**) Histograms show quantification of each protein, normalized on cellular total protein content. Data expressed as mean ± SD ($n = 4$) * $p < 0.05$, ** $p < 0.01$.

7.3.4 GO and GO-PEI Alter Secretion of miRNAs in hAFSCs

Since the secretion of microparticles (MPs) from stem cells is crucial as they play a significant role in intercellular communication and the modulation of the cellular environment, we evaluated whether the GO and GO-PEI substrates were able to affect the secretion of miRNAs from hAFSCs. Therefore, at 48 h after seeding, MPs were collected from the cells growing on the substrates and the miRNA content was analyzed. More specifically, the analyses focused on the expression of miRNAs involved in the regulation of cell proliferation, apoptosis, differentiation capacity, and mitochondrial functionality[24–30]. The data showed a downregulation of miR-16, 17, 19b, 30b, 92a, 106a, 126, and 142-3p in both GO and GO-PEI with respect to the CTRL condition. On the other hand, miR-4255p and miR-484 were significantly modulated only on GO

supports (Figure 6A). More interestingly, miR-93, which has a role in neuronal progenitor cell proliferation, neuronal growth, and reduces inflammatory cytokines expression[31], was downregulated in GO and totally undetectable in the MPs from the GO-PEI condition. Similarly, miR-374-5p, 18a, 26a, and 150 were reduced to very low levels in GO-PEI and not detected in GO (Figure 5B). Moreover, miR-7e, 20a 24, 29a, 99a, 221 451, and 597 were not modulated either in GO nor in GO-PEI (Supplementary Figure S4). These data suggest that substrates for cell cultures can alter the cargo from MPs influencing cell-to-cell communication.

Figure 6. GO and GO-PEI substrates influence miRNA cargo of MPs released from hAFSCs. (**A**) miRNAs present in MPs from hAFSCs cultured in CTRL, GO, and GO-PEI; or (**B**) miRNAs present only in MPs from hAFSCs cultured on CTRL and GO or GO-PEI substrates. Fold changes were obtained using ΔΔCT method and normalized on CTRL condition. Data presented as mean ± SD of three independent experiments, * $p \leq 0.05$, ** $p \leq 0.01$, *** $p \leq 0.001$.

7.4 Discussion

Cell culture substrates play a pivotal role in influencing cell behavior, including adhesion, proliferation, differentiation, and overall functionality. Indeed, thanks to physical, chemical, and topographical properties, cell supports can significantly affect the interaction between the stem cells and the environment. A well-designed substrate can mimic the natural extracellular matrix, providing essential cues that guide stem cell fate and function[32]. For instance, surface chemistry can promote or inhibit cellular adhesion,while mechanical properties can influence differentiation[32]. The importance of substrate selection is underscored by studies showing that modifications such as functionalization with bioactive molecules can enhance cellular responses, leading to improved outcomes in tissue engineering and regenerative medicine[33]. Understanding and optimizing the interaction between stem cells and their substrates is therefore crucial for advancing stem cell-based therapies and achieving successful tissue regeneration[33]. In this scenario, graphene and GO have emerged as promising materials in stem cell research due to their unique physical and chemical properties, which can significantly influence stem cell behavior[34]. Graphene has exceptional strength and high electron conductivity, making it an attractive scaffold for supporting cell growth, the differentiation of nerve tissues, and cardiac tissue repair[34]. However, pure graphene has a hydrophobic nature and can hinder cellular attachment and proliferation. In contrast, GO, with its hydrophilic surface and abundant oxygen-containing functional groups, offers a better interaction with cells but can still present challenges such as reduced cell adhesion and potential cytotoxicity[35]. This highlights the necessity for further research to improve graphene-derived supports. Despite the fact that previous studies have reported that the functionalization of GO with PEI can improve the biocompatibility of GO, making it a more attractive substrate for biological studies[8], its effects have never been investigated on the behavior of stem cells. Here, we focused on hAFSCs, fetal annexes-derived stem cells that can be considered a safer and cheaper alternative to hiPSCs for mesenchymal but also cardiac and neuronal differentiation[11,13]. In this scenario, a scaffold that helps the cells to

maintain all their biological and stemness features, also supporting their differentiation, is becoming very attractive for the scientific community. Here, for the first time, we demonstrated that GO-PEI (1) significantly favors hAFSC proliferation; (2) allows for the maintenance of a healthy mitochondrial respiratory chain, which is fundamental to maintain the integrity of their differentiation potential; and (3) can influence the miRNA content of MPs released from hAFSCs. Cell proliferation plays a crucial role in regulating tissue homeostasis, repair, and development[36]. Our data clearly demonstrated that, despite both GO-PEI and GO reducing cellular adhesion at 24 h after seeding, GO-PEI favors the maintenance of a cellular proliferation rate comparable to the CTRL, whereas it was significantly decreased on the GO supports. Results obtained from the GO-PEI substrates are in line with the literature, showing that this coating does not alter cell viability and proliferation[37]. The effects of GO are more controversial, indeed some research groups reported that this coating inhibits the formation of glioblastoma spheroids or inhibited breast cancer cell growth[38,39], whereas Zheng et al. reported an increased proliferation of prostate cancer cells[40]. These differences could be due to the different GO concentration used in the studies, oxygen content and dimensions of GO flakes, different GO–cell interactions, and different biological features of cancer cell types. For example, Wang et al. used GO flakes of 0.2–22 μm in the culture medium[38], while Zheng et al. investigated much smaller 200–900 nm sized GO flakes[40]. In both studies, GO flakes were simply added at different concentrations in the culture medium rather than covalently bound to the glass substrate, as reported in the present study. The reduced attachment of our hAFSCs on GO and GO-PEI substrates suggests that they may interfere with the initial cellular adhesion processes. Indeed, it was shown that graphene-based materials could affect the integrin signaling pathways that are fundamental for cell adhesion[41]. Despite that, GO-PEI seems to allow normal proliferation, potentially due to the probably positive charged PEI polymers of GO-PEI that interact favorably with the negatively charged cell membrane[42], improving the biocompatibility. Therefore, the surface properties of GO-PEI may create a more suitable environment for

hAFSCs, supporting the maintenance of a good cell proliferation rate that is necessary for cellular expansion in many therapeutics applications and differentiation processes[43]. On the other hand, GO may create a less biocompatible environment that may alter the cell cycle progression and cytoskeleton structures that were already observed for graphene derivate materials[44]. Anyway, further analyses are required to elucidate in detail the molecular mechanism underlying the effects of GO and GO-PEI supports on cell adhesion and proliferation. In stem cells, the maintenance of healthy mitochondria plays a pivotal role[45]. They are complex organelles essential for cellular energy production and the regulation of cellular pathways involved in proliferation, differentiation, cell cycle progression, and apoptosis[46]. Maintaining the integrity of MMP and the oxidative phosphorylation chain is crucial for preserving mitochondrial structure and function. Their disruption is associated with impaired cell proliferation and differentiation, stem cell aging, and cell death[47–49]. Moreover, it was demonstrated that glycolysis and OXPHOS are critical regulators of stem cells fates since they contribute to regulating both self-renewal and differentiation capacity[50]. More specifically, it was reported that stem cells have a metabolic transition from glycolysis to OXPHOS metabolism during the differentiation process, and OXPHOS inhibition leads to an impairment of differentiation capacity in embryonic stem cells[51,52]. Our data demonstrated that the GO-PEI substrate did not affect the expression of the mitochondrial respiratory complexes, whereas GO supports altered the expression of CIISDHB and CV-ATP5A. In particular, the latter complex is responsible for the production of ATP[53] and the reduction in this molecule could lead to cell energy depletion that consequently may contribute to a decrease in cell proliferation rate and cause cell death[54]. Despite the reduced expression of the two OXPHOS complexes in cells growing on GOcoated supports, the HSC stain did not detect any changes in MMP, probably because CII-SDHB and CV-ATP5A are the only two mitochondrial respiratory complexes that are not involved in the formation of MMP[55,56]. Anyway, it was reported that the insufficient ATP synthase phosphorylating capacity can result in an impaired energy provision and an increased

ROS production[57] that could lead to altered cellular biological functions and cell death. Our data on GO supports are also in line with Wierzbiki et al., who reported that muscle cell progenitors showed a reduced expression of CV-ATP5A, when cultured on a GO scaffold, with a potential impact on cell proliferation[58]. In addition, CII-SDHB and CV-ATP5A deregulation might alter the differentiation potential of hAFSCs, especially through the cardiac and neuronal fates, since they require an increase in the OXPHOS metabolisms to begin commitment[59,60], but additional experiments are required to specifically address this point. Very interestingly, the data demonstrated that functionalized supports were able also to influence the miRNA content in MPs released from hAFSCs. Our data showed that many miRNAs detected in MPs from hAFSC growing on GO and GO-PEI supports regulate the Pi3K-AKT pathway, cell proliferation, and mitochondrial functionality, but also neuronal differentiation[24–27,29,30,61–63]. More specifically, modulation of miR-425-5p and miR-484 in the GO condition aligns with the observed alteration in mitochondrial function since they are involved in regulating mitochondrial biogenesis and oxidative stress[28,64]. miR-93, which is reported to be upregulated in Parkinson's disease (PD)[65], is downregulated or totally absent in the MPs from hAFSCs growing on GO and GO-PEI, respectively, suggesting a potential use of these extracellular vesicles in in vitro models of Parkinson's disease to investigate their capacity of milder PD phenotypes. However, many miRNAs involved in the control of cell proliferation (miR-17, miR-106a, miR-30b, miR-92a[24,25,66,67]) were also downregulated in the GO-PEI condition, despite the fact that the Ki67 expression was comparable to the CTRL condition. This apparent discrepancy can be explained by the fact that miRNAs in MPs might not always correlate directly with the immediate cellular phenotype, considering that they are involved in cell-to-cell communication and can affect the neighboring cells in the microenvironment. Therefore, these data suggest that different coatings can influence hAFSCs through direct effects on cell behavior and indirect effects on recipient cells that can be located also far away by the alteration of the MP cargo content.

7.5 Conclusions

The present study revealed that GO-PEI coverslips promoted stem cell proliferation and growth, and restored OXPHOS metabolisms compared to GO substrates, which conversely poses some challenges on these cell functions. Overall, these findings underscore the importance of surface modification in influencing stem cell behavior and showed a higher biocompatibility of GO-PEI, since the alteration of proliferation and mitochondrial functionality could also impair the differentiation capacity of hAFSCs. These data may pave the way for the development of 3D GO-PEI scaffolds to potentially optimize stem cell proliferation and differentiation for applications in regenerative medicine and tissue engineering, especially for cardiac and neuronal differentiation. Indeed GO-PEI, displaying both the conductivity properties of graphene and the biocompatibility of PEI, may also improve and sustain the electrical properties of mature cardiomyocytes and neurons, paving the way to the generation of 3D transplantable scaffolds for in vivo tissue regeneration.

References

(1) Maleki, M.; Zarezadeh, R.; Nouri, M.; Sadigh, A.R.; Pouremamali, F.; Asemi, Z.; Kafil, H.S.; Alemi, F.; Yousefi, B. Graphene Oxide: A Promising Material for Regenerative Medicine and Tissue Engineering. Biomol. Concepts 2020, 11, 182–200, doi: 10.1515/bmc-2020-0017

(2) Gaggi, G.; Di Credico, A.; Izzicupo, P.; Sancilio, S.; Di Mauro, M.; Iannetti, G.; Dolci, S.; Amabile, G.; Di Baldassarre, A.; Ghinassi, B. Decellularized Extracellular Matrices and Cardiac Differentiation: Study on Human Amniotic Fluid-Stem Cells. Int. J. Mol. Sci. 2020, 21, 6317, doi: 10.3390/ijms21176317

(3) Geetha Bai, R.; Muthoosamy, K.; Manickam, S.; Hilal-Alnaqbi, A. Graphene-Based 3D Scaffolds in Tissue Engineering: Fabrication, Applications, and Future Scope in Liver Tissue Engineering. Int. J. Nanomed. 2019, 14, 5753–5783, doi: 10.2147/IJN.S192779.

(4) Convertino, D.; Trincavelli, M.L.; Giacomelli, C.; Marchetti, L.; Coletti, C. Graphene-Based Nanomaterials for Peripheral Nerve Regeneration. Front. Bioeng. Biotechnol. 2023, 11, 1306184, doi: 10.3389/fbioe.2023.1306184

(5) Halim, A.; Luo, Q.; Ju, Y.; Song, G. A Mini Review Focused on the Recent Applications of Graphene Oxide in Stem Cell Growth and Differentiation. Nanomaterials 2018, 8, 736, doi: 10.3390/nano8090736

(6) Musto, M.; Parisse, P.; Pachetti, M.; Memo, C.; Di Mauro, G.; Ballesteros, B.; Lozano, N.; Kostarelos, K.; Casalis, L.; Ballerini, L. Shedding Plasma Membrane Vesicles Induced by Graphene Oxide Nanoflakes in Brain Cultured Astrocytes. Carbon 2021, 176, 458–469, doi: 10.1016/j.carbon.2021.01.142

(7) Cerverò-Varona, A.; Canciello, A.; Peserico, A.; Haidar Montes, A.A.; Citeroni, M.R.; Mauro, A.; Russo, V.; Moffa, S.; Pilato, S.; Di Giacomo, S.; et al. Graphene Oxide Accelerates TGFβ-Mediated Epithelial-Mesenchymal Transition and Stimulates pro-Inflammatory Immune Response in Amniotic Epithelial Cells. Mater. Today Bio 2023, 22, 100758, doi: 10.1016/j.mtbio.2023.100758.

(8) Pilato, S.; Moffa, S.; Siani, G.; Diomede, F.; Trubiani, O.; Pizzicannella, J.; Capista, D.; Passacantando, M.; Samorì, P.; Fontana, A. 3D Graphene Oxide-Polyethylenimine Scaffolds for Cardiac Tissue Engineering. ACS Appl. Mater. Interfaces 2023, 15, 14077–14088, doi: 10.1021/acsami.3c00216

(9) Gaggi, G.; Izzicupo, P.; Di Credico, A.; Sancilio, S.; Di Baldassarre, A.; Ghinassi, B. Spare Parts from Discarded Materials: Fetal Annexes in Regenerative Medicine. Int. J. Mol. Sci. 2019, 20, 1573, doi: 10.3390/ijms20071573.

(10) Zuliani, C.C.; Damas, I.I.; Andrade, K.C.; Westin, C.B.; Moraes, Â.M.; Coimbra, I.B. Chondrogenesis of Human Amniotic Fluid Stem Cells in Chitosan-Xanthan Scaffold for Cartilage Tissue Engineering. Sci. Rep. 2021, 11, 3063, doi: 10.1038/s41598-021-82341-x.

(11) Di Baldassarre, A.; D'Amico, M.A.; Izzicupo, P.; Gaggi, G.; Guarnieri, S.; Mariggiò, M.A.; Antonucci, I.; Corneo, B.; Sirabella, D.; Stuppia, L.; et al. Cardiomyocytes Derived from Human CardiopoieticAmniotic Fluids. Sci. Rep. 2018, 8, 12028, doi: 10.1038/s41598-018-30537-z.

(12) Gaggi, G.; Di Credico, A.; Izzicupo, P.; Antonucci, I.; Crescioli, C.; Di Giacomo, V.; Di Ruscio, A.; Amabile, G.; Alviano, F.; Di Baldassarre, A.; et al. Epigenetic Features of Human Perinatal Stem Cells Redefine Their Stemness Potential. Cells 2020, 9, 1304, doi: 10.3390/cells9051304.

(13) Gaggi, G.; Di Credico, A.; Guarnieri, S.; Mariggiò, M.A.; Di Baldassarre, A.; Ghinassi, B. Human Mesenchymal Amniotic Fluid Stem Cells Reveal an Unexpected Neuronal Potential Differentiating into Functional Spinal Motor Neurons. Front. Cell Dev. Biol. 2022, 10, 936990, doi: 10.3389/fcell.2022.936990.

(14) Dey, B.K.; Mueller, A.C.; Dutta, A. Long Non-Coding RNAs as Emerging Regulators of Differentiation, Development, and Disease. Transcription 2014, 5, e944014, doi: 10.4161/21541272.2014.944014

(15) Ferrari, I.; Motta, A.; Zanoni, R.; Scaramuzzo, F.A.; Amato, F.; Dalchiele, E.A.; Marrani, A.G. Understanding the Nature of Graphene Oxide Functional Groups by Modulation of the Electrochemical Reduction: A Combined Experimental and Theoretical Approach. Carbon 2023, 203, 29–38, doi: 10.1016/j.carbon.2022.11.052

(16) Luo, Z.; Cong, C.; Zhang, J.; Xiong, Q.; Yu, T. The Origin of Sub-Bands in the Raman D-Band of Graphene. Carbon 2012, 50, 4252–4258, doi: 10.1016/j.carbon.2012.05.008.

(17) Zhang, C.; Dabbs, D.M.; Liu, L.-M.; Aksay, I.A.; Car, R.; Selloni, A. Combined Effects of Functional Groups, Lattice Defects, and Edges in the Infrared Spectra of Graphene Oxide. J. Phys. Chem. C 2015, 119, 18167–18176, doi: 10.1021/acs.jpcc.5b02727

(18) Acik, M.; Lee, G.; Mattevi, C.; Pirkle, A.; Wallace, R.M.; Chhowalla, M.; Cho, K.; Chabal, Y. The Role of Oxygen during Thermal Reduction of Graphene Oxide Studied by Infrared Absorption Spectroscopy. J. Phys. Chem. C 2011, 115, 19761–19781, doi: 10.1021/jp2052618.

(19) Saleem, H.; Haneef, M.; Abbasi, H.Y. Synthesis Route of Reduced Graphene Oxide via Thermal Reduction of Chemically Exfoliated Graphene Oxide. Mater. Chem. Phys. 2018, 204, 1–7, doi: 10.1016/j.matchemphys.2017.10.020

(20) Lakard, S.; Herlem, G.; Lakard, B.; Fahys, B. Theoretical Study of the Vibrational Spectra of Polyethylenimine and Polypropylenimine. J. Mol. Struct. THEOCHEM 2004, 685, 83–87, doi: 10.1016/j.theochem.2004.06.042

(21) Xin, Q.; Li, Z.; Li, C.; Wang, S.; Jiang, Z.; Wu, H.; Zhang, Y.; Yang, J.; Cao, X. Enhancing the CO2 Separation Performance of Composite Membranes by the Incorporation of Amino Acid-Functionalized Graphene Oxide. J. Mater. Chem. A 2015, 3, 6629–6641, doi: 10.1039/C5TA00506J

(22) Mandal, S.; Lindgren, A.G.; Srivastava, A.S.; Clark, A.T.; Banerjee, U. Mitochondrial Function Controls Proliferation and Early Differentiation Potential of Embryonic Stem Cells. Stem Cells 2011, 29, 486–495, doi: 10.1002/stem.590

(23) Fu, Z.-J.; Chen, Y.; Xu, Y.-Q.; Lin, M.-A.; Wen, H.; Chen, Y.-T.; Pan, P.-L. Regulation of miR-30b in Cancer Development, Apoptosis, and Drug Resistance. Open Life Sci. 2022, 17, 102–106, doi: 10.1515/biol-2022-0017.

(24) Cui, X.; Wang, X.; Zhou, X.; Jia, J.; Chen, H.; Zhao, W. miR-106a Regulates Cell Proliferation and Autophagy by Targeting LKB1 in HPV-16–Associated Cervical Cancer. Mol. Cancer Res. 2020, 18, 1129–1141, doi: 10.1158/1541-7786.MCR-19-1114

(25) Lechman, E.R.; Gentner, B.; Ng, S.W.K.; Schoof, E.M.; van Galen, P.; Kennedy, J.A.; Nucera, S.; Ciceri, F.; Kaufmann, K.B.; Takayama, N.; et al. miR-126 Regulates Distinct Self-Renewal Outcomes in Normal and Malignant Hematopoietic Stem Cells. Cancer Cell 2016, 29, 214–228, doi: 10.1016/j.ccell.2015.12.011

(26) Liu, B.; Cheng, M.; Hu, S.; Wang, S.; Wang, L.; Tu, X.; Huang, C.; Jiang, H.; Wu, G. Overexpression of miR-142-3p Improves Mitochondrial Function in Cardiac Hypertrophy. Biomed. Pharmacother. 2018, 108, 1347–1356, doi: 10.1016/j.biopha.2018.09.146.

(27) Wang, K.; Long, B.; Jiao, J.-Q.; Wang, J.-X.; Liu, J.-P.; Li, Q.; Li, P.-F. miR-484 Regulates Mitochondrial Network through Targeting Fis1. Nat. Commun. 2012, 3, 781, doi: 10.1038/ncomms1770.

(28) Wu, Z.; Guo, J.; Zhang, Y.; Liu, J.; Ma, H.; Tang, Y. MiR-425-5p Accelerated the Proliferation, Migration, and Invasion of Ovarian Cancer Cells via Targeting AFF4. J. Ovarian Res. 2021, 14, 138, doi: 10.1186/s13048-021-00894-x

(29) Li, X.; Zhang, Z.; Li, Y.; Zhao, Y.; Zhai, W.; Yang, L.; Kong, D.; Wu, C.; Chen, Z.; Teng, C.-B. miR-18a Counteracts AKT and ERK Activation to Inhibit the Proliferation of Pancreatic Progenitor Cells. Sci. Rep. 2017, 7, 45002, doi: 10.1038/srep45002

(30) Burrows, K.; Figueroa-Hall, L.K.; Stewart, J.L.; Alarbi, A.M.; Kuplicki, R.; Hannafon, B.N.; Tan, C.; Risbrough, V.B.; McKinney, B.A.; Ramesh, R.; et al. Exploring the Role of Neuronal-Enriched Extracellular Vesicle miR-93 and Interoception in Major Depressive Disorder. Transl. Psychiatry 2024, 14, 199, doi: 10.1038/s41398-024-02907-x.

(31) Gattazzo, F.; Urciuolo, A.; Bonaldo, P. Extracellular Matrix: A Dynamic Microenvironment for Stem Cell Niche. Biochim. Biophys. Acta BBA-Gen. Subj. 2014, 1840, 2506–2519, doi: 10.1016/j.bbagen.2014.01.010.

(32) Nitti, P.; Narayanan, A.; Pellegrino, R.; Villani, S.; Madaghiele, M.; Demitri, C. Cell-Tissue Interaction: The Biomimetic Approach to Design Tissue Engineered Biomaterials. Bioengineering 2023, 10, 1122, doi: 10.3390/bioengineering10101122

(33) Da Silva, L.P.; Kundu, S.C.; Reis, R.L.; Correlo, V.M. Electric Phenomenon: A Disregarded Tool in Tissue Engineering and Regenerative Medicine. Trends Biotechnol. 2020, 38, 24–49, doi: 10.1016/j.tibtech.2019.07.002.

(34) Morotomi-Yano, K.; Hayami, S.; Yano, K. Adhesion States Greatly Affect Cellular Susceptibility to Graphene Oxide: Therapeutic Implications for Cancer Metastasis. Int. J. Mol. Sci. 2024, 25, 1927, doi: 10.3390/ijms25031927.

(35) Loftus, L.V.; Amend, S.R.; Pienta, K.J. Interplay between Cell Death and Cell Proliferation Reveals New Strategies for Cancer Therapy. Int. J. Mol. Sci. 2022, 23, 4723, doi: 10.3390/ijms23094723.

(36) Khanam, N.; Mikoryak, C.; Draper, R.K.; Balkus, K.J. Electrospun Linear Polyethyleneimine Scaffolds for Cell Growth. Acta Biomater. 2007, 3, 1050–1059, doi: 10.1016/j.actbio.2007.06.005.

(37) Wang, X.; Zhou, W.; Li, X.; Ren, J.; Ji, G.; Du, J.; Tian, W.; Liu, Q.; Hao, A. Graphene Oxide Suppresses the Growth and Malignancy of Glioblastoma Stem Cell-like Spheroids via Epigenetic Mechanisms. J. Transl. Med. 2020, 18, 200, doi: 10.1186/s12967-020-02359-z.

(38) Chen, S.; Zhang, S.; Wang, Y.; Yang, X.; Yang, H.; Cui, C. Anti-EpCAM Functionalized Graphene Oxide Vector for Tumor Targeted siRNA Delivery and Cancer Therapy. Asian J. Pharm. Sci. 2021, 16, 598–611, doi: 10.1016/j.ajps.2021.04.002.

(39) Zheng, Z.; Halifu, A.; Ma, J.; Liu, L.; Fu, Q.; Yi, B.; Du, E.; Tian, D.; Xu, Y.; Zhang, Z.; et al. Low-Dose Graphene Oxide Promotes Tumor Cells Proliferation by Activating PI3K-AKT-mTOR Signaling via Cellular Membrane Protein Integrin αV. Environ. Pollut. 2023, 330, 121817, doi: 10.1016/j.envpol.2023.121817.

(40) Jing, G.; Li, K.; Sun, F.; Niu, J.; Zhu, R.; Qian, Y.; Wang, S. Layer-Number-Dependent Effects of Graphene Oxide on the Pluripotency of Mouse Embryonic Stem Cells Through the Regulation of the Interaction Between the Extracellular Matrix and Integrins. Int. J. Nanomed. 2021, 16, 3819–3832, doi: 10.2147/IJN.S301892

(41) Ou, L.; Lan, Y.; Feng, Z.; Feng, L.; Yang, J.; Liu, Y.; Bian, L.; Tan, J.; Lai, R.; Guo, R. Functionalization of SF/HAP Scaffold with GO-PEI-miRNA Inhibitor Complexes to Enhance Bone Regeneration through Activating Transcription Factor 4. Theranostics 2019, 9, 4525–4541, doi: 10.7150/thno.34676.

(42) Melnik, S.; Werth, N.; Boeuf, S.; Hahn, E.-M.; Gotterbarm, T.; Anton, M.; Richter, W. Impact of C-MYC Expression on Proliferation, Differentiation, and Risk of Neoplastic Transformation of Human Mesenchymal Stromal Cells. Stem Cell Res. Ther. 2019, 10, 73, doi: 10.1186/s13287-019-1187-z.

(43) Wang, Y.; Xu, J.; Xu, L.; Tan, X.; Feng, L.; Luo, Y.; Liu, J.; Liu, Z.; Peng, R. Functionalized Graphene Oxide Triggers Cell Cycle Checkpoint Control through Both the ATM and the ATR Signaling Pathways. Carbon 2018, 129, 495–503, doi: 10.1016/j.carbon.2017.12.012

(44) Wang, Y.; Barthez, M.; Chen, D. Mitochondrial Regulation in Stem Cells. Trends Cell Biol. 2024, 34, 685–694, doi: 10.1016/j.tcb.2023.10.003

(45) Osellame, L.D.; Blacker, T.S.; Duchen, M.R. Cellular and Molecular Mechanisms of Mitochondrial Function. Best Pract. Res. Clin. Endocrinol. Metab. 2012, 26, 711–723, doi: 10.1016/j.beem.2012.05.003.

(46) Zhang, C.; Meng, Y.; Han, J. Emerging Roles of Mitochondrial Functions and Epigenetic Changes in the Modulation of Stem Cell Fate. Cell. Mol. Life Sci. 2024, 81, 26, doi: 10.1007/s00018-023-05070-6.

(47) Yan, X.-J.; Yu, X.; Wang, X.-P.; Jiang, J.-F.; Yuan, Z.-Y.; Lu, X.; Lei, F.; Xing, D.-M. Mitochondria Play an Important Role in the Cell Proliferation Suppressing Activity of Berberine. Sci. Rep. 2017, 7, 41712, doi: 10.1038/srep41712

(48) Seo, B.J.; Yoon, S.H.; Do, J.T. Mitochondrial Dynamics in Stem Cells and Differentiation. Int. J. Mol. Sci. 2018, 19, 3893, doi: 10.3390/ijms19123893.

(49) Shyh-Chang, N.; Ng, H.-H. The Metabolic Programming of Stem Cells. Genes Dev. 2017, 31, 336–346, doi: 10.1101/gad.293167.116

(50) Ludikhuize, M.C.; Rodríguez Colman, M.J. Metabolic Regulation of Stem Cells and Differentiation: A Forkhead Box O Transcription Factor Perspective. Antioxid. Redox Signal. 2021, 34, 1004–1024, doi: 10.1089/ars.2020.8126

(51) Yan, W.; Diao, S.; Fan, Z. The Role and Mechanism of Mitochondrial Functions and Energy Metabolism in the Function Regulation of the Mesenchymal Stem Cells. Stem Cell Res. Ther. 2021, 12, 140, doi: 10.1186/s13287-021-02194-z.

(52) Jonckheere, A.I.; Smeitink, J.A.M.; Rodenburg, R.J.T. Mitochondrial ATP Synthase: Architecture, Function and Pathology. J. Inherit. Metab. Dis. 2012, 35, 211–225, doi: 10.1007/s10545-011-9382-9.

(53) Izyumov, D.S.; Avetisyan, A.V.; Pletjushkina, O.Y.; Sakharov, D.V.; Wirtz, K.W.; Chernyak, B.V.; Skulachev, V.P. "Wages of Fear": Transient Threefold Decrease in Intracellular ATP Level Imposes Apoptosis. Biochim. Biophys. Acta BBA-Bioenerg. 2004, 1658, 141–147, doi: 10.1016/j.bbabio.2004.05.007.

(54) Zorova, L.D.; Popkov, V.A.; Plotnikov, E.Y.; Silachev, D.N.; Pevzner, I.B.; Jankauskas, S.S.; Babenko, V.A.; Zorov, S.D.; Balakireva, A.V.; Juhaszova, M.; et al. Mitochondrial Membrane Potential. Anal. Biochem. 2018, 552, 50–59, doi: 10.1016/j.ab.2017.07.009.

(55) Pradeepkiran, J.A.; Reddy, P.H. Defective Mitophagy in Alzheimer's Disease. Ageing Res. Rev. 2020, 64, 101191, doi: 10.1016/j.arr.2020.101191

(56) Mayr, J.A.; Havlickova, V.; Zimmermann, F.; Magler, I.; Kaplanova, V.; Jesina, P.; Pecinova, A.; Nuskova, H.; Koch, J.; Sperl, W.; et al. Mitochondrial ATP Synthase Deficiency Due to a Mutation in the ATP5E Gene for the F1 Subunit. Hum. Mol. Genet. 2010, 19, 3430–3439, doi: 10.1093/hmg/ddq254

(57) Wierzbicki, M.; Hotowy, A.; Kutwin, M.; Jaworski, S.; Bałaban, J.; Sosnowska, M.; Wójcik, B.; Wędzińska, A.; Chwalibog, A.; Sawosz, E. Graphene Oxide Scaffold Stimulates Differentiation and Proangiogenic Activities of Myogenic Progenitor Cells. Int. J. Mol. Sci. 2020, 21, 4173, doi: 10.3390/ijms21114173

(58) Zheng, X.; Boyer, L.; Jin, M.; Mertens, J.; Kim, Y.; Ma, L.; Ma, L.; Hamm, M.; Gage, F.H.; Hunter, T. Metabolic Reprogramming during Neuronal Differentiation from Aerobic Glycolysis to Neuronal Oxidative Phosphorylation. eLife 2016, 5, e13374, doi: 10.7554/eLife.13374.

(59) Chung, S.; Dzeja, P.P.; Faustino, R.S.; Perez-Terzic, C.; Behfar, A.; Terzic, A. Mitochondrial Oxidative Metabolism Is Required for the Cardiac Differentiation of Stem Cells. Nat. Clin. Pract. Cardiovasc. Med. 2007, 4, S60–S67, doi: 10.1038/ncpcardio0766

(60) Rui, J.; Fang, S.; Wang, Y.; Lv, B.; Yu, B.; Li, S. Inhibition of microRNA-16 Protects Mesenchymal Stem Cells against Apoptosis. Mol. Med. Rep. 2018, 18, 902–910, doi: 10.3892/mmr.2018.9012.

(61) Ohta, K.; Hoshino, H.; Wang, J.; Ono, S.; Iida, Y.; Hata, K.; Huang, S.K.; Colquhoun, S.; Hoon, D.S.B. MicroRNA-93 Activates c-Met/PI3K/Akt Pathway Activity in Hepatocellular Carcinoma by Directly Inhibiting PTEN and CDKN1A. Oncotarget 2015, 6, 3211–3224, doi: 10.18632/oncotarget.3085

(62) Liao, W.; Deng, X.; Chen, G.; Yang, J.; Li, Y.; Li, L.; Zhong, L.; Tao, G.; Hou, J.; Li, M.; et al. MiR-150-5p Contributes to Unexplained Recurrent Spontaneous Abortion by Targeting VEGFA and Downregulating the PI3K/AKT/mTOR Signaling Pathway. J. Assist. Reprod. Genet. 2024, 41, 63–77, doi: 10.1007/s10815-023-02959-w.

(63) Hu, Y.-B.; Zhang, Y.-F.; Wang, H.; Ren, R.-J.; Cui, H.-L.; Huang, W.-Y.; Cheng, Q.; Chen, H.-Z.; Wang, G. miR-425 Deficiency Promotes Necroptosis and Dopaminergic Neurodegeneration in Parkinson's Disease. Cell Death Dis. 2019, 10, 589, doi: 10.1038/s41419-019-1809-5.

(64) Wang, X.; Liu, Z.; Wang, F. MicroRNA-93 Blocks Signal Transducers and Activator of Transcription 3 to Reduce Neuronal Damage in Parkinson's Disease. Neurochem. Res. 2021, 46, 1859–1868, doi: 10.1007/s11064-021-03333-x

(65) Huang, C.; Liu, J.; Xu, L.; Hu, W.; Wang, J.; Wang, M.; Yao, X. MicroRNA-17 Promotes Cell Proliferation and Migration in Human Colorectal Cancer by Downregulating SIK1. Cancer Manag. Res. 2019, 11, 3521–3534, doi: 10.2147/CMAR.S191087.

(66) Wang, Y.; Tian, Y.; Li, Z.; Zheng, Z.; Zhu, L. miR-92 Regulates the Proliferation, Migration, Invasion and Apoptosis of Glioma Cells by Targeting Neogenin. Open Med. 2020, 15, 283–291, doi: 10.1515/med-2020-0040

(67) Gaggi, G.; Di Credico, A.; Barbagallo, F.; Ghinassi, B.; Di Baldassarre, A. Bisphenols and Perfluoroalkyls Alter Human Stem Cells Integrity: A Possible Link with Infertility. Environ. Res. 2023, 235, 116487, doi: 10.1016/j.envres.2023.116487

(68) Di Credico, A.; Gaggi, G.; Bucci, I.; Ghinassi, B.; Di Baldassarre, A. The Effects of Combined Exposure to Bisphenols and Perfluoroalkyls on Human Perinatal Stem Cells and the Potential Implications for Health Outcomes. Int. J. Mol. Sci. 2023, 24, 15018, doi: 10.3390/ijms241915018.

8 Nanosystems

During the PhD, the effect of GO on biological systems was simulated using liposomes. Indeed, liposomes were and are used to simulate biological membranes because of their similar phospholipidc nature. The use of liposomes allows therefore to understand the kind of interactions and mechanisms that occur when graphene oxide interacts with cellular's membrane and what are the consequences of this interaction in terms of membrane composition and fluidity. The model used in this case was based on dioleylphosphatidylcholinene and cholesterol.

Raman spectroscopy and other above mentioned biophysical techniques were exploited in a different study in order to characterize the physicochemical interactions between phenolic monoterpenes, used as guests, and the POPC liposomal bilayers, Molecular dynamics simulations were used to support experimental data. The results show that these molecules localise at the solvent-membrane interface, specifically near the lipid headgroup and upper acyl chain regions. This insertion increases membrane fluidity and permeability, with the free hydroxyl group of natural terpenes playing a crucial role in promoting significant leakage from the aqueous liposomal core. These findings provide a molecular framework for the rational design of new antimicrobial agents and drug delivery systems.

In a different study, exosomes were characterized. Liposomes and exosomes are both nano-sized vesicles composed of a phospholipid bilayer surrounding an internal aqueous core, a structure that allows them to encapsulate and transport molecular cargoes. Due to these shared biophysical properties, both are utilized as versatile delivery systems in medicine, liposomes as synthetic vehicles for drug delivery and exosomes as natural carriers for biomarkers and intercellular signalling.

Exosomes were recovered from urine of individuals who practiced trekking at 4556 meters. The study investigated the impact of high-altitude hypoxia on urinary biomarkers and extracellular vesicles (uEVs). Findings show significant increases in the albumin-to-creatinine ratio, IL-6, and 8-isoprostane, indicating sub-clinical renal dysfunction and an increased oxinflammatory burden. Biophysical analysis using AFM and Raman spectroscopy revealed that high-altitude uEVs are more

prone to fusion and contain more contaminants compared to low-altitude samples. Ultimately, the research suggests that monitoring the biophysical and chemical features of urine offers a non-invasive method for assessing physiological responses to hypoxic stress.

The Evolution of Liposomal Science

8.1 Introduction

The discipline of drug delivery has undergone a tectonic shift over the last six decades, moving away from the systemic administration of free therapeutic agents toward the development of sophisticated, programmable nanocarriers. At the center of this evolution lies the liposome, a self-assembled phospholipid vesicle that has arguably become the most successful nanoplatform in clinical history.

The story of the liposome began in 1961 at the Babraham Institute in Cambridge, where British haematologist Alec D. Bangham first observed that phospholipids in aqueous media spontaneously organize into closed bilayer structures[215]. Initially termed "multilamellar smectic mesophases," these vesicles were first employed by biophysicists as biomimetic models to study the permeability and electrical properties of biological membranes[216]. Researchers such as *Gregoriadis et al*., demonstrated that liposomes could sequester toxic drugs within their aqueous cores or lipid bilayers, thereby altering their pharmacokinetics and protecting them from metabolic degradation[217].

The fundamental utility of a liposome is derived from its amphiphilic nature. Supported by the seminal work of *Akbarzadeh et al***.** the structural integrity of these vesicles is governed by the thermodynamics of the hydrophobic effect[218].

The selection of phospholipids is the primary determinant of a liposome's biological performance. Natural phospholipids, such as phosphatidylcholine (PC) derived from egg yolk or soybean, remain popular due to their inherent biocompatibility. However, for controlled delivery applications,

synthetic lipids like dipalmitoylphosphatidylcholine (DPPC) or distearoylphosphatidylcholine (DSPC) are preferred.

A critical parameter in this selection is the phase transition temperature (T_m). Below the T_m, the lipid bilayer exists in a rigid, well-ordered "gel" state; above it, the membrane transitions into a fluid, "liquid-crystalline" state[219]. This transition significantly impacts the rate of drug diffusion; for instance, liposomes composed of DSPC (high T_m of 55°C) remain stable and leak-proof at physiological temperatures, whereas those composed of unsaturated lipids like DOPC (low T_m, below -17°C) are highly fluid and permeable.

To bridge the gap between stability and fluidity, cholesterol is frequently intercalated into the bilayer. As noted by *Kaddah et al. (2018),* cholesterol acts as a fluidity regulator. In fluid-state bilayers, it reduces the mobility of the hydrocarbon chains, thereby decreasing permeability and increasing mechanical strength[220]. Conversely, in gel-state bilayers, it prevents the tight packing of lipids, maintaining a level of flexibility that prevents the membrane from becoming brittle. Crucially, the presence of cholesterol (typically at 30–50 mol%) inhibits the binding of plasma proteins (opsonins), which would otherwise trigger rapid clearance by the mononuclear phagocyte system (MPS)[221].

8.1.2 Classification

The classification of liposomes is traditionally based on two parameters: size and lamellarity (the number of bilayers). As categorized[222] by *Nsairat et al.:*

- Small Unilamellar Vesicles (SUVs): These range from 20 to 100 nm. Their small size allows for long circulation times and better penetration into tumor interstitium via the Enhanced Permeability and Retention (EPR) effect.
- Large Unilamellar Vesicles (LUVs): These vesicles (>100 nm) are optimized for carrying hydrophilic cargo due to their large internal aqueous volume.

- Multilamellar Vesicles (MLVs): Consisting of several concentric bilayers, MLVs are excellent for the delivery of lipophilic drugs but are rapidly sequestered by the liver due to their larger size.
- Multivesicular Vesicles (MVVs): These contain multiple smaller vesicles within a single large outer membrane, often utilized for sustained-release local injections.

8.1.3 Conventional and Stealth Liposomes

The first generation, or conventional liposomes, were limited by their short half-life in the bloodstream. This was resolved in the 1990s with the advent of PEGylation. By grafting polyethylene glycol (PEG) to the lipid headgroups, a "stealth" effect is achieved. The hydrophilic PEG chains create a hydration layer that sterically hinders opsonization[223]. This technology paved the way for Doxil® (liposomal doxorubicin), the first FDA-approved nanomedicine in 1995, which significantly reduced the cardiotoxicity associated with free doxorubicin[224].

8.1.4 Active Targeting

Third-generation liposomes utilize ligands (antibodies, peptides, or aptamers) to achieve active targeting. By binding specifically to receptors overexpressed on tumor cells, such as HER2 or EGFR, these vesicles can be internalised via receptor-mediated endocytosis[225].

The fourth generation, currently the focus of intensive research, involves stimuli-responsive liposomes. These are engineered to remain stable in the blood but release their cargo instantly when exposed to a trigger, such as the acidic pH of the tumor microenvironment (pH-sensitive) or external triggers like near-infrared light or ultrasound.

8.2 Methodologies of Liposomal Fabrication

The transition of liposomes from experimental curiosities to reproducible pharmaceutical products necessitated the development of robust fabrication techniques. These methods are generally

categorized into "Top-Down" and "Bottom-Up" approaches, each influencing the final vesicle size, lamellarity, and polydispersity.

8.2.1 The classic Thin-Film Hydration Method

The most enduring technique remains the thin-film hydration method, originally pioneered by *Bangham et al.* in 1965. In this process, lipids are dissolved in an organic solvent (typically chloroform or a methanol-chloroform mixture) to ensure a homogeneous distribution. Following the evaporation of the solvent under vacuum, a thin "stacked" lipid film is formed on the vessel walls. Upon the addition of an aqueous buffer and mechanical agitation, the film swells and detaches, spontaneously forming large multilamellar vesicles (MLVs). While simple, this method often yields heterogeneous populations that require secondary processing, such as extrusion through polycarbonate membranes or ultrasonication, to achieve the desired nanometer range.

8.2.2 Solvent Injection and Detergent Removal

To circumvent the limitations of thin-film hydration, the ethanol injection method[226] has been introduced. Here, a lipid-ethanol solution is rapidly injected into an aqueous buffer. The sudden change in solvent polarity causes the lipids to precipitate and reorganize into unilamellar vesicles. This method is praised for its relative simplicity and ability to be scaled for larger volumes. Alternatively, detergent removal techniques involve the formation of mixed micelles of lipids and detergents (like bile salts). The slow removal of the detergents induces a transition from micelles to vesicles, often resulting in highly uniform LUVs .

8.2.3 Microfluidics and High-Pressure Homogenization

Modern nanomedicine demands a level of precision that traditional "batch" methods cannot provide. Microfluidics has emerged as a transformative technology in this regard. By precisely controlling the laminar flow and mixing of lipid and aqueous phases at the microscale, researchers can produce liposomes with an extremely narrow Polydispersity Index (PDI) and high encapsulation efficiency[227].

8.2.4 Mechanisms of Drug Encapsulation: Passive vs. Active Loading

The therapeutic utility of a liposome is fundamentally defined by its ability to sequester and retain a payload. The loading strategy is dictated by the physicochemical properties of the drug, specifically its partition coefficient (logP) and molecular weight.

Passive Loading

Passive loading occurs during the formation of the vesicles themselves. Hydrophilic drugs are dissolved in the aqueous hydration buffer, while lipophilic drugs are incorporated into the initial organic lipid solution. However, passive loading is often inefficient for hydrophilic molecules, as much of the drug remains in the external medium and is lost during purification.

Remote Loading

For amphipathic weak bases, such as doxorubicin or vincristine, the Remote Loading technique, often utilising a transmembrane pH or ion gradient, is the gold standard. In this process, liposomes are first prepared with an acidic internal environment (e.g., using ammonium sulfate). When the neutral drug is added to the external medium, it diffuses across the bilayer in its uncharged state. Once inside the acidic core, the drug becomes protonated (charged) and is trapped, often forming a crystalline precipitate within the vesicle[228].

8.3 Stability Challenges

Despite their advantages, liposomes are thermodynamically unstable systems susceptible to both chemical and physical degradation

8.3.1 Chemical Degradation: Oxidation and Hydrolysis

Phospholipids containing unsaturated fatty acid chains are highly prone to lipid peroxidation, particularly when exposed to light, oxygen, or heavy metal ions. This leads to the formation of cyclic peroxides and malondialdehyde, which can compromise membrane integrity. Furthermore, the ester bonds in phospholipids are susceptible to hydrolysis, yielding lysophospholipids and free fatty acids, which act as detergents and "solubilize" the bilayer, leading to premature drug leakage.

8.3.2 Physical Instability: Aggregation and Fusion

Vesicles may undergo aggregation (reversible clumping) or fusion (irreversible merging into larger vesicles). These processes are driven by the minimization of surface free energy. To mitigate these risks, formulations are often lyophilized (freeze-dried) in the presence of cryoprotectants like sucrose or trehalose, which form a "vitreous" (glassy) matrix that protects the vesicles during the freezing and dehydration cycles[229]

8.4 Smart Nanocarriers: The Mechanics of Triggered Release

A central theme in modern liposomal research is the shift from passive accumulation to active, triggered release. This ensures that the drug is only "bioavailable" at the site of pathology, further reducing off-target toxicity.

8.4.1 pH-Sensitive Liposomes

Exploiting the fact that the tumour microenvironment and endosomes are more acidic (pH 5.5-6.5) than healthy tissue (pH 7.4) researchers utilize pH-sensitive lipids like dioleoylphosphatidylethanolamine (DOPE). As detailed by *Mura et al.*, these lipids are typically stabilized at neutral pH but undergo a conformational change into a hexagonal phase under acidic conditions, triggering the immediate collapse of the vesicle and release of the payload[230].

8.4.2 Thermo-Responsive Liposomes

Temperature-sensitive liposomes (TSLs) are designed to release their contents when the local temperature is raised (typically to 40–42°C) via external hyperthermia. This is achieved by using lipids with a phase transition temperature (Tm) just above body temperature, such as DPPC. The most famous example, ThermoDox®, is currently being investigated for its ability to release doxorubicin specifically within the heated margins of a tumour during radiofrequency ablation[231].

8.5 Purification and Separation Processes of the Unencapsulated Drug

The final phase of liposomal formulation requires the systematic removal of the unencapsulated drug and organic solvent residues. This process is essential not only for determining the Encapsulation Efficiency (EE%) but also for preventing systemic toxicity caused by the immediate release of the free drug (burst release) once injected.

8.5.1 Dialysis and Centrifugation

According to *Akbarzadeh et al*., dialysis is one of the most common techniques for purification at the laboratory scale[218]. The sample is placed in a semi-permeable membrane bag with a specific molecular weight cut-off (MWCO); the free drug molecules and solvents diffuse through the membrane into an external buffer solution following a concentration gradient. Although effective and gentle on the vesicular structure, dialysis is a slow process that requires significant solvent volumes and prolonged times.

8.5.2 Size Exclusion Chromatography (SEC)

To achieve a faster and more precise separation, Size Exclusion Chromatography (SEC), also known as gel filtration, is a methodology of choice. By exploiting the size difference between large liposomal aggregates and small free drug molecules, SEC allows for differentiated elution.

8.5.3 Determination of Encapsulation Efficiency

Purification is the prerequisite for calculating loading parameters. Nsairat et al. (2022) emphasize that, once the free fraction is separated, the drug content within the liposomes is quantified after lysing the vesicles with detergents (such as Triton X-100) and subsequent spectrophotometric or HPLC analysis. The Encapsulation Efficiency EE (%) is then calculated as:

EE (%) = (Mass of encapsulated drug /Total mass of drug added) * 100

This metric is fundamental for establishing the economic feasibility of the process and for ensuring that the administered therapeutic dose is consistent with established clinical protocols[232].

9.1 Exosomes

Despite the remarkable clinical success of liposomes, their synthetic nature inevitably imposes biological limitations, particularly in terms of immune recognition, long-term biocompatibility, and complex in vivo interactions. In this context, increasing attention has been directed toward exosomes, nanoscale extracellular vesicles (30–150 nm) naturally secreted by almost all cell types, as a biologically evolved alternative to synthetic nanocarriers.

Exosomes originate from the endosomal pathway and are released upon fusion of multivesicular bodies with the plasma membrane, carrying a complex cargo of lipids, proteins, and nucleic acids reflective of their parent cell. Unlike liposomes, exosomes possess an intrinsic biological identity, characterised by membrane proteins such as tetraspanins (CD9, CD63, CD81) and adhesion molecules that enable efficient cellular uptake, immune evasion, and targeted biodistribution.

These features position exosomes as nature's own delivery system, offering a compelling blueprint for the development of next-generation, biomimetic nanomedicines that seek to combine the controllability of liposomal systems with the biological sophistication of endogenous vesicles. The evolution of liposomal science has fundamentally informed our understanding of vesicular transport, yet the field is increasingly focusing on exosomes.

Exosomes are defined as endosome-derived nanovesicles, typically ranging from 40 to 160 nm in diameter.

9.2 Biogenesis and Structural Complexity

Unlike the spontaneous self-assembly of synthetic liposomes, exosome biogenesis is a complex, multi-step intracellular process. It involves the double invagination of the plasma membrane, resulting in the formation of early-sorting endosomes (ESEs) that mature into late-sorting endosomes (LSEs) and finally into multivesicular bodies (MVBs). These MVBs contain intraluminal vesicles (ILVs), which are released into the extracellular space as exosomes upon the fusion of the MVB with the cell surface.

This biogenic pathway, as reviewed by van *Niel et al*. (2018**)** and *Mathieu et al*. (2019), involves a sophisticated molecular machinery including the ESCRT (endosomal sorting complexes required for transport) proteins, the Rab GTPase family, and tetraspanins such as CD9, CD63, and CD81. These proteins not only facilitate vesicle formation but also serve as definitive biomarkers for exosomal identification[233,234].

9.3 Composition and Heterogeneous Cargo

The "cargo" of an exosome is significantly more heterogeneous than that of a synthetic liposome, reflecting the genomic and metabolic status of its parent cell. This cargo includes a diverse array of:

- Nucleic Acids: Genomic DNA, mitochondrial DNA (mtDNA), mRNA, and various non-coding RNA species such as microRNAs (miRNAs) and circular RNAs (circRNAs).
- Proteins and Lipids: Including transmembrane proteins, cytosolic enzymes, and specific lipids like cholesterol, sphingomyelin, and ceramides that maintain structural integrity and signaling capacity.

- Metabolites**:** Including amino acids and other small molecules that can be transferred to recipient cells to alter their biological response.

9.4 Physiological Roles and Clinical Translation

Exosomes function as critical mediators of both near and long-distance intercellular communication in both healthy and diseased states. They facilitate the transfer of functional biological information, influencing processes such as immune response regulation, angiogenesis, and metabolic reprogramming.

From a clinical perspective, exosomes offer revolutionary potential in two primary areas:

1. Diagnostics (Liquid Biopsy): Because exosomes are present in all biological fluids (e.g., blood, urine, breast milk), they serve as accessible reservoirs of disease-specific biomarkers. This allows for "liquid biopsies" that provide a multicomponent diagnostic readout for cancer and neurodegenerative diseases.

2. Therapeutics and Drug Delivery: Engineered exosomes are being developed to deliver therapeutic payloads with superior bioavailability and minimal immune clearance compared to synthetic systems. A notable clinical advancement is the development of "dexosomes" (dendritic cell-derived exosomes), which have been tested in clinical settings to induce antitumor immune responses in cancer patients.

10 Study of the interaction between Graphene Oxide and cholesterol using different artificial membrane models

10.1 Introduction

Graphene, a single layer of sp^2-hybridized carbon atoms derived from graphite, has gained remarkable attention as a promising nanomaterial since its discovery in 2004.[1] Due to its atomic structure, graphene possesses remarkable physico-chemical properties, including high electrical and thermal conductivity, excellent mechanical strength, large specific surface area and unique optical behaviors.[2] These properties allow graphene to be considered as an ideal material for various fields ranging from nanoelectronics to energy storage devices, catalysts, electrochemical sensors and biomaterials.[2] In the field of nanomedicine, graphene and its derivatives have emerged as new biomaterials that provide exciting opportunities for the development of a broad range of applications, including biosensors, nanocarriers for drug delivery, biomaterials for tissue engineering and regenerative medicine, probes for cell and biological imaging.[3-10] Graphene sheets can be transformed by physical and chemical modifications into graphene-related materials such as single and multilayered graphene, graphene oxide (GO) and reduced GO (rGO).[11] Graphene oxide (GO), an oxidized graphene derivative, is characterized by the presence of functional groups such as hydroxyl (-OH) and epoxy (C-O-C) groups bonded to the graphene plane, while the edges of the sheet are functionalized with carboxylic groups (-COOH).[2,12] Thanks to the presence of these oxygen-containing functional groups, GO can be easily dispersed in water producing homogeneous aqueous suspensions, while maintaining some typical properties of graphene, such as strength, high mechanical stiffness, transparency, and flexibility. The growing use of GO as biomaterial brings to light many important questions regarding its interaction mechanism with biological systems and its possible toxicity to organs, tissues and cells. Its amphiphilic nature, high surface-area-to-volume ratio, and oxygen-containing functional groups

enable strong interactions with biological macromolecules and cellular membranes.[13,14] Biological membranes, primarily composed of lipid bilayers, represent dynamic barriers that regulate the transport of molecules into and out of cells, maintain cellular homeostasis, and support signaling and structural integrity.[15] The interaction between GO and biological membranes is a complex process influenced by the physico-chemical properties of GO, including its size, shape, surface charge, functionalization and oxidation degree. For example, GO's abundant oxygen-containing groups contribute to its hydrophilicity and enable hydrogen bonding, electrostatic interactions, and even insertion into or adsorption onto lipid bilayers. Depending on its concentration and surface chemistry, GO can either interact with the membrane without causing significant disruption or, conversely, induce membrane destabilization, lipid extraction, or pore formation.[16] For this reason, understanding how GO can modulate the properties of biological membranes, in terms of permeability, fluidity and integrity, is of extreme importance, particularly in systems involving delicate membrane dynamics such as those found in reproductive cells.[17] As it is well known, sperm cells, immediately after ejaculation, are unable to fertilize the female gamete and they only reach their fertilizing ability after residing for hours within the female genital tract. Here they complete their functional maturation, called capacitation, under the guidance of endocrine signals from the surrounding female environment.[18] This process is mandatory and can be achieved both *in vivo* within the female tract or *in vitro*, by adding some specific components (BSA, bicarbonate) to the capacitating culture medium.[18] The capacitation begins with the alteration of membrane physico-chemical characteristics, the so called "lipid remodeling". In particular, the incubation of spermatozoa in the presence of Ca^{2+} and bicarbonate activates a cAMP/PKA-dependent pathway that leads to the rupture of membrane asymmetry with the consequent exposure of cholesterol on the outer side of plasma membrane. Once exposed, cholesterol is removed from the anterior area of sperm head by extracellular acceptors, thus promoting the increase of membrane fluidity and the ability to fuse with the outer acrosome membrane the oocyte zona pellucida.[18]

In previous works, a significant improvement in fertility has been found when sperm cells were exposed to different concentrations of GO under capacitating conditions, as recently published in swine[17] and bovine models[19,20], probably due to an extraction of cholesterol from the sperm membrane and thus an intense lipid membrane remodeling. In detail, low concentrations of GO (0.5 and 1 μg/mL) were able to induce an increase in the fluidity of the apical membrane of mammalian spermatozoa, accompanied by a reduction of cholesterol-to-phospholipidic ratio in a dose/dependent manner without causing any harmful effects.[21] In this way, cholesterol's extraction promoted a modification of the physico-chemical properties of the membrane which can positively influence the function of male gametes without losing the ability to interact physiologically with the environment of the female genital tract. Indeed, these alterations did not affect the integrity of the lipid raft microdomains, a critical feature for preserving essential membrane-mediated signaling pathways and functions.[21] Interestingly, these structural modifications were associated with improved *in vitro* sperm fertilizing ability in a more effective way than that promoted by the gold standard cholesterol extractor methyl-β-cyclodextrin, thereby opening a novel approach for the use of GO in enhancing assisted reproduction technologies.[22-24]

Building on this evidence, to investigate the underlying mechanisms of GO-induced membrane remodeling and its specificity for cholesterol extraction, the present study employs artificial lipid systems as simplified models of biological lipid membranes.[25] Liposomes are vesicular structures, spherical in shape, consisting of a phospholipid bilayer with a polar head group and a hydrophobic tail. Because of their amphipathic nature, they can uniquely encapsulate many substances, including drugs, nucleic acids, and imaging agents. They are widely used in pharmacological and biomedical fields, such as drug[26,27] and gene delivery[28], antimicrobial[29], but also for food and cosmetic applications.[30] Liposomes act as vehicles that can transport and control drug leakage.[31] Furthermore, due to their similarity to cell membranes, liposomes can serve as a well-established model for mimicking biological membranes, allowing for an artificial controlled environment, useful to

investigate lipid-GO interactions at the molecular level.[32,33,34] Specifically, small unilamellar vesicles (SUVs) consisting of 1,2-dioleoyl-*sn*-glycero-3-phosphocholine (DOPC) and cholesterol were used, mimicking the lipid composition of mammalian plasma membranes and offering a stable platform for biophysical and spectroscopic analyses. Two different fluorescent markers, such as 5(6)-carboxyfluorescein (CF) and Filipin III, were employed to probe GO effects on membrane structure and composition. CF was embedded into the aqueous core of the liposomes and changes in leakage kinetics from liposomes in the presence of GO provided insights into the stability and integrity of the lipid bilayer.[35] Filipin III marker, a polyene antibiotic known for its specific interaction with free cholesterol, was used to evaluate cholesterol availability and distribution within the liposomal membranes after GO treatment through fluorescence excitation spectra analysis.[36] Liposomes treated with GO were also characterized in terms of dimension, morphology and phase transition temperature by dynamic laser light scattering (DLS), atomic force microscopy (AFM) and differential scanning calorimetry (DSC) analyses. DLS and AFM measurements provided information on vesicle size distribution and possible aggregation or disruption phenomena induced by GO, while DSC analysis enabled assessment of phase transition temperatures, indicative of alterations in membrane thermotropic behavior and lipid packing density upon GO interaction. In addition, Raman spectroscopy analysis, with its high sensitivity to molecular vibrations, was used to analyze lipid chain conformation and packing order, and therefore the variation of fluidity of liposomes membrane treated with GO. In parallel, nuclear magnetic resonance (^{1}H NMR) spectroscopy was employed to quantify the DOPC and cholesterol content before and after GO treatment, directly assessing the extraction capability of GO from DOPC-cholesterol bilayers. Additionally, a droplet interface bilayer (DIB) was employed as a biomimetic membrane model to assess how GO influences passive water permeation, a critical process for cellular physiology. This technique exhibits demonstrated sensitivity in water transport, dependent on bilayer composition, structure, and interactions with exogenous molecules.[37-40] By integrating these complementary techniques, the study provides a detailed biophysical characterization of the interaction between GO and lipid membranes, with a particular

emphasis on cholesterol dynamics. The results contribute to a mechanistic understanding of how GO modulates membrane composition and organization in artificial membrane models, thereby offering valuable insight into its potential application in modulating cellular membranes in reproductive contexts.

Experimental Section

10.2.1 Materials

1,2-Dioleoyl-*sn*-glycero-3-phosphocoline and cholesterol were purchased from Avanti Polar Lipids Inc (Alabaster, AL, USA). Graphene oxide (GO) aqueous suspension 4 g/L was purchased from Graphenea, San Sebastian, Spain. The fluorescent probes 5(6)-carboxyfluorescein (CF), Filipin III solution, $CHCl_3$, $CDCl_3$, 3-aminopropyltriethoxysilane (APTES), Sephadex G-25, Triton X-100 and the salts used for the preparation of the buffer were purchased from Merck Life Science (MerkGaA, Darmstadt, Germany) and used without further purification processes. All chemicals used were of analytical grade and all experiments were conducted with freshly prepared solutions.

10.2.2 Instruments

Fluorimetric measurements have been carried out on Jasco FP-6500 spectrofluorimeter. UV-vis spectra have been recorded by a Varian Cary BIO UV-Vis spectrophotometer. The size and ζ potential values of GO flakes and liposomal systems were measured by using a 90Plus/BI-MAS ZetaPlus multiangle particle size analyzer (Brookhaven Instruments Corp., Holtsville, NY). AFM analyses were performed on Multimode 8 AFM (Bruker, Billerica, Massachusetts, US) with Nanoscope V controller, operating in TappingMode™ in air. GO flakes were characterized by the silicon tip RTESPA-300 (cantilever resonance frequency 300 kHz and nominal spring constant 40 N/m) while liposomes dimensions and morphology were evaluated with the silicon tip RTESPA-150 (cantilever

resonance frequency 150 kHz and nominal spring constant 5 N/m). Images of 512 × 512 pixels were collected with scan sizes of 1 μm × 1 μm and were elaborated using Nanoscope Analysis 1.8 software (Bruker, Billerica, Massachusetts, US). Nuclear magnetic resonance (NMR) spectra were recorded on a Bruker Avance 300 spectrometer with ^{1}H at 300.060 MHz. Proton chemical shifts were reported in parts per million (ppm, δ units). Differential scanning calorimetry was conducted using a DSC25 (TA Instrument, New Castle, DE 19720, USA) while all data collection and manipulation were carried out using TA Instrument TRIOS (version 5.6.0.87). Raman spectra were collected by confocal and high-performance Raman microscope (XploRA PLUS, HORIBA, Japan) with deep-cooled CCD detector technology. LabSpec 6.6.1.14 (Horiba, Japan) was employed to control, optimize and process the acquired data. Water permeability was measured using a DIB protocol as previously described.[41,42] In brief, the system consists of an inverted microscope (Nikon Eclipse Ti-S, halogen lamp) combined with two hydraulic micropipet manipulators (Narishige), supported on a vibration-isolated workstation (Newport), with an sCMOS camera (Andor Zyla) for real time recording of droplet formation and size changes. Experiments were performed at 30 °C in a temperature-controlled microchamber, and droplet size changes were analyzed with custom image analysis software.

10.2.3 Preparation of GO suspension

An aqueous solution of 4 g/L of graphene oxide was added to Ultrapure MilliQ water (electric resistance > 18.2 M/cm) from a Millipore Corp. model Direct-Q 3 system, to reach the desired concentration and bath-ultrasonicated for 30 min (37 kHz, 180 W; Elmasonic P60H, Elma). The concentration of GO was checked spectrophotometrically at λ_{max} of 230 nm while GO flake dimensions and ζ-potential were determined by using dynamic laser light scattering (DLS) on properly diluted aqueous suspension.

10.2.4 Activation and functionalization of substrates with GO

Silicon wafer SiO_2 substrates were functionalized with GO flakes, according to a published procedure[8,43], and used for the incubation of DOPC and DOPC-Chol liposomal formulations. All the employed substrates were previously washed and ultrasonicated in isopropanol and acetone. The polished side of the substrates was activated with a UV-ozone lamp (PSD-UV4 Novascan UV Ozone System Base model, Novascan Technologies, Boone, NC) for 30 min to increase the hydrophilicity of the surface and to improve the covalent binding of GO flakes. After the activation, the substrates were dipped for 1h in a 1M 3-(aminopropyl)triethoxysilane (APTES) solution in ethanol to form the silanized derivatives and then rinsed with ethanol to remove the excess of free APTES molecules. The last step consisted in pouring an aqueous suspension of 1 mg/mL GO on the APTES-functionalized substrates for 5 minutes, and spin coating each silicon wafer at 500 rpm, 800 rpm and 1600 rpm for 30s/each step.[44] This procedure was repeated by adding consecutive aliquots of the GO suspension until complete surface saturation with a uniform and thin GO layer was achieved. The GO-coated substrates were left to dry for 1h before washing with water to remove the unbound material. The final scaffolds were dried at room temperature overnight and characterized by AFM before use.

10.2.5 Preparation of liposomal systems

Small DOPC and DOPC-Cholesterol unilamellar vesicles were prepared by the thin film hydration method, following the procedure reported in the literature.[27,31,35] Briefly, desired amounts of DOPC and cholesterol were dissolved in chloroform to prepare DOPC-Cholesterol vesicles with different cholesterol molar contents of 0%, 5%, 10%, 15%, 20%, 30%, 40%, 50% and 60%. The lipid mixture was evaporated at 40°C under reduced pressure and then the obtained thin lipid film formed on the wall of the flask was rehydrated with MilliQ water or the appropriate buffer solution, depending on the type of experiment. After a hydration period of 30 min at room temperature, the lipid suspension

was extruded at room temperature and at a nitrogen pressure of ~ 500 psi with 5 passes through polycarbonate membranes (pore size 100 nm, Nucleopore Track-Etched Membranes, Whatman, GE, Healthcare, USA) mounted on an extruder (Lipex Biomembranes, Vancouver). The desired final lipid concentration was 4 mM for all experiments performed, with the exception of DSC analysis which requires higher lipid concentrations for optimal response.[45]

10.2.6 GO treatment of liposomes

To evaluate the effect of graphene oxide on DOPC and DOPC-cholesterol formulations, the prepared liposomes were subjected to two different GO treatment procedures reported below, depending on the type of analysis. In the first case, after extrusion, an appropriate amount of GO aqueous suspension was added to the liposomes to obtain a GO:cholesterol weight ratio of 2:1. The resulting GO-liposomal suspension was kept under magnetic stirring for 24 hours at room temperature. In the second case, liposomes were incubated with the SiO_2 substrate covalently functionalized with GO for 24 h under stirring. The latter treatment was chosen in order to promote the GO-bilayer interactions, having an easy method to remove excess GO from the dispersion and facilitate the analysis of treated phospholipid bilayers.

10.2.6 Dynamic Laser Light Scattering (DLS) analysis

The average hydrodynamic diameter and surface charge of DOPC and DOPC-Chol vesicles before and after GO treatment were determined by DLS analysis. For DLS measurements, the phospholipid thin films were rehydrated with MilliQ water and after extrusion incubated for 24h with GO-functionalized substrates. An aliquot of 50 µL of liposomes treated and untreated with GO was diluted in 1.5 mL MilliQ water for size measurements.

10.2.7 Atomic Force Microscopy

Atomic force microscopy (AFM) was carried out to investigate the morphology and size distribution of the DOPC and DOPC-Chol (50:50) liposomes before and after GO treatment. For AFM analysis, liposomes dispersed in MilliQ water were incubated for 24h with GO-functionalized SiO_2 substrates. After GO treatment, the AFM samples were prepared by depositing a drop of diluted suspension of liposomes on glass coverslips, followed by drying at room temperature overnight.

10.2.8 CF dye release experiments

DOPC and DOPC-Chol (50:50 mol %) vesicles encapsulated with 5(6)-carboxyfluorescein dye were prepared according to previous studies.[35] Briefly, the phospholipid thin film was hydrated with a 50 mM CF solution in a buffer prepared from NaCl (121.5 mM), Na_2HPO_4 (25.2 mM) and KH_2PO_4 (4.8 mM). The CF concentration was chosen in order to achieve a quenching concentration in the inner aqueous core. The unentrapped dye was removed by passing the liposomal suspension through a Sephadex G-25 column at room temperature. The liposome suspension was then diluted with an isosmotic buffer (578 mOsm – pH 7.4) from NaCl (174 mM), Na_2HPO_4 (105 mM), and KH_2PO_4 (20 mM) to obtain a final lipid concentration of 13.2 µM. For CF-leakage experiments an aliquot of GO aqueous suspension was added to the cuvettes maintaining a GO:cholesterol weight ratio of 2:1. The increase in fluorescence emission intensity at λ = 516 nm, using 490 nm as the excitation wavelength, due to the CF de-quenching which occurs after the leakage of the entrapped CF from the liposomes, was monitored over a period of 24 h.

10.2.9 ^{1}H NMR cholesterol quantification

Liposomal DOPC and cholesterol content before and after GO treatment was calculated by ^{1}H NMR spectroscopy. After the incubation with GO-functionalized substrates, an aliquot of 500 µL of the liposomes suspension was transferred into a glass vial and N_2 was used to remove water molecules

to not interfere in NMR analysis. The resulting dry lipids were then dissolved in 500 µL of deuterated chloroform ($CDCl_3$), containing 4 mM of DMSO used as internal standard.[46] The sample was stirred for 1h to ensure complete dissolution of the lipid components and transferred to an NMR tube. The calculations were assessed by comparing the integrated areas of different peaks of DOPC and cholesterol, as reported in the literature. In detail, the peak of cholesterol at 0.65-0.8 ppm, which corresponds to the three hydrogens of the methyl group at the junction between cholesterol's cyclohexyl and cyclopentane rings, and the DOPC's signal at 3.4 ppm, related to the nine hydrogens of choline methyls, were selected for the integration.[47,48] The DMSO peak at 2.6-2.7 ppm, coupled to the six methyl hydrogens, was used to calculate DOPC and cholesterol concentration by applying the following formula:[49]

$$C_{product} = C_{standard} \times \frac{I_{product} \times H_{standard}}{H_{product} \times I_{standard}}$$

where $C_{standard}$, $I_{standard}$ and $H_{standard}$ are the concentration of the prepared DMSO standard (4 mM), the integrated area of the internal standard and the number of hydrogen present on the standard, respectively. The $C_{product}$, $I_{product}$ and $H_{product}$ are the concentration, the integrated area of the product peak, and the number of hydrogens present in the product molecule, respectively.

10.2.10 Raman experiments

For Raman spectroscopy experiments, liposomal formulation treated with the GO suspension was analyzed. A drop of suspension of pure DOPC and DOPC-Chol liposomes before and after GO treatment was deposited on a silicon wafer substrate. For comparison, Raman spectra were also performed on DOPC and DOPC-cholesterol samples treated with a solution of methyl-β-cyclodextrin (MβCD) in order to obtain a cholesterol/MβCD weight ratio of 2:1. The Raman peaks were observed under a 532 nm laser with optical grating of 1800-line/mm. All Raman spectroscopic measurements were collected in the spectral range 2400-3400 cm^{-1}, with the same measurement parameters (10s

integration time, 15 accumulations and ~ 10 mW laser power at the sample surface) focusing on the surface with a 50× objective, to avoid laser-induced heating.

10.2.11 Differential Scanning Calorimetry

The thermal transition properties of the lipid vesicles prepared from DOPC and DOPC-Chol, before and after GO treatment, were measured by using DSC. The phospholipid thin film was rehydrated with MilliQ water to obtain a final lipid concentration of 14 mM. After the extrusion the DOPC and DOPC-Chol vesicles were treated with GO-functionalized substrate for 24h and then 25 µL of the liposomal suspension were loaded in a pre-weighed, hermetically sealed DSC pan. The reference pan was filled with the same components of the sample except the lipid phase. DSC experiments were performed by cooling the sample from 25°C to -30°C on a TA Instrument Discovery DSC25 (TA Instrument, New Castle, DE) and then the gel-to-liquid phase transition was monitored from -30°C to -10°C at a rate of 2°C/min. The entire procedure was repeated to ensure reproducibility. All data used for the analysis were taken from the heating scans, while cooling scans were used to check for hysteresis of the transitions. The thermal behavior of liposomes was evaluated by determining the main transition temperature (T_m) and the enthalpy of the transition (ΔH_m) expressed as J/g of liposomes in the sample.

10.2.12 Filipin III-cholesterol interaction study

Filipin III is a polyene macrolide antibiotic and the major component isolated from cultures of Streptomyces filipinensis. Due to its ability to fluoresce and bind cholesterol, Filipin has been widely used as a probe for cholesterol location in biological membranes.[50,51] Indeed, Filipin III marker is known to form complexes 1:1 with cholesterol and this interaction alters its absorption and

fluorescence spectra. For this reason, the analysis of its characteristic excitation spectra has been used to study the mechanism of interaction between GO and DOPC and DOPC-Chol liposomal bilayers, suggesting either cholesterol extraction or membrane remodeling induced by GO.[36] For fluorescence measurements with Filipin III, the phospholipid thin films of DOPC and DOPC-Chol, at different cholesterol molar contents, were rehydrated with MilliQ water to obtain the desired lipid concentration of 4 mM. After the extrusion and the incubation with GO-SiO_2 substrates for 24 h, an aliquot of liposomes was diluted in 2 mL of MilliQ water to reach a total lipid concentration of 100 μM. According to standardized procedure,[52] 5 μL of a stock solution 1.5 mM of Filipin III in DMSO was added in each quartz cuvette of lipid suspension until a final concentration of 3.9 μM was reached. The total amount of added DMSO never exceeded 0.25% (v/v) to avoid alterations in the phospholipid structure.[53] After an incubation time of 2 h in the dark for probe incorporation in liposomal bilayers, the excitation spectra were recorded in the spectral range of 250-400 nm to evaluate any changes in shape and intensity related to the interaction of Filipin III with different cholesterol concentrations. The liposomal samples already incubated with Filipin III marker and monitored by spectrofluorimetric analysis were filtered on Sephadex G-25 column pre-equilibrated with water. This additional filtration step allowed to remove any Filipin III aggregates present in the bulk liposomal dispersion and was performed to evaluate the ability of the probe to insert into the membrane in the presence and absence of cholesterol. After the Sephadex G-25 filtration, the fluorescence excitation spectra of filtered liposomal suspensions were again recorded.

10.2.13 Water permeability measurements

A droplet interface bilayer (DIB) forms when two lipid-coated aqueous microdroplets contact, creating a bilayer that closely mimics the structure of cell membrane.[54] For water permeability measurements, a pair of osmotically unbalanced aqueous droplets was created and dispensed into a

lipid-containing oil solution, each droplet pair respectively consisting of pure water and a 0.2 M sucrose solution with varying concentrations of GO. Each droplet was about 100 μm in diameter and was suspended in squalene solvent containing DOPC or DOPC–cholesterol mixtures. An osmotic imbalance between the droplets drives water transport across the DIB, enabling the assessment of membrane water permeability under various lipid compositions, as a function of GO concentrations. Each data point represents the mean of at least 20 independent measurements, with standard deviations shown as error bars. Additional details on the determination of water permeability are described in Supplementary Material (Text S1 and Figure S6).

10.3 Results and Discussion

10.3.1 Characterization of GO

The GO flakes were characterized in terms of concentration, size and surface charge. The concentration of the GO dispersed in Milli-Q water was determined by using UV-Vis spectroscopy which revealed a characteristic absorption band at 230 nm (Fig. 1A), related to the π- π* transitions for aromatic C-C bonds, along with a shoulder at 290-300 nm being the fingerprint of n- π* transitions of carbonyl groups.[55] Preliminary DLS and ζ-potential measurements evidenced that GO dispersion comprised large-sized (average diameter of 631.0 ± 23.2 nm) and negatively charged (-25.02 ± 1.65 mV) flakes, with a polydispersity index of 0.358 ± 0.014, reflecting a moderate size uniformity (see Supplementary Material S1). Atomic force microscopy (AFM) images (Fig. 1B) confirmed the sheet-like morphology of the GO flakes on the support surface with lateral dimension ranging from 150 nm to 3.0 μm, consistent with the polydispersity index and the presence of different subpopulations detected by DLS. The ultrasound vibrations of the bath sonicator, used to promote the GO dispersion, favored the breaking of the sheets into smaller and more irregularly shaped flakes. Individual GO sheets were clearly visible on the surface of GO-functionalized samples. Moreover, topographical AFM analysis was employed to assess the thickness of the GO flakes present onto coverslips surface.

The AFM images were processed using Nanoscope Analysis 1.8 software by tracing multiple cross sections on the GO-functionalized area and recording vertical distance values. The height profiles confirmed the presence of single layers of GO sheets with a thickness ranging from 0.8-1.7 nm, as reported in Figure 1C. Brighter and thicker ripples were also observed within the same sample, likely resulting from random interactions between the GO flakes and the APTES-activated surface, leading to the sheets overlapping.[8]

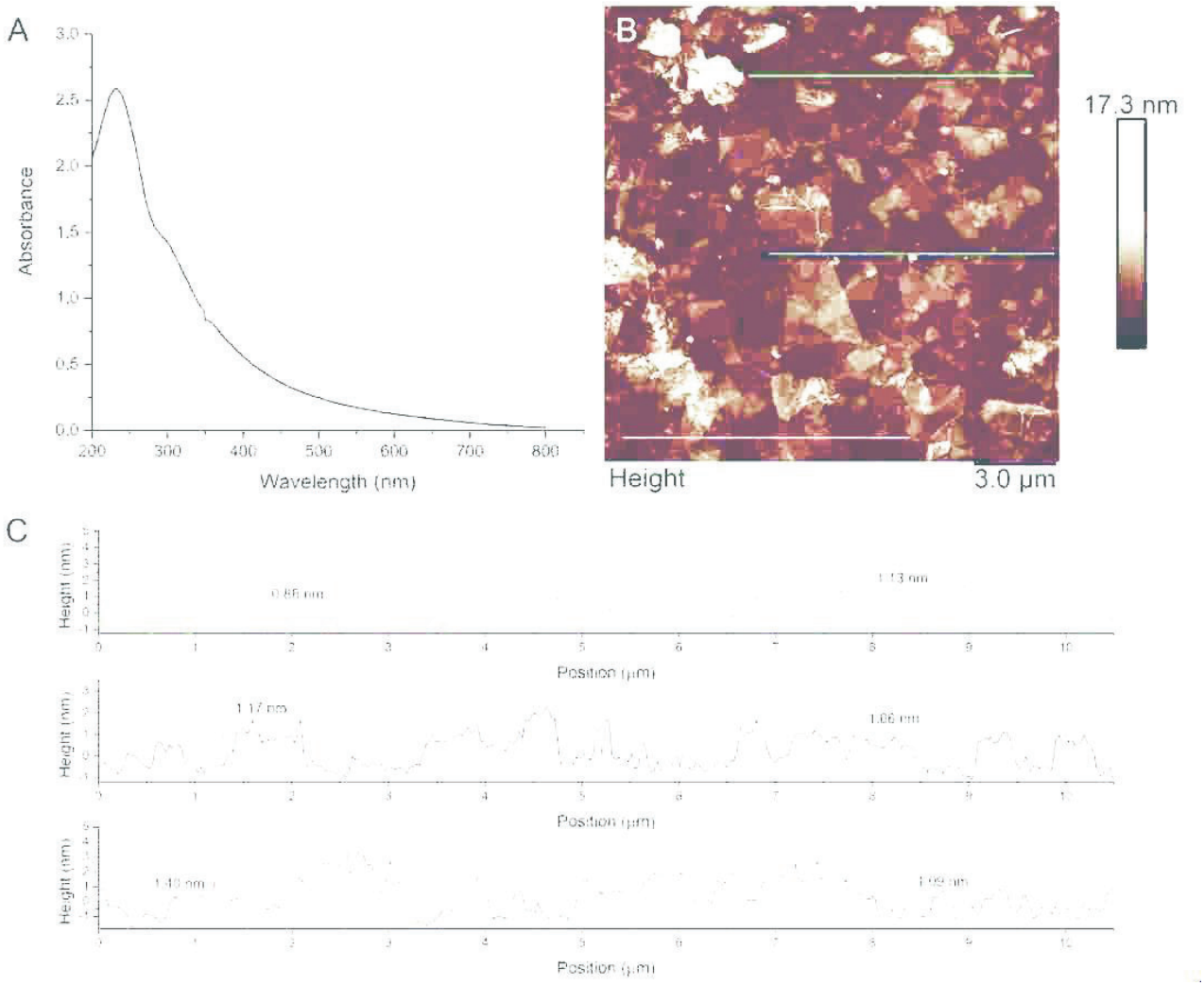

Figure 1. UV-Vis spectra of diluted GO aqueous dispersion (A). AFM image of surface topography (B) and corresponding height cross-sectional profiles (C) of GO-functionalized substrates.

10.4 Morphological characterization of liposomal systems

10.4.1 Particle size and zeta potential

To investigate the interaction between graphene oxide (GO) and cholesterol within artificial membrane models, the physico-chemical properties of DOPC and DOPC–cholesterol (DOPC-Chol) liposomes were analyzed. Dynamic light scattering (DLS) and ζ-potential measurements were performed to evaluate the size distribution and surface charge of DOPC and DOPC-Chol liposomes before and after GO treatment. Indeed, the characterization of liposomal size and zeta potential is essential to understand the structural and surface properties of lipid bilayers and how these are influenced by cholesterol content and external agents such as GO. In DOPC-based liposomes, the mean diameter reflects membrane fluidity and packing, while the zeta potential provides information on surface charge, which influences colloidal stability and membrane interactions. Firstly, the effect of cholesterol on DOPC liposomes dimension was investigated by varying the cholesterol molar ratio from 0% to 60%. DLS analysis revealed that pure DOPC liposomes showed a mean diameter of 101.1 ± 0.7 nm. Upon the addition of increasing cholesterol content, liposome size increased in a non-monotonic manner, as reported in Table S1. This trend reflects the complex role of cholesterol in modulating membrane structure, as already described in previous literature.[56-59] At low cholesterol concentrations, the insertion of cholesterol between lipid chains close to the head groups of phospholipid molecules can disrupt the regular packing of lipid chains, creating inter-lipid spacing and resulting in membrane expansion. As cholesterol content increases further, it enhances membrane rigidity by intercalating among hydrocarbon chains, increasing chain packing and reducing membrane fluidity, which in turn can influence the curvature and packing of the bilayer, contributing to vesicle size enlargement.

To explore the influence of GO on liposomal systems, the mean diameter and ζ-potential of DOPC and DOPC-Chol (50:50 mol/mol) liposomes were assessed before and after GO exposure (Table 1). As stated before, pure DOPC liposomes exhibited a mean diameter of 101.1 ± 0.7 nm and a surface

charge of -31.90 ± 6.86 mV, indicating a stable and negatively charged vesicle population.[60] The incorporation of 50% cholesterol led to a size increase to 122.0 ± 1.3 nm and a slightly less negative ζ-potential of -27.98 ± 3.60 mV, consistent with cholesterol's ability to modulate fluidity and reduce membrane surface charge. Indeed, the introduction of cholesterol into DOPC membranes generally leads to a slight reduction in the magnitude of the negative zeta-potential, as cholesterol disrupts the regular arrangement of charged phospholipid head groups, reduces the overall membrane surface charge density and decreases the mobility of the first few methylene groups within the phospholipid fatty acid chains. Upon addition of GO, the mean diameter increased notably to 119.2 nm for DOPC+GO and to 158.0 nm for DOPC-Chol + GO samples, suggesting interactions between GO flakes and the liposomal membranes. Considering these results, GO interacts with both types of liposomes, leading to vesicle enlargement likely due to surface adsorption or partial wrapping of GO flakes on liposomal surface. Correspondingly, ζ-potential values became slightly less negative in DOPC+GO (-26.73 ± 5.31 mV), while DOPC-Chol + GO maintained a relatively more negative charge (-29.10 ± 4.44 mV), suggesting differential interaction between GO and cholesterol-containing liposomes.

Table 1. Hydrodynamic diameters and ζ-potential values obtained for the DOPC and DOPC-Chol 50:50 mol/mol liposomes before and after GO exposure. Data represent the mean ± standard deviation of at least three independent measurements.

Liposomal system	Mean diameter	ζ- potential
DOPC	**101.1 ± 0.7 nm**	**-31.80 ± 6.86 mV**
DOPC + GO	**119.2 ± 4.8 nm**	**-26.73 ± 5.31 mV**
DOPC-Chol	**122.0 ± 1.3 nm**	**-27.98 ± 3.60 mV**
DOPC-Chol + GO	**158.0 ± 7.4 nm**	**-29.10 ± 4.44 mV**
GO flakes	**631.0 ± 23.2 nm**	**-25.02 ± 1.65 mV**

10.4.2 AFM analysis of liposomes

Atomic Force Microscopy (AFM) represents a powerful technique for investigating nanoscale interactions and morphological changes in lipid-based systems. In this work AFM was employed to obtain high-resolution topographical imaging for assessing the impact of GO exposure on liposomal integrity and stability. Figure 2 shows, as an example, the AFM 2D height channel of diluted DOPC-Chol liposomes before and after GO treatment. The resulting images revealed the formation of bilayer films in the background, spread over the surface, particularly for the DOPC-Chol + GO sample. This evidence reflects the tendency of liposomes to rupture and spread, forming supported lipid bilayers when deposited onto solid substrates. Although this behavior poses challenges for liposomal imaging, intact vesicles are still present and are clearly visible on the top of these fused bilayers. DOPC-Chol liposomes maintained their characteristic globular morphology and structural integrity despite the interaction with the GO surface, as already demonstrated by Huang et al.[61] In their work the interaction between liposomes and graphene oxide was evaluated on the basis of Cryo-TEM measurements, allowing to demonstrate that DOPC liposomes were able to be adsorbed as intact liposomes near the hydrophilic edge of the GO sheets. The cross-sectional height profiles of individual vesicles and the particle analysis of several images using Nanoscope software showed that the mean diameter falls in the range of 80-120 nm for both treated and untreated DOPC-Chol liposomes, in quite good agreement with DLS data.

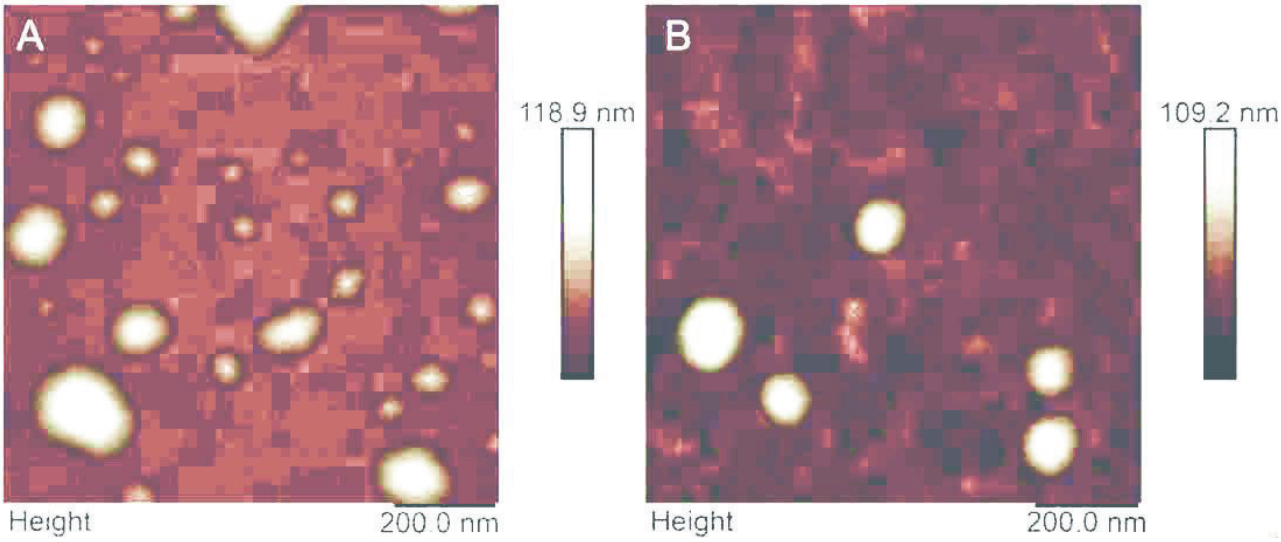

Figure 2. AFM micrographs of DOPC-Chol liposomes before (A) and after (B) treatment with GO-functionalized SiO_2 substrate.

10.4.3 CF leakage experiments

To evaluate the effect of GO on liposomal membrane stability, CF release experiments were conducted on DOPC and DOPC-Chol (50:50 % mol) liposomes. CF, a self-quenching fluorescent dye, was encapsulated within aqueous core of liposomes and its release upon membrane destabilization in presence and absence of GO solution was monitored fluorimetrically. The leakage of CF into the external medium leads to dilution and dequenching of the dye, producing a measurable increase in fluorescence intensity. Figure 3 presents the kinetic profiles of spontaneous release of CF from DOPC and DOPC-Chol vesicles, with the values of the calculated first-order rate constants, k_{obs}, for each system listed in Table 2.

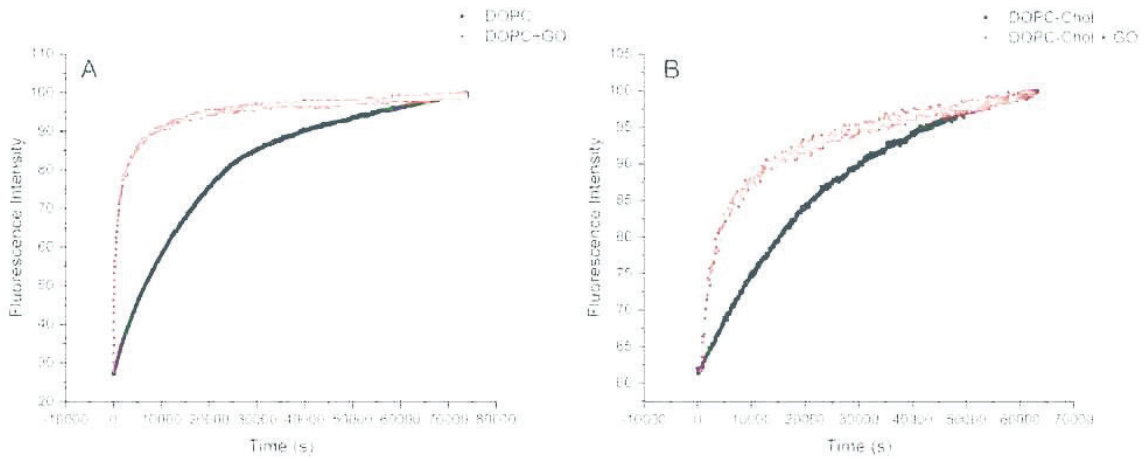

Figure 3. Representative kinetic profiles of the spontaneous CF release at 25°C from DOPC (A) and DOPC-Chol (B) liposomes in presence (red curve) and absence (black curve) of GO solution.

Table 2. First order rate constants, k_{obs}, for the CF release from the investigated liposomal systems with and without GO.

Liposomal system	**$k_{obs} \times 10^{-4}$ (s^{-1})**
DOPC	**0.627 ± 0.035**
DOPC + GO solution	**2.967 ± 0.096**
DOPC-Chol	**0.386 ± 0.044**
DOPC-Chol + GO solution	**3.292 ± 0.050**

The results clearly show that untreated DOPC liposomes exhibited a relatively low leakage rate, indicating good membrane stability under baseline conditions. Upon GO exposure, the same DOPC liposomes displayed a significant increase in CF release, with k_{obs} rising from 0.627×10^{-4} s^{-1} to 2.967×10^{-4} s^{-1}. This nearly five-fold enhancement indicates that GO reduces the stability of pure DOPC membranes, likely due to strong interactions with the phospholipid bilayer that promote membrane permeabilization to CF. As reported in Table 2, the incorporation of cholesterol into the DOPC

membrane led to a noticeable stabilizing effect. DOPC-Chol liposomes exhibited a lower CF release rate (k_{obs} 0.386 × 10^{-4} s^{-1}) when compared to pure DOPC, consistent with the known condensing and ordering effects of cholesterol, which reduces bilayer fluidity and leakage of entrapped dyes.[62] Interestingly, when these cholesterol-containing liposomes were treated with GO solution (GO:cholesterol weight ratio of 2:1), the kinetic constant dramatically increased to 3.292 × 10^{-4} s^{-1}, even exceeding the GO-treated pure DOPC liposomal system. A comparison of the ratios between the kinetic constants was evaluated to provide further insights into the destabilizing effect of GO towards liposomal systems. Indeed, a k_{obs} ratio of 4.73 between the DOPC+GO and DOPC was calculated, confirming a substantial increase in membrane permeability due to GO interaction. Even more pronounced was the effect observed in the DOPC-Chol system, where the ratio between the k_{obs} of GO-treated and untreated liposomes reached 8.53. This result suggests that GO may interact more effectively or differently with the cholesterol-containing bilayer, leading to a greater destabilization than in the cholesterol-free system. Indeed, as reported by Seth et al., the presence of cholesterol in lipid monolayers facilitates adsorption and attachment of GO, thanks to a favorable interaction between the hydrophilic part of cholesterol and the polar part of GO.[63] Nevertheless, despite the pronounced destabilizing effect of GO, liposomes remained structurally intact over the 24-hour monitoring period. Indeed, this was confirmed by the addition of Triton X-100 to the liposomes-containing cuvettes after reaching the CF release plateau. TX-100 is a non-ionic surfactant known to completely solubilize lipid bilayers, leading to total release of any encapsulated content.[64] Upon TX-100 addition, a further marked increase in fluorescence was recorded (Supplementary Material, Figure S2), indicating that a significant fraction of CF was still retained inside the vesicles after the interaction with GO, prior to their complete disruption following the addition of Triton X-100. This final fluorescence rise confirms that GO does not fully rupture liposomes but rather increases their permeability, allowing for partial leakage while preserving the overall vesicular structure, as also supported by AFM analysis.

10.4.5 Raman spectroscopy analysis

Raman spectroscopy offers a highly sensitive, non-destructive method for characterizing lipid membranes and probing molecular interactions at the nanoscale, making it particularly well-suited to study the effects of GO on cholesterol-containing DOPC liposomes.[65,66] In this study, it was employed to assess how GO exposure alters liposomal packing, membrane fluidity, and cholesterol distribution. Indeed, Raman spectroscopy enables the detection of molecular interactions and structural perturbations within lipid bilayers by focusing on specific regions of the vibrational spectrum. In particular, the range between 2700 cm^{-1} and 3050 cm^{-1} is highly informative for examining the structural and dynamic characteristics of phospholipid acyl chains. Within this region, three prominent peaks are typically observed: the symmetric C-H stretching of methylene ($-CH_2$) groups around 2850 cm^{-1} ($\nu_s(CH_2)$), the asymmetric C-H stretching of methylene groups near 2890 cm^{-1} ($\nu_a(CH_2)$), and the symmetric C-H stretching of terminal methyl ($-CH_3$) groups at approximately 2930 cm^{-1} ($\nu_s(CH_3)$).[67] Raman spectra were analyzed by applying a Lorentzian deconvolution to these key vibrational modes in C-H stretching region, to resolve overlapping peaks into individual components, as shown in Figure 4.

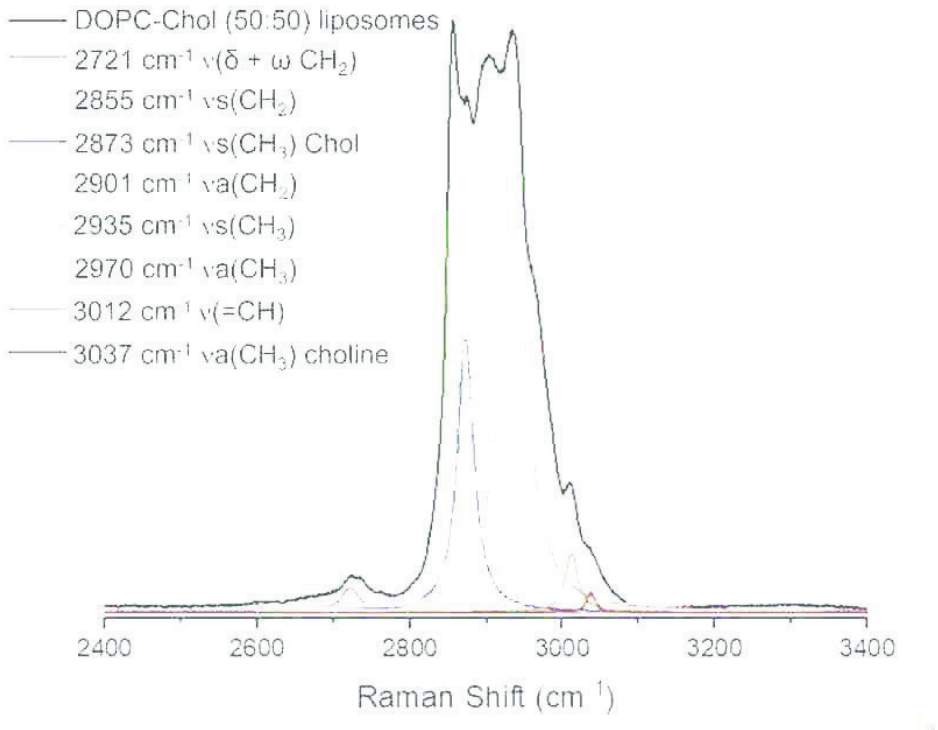

Figure 4. Lorentzian deconvolution of Raman spectra from 2400 cm^{-1} to 3400 cm^{-1} of DOPC-Chol liposomes with the corresponding peak assignments. Mode assignments: □a (asymmetric stretching), □s (symmetric stretching), δ (scissoring) and ω (wagging).[65,67-69]

The membrane fluidity was quantified using intensity ratios such as $I_{vs(CH3)}/I_{vs(CH2)}$ and $I_{vs(CH3)}/I_{va(CH2)}$, that serve as sensitive indicators of lipid packing density and acyl chain order.[70] Indeed it is worth noting that the asymmetric methylene (-CH_2) stretching vibration, typically located at 2890 cm^{-1}, is associated to a notable shift to ca. 2900 cm^{-1} for the highly unsaturated DOPC.[65] The interaction of GO with liposomal lipid membranes can influence the conformation and packing of lipid tails, producing detectable variations in these spectral features. In particular, a marked increase in $I_{vs(CH3)}/I_{vs(CH2)}$ value indicates an increase in rotational disorder and freedom of motion, while an increase in $I_{vs(CH3)}/I_{va(CH2)}$ value is related to a decrease in intramolecular (gauche/trans) and intermolecular (chain packing) interactions. In addition, the ~2872 cm^{-1} band $I_{vs(CH3)\ Chol}$, due to symmetric stretching vibrations from the methyl groups, is specific for cholesterol and is absent in pure DOPC Raman spectrum.[71,72] Therefore the $I_{vs(CH3)\ Chol}/I_{vs(CH2)}$ ratio was used to monitor changes

in cholesterol content before and after liposomal incubation with GO. The freshly prepared liposomal samples were deposited on SiO_2 wafer by simple drop-coating and dried at room temperature. Raman analysis was performed at the edge of the drop of DOPC and DOPC-Chol liposomes untreated and incubated with GO or methyl-β-cyclodextrin (MβCD), a known cholesterol extraction agent.[73,74]

It is worthnoting that the monomodal increase in those peak intensity ratio, connected with the increase in cholesterol percentage, cannot be discuss in terms of membrane fluidity since the presence of the band of the symmetric stretching vibrations from the methyl groups of cholesterol band at ≈ 2873 cm^{-1} interferes with the values of $I_{vs(CH3)}/I_{vs(CH2)}$ and $I_{vs(CH3)}/I_{va(CH2)}$ with respect to the not-cholesterol containing membranes. Instead, the differences in the Raman spectra of each liposomal system before and after treatment with GO or MβCD have been analyzed, and the peak intensity ratios have been calculated and reported in Figure 5.

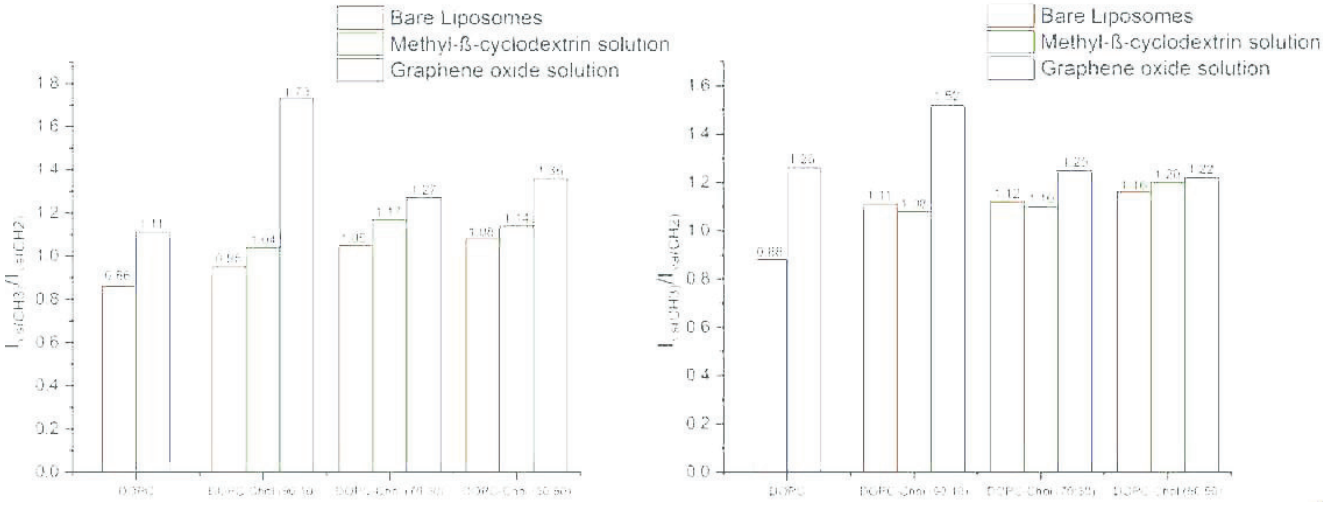

Figure 5. *Peak intensity ratios $I_{vs(CH3)}/I_{vs(CH2)}$ and $I_{vs(CH3)}/I_{va(CH2)}$ calculated from Raman spectra of the investigated liposomal systems treated and untreated with GO or MβCD.*

As shown in Figure 5, GO treatment led to a significant increase in the $I_{vs(CH3)}/I_{vs(CH2)}$ ratio across all cholesterol concentrations, with the most pronounced effect observed at 10% cholesterol (1.73). This suggests a strong effect of GO, even greater than that observed with MβCD, particularly effective at

the cholesterol concentration that most disrupt the packing of phospholipids in the membrane, i.e. 10% cholesterol sample, associated with an increase of inter-lipid spacing (see also section 3.2.1). Reminding the study of H.-J. Kaiser et al.,[75] it seems that at low cholesterol concentration the membrane evidences a liquid-disordered (Ld) phase, whereas at high cholesterol content acyl chains tend to pack into a liquid-ordered (Lo) phase, which exhibits several features of lipid rafts in cell membranes. This trend is also evident in the Raman spectra (Supplementary Material, Figure S3), which display notable changes in the spectral profiles within the 2700-3100 cm^{-1} range. GO-treated samples also showed higher $I_{vs(CH3)}/I_{va(CH2)}$ values with respect to not GO-treated and MβCD-added samples, reflecting a reduction in both intramolecular (gauche/trans) and intermolecular (lipid packing) interactions, while MβCD and control samples exhibited relatively stable values. These findings suggest that graphene oxide exerts a stronger influence on membrane packing compared to methyl-β-cyclodextrin, particularly considering that, at the applied concentration ratio (2:1 MβCD:cholesterol), only a modest effect has been previously reported in the literature for DPPC liposomes.[76]

To gain deeper insight into the underlying mechanism, the individual spectral contributions of cholesterol and phospholipids were quantitatively assessed. In particular, the ratio $I_{vs(CH3)\ Chol}/I_{vs(CH2)}$, was used to monitor the relative contribution of cholesterol to the bilayer and was reported in Figure 6. By using two bands, associated with cholesterol and lipid respectively, the ratio score is independent of absolute photon counts and allows to compare the effect of βMCD and GO at the different percentages of cholesterol.[77]

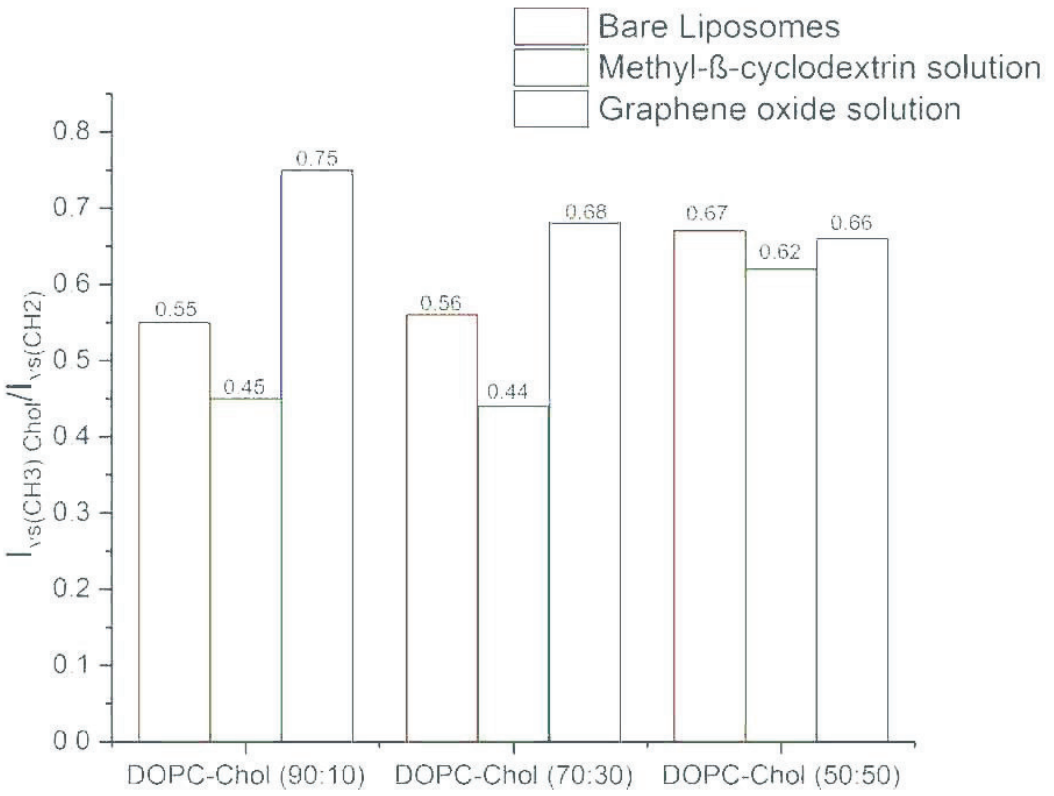

Figure 6. *Peak intensity ratio $I_{vs(CH3)\ Chol}/I_{vs(CH2)}$ calculated from Raman spectra of the investigated liposomal systems treated and untreated with GO or MβCD.*

Interestingly, while MβCD caused a decrease in the $I_{vs(CH3)\ Chol}/I_{vs(CH2)}$ ratio due to cholesterol removal, liposomal systems treated with GO showed increased values with respect to the controls, suggesting a distinct mechanism of action, that targets the phospholipid matrix rather than depleting membrane cholesterol. These findings indicate that GO has a potent, cholesterol-independent ability to reduce lipid packing and increase membrane fluidity in liposomal systems. This effect could be probably due to its amphiphilic nature, allowing interactions with both phospholipid and cholesterol components, as also demonstrated by complementary NMR and fluorescence analysis (see below paragraph 3.5 and 3.7 respectively).

To further confirm the strong affinity of GO for DOPC, the membrane fluidity of liposomes composed by only DOPC phospholipids was also evaluated. As reported in Figures 5, even in cholesterol-free

DOPC liposomes, GO dramatically enhanced membrane fluidity (e.g., $I_{vs(CH3)}/I_{vs(CH2)}$ increasing from 0.86 in untreated liposomes to 1.11 after GO exposure), indicating that GO interacts strongly with the phospholipid bilayer regardless of cholesterol presence. This strong interaction between GO and membrane phospholipids is also well-documented in the literature. Several studies have already demonstrated that GO can interact directly with the lipid bilayer, disrupting its organization and promoting lipid extraction or favoring porous formation with negligible damage to the membrane integrity. For instance, Zhang et al. have described how GO with a low degree of oxidation is capable of inserting into the lipid membrane through a synergistic mechanism of weak interfacial interactions, resulting in lipid destabilization, whereas GO with a high oxidation degree does not affect DOPC membrane integrity.[78] Similarly, another study provides further evidence that GO can compromise membrane integrity of lipid vesicles through strong interactions with phospholipids, reinforcing the hypothesis that its effects on membrane fluidity are primarily driven by direct interaction with lipid components rather than cholesterol extraction.[32] On the contrary, Huang et al. evidenced, through ITC measurements, that DOPC liposomes adsorb onto GO flakes prevailingly as intact liposomes at the GO edges by exploiting water mediated hydrogen bonding interactions.[61] Together with the increase of $I_{vs(CH3)}/I_{vs(CH2)}$, a sharp rise in Raman intensity ratio $I_{vs(CH3)}/I_{va(CH2)}$ was registered (from 0.88 to 1.26), indicative of reduced intramolecular (gauche/trans) and intermolecular (chain packing) interactions.

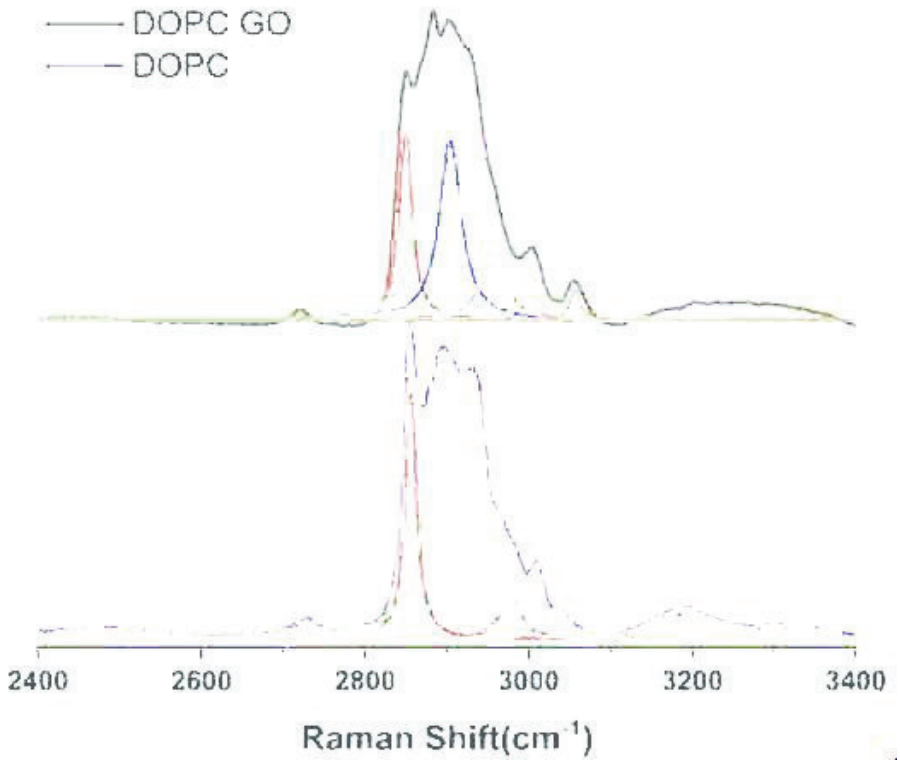

Figure 7. *Raman spectra of DOPC (black line) and GO-treated DOPC liposomes (violet line) with Lorentzian deconvolutions recorded at 2400-3400 cm^{-1} range. Mode assignement: symmetric stretching of the terminal methyl (light blue band); symmetric methylene stretching (red band); asymmetric methylene stretching (green and blue bands).*

Furthermore, Figure 7 confirmed that the spectral profiles of DOPC liposomes underwent significant changes following GO treatment, particularly in the C-H stretching region which is highly sensitive to the conformational state of unsaturated phospholipids such as DOPC.[65] In untreated DOPC liposomes, the asymmetric C-H methylene stretching band is centered at ~2895 cm^{-1}, whereas upon exposure to GO, this feature is redistributed into two components at 2884 and 2906 cm^{-1}. This splitting and frequency shifts reflect a change in the molecular environment of lipid chains induced by GO. According to Giancaspro et al., the frequency of the asymmetric C-H methylene stretching mode serves as an indicator of conformational order and interchain coupling: an upshift of this band corresponds to a greater number of isolated methylene groups, caused by reduced interactions with adjacent methylene groups, and thus indicates enhanced chain decoupling.[65] The appearance of two different bands can be interpreted in terms of the existence of two different neighboring for phospholipidic chains in the DOPC+GO spectra. Indeed, the higher-frequency band highlights the

presence of regions where phospholipids are characterized by reduced interchain interactions and increased lipid chain disorder, consistent with a GO-induced perturbation of membrane packing. In addition, the disappearance or shift of the characteristic choline C-H stretching band at 3037 cm^{-1} to approximately 3057 cm^{-1} following GO treatment, further supports the hypothesis of strong GO-lipid headgroup interactions. Literature evidence also indicates reduced GO activity in liposomes containing negatively charged lipids, likely due to electrostatic repulsion.[79] The strong Raman response observed here may be attributed to the amphiphilic nature of GO, which enables simultaneous hydrophobic and hydrophilic interactions with the phospholipids even in the absence of cholesterol – a mechanism consistent with findings reported in previous studies.[80,63] Overall, Raman spectroscopy revealed that GO has a pronounced impact on lipid membrane structure, enhancing fluidity through mechanisms distinct from conventional cholesterol-extracting agents like MβCD.

10.4.7 NMR quantification

^1H NMR spectroscopy was employed to quantitatively assess the phospholipid and cholesterol content in DOPC and DOPC-Chol liposomes before and after treatment with GO. The analysis was carried out on liposomal samples treated and untreated with GO for 24h, dried with N_2 and then dissolved in deuterated chloroform ($CDCl_3$), using 4 mM DMSO as an internal standard. The samples were stirred for 1 hour to ensure full dissolution of all lipid components, then transferred into NMR tubes for measurement. Quantification was based on the integration of specific proton signals characteristic of DOPC and cholesterol, as reported in Figure S4 (Supplementary Materials). In particular, the methyl group signal of cholesterol located at 0.65–0.8 ppm, corresponding to three hydrogens at the junction of the cyclohexyl and cyclopentane rings, and the choline methyl groups signal of DOPC at 3.4 ppm, associated with nine hydrogens, were used for the calculations. The DMSO signal at 2.6–2.7 ppm, corresponding to six methyl hydrogens, served as the internal reference

for the concentration determination. This method allowed to compare lipid component concentrations across different liposomal systems.

Table 3. DOPC and Cholesterol concentration values obtained from ^{1}H NMR spectra for the different liposomal systems before and after GO treatment.

Liposomal system (nominal ratio)	[DOPC]	[Chol]	DOPC/Chol molar ratio	DOPC/Chol w/w ratio
DOPC	**4 mM**	**-**		
DOPC + GO	**2.89 mM**	**-**		
DOPC-Chol (95:5)	**4.29 mM**	**0.29 mM**	**94/6**	**96.8/3.2**
DOPC-Chol (95:5) + GO	**2.50 mM**	**0.10 mM**	**96/4**	**98.1/1.9**
DOPC-Chol (90:10)	**3.65 mM**	**0.31 mM**	**92/8**	**96.0/4.0**
DOPC-Chol (90:10) + GO	**2.92 mM**	**0.25 mM**	**92/8**	**95.9/4.1**
DOPC-Chol (80:20)	**2.25 mM**	**0.45 mM**	**83/17**	**91.0/9.0**
DOPC-Chol (80:20) + GO	**1.4 mM**	**0.43 mM**	**76/24**	**86.9/13.1**
DOPC-Chol (50:50)	**2 mM**	**2.3 mM**	**46/54**	**63.9/36.1**
DOPC-Chol (50:50) + GO	**1 mM**	**1.46 mM**	**41/59**	**58.2/41.8**

The results, obtained from NMR spectra and listed in Table 3, confirmed the expected composition of the initial formulations and revealed a notable variation in the DOPC and cholesterol concentrations upon exposure to GO. In the case of pure DOPC liposomes, the DOPC concentration decreased from 4 mM in untreated samples to 2.89 mM after GO treatment, indicating partial extraction or uptake of the phospholipid component due to interaction with GO. In the other DOPC-Chol systems the data evidence that GO interacts with both phospholipids and cholesterol, promoting a remodeling of both components from the bilayer. In particular, for the DOPC-Chol 95:5 and 90:10

formulations, both DOPC and cholesterol concentrations decreased after GO treatment, although this reduction did not significantly alter the DOPC/chol molar ratio. As cholesterol concentration increases, i.e. DOPC-Chol 80:20 and 50:50 samples, the effect of GO becomes progressively more evident, even leading to an increase in the percentage of cholesterol in the GO-treated samples. This apparent enrichment is likely due to a preferential interaction of GO with DOPC rather than with cholesterol and therefore the achievement of a more drastic reduction of the DOPC concentration, which causes an altered DOPC-cholesterol balance when compared with the starting material. This suggests a strong remodeling action of GO in cholesterol rich membranes, likely mediated by both hydrophobic and polar interactions with the bilayer components and water. This apparent decreased ratio of DOPC/cholesterol in the bilayer on addition of GO is quite unexpected, overall if we compare the effect of GO with that of the well known cholesterol extractor βMCD.

10.4.8 DSC analysis

Differential Scanning Calorimetry (DSC) is a widely used technique to characterize the thermotropic behavior of liposomal systems. Indeed, phospholipid membranes can adopt different structural phases – gel or liquid crystalline – depending on temperature.[81] The transformation between these states, referred to as the gel-to-liquid crystalline phase transition, is defined by a characteristic transition temperature (T_m) and an associated enthalpy change (ΔH_m). In the gel phase, occurring below T_m, the aliphatic chains of phospholipids are tightly packed, aligned parallel in the *trans* conformation, and exhibit low mobility. When the temperature exceeds T_m, the system enters the liquid crystalline phase, where the chains become more disordered, gain mobility, and adopt *gauche* conformation. In particular, the transition from an ordered to a disordered arrangement requires the absorption of heat, which appears as an endothermic peak in the DSC thermogram, the area of which can be integrated to calculate the variation of enthalpy. The value of T_m reflects the packing stability of the bilayer: an increase in T_m is generally associated with tighter lipid packing and reduced fluidity, while a decrease

in T_m indicates membrane destabilization and increased acyl chain mobility. The transition enthalpy (ΔH_m) measures the cooperativity of the phase transition and the number of lipids participating; higher values indicate a more ordered and homogeneous bilayer, whereas lower values suggest reduced cooperativity or partial lipid loss. In the present work, DSC analysis was carried out on pure DOPC and DOPC-Chol liposomes, both treated and untreated with GO prior to being analyzed. Representative DSC profiles are presented in Figure 8, and all thermodynamic parameters are listed in Table 4.

Table 4. Thermotropic parameters obtained from the DSC thermograms of DOPC and DOPC-Chol liposomes, both treated and untreated with GO.

Liposomal system	T_m (°C)	ΔH_m (J/g)
DOPC	**-17.85**	**0.3791**
DOPC + GO	**-17.97**	**0.3492**
DOPC-Chol (95:5)	**-18.42**	**0.3211**
DOPC-Chol (95:5) + GO	**-18.99**	**0.3185**
DOPC-Chol (90:10)	**-19.15**	**0.2609**
DOPC-Chol (90:10) + GO	**-19.28**	**0.2511**
DOPC-Chol (80:20)	**-21.44**	**0.0821**
DOPC-Chol (80:20) + GO	**-21.80**	**0.0199**
DOPC-Chol (50:50)	**n.d.**	**n.d.**
DOPC-Chol (50:50) + GO	**n.d.**	**n.d.**

As shown in the DSC thermograms reported in Figure 8A, the liposomal bilayer of pure DOPC liposomes displayed a typical sharp peak at -17.85 °C, consistent with those reported in literature.[82]

This low transition temperature value is due to DOPC's unsaturated acyl chains, which introduce kinks in the hydrocarbon chains and prevent tight packing, thereby stabilizing the liquid-crystalline phase even at relatively low temperatures.

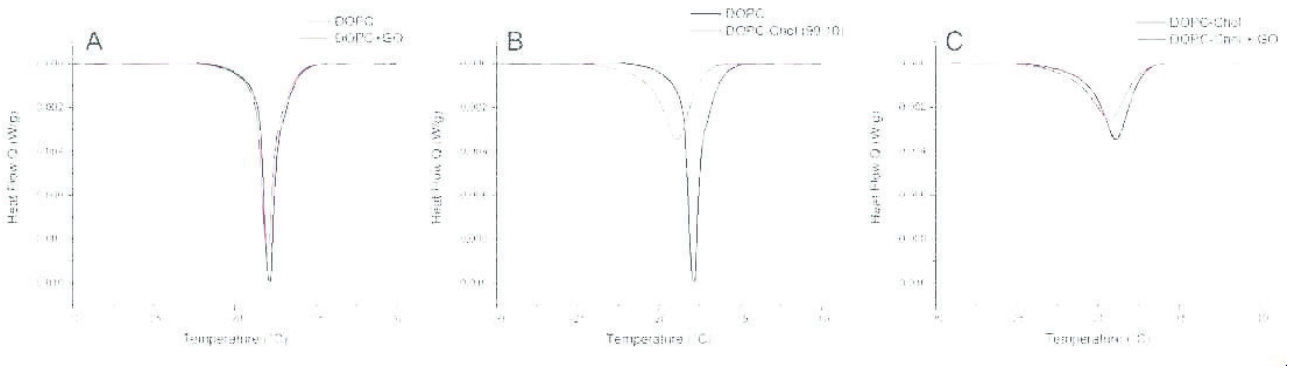

Figure 8. Representative DSC profiles of the gel-to-liquid state transition of pure DOPC vs. DOPC+**GO** (A), DOPC vs. DOPC-Chol (90:10) (B), and DOPC-Chol (90:10) vs. DOPC-Chol (90:10) +**GO** (C).

For pure DOPC liposomes, GO exposure led to a slight decrease in T_m (from -17.85°C to -17.97°C) and a more noticeable reduction in ΔH_m (from 0.3791 J/g to 0.3492 J/g). This change can be attributed to lipid extraction from the bilayer and loss of cooperative lipid packing, as also confirmed by NMR data (Table 3). Untreated DOPC-Chol liposomes showed a significant broadening of transition peaks with increasing cholesterol concentrations when compared to pure DOPC liposomes, as shown in Figure 8B. Furthermore, a progressive and linear reduction in ΔH_m with increasing cholesterol content was also registered (Figure S5), in agreement with literature reporting cholesterol's ability to disrupt the sharp, cooperative gel-liquid crystalline transition of phospholipids.[59,83] This role as a fluidity buffer results in broadening and/or suppression of the main transition, along with a reduction in the associated enthalpy variation. In our samples, ΔH_m decreased from 0.3211 J/g at 5 % mol cholesterol [DOPC-Chol (95:5)] to 0.0821 J/g at 20 % mol cholesterol [DOPC-Chol (80:20)]. Indeed, for the DOPC-Chol (50:50) sample, no DSC peak could be detected and, consequently, T_m and ΔH_m values could not be calculated. This finding is consistent with the well-documented effect of high cholesterol levels (> 40% w/w) in completely abolishing the cooperative main transition of phospholipid bilayers.[59] A direct comparison between untreated and GO-treated DOPC-Chol samples reveals that

GO exposure generally caused further decreases in ΔH_m and small shifts in T_m (Figure 8C and S5), with the extent of change related to the variation in lipid composition induced by GO. For example, at low cholesterol contents (DOPC-Chol 95:5 and 90:10), the enthalpy reduction observed after GO treatment is moderate but consistent with NMR data of relative content ratio, which indicate a parallel decrease in both DOPC and cholesterol concentrations without significant alteration of their molar ratio. For samples with higher cholesterol fractions (i.e., DOPC-Chol 80:20), the reduction in ΔH_m after GO exposure is more pronounced, from 0.0821 J/g to 0.0199 J/g, corresponding to a drop in DOPC content consistent with a relative increase, with respect to the theoretical value, of cholesterol/DOPC ratio due to lipid removal. Such compositional changes also contribute to the further lowering of Tm, indicating a reduced degree of cooperative lipid packing. These observations may be attributed to the ability of GO to interact with liposomal systems, weakening the cohesive forces between lipid molecules and thereby reducing the amount of thermal energy required to transition from an ordered lipid arrangement to a more disordered state. These variations confirmed that GO interacts with both phospholipids and cholesterol, as also demonstrated by Raman and NMR analyses, altering the relative lipid composition (see Section 3.5) and thereby influencing bilayer thermotropic behavior.

10.4.6 Cholesterol detection by Filipin III

Filipin III is a well-established fluorescent polyene probe that binds unesterified cholesterol with a 1:1 stoichiometry, both in aqueous solution and when complexed to membrane sterols. For this reason, it is widely used to detect and quantify accessible cholesterol molecules in model and cellular membranes.[84,85] In this work, the analysis of Filipin III excitation spectra has been used to better understand the mechanism of interaction of GO with cholesterol present in the liposomal membranes. For this purpose, we first verified the GO ability to not quench Filipin III fluorescence under the experimental conditions used, thereby allowing us to interpret subsequent changes in Filipin III signal

as arising from alteration in Filipin-cholesterol interactions rather than from direct GO quenching. Preliminary experiments were conducted by incubating liposomal formulations at different cholesterol concentrations with Filipin III probe and recording the excitation spectra in the spectral range of 250-400 nm.

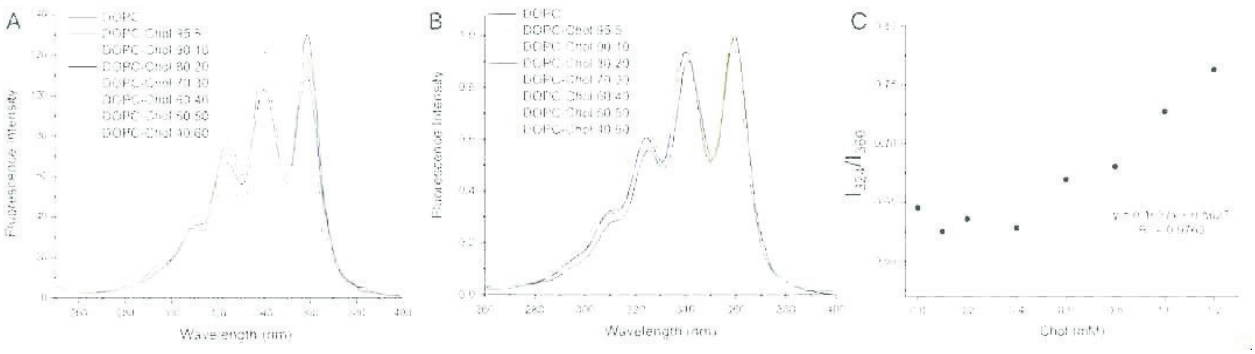

Figure 9. Raw (A) and normalized (B) fluorescent excitation spectra of Filipin III in DOPC-Chol liposomal systems. (C) Plot of the I_{324}/I_{360} ratio versus cholesterol concentration.

As shown in Figure 9A, the raw (not normalized) spectra for DOPC-Chol liposomes incubated with Filipin III exhibited an overall decrease in absolute fluorescence intensity as cholesterol content increased, whereas the normalized spectra (Figure 9B) revealed that the relative contribution of the shoulder at ~310 nm became more pronounced on increasing the cholesterol percentage, consistent with changes in the Filipin electronic environment upon sterol binding.[86] Since the Filipin-cholesterol interaction alters the probe's excitation profile, the literature-standard diagnostic parameter I_{324}/I_{360} (intensity ratio between the ~324 nm and ~360 nm excitation peaks) was used to quantify cholesterol availability.[84,52] The calibration curve, obtained by plotting I_{324}/I_{360} ratios as a function of cholesterol concentrations (Figure 9C), shows that above ~0.4 mM cholesterol the I_{324}/I_{360} ratio increases approximately linearly with cholesterol concentration, validating the use of this ratio as a semi-quantitative measure of cholesterol in the liposomal system (Supplementary Material, Table S2).

Once the Filipin III response in the DOPC-Chol liposomes series was characterized, the fluorescent dye was used to study the effect of GO on DOPC and DOPC-Chol (50:50) liposomes.

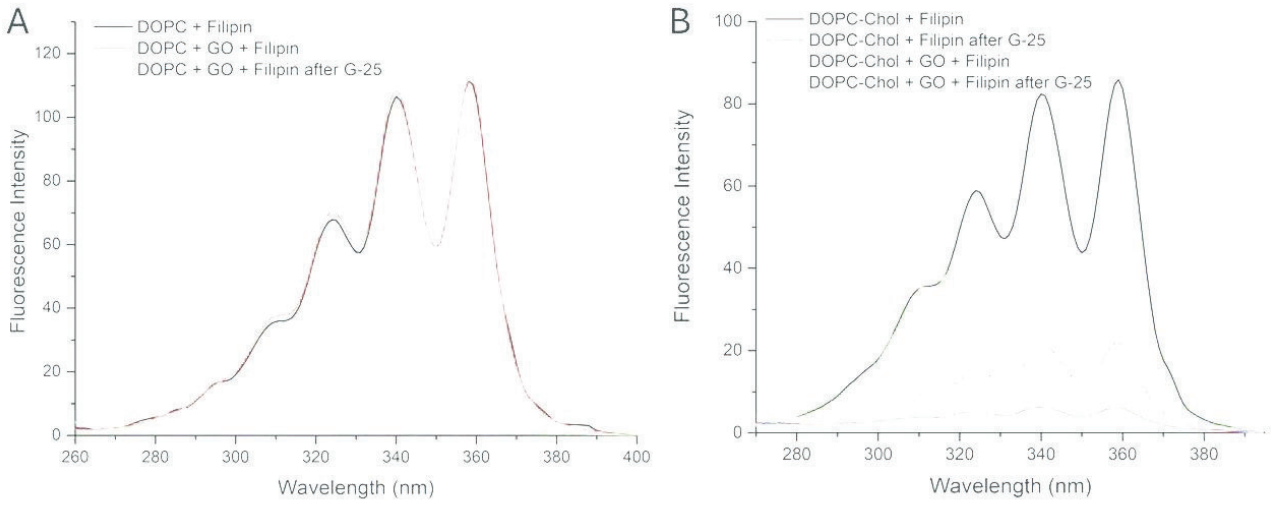

Figure 10. *Fluorescent excitation spectra of Filipin III in DOPC (A) and DOPC-Chol (B) liposomal systems.*

As reported in Figure 10A, the spectral profile of Filipin III in the presence of pure DOPC vesicles remained unchanged after GO treatment. In fact, the I_{324}/I_{360} ratio for DOPC+GO sample (0.653) was very similar to that of DOPC (0.645) and Filipin in water (0.644), indicating a lack of formation of Filipin-membrane complexes in the absence of sterol and no direct interaction between GO and Filipin that would have altered the probe spectrum. To determine whether Filipin III remained free in solution or associated with vesicles, DOPC+GO sample was subjected to a filtration step through a Sephadex G-25 column: the resulting post-column spectrum (green curve, Figure 10A) was essentially flat, indicating that Filipin fluorescence was completely removed by the column. This evidence suggests that Filipin, in absence of cholesterol, does not appreciably internalize into liposomal bilayers and tends to form small aggregates which give fluorescence excitation but are easily retained by the G-25 column. In contrast, DOPC-Chol liposomes incubated with the probe showed a fluorescent response that was altered upon exposure to GO, as illustrated in Figure 10B. After GO treatment, the Filipin fluorescence intensity (green line) decreased with respect to untreated DOPC-Chol liposomes (black line), in line with the I_{324}/I_{360} ratio increase from 0.727 for untreated

DOPC-Chol liposomes to 0.852 for GO-incubated vesicles. This pattern suggests that the contact between GO and cholesterol-containing liposomes increases the amount of Filipin bonded to cholesterol, promoting the formation of Filipin-cholesterol complexes that exhibit a lower excitation intensity but higher I_{324}/I_{360} ratio, since complexation with cholesterol modifies the spectral properties of Filipin. Gel filtration of the untreated DOPC-Chol sample (red line) reduced fluorescence excitation of the probe, but the decrease was not as complete as for the DOPC sample, indicating that a fraction of Filipin remains tightly associated with cholesterol in liposomal membrane and is co-eluted with the vesicles. Interestingly, the GO-treated DOPC-Chol sample after the filtration step (blue line) retained a higher residual fluorescence than the untreated and filtered sample (red line), implying that GO enhances the formation and/or surface exposure of Filipin-cholesterol complexes that remain associated with liposomes and are not completely removed by gel filtration. Overall, these observations support a mechanistic interpretation in which GO neither inhibits Filipin nor causes complete internalization of the probe into vesicles; rather, GO appears to rearrange the membrane or cholesterol distribution such that more cholesterol becomes accessible to Filipin at the outer leaflet or in membrane regions exposed to the aqueous phase. This increased accessibility favors the formation of the Filipin-cholesterol complexes (higher I_{324}/I_{360}) with altered photophysical properties that reduce net fluorescence intensity. Gel filtration data further indicate that, in cholesterol-containing vesicles, a measurable fraction of these complexes remains stably associated with liposomes after GO treatment, which is consistent with GO-induced sterol redistribution/exposure due to perturbation of lipid packing rather than simple extraction into the solution.

10.4.7 Water Permeability measurements

Water permeability is as a sensitive indicator of membrane barrier properties and therefore provides a useful metric for assessing the effects of GO on lipid bilayers of varying compositions.[37] Figure 11 and Table 5 summarize the osmotic water permeability coefficients (P_f) of DOPC and DOPC-Chol (50:50) membranes at two different concentrations of GO (10 µg/mL and 100 µg/mL) at 30 °C. For

DOPC alone, P_f showed only minor changes, increasing slightly from 72 μm/s (pure DOPC, control) to 73 μm/s at 10 μg/mL GO, and 74 μm/s at 100 μg/mL GO. In contrast, cholesterol-containing bilayers exhibited a more pronounced response: P_f increased from 66 μm/s in the control to 69 μm/s and 74 μm/s at 10 μg/mL GO and 100 μg/mL GO, respectively.

For comparison, MβCD, well known for its cholesterol-extracting activity, also increased P_f in DOPC:Chol membranes, but to a lesser extent, reaching 69 μm/s at 10 μg/mL and 71 μm/s at 100 μg/mL. Incorporation of cholesterol itself reduced baseline water permeability (qualitatively consistent with the literature,[87] from 72 μm/s in pure DOPC to 66 μm/s in the 50:50 mixture, reflecting the known ordering effect of cholesterol on lipid bilayers.

Water permeability reflects the physical properties of lipid bilayers, including bilayer thickness, packing density, and fluidity,[87,88] and increased water permeability generally suggest decreased membrane order and increased fluidity.[89,90] Therefore, our results suggest that GO perturbs membrane structure by disrupting cholesterol-dependent packing constraints and exerting a fluidizing effect on the membrane. Compared with MβCD, GO promotes a greater increase in permeability for cholesterol-containing membranes, consistent with an enhanced fluidizing effect and/or the generation of voids within the bilayer. Overall, our water permeability data aligns well with the findings described in the previous section that GO interacts with cholesterol-rich bilayers more strongly than with cholesterol-free bilayers, and reduces their barrier function.

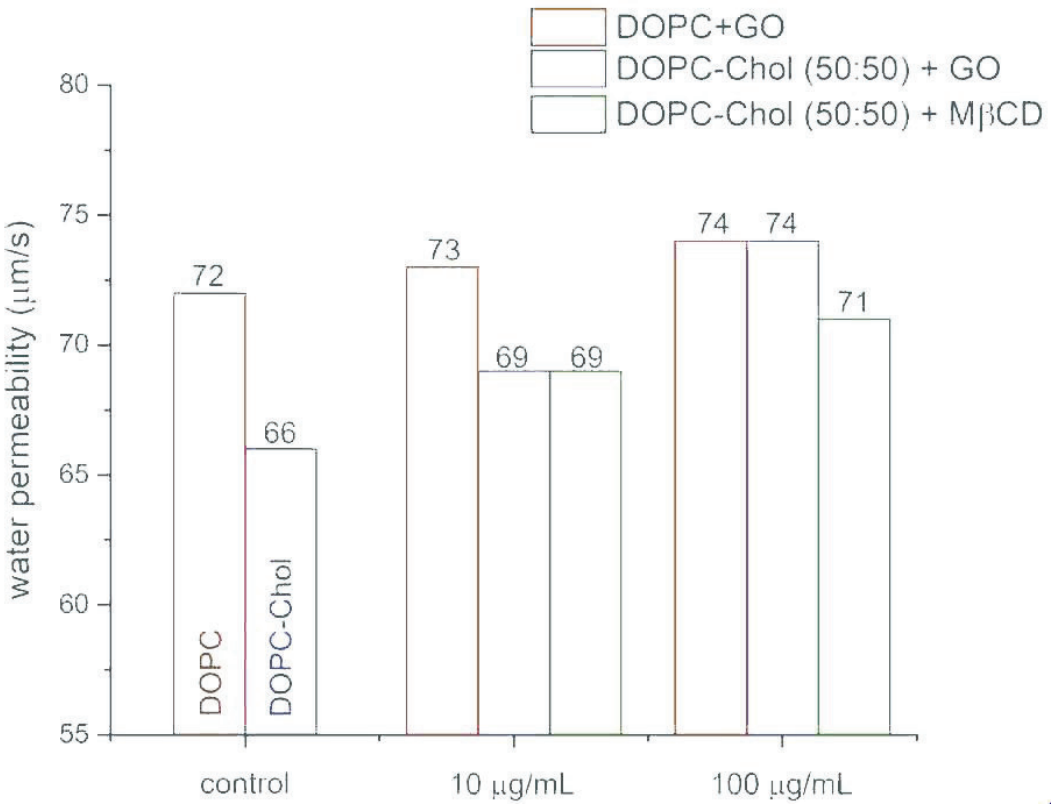

Figure 11. *Osmotic water permeability coefficients (μm/s) of DOPC and DOPC:Chol (50:50) bilayers at 30 °C with two different GO or MβCD concentrations.*

Table 5. *Effect of GO or MβCD on osmotic water permeability of DOPC and DOPC-Chol membranes at 30 °C.*

Conc. (μg/mL)	**DOPC, μm/s**	**DOPC-Chol (50:50), μm/s**	
	GO	**GO**	**MβCD**
0	72 ± 3	66 ± 2	
10	73 ± 2	69 ± 2	69 ± 2
100	74 ± 3	74 ± 4	71 ± 2

* Each data represents an average of individual permeability runs (n≥20 independent samples)

10.5 Conclusion

This study presents a comprehensive physico-chemical characterization of the interactions between graphene oxide (GO) and model lipid membranes composed of pure DOPC and DOPC-cholesterol liposomes. Through an integrated approach involving fluorescent probe release, differential scanning calorimetry (DSC), water permeability assays, NMR spectroscopy, Raman spectroscopy, and spectrofluorimetric analysis, we have elucidated the structural and functional modifications induced by GO. The release kinetics of the fluorescent probe revealed membrane susceptibility without complete disruption, while DSC data indicated thermal transitions consistent with GO-mediated weakening of lipid-lipid cohesive forces and enhanced molecular disorder. Similarly, Raman analysis identified, on addition of GO, a strong influence on membrane packing with increased fluidity in both DOPC and DOPC-cholesterol membranes, the appearance in DOPC liposomes of a new phospholipidic molecular environment characterized by significantly reduced interactions among adjacent chains and, finally, the evidence of relatively high GO-lipid headgroup interactions. NMR quantification demonstrated a reduction in the DOPC/cholesterol ratio within the bilayer, suggesting cholesterol displacement or reorganization. Increased bilayer leakage of carboxyfluorescein (CF), elevated membrane fluidity, and enhanced water permeability, confirmed by DIB experiments, further support the disruptive influence of GO on membrane integrity. Spectrofluorimetric analysis of Filipin III-cholesterol complexes revealed cholesterol exposure at the outer leaflet, indicating a reorientation of cholesterol within the bilayer. Notably, these effects were observed both when GO was introduced as an aqueous dispersion and when applied in the form of a GO-functionalized silicon wafer, underscoring its versatility and potency. Compared to methyl-β-cyclodextrin (MβCD), the gold standard cholesterol extractor, GO exhibits a more profound impact: not only does it promote cholesterol exposure and increased fluidity, but it also significantly attenuates intermolecular phospholipid interactions and enhances water permeability.

These findings suggest that GO may mimic the effect of introducing an additional hydrophilic head group to cholesterol, thereby increasing its interaction with water and facilitating deeper penetration

of water into the bilayer.[91] Overall, this study provides detailed mechanistic insights into the differential effects of graphene oxide (GO) and methyl-β-cyclodextrin (MβCD) on the structural and dynamic properties of phospholipid membranes. The ability of GO to modulate membrane fluidity, permeability, and lipid organization, beyond mere cholesterol extraction, highlights its potential as a versatile nanomaterial for targeted manipulation of the sperm apical membrane. These findings open new avenues for the development of colloid-based strategies aimed at enhancing *in vitro* fertilization outcomes through precise control of membrane biophysics.

References

(1) Geim, A.K.; Novoselov, K.S. The Rise of Graphene. Nat. Mater. 2007, 6, 183–191, doi: 10.1038/nmat1849

(2) Zhu, Y.; Murali, S.; Cai, W.; Li, X.; Suk, J.W.; Potts, J.R.; Ruoff, R.S. Graphene and Graphene Oxide: Synthesis, Properties, and Applications. Adv. Mater. 2010, 22, 3906–3924, doi: 10.1002/adma.201001068

(3) Chung, C.; Kim, Y.-K.; Shin, D.; Ryoo, S.-R.; Hong, B.H.; Min, D.-H. Biomedical Applications of Graphene and Graphene Oxide. Acc. Chem. Res. 2013, 46, 2211–2224, doi: 10.1021/ar300159f.

(4) Wang, Y.; Li, Z.; Wang, J.; Li, J.; Lin, Y. Graphene and Graphene Oxide: Biofunctionalization and Applications in Biotechnology. Trends Biotechnol. 2011, 29, 205–212, doi: 10.1016/j.tibtech.2011.01.008.

(5) Feng, L.; Wu, L.; Qu, X. New Horizons for Diagnostic and Therapeutic Applications of Graphene and Graphene Oxide. Adv. Mater. 2013, 25, 168–186, doi: 10.1002/adma.201203229.

(6) Liu, J.; Cui, L.; Losic, D. Graphene and Graphene Oxide as New Nanocarriers for Drug Delivery Applications. Acta Biomater. 2013, 9, 9243–9257, doi: 10.1016/j.actbio.2013.08.016.

(7) Radunovic, M.; Pavic, A.; Milivojevic, M.; Radovic, I.; Di Carlo, R.; Pilato, S.; Fontana, A.; Piattelli, A.; Petrovic, S. Biocompatibility and Antibiofilm Activity of Graphene Oxide Functionalized Titanium Discs and Collagen Membranes. Dent. Mater. 2022, 38, 1117–1127, doi: 10.1016/j.dental.2022.04.024.

(8) Pilato, S.; Moffa, S.; Siani, G.; Diomede, F.; Trubiani, O.; Pizzicannella, J.; Capista, D.; Passacantando, M.; Samorì, P.; Fontana, A. 3D Graphene Oxide-Polyethylenimine Scaffolds for Cardiac Tissue Engineering. ACS Appl. Mater. Interfaces 2023, 15, 14077–14088, doi: 10.1021/acsami.3c00216.

(9) Yang, K.; Feng, L.; Shi, X.; Liu, Z. Nano-graphene in Biomedicine: Theranostic Applications. Chem. Soc. Rev. 2013, 42, 530–547, doi: 10.1039/C2CS35342C

(10) Shen, H.; Zhang, L.; Liu, M.; Zhang, Z. Biomedical Applications of Graphene. Theranostics 2012, 2, 283–294, doi: 10.7150/thno.3642.

(11) Goenka, S.; Sant, V.; Sant, S. Graphene-based Nanomaterials for Drug Delivery and Tissue Engineering. J. Control. Release 2014, 173, 75–88, doi: 10.1016/j.jconrel.2013.10.017.

(12) Shahriari, S.; Sastry, M.; Panjikar, S.; Raman, R.K.S. Graphene and Graphene Oxide as Support for Biomolecules in the Development of Biosensors. Nanotechnol. Sci. Appl. 2021, 14, 197–220, doi: 10.2147/NSA.S332754

(13) Lanai, V.; Chen, Y.; Naumovska, E.; Pandit, S.; Schröder, E.; Mijakovic, I.; Rahimi, S. Differences in Interaction of Graphene/Graphene Oxide with Bacterial and Mammalian Cell Membranes. Nanoscale 2024, 16, 1156–1166, doi: 10.1039/D3NR05354G

(14) Romero-Vargas Castrillón, S.; Perrault, F.; de Faria, A.F.; Elimelech, M. Interaction of Graphene Oxide with Bacterial Cell Membranes: Insights from Force Spectroscopy. Environ. Sci. Technol. Lett. 2015, 2, 112–117, doi: 10.1021/acs.estlett.5b00084.

(15) Nicolson, G.L. The Fluid-Mosaic Model of Membrane Structure: Still Relevant to Understanding the Structure, Function and Dynamics of Biological Membranes after More than 40 Years. Biochim. Biophys. Acta 2014, 1838, 1451–1466, doi: 10.1016/j.bbamem.2013.10.019.

(16) Chen, Y.; Pandit, S.; Rahimi, S.; Mijakovic, I. Interactions Between Graphene-Based Materials and Biological Surfaces: A Review of Underlying Molecular Mechanisms. Adv. Mater. Interfaces 2021, 8, 2101132, doi: 10.1002/admi.202101132.

(17) Bernabò, N.; Fontana, A.; Ramal Sanchez, M.; Valbonetti, L.; Capacchietti, G.; Zappacosta, R.; Greco, L.; Marchisio, M.; Lanuti, P.; Ercolino, E.; Barboni, B. Graphene Oxide Affects In Vitro Fertilization Outcome by Interacting with Sperm Membrane in an Animal Model. Carbon 2018, 129, 428–437, doi: 10.1016/j.carbon.2017.12.004.

(18) S.S. Suarez, Regulation of sperm storage and movement in the mammalian oviduct, Int. J. Dev. Biol 2008, 52, 455-462.

(19) Ramal-Sanchez, M.; Valbonetti, L.; Tsikis, G.; Dubuisson, F.; Blache, M.C.; Labas, V. Graphene Oxide: A Glimmer of Hope for Assisted Reproductive Technology. Carbon 2019, 150, 518–530, doi: 10.1016/j.carbon.2019.05.059.

(20) Bernabò, N.; Machado-Simoes, J.; Valbonetti, L.; Ramal-Sanchez, M.; Capacchietti, G.; Fontana, A.; Zappacosta, R.; Palestini, P.; Botto, L.; Marchisio, M.; Lanuti, P.; Ciulla, M.; Di Stefano, A.; Fioroni, E.; Spina, M.; Barboni, B. Graphene Oxide Increases Mammalian Spermatozoa Fertilizing Ability by Extracting Cholesterol from Their Membranes and Promoting Capacitation. Sci. Rep. 2019, 9, 8155, doi: 10.1038/s41598-019-44702-5.

(21) Bernabò, N.; Valbonetti, L.; Raspa, M.; Fontana, A.; Palestini, P.; Botto, L.; Paoletti, R.; Fray, M.; Allen, S.; Machado-Simoes, J.; Ramal-Sanchez, M.; Pilato, S.; Scavizzi, F.; Barboni, B. Graphene Oxide Improves in

Vitro Fertilization in Mice With No Impact on Embryo Development and Preserves the Membrane Microdomains Architecture. Front. Bioeng. Biotechnol. 2020, 8, 629, doi: 10.3389/fbioe.2020.00629.

(22) Sanchez, S.A.; Gunther, G.; Tricerri, M.A.; Gratton, E. Methyl-β-cyclodextrins Preferentially Remove Cholesterol from the Liquid Disordered Phase in Giant Unilamellar Vesicles. J. Membr. Biol. 2011, 241, 1–10, doi: 10.1007/s00232-011-9348-8

(23) van Gestel, R.A.; Helms, J.B.; Brouwers, J.F.H.M.; Gadella, B.M. Effects of Methyl-β-Cyclodextrin-Mediated Cholesterol Depletion in Porcine Sperm Compared to Somatic Cells. Mol. Reprod. Dev. 2005, 72, 386–395, doi: 10.1002/mrd.20351.

(24) Ramal-Sanchez, M.; Fontana, A.; Valbonetti, L.; Ordinelli, A.; Barboni, B.; Bernabò, N. Graphene and Reproduction: A Love-Hate Relationship. Nanomaterials 2021, 11, 547, doi: 10.3390/nano11020547

(25) Siontorou, C.G.; Nikoleli, G.P.; Nikolelis, D.P.; Karapetis, S.K. Artificial Lipid Membranes: Past, Present, and Future. Membranes 2017, 7, 38, doi: 10.3390/membranes7030038

(26) Jash, A.; Ubeyitogullari, A.; Rizvi, S.S.H. Liposomes for Oral Delivery of Protein and Peptide-Based Therapeutics: Challenges, Formulation Strategies, and Advances. J. Mater. Chem. B 2021, 9, 4773–4792, doi: 10.1039/D1TB00126D

(27) Cortese, K.; Marconi, S.; Aiello, C.; Cagliani, M.C.; Pilato, S.; Zappacosta, R.; Fontana, A.; Castagnola, P. Liposomes Loaded with the Proteasome Inhibitor z-Leucinyl-Leucinyl-Norleucinal Are Effective in Inducing Apoptosis in Colorectal Cancer Cell Lines. Membranes 2020, 10, 91, doi: 10.3390/membranes10050091

(28) Wang, Y.; Miao, L.; Satterlee, A.; Huang, L. Delivery of Oligonucleotides with Lipid Nanoparticles. Adv. Drug Deliv. Rev. 2015, 87, 68–80, doi: 10.1016/j.addr.2015.02.007.

(29) Suhaimi, N.A.A.; Ahmad, S.; Husna, S.M.N.; Sarmiento, M.E.; Acosta, A.; Norazmi, M.N.; Ibrahim, J.; Mohamud, R.; Kadir, R. Application of Liposomes in the Treatment of Infectious Diseases. Life Sci. 2022, 305, 120734, doi: 10.1016/j.lfs.2022.120734

(30) A. Laouini, C. Jaafar-Maalej, I. Limayem-Blouza, S. Sfar, C. Charcosset, H. Fessi, Preparation, Characterization and Applications of Liposomes: State of the Art, J. Colloid Sci. Biotechnol. 2012, 1, 147-168.

(31) Moffa, S.; Carradori, S.; Melfi, F.; Fontana, A.; Ciulla, M.; Di Profio, P.; Aschi, M.; Wolicki, R.D.; Pilato, S.; Siani, G. Fine Tuning of Membrane Permeability by Reversible Photoisomerization of Aryl-Azo Derivatives

of Thymol Embedded in Lipid Nanoparticles. Colloids Surf. B Biointerfaces 2024, 241, 114043, doi: 10.1016/j.colsurfb.2024.114043.

(32) Zucker, I.; Werber, J.R.; Fishman, Z.S.; Hashmi, S.M.; Gabinet, U.R.; Lu, X.; Osuji, C.O.; Pfefferle, L.D.; Elimelech, M. Loss of Phospholipid Membrane Integrity Induced by Two-Dimensional Nanomaterials. Environ. Sci. Technol. Lett. 2017, 4, 404–409, doi: 10.1021/acs.estlett.7b00358.

(33) Liu, X.; Chen, K.L. Interactions of Graphene Oxide with Model Cell Membranes: Probing Nanoparticle Attachment and Lipid Bilayer Disruption. Langmuir 2015, 31, 12076–12086, doi: 10.1021/acs.langmuir.5b02414

(34) Feng, Y.; Zhang, Y.; Liu, G.; Liu, X.; Gao, S. Interaction of Graphene Oxide with Artificial Cell Membranes: Role of Anionic Phospholipid and Cholesterol in Nanoparticle Attachment and Membrane Disruption. Colloids Surf. B Biointerfaces 2021, 202, 111685, doi: 10.1016/j.colsurfb.2021.111685.

(35) Pilato, S.; Aschi, M.; Bazzoni, M.; Cester Bonati, F.; Cera, G.; Moffa, S.; Canale, V.; Ciulla, M.; Secchi, A.; Arduini, A.; Fontana, A.; Siani, G. Calixarene-Based Artificial Ionophores for Chloride Transport across Natural Liposomal Bilayer: Synthesis, Structure–Function Relationships, and Computational Study. Biochim. Biophys. Acta Biomembr. 2021, 1863, 183667, doi: 10.1016/j.bbamem.2021.183667.

(36) O. Beknke, J. Tranum-Jensen, B. van Deurs, Filipin as a cholesterol probe. Morphology of filipin-cholesterol interaction in lipid model systems, Eur. J. Cell Biol 1984, 35, 189-199.

(37) Lee, S. Good to the Last Drop: Interfacial Droplet Chemistry, from Crystals to Biological Membranes. Acc. Chem. Res. 2018, 51 (10), 2524-2534, doi: 10.1021/acs.accounts.8b00277.

(38) Milianta, P. J.; Muzzio, M.; Denver, J.; Cawley, G.; Lee, S. Water Permeability across Symmetric and Asymmetric Droplet Interface Bilayers: Interaction of Cholesterol Sulfate with DPhPC. Langmuir 2015, 31 (44), 12187-12196, doi: 10.1021/acs.langmuir.5b03421

(39) Wood, M.; Morales, M.; Miller, E.; Braziel, S.; Giancaspro, J.; Scollan, P.; Rosario, J.; Gayapa, A.; Krmic, M.; Lee, S. Ibuprofen and the Phosphatidylcholine Bilayer: Membrane Water Permeability in the Presence and Absence of Cholesterol. Langmuir 2021, 37 (15), 4468-4480, doi: 10.1021/acs.langmuir.0c03638

(40) Krmic, M.; Perez, E.; Scollan, P.; Ivanchenko, K.; Hernandez, A. G.; Giancaspro, J.; Rosario, J.; Ceja-Vega, J.; Gudyka, J.; Porteus, R.; Lee, S. Aspirin Interacts with Cholesterol-Containing Membranes in a pH-Dependent Manner. Langmuir 2023, 39 (46), 16444-16456, doi: 10.1021/acs.langmuir.3c02242

(41) Lopez, M.; Evangelista, S. E.; Morales, M.; Lee, S. Enthalpic Effects of Chain Length and Unsaturation on Water Permeability across Droplet Bilayers of Homologous Monoglycerides. Langmuir 2017, 33 (4), 900-912, doi: 10.1021/acs.langmuir.6b03932.

(42) Lopez, M.; Denver, J.; Evangelista, S. E.; Armetta, A.; Di Domizio, G.; Lee, S. Effects of Acyl Chain Unsaturation on Activation Energy of Water Permeability across Droplet Bilayers of Homologous Monoglycerides: Role of Cholesterol. Langmuir 2018, 34 (5), 2147-2157, doi: 10.1021/acs.langmuir.7b03590.

(43) Di Credico, A.; Gaggi, G.; Bibbò, S.; Pilato, S.; Di Giacomo, S.; Siani, G.; Fontana, A.; Moffa, S.; Konstantinidou, F.; Stuppia, L.; Gatta, V.; Di Baldassarre, A.; Donato, M.; Ghinassi, B. Exploring Potential Impact of Graphene Oxide and Graphene-Oxide-Polyethylenimine on Biological Behavior of Human Amniotic Fluid-Derived Stem Cells. Int. J. Mol. Sci. 2024, 25, 13598:1-17, doi: 10.3390/ijms252413598.

(44) RDi Carlo, R.; Di Crescenzo, A.; Pilato, S.; Ventrella, A.; Piattelli, A.; Recinella, L.; Chiavaroli, A.; Giordani, S.; Baldrighi, M.; Camisasca, A.; Zavan, B.; Falconi, M.; Cataldi, A.; Fontana, A.; Zara, S. Osteoblastic differentiation on graphene oxide-functionalized titanium surfaces: an in vitro study, Nanomaterials 2020, 10, 654:1-16, doi: 10.3390/nano10040654.

(45) Sturm, L.; Poklar Ulrih, N. Basic Methods for Preparation of Liposomes and Studying Their Interactions with Different Compounds, with the Emphasis on Polyphenols, Int. J. Mol. Sci. 2021, 22(12):6547, doi: 10.3390/ijms22126547

(46) Chatterjee, T.; Boutin, E.; Robert, M. Manifesto for the Routine Use of NMR for the Liquid Product Analysis of Aqueous CO2 Reduction: From Comprehensive Chemical Shift Data to Formaldehyde Quantification in Water. Dalton Trans. 2020, 49, 4257-4265, doi: 10.1039/c9dt04749b.

(47) Marzorati, M.; Bigler, P.; Vermathen, M. Interactions between Selected Photosensitizers and Model Membranes: an NMR Classification. Biochim. Biophys. Acta 2011, 1808 (6), 1661-1672, doi: 10.1016/j.bbamem.2011.01.013.

(48) Stevens, M. M.; Honerkamp-Smith, A. R.; Keller, S. L. Solubility limits of cholesterol, lanosterol, ergosterol, stigmasterol, and β-sitosterol in electroformed lipid vesicles. Soft Matter 2010, 6, 5882-5890, doi: 10.1039/C0SM00373E

(49) Burwell, T.; Thangamuthu, M.; Aliev, G. N.; Ghaderzadeh, S.; Kohlrausch, E. C.; Chen, Y.; Theis, W.; Norman, L. T.; Fernandes, J. A.; Besley, E.; Licence, P.; Khlobystov, A. N. Direct Formation of Copper

Nanoparticles from Atoms at Graphitic Step Edges Lowers Overpotential and Improves Selectivity of Electrocatalytic CO2 Reduction. Commun. Chem. 2024, 7, 140, doi: 10.1038/s42004-024-01218-y

(50) Drabikowski, W.; Łagwińska, E.; Sarzała, M. G. Filipin as a fluorescent probe for the location of cholesterol in the membranes of fragmented sarcoplasmic reticulum, Biochim. Biophys. Acta-Biomembr. 1973, 291, 61-70, doi: 10.1016/0005-2736(73)90060-6.

(51) G. Sessa, G. Weissmann, Effects of Four Components of the Polyene Antibiotic, Filipin, on Phospholipid Spherules (Liposomes) and Erythrocytes, J. Bio. Chem. 1968, 243, 16, 4364-4371.

(52) M.A.R.B. Castanho, A. Coutinho, M.J.E Prieto, Absorption and Fluorescence Spectra of Polyene Antibiotics in the presence of Cholesterol, J. Bio. Chem. 1992, 267, 204-209.

(53) Amaral, L. M. P. F.; Rangel, M.; Bastos, M. Effect of DMSO on Structural Properties of DMPC and DPPC Liposome Suspensions. J. Funct. Biomater. 2024, 15 (3), 67, doi: 10.3390/jfb15030067.

(54) Funakoshi, K.; Suzuki, H.; Takeuchi, S. Lipid Bilayer Formation by Contacting Monolayers in a Microfluidic Device for Membrane Protein Analysis. Anal. Chem. 2006, 78 (24), 8169-8174, doi: 10.1021/ac0613479.

(55) Liu, J.; Li, X.; Jia, W.; Li, Z.; Zhao, Y.; Ren, S. Demulsification of Crude Oil-in-Water Emulsions Driven by Graphene Oxide Nanosheets. Energy Fuels 2015, 29 (7), 4644-4653, doi: 10.1021/acs.energyfuels.5b00966

(56) Choi, S.; Kang, B.; Yang, E.; Kim, K.; Kwak, M. K.; Chang, P. S.; Jung, H. S. Precise control of liposome size using characteristic time depends on solvent type and membrane properties. Sci. Rep. 2023, 13 (1), 4728, doi: 10.1038/s41598-023-31895-z.

(57) Jovanović, A. A.; Balanč, B. D.; Ota, A.; Grabnar, P. A.; Djordjević, V. B.; Šavikin, K. P.; Bugarski, B. M.; Nedović, V. A.; Poklar Ulrih, N. Comparative Effects of Cholesterol and β-Sitosterol on the Liposome Membrane Characteristics. Eur. J. Lipid Sci. Technol. 2018, 120 (9), 1800039, doi: 10.1002/ejlt.201800039.

(58) Verma, S.; Dhenadhayalan, N.; Lin, K. C. Study of Cholesterol Phase Effect on the Dynamics of DOPC and DPPC Small Vesicle Membranes Using Single-Molecule Fluorescence Correlation Spectroscopy. J. Mol. Liq. 2022, 353, 118806, doi: 10.1016/j.molliq.2022.118806

(59) Bolean, M.; Simão, A. M. S.; Favarin, B. Z.; Millán, J. L.; Ciancaglini, P. The effect of cholesterol on the reconstitution of alkaline phosphatase into liposomes. Biophys. Chem. 2010, 152 (1-3), 74-79, doi: 10.1016/j.bpc.2010.08.002

(60) Won, D. H.; Kim, S. Y.; Lim, G. N.; Park, S. N. A Study on the Stability of DOPC Liposome. J. Soc. Cosmet. Sci. Korea 2011, 37 (1), 55-60, doi: 10.15230/SCSK.2011.37.1.055.

(61) Huang, P. J. J.; Wang, F.; Liu, J. Liposome/Graphene Oxide Interaction Studied by Isothermal Titration Calorimetry. Langmuir 2016, 32 (10), 2458-2463, doi: 10.1021/acs.langmuir.6b00006.

(62) Senior, J.; Gregoriadis, G. Stability of Small Unilamellar Liposomes in Serum and Clearance from the Circulation: The Effect of the Phospholipid and Cholesterol Components. Life Sci. 1982, 30 (24), 2123-2136, doi: 10.1016/0024-3205(82)90455-6.

(63) Seth, A.; Giri, R. P.; Hayen, N.; Hitaishi, P.; Murphy, B. M.; Ghosh, S. K. Cholesterol Modulated Assembly of Graphene Oxide Nano-Flakes at a Phospholipid Interface. Colloids Surf. B Biointerfaces 2025, 255, 114934, doi: 10.1016/j.colsurfb.2025.114934.

(64) Kashapov, R. R.; Rassadkina, R. I.; Ziganshina, A. Y.; Mukhitova, R. K.; Mamedov, V. A.; Zhukova, N. A.; Kadirov, M. K.; Nizameev, I. R.; Zakharova, L. Y.; Sinyashin, O. G. Controlling the release of hydrophobic compounds by a supramolecular amphiphilic assembly. RSC Adv. 2016, 6, 38548-38552, doi: 10.1039/C6RA03838G

(65) Giancaspro, J.; Scollan, P.; Rosario, J.; Miller, E.; Braziel, S.; Lee, S. Structural determination of model phospholipid membranes by Raman spectroscopy: laboratory experiment. Biochem. Mol. Biol. Educ. 2022, 50 (2), 181-192, doi: 10.1002/bmb.21603

(66) Faried, M.; Suga, K.; Okamoto, Y.; Shameli, K.; Miyake, M.; Umakoshi, H. Membrane Surface-Enhanced Raman Spectroscopy for Cholesterol-Modified Lipid Systems: Effect of Gold Nanoparticle Size. ACS Omega 2019, 4 (9), 13687-13695, doi: 10.1021/acsomega.9b01073.

(67) Orendorff, C. J.; Ducey Jr, M. W.; Pemberton, J. E. Quantitative Correlation of Raman Spectral Indicators in Determining Conformational Order in Alkyl Chains. J. Phys. Chem. A 2002, 106 (30), 6991-6998, doi: 10.1021/jp014311n.

(68) Di Napoli, C.; Masia, F.; Pope, I.; Otto, C.; Langbein, W.; Borri, P. Chemically-Specific Dual/Differential CARS Micro-Spectroscopy of Saturated and Unsaturated Lipid Droplets. J. Biophotonics 2014, 7 (1-2), 68-76, doi: 10.1002/jbio.201200197.

(69) Czamara, K.; Majzner, K.; Pacia, M. Z.; Kochan, K.; Kaczor, A.; Baranska, M. Raman Spectroscopy of Lipids: a Review. J. Raman Spectrosc. 2015, 46 (1), 4-20, doi: 10.1002/jrs.4607.

(70) Gharib, R.; Auezova, L.; Charcosset, C.; Greige-Gerges, H. Effect of a Series of Essential Oil Molecules on DPPC Membrane Fluidity: a Biophysical Study. J. Iran. Chem. Soc. 2018, 15, 75-84, doi: 10.1007/s13738-017-1210-1.

(71) Tantipolphan, R.; Rades, T.; Strachan, C. J.; Gordon, K. C.; Medlicott, N. J. Analysis of lecithin-cholesterol mixtures using Raman spectroscopy. J. Pharm. Biomed. Anal. 2006, 41 (2), 476-484, doi: 10.1016/j.jpba.2006.01.031.

(72) Suga, K.; Umakoshi, H. Detection of Nanosized Ordered Domains in DOPC/DPPC and DOPC/Ch Binary Lipid Mixture Systems of Large Unilamellar Vesicles Using a TEMPO Quenching Method. Langmuir 2013, 29 (15), 4830-4838, doi: 10.1021/la304768f.

(73) Kočišová, E.; Antalík, A.; Procházka, M. Drop Coating Deposition Raman Spectroscopy of Liposomes: Role of Cholesterol. Chem. Phys. Lipids 2013, 172-173, 1-5, doi: 10.1016/j.chemphyslip.2013.04.002.

(74) Mahammad, S.; Parmryd, I. Cholesterol depletion using methyl-β-cyclodextrin. Methods Mol. Biol. 2015, 1232, 91-102, doi: 10.1007/978-1-4939-1752-5_8

(75) Kaiser, H.-J.; Lingwood, D.; Levental, I.; Sampaio, J. L.; Kalvodova, L.; Rajendran, L.; Simons, K. Order of Lipid Phases in Model and Plasma Membranes. Proc. Natl. Acad. Sci. U. S. A. 2009, 106, 16645-16650, doi: 10.1073/pnas.0908987106..

(76) Gharib, R.; Fourmentin, S.; Charcosset, C.; Greige-Gerges, H. Effect of Hydroxypropyl-β-cyclodextrin on Lipid Membrane Fluidity, Stability and Freeze-Drying of Liposomes. J. Drug Deliv. Sci. Technol. 2018, 44, 101-107, doi: 10.1016/j.jddst.2017.12.010.

(77) Baria, E.; Dallari, C.; Mattii, F.; Pavone, F. S.; Credi, C.; Cicchi, R.; Morrone, A.; Capitini, C.; Calamai, M. Evaluating Pathological Levels of Intracellular Cholesterol through Raman and Surface-Enhanced Raman Spectroscopies. Sci. Rep. 2024, 14, 28566, doi: 10.1038/s41598-024-76621-5.

(78) Zhang, X.; Cao, F.; Wu, L.; Jiang, X. Understanding the Synergic Mechanism of Weak Interactions between Graphene Oxide and Lipid Membrane Leading to the Extraction of Lipids. Langmuir 2019, 35 (43), 14098-14107, doi: 10.1021/acs.langmuir.9b02536

(79) Mandal, P.; Giri, R. P.; Murphy, B. M.; Ghosh, S. K. Self-Assembly of Graphene Oxide Nanoflakes in a Lipid Monolayer at the Air–Water Interface. ACS Appl. Mater. Interfaces 2021, 13 (48), 57023-57035, doi: 10.1021/acsami.1c19004.

(80) Tan, B.; Hu, J.; Wu, F. Cholesterols Induced Distinctive Entry of the Graphene Nanosheet into the Cell Membrane. ACS Omega 2024, 9 (8), 9216-9225, doi: 10.1021/acsomega.3c08236.

(81) D. Marsh, General features of phospholipid phase transitions, Chem. Phys. Lipids 1991, 57, 109-120.

(82) Ulrich, A. S.; Sami, M.; Watts, A. Hydration of DOPC Bilayers by Differential Scanning Calorimetry. Biochim. Biophys. Acta 1994, 1191 (1), 225-230, doi: 10.1016/0005-2736(94)90253-4.

(83) McMullen, T. P.; Lewis, R. N.; McElhaney, R. N. Differential Scanning Calorimetric Study of the Effect of Cholesterol on the Thermotropic Phase Behavior of a Homologous Series of Linear Saturated Phosphatidylcholines. Biochemistry 1993, 32 (2), 516-522, doi: 10.1021/bi00053a016.

(84) Katzenstein, I. P.; Spielvogel, A. M.; Norman, A. W. Stoichiometry of interaction of the polyene antibiotic, Filipin, with free and liposomal-bound cholesterol. J. Antibiot. 1974, 27 (12), 943-951, doi: 10.7164/antibiotics.27.943

(85) A. W. Norman, R. A. Demel, B. de Kruyff, L. L. van Deenen, Studies on the biological properties of polyene antibiotics. Evidence for the direct interaction of filipin with cholesterol, J. Biol. Chem. 1972, 247, 6, 1918-1929.

(86) F. Schroeder, J. F. Holland, L. L. Bieber, Fluorometric evidence for the binding of cholesterol to the Filipin complex, J. Antibiot. 1971, 24, 12, 846-849.

(87) Mathai, J. C.; Tristram-Nagle, S.; Nagle, J. F.; Zeidel, M. L. Structural Determinants of Water Permeability through the Lipid Membrane. J. Gen. Physiol. 2008, 131 (1), 69-76, doi: 10.1085/jgp.200709848

(88) Olbrich, K.; Rawicz, W.; Needham, D.; Evans, E. Water Permeability and Mechanical Strength of Polyunsaturated Lipid Bilayers. Biophys. J. 2000, 79 (1), 321-327, doi: 10.1016/S0006-3495(00)76294-1.

(89) Gudyka, J.; Ceja-Vega, J.; Ivanchenko, K.; Morocho, Z.; Panella, M.; Gamez Hernandez, A.; Clarke, C.; Perez, E.; Silverberg, S.; Lee, S. Concentration-Dependent Effects of Curcumin on Membrane Permeability and Structure. ACS Pharmacol. Transl. Sci. 2024, 7 (5), 1546-1556, doi: 10.1021/acsptsci.4c00093

(90) Fosella, J.; Ceja-Vega, J.; Rabadi, A.; Panella, M.; Said, J.; Perla, W.; Poust, C.; Herrera, M.; Lee, S. Biophysical Consequences for Exposure of Model Cell Membranes to Perfluoroalkyl Substances. J. Phys. Chem. B 2025, 129 (31), 7951-7963, doi: 10.1021/acs.jpcb.5c02472.

(91) F. de Meyer, B. Smit, Effect of cholesterol on the structure of a phospholipid bilayer, PNAS 2009, 106(10), 3654 –3658.

11 Urineprint of high-altitude: Insights from analyses of urinary biomarkers and bio-physical-chemical features of extracellular vesicles

DOI: https://doi.org/10.1016/j.bpc.2024.107351

11.1 Introduction

The impairment in urinary function due to high altitude is known since decades ago, although rather than hypoxia per se the effects were attributed to vibration, noise and temperature[1]. However, the effect on micturition due to hypoxia can be also exerted via neurological and humoral systems. As many expeditioners have experienced on themselves, humans exposed to acute hypoxia undergo diuresis and natriuresis[2].

Uroflowmetry and urodynamic test can reveal transient dysfunctions, although the pathological significance remains debated[3-5].

Urine is a non-invasive biological matrix that can serve for monitoring some human responses to hypoxia, in particular: 1) dehydration, as inferred from urine osmolality[6], and 2) renal acid-base compensation, which occurs to compensate respiratory alcalosis through HCO 3 excretion[7].

For what concerns biomarkers of urinary functions, glomerular filtration rate (GFR) is largely used, as it allows to achieve a simple, rapid and reproducible measurement from blood samples[8]. Blood creatinine and cystatin-C, despite being widely used, have limitations in determining the real GFR. Radio labeled markers are cheap but unsafe. Inulin represents the most precise method but is difficult to implement in a clinical environment due to the costs and complexity of the procedure. Iothalamate is less precise than inulin but more convenient and easier to use.

Iohexol represents a precise and safe method but yet to be implemented in humans. The ideal method should avoid 24-h urine collection, reduce the amount of blood, avoid radio labeled substances, and

be rapid. In addition, 24-h urine collection for assessing creatinine excretion can be difficult in field study, and sampling spot blood, although minimally, is an invasive method. Sampling spot urine can represent a good alternative by accounting for the feasibility and non-invasiveness of sampling during high altitude expeditions.

Spot values can be used as a surrogate of continuous assessment for quantifying urinalysis parameters. Indeed, in most cases the measurement of urinary albumin and creatinine is performed on extemporaneous urine samples and the albumin/creatinine ratio (ACR) is calculated. Creatinine is a product of muscle metabolism normally excreted in the urine at a constant rate.

Therefore, its quantity usually serves as an indicator of the concentration of the urine, and it is used as a corrective factor, as for computing the albumin/creatinine ratios (ACR), that is used in the diagnosis of microalbuminuria, which indicates an alteration of the filter function of the renal glomerulus. To this extent, first morning void better represents 24-h collection than spot urine[9]. Indeed, recent guidelines advocate the use of ACR from spot urine, and a large sample study reported high agreement between early morning void and 24-h collection for quantifying ACR, with 88 % of participants in the three categories of 300 mg/g[10]; the three categories refer to low, moderately increased and severely increased risk for kidney disease, respectively.

The usefulness of urine as a biological matrix is not limited to bio markers that are clinically relevant in urinary medicine. Among a plethora of possible investigations, urine represents a valuable biological source for studying inflammatory markers in a non-invasive way that can be used in daily comparisons, thus limiting the burden for participants while providing an integrative measure of inflammation due to the presence of molecules which can cross the glomerular filtration barrier[11]. The combined study of inflammation and redox system disruption, named “OxInflammation”, has been demonstrated to be affected by the cumulative stressor of high-altitude exposure and trekking by our group[12]. Our group also detected an altered oxi- inflammatory status as a response of running at hypoxia in samples of urinary extracellular vesicles (uEVs)[13]. The presence of EVs in urine has

been known since decades ago. From the initial discovery of proteome cargoed by uEVs, the topical research has exponentially grown for the possibility of obtaining unexplored pathological biomarkers. However, given the heterogeneity of biochemical composition and the complex biophysical features of EVs, the identification of putative biomarkers is challenging.

Beyond kidneys, bladder and urogenital tract, uEVs can refer to distant sites thereby providing a systemic readout of states, whose collection methods are non-invasive and allow to sample large quantities[14]. EVs thus reflect internal pathways; moreover, among their various functions, EVs serve as a mechanism for eliminating extracellularly toxic molecules[15].

Environmental factors of different nature influence physiological systems in ways that can be captured in part by the biophysical and molecular alterations of EVs. Among environmental stressors, a growing body of research investigated hypoxia-induced EVs, mostly focusing on cancer models, using incubation of cells with variable oxygen levels, and isolating EVs by ultracentrifugation protocols[16].

However, the growing interest in altitude travelling and the non-negligible presence of people living at high altitude rises the need to produce robust efforts in identifying the effect of hypobaric hypoxia on human EVs.

11.2 Aims of the study

Hypoxia affects urinary system and uEVs are increasingly considered as biomarkers of the renal system. Nevertheless, there is no specific evidence of the effect of hypoxia on uEVs in humans. Given this background, this study aimed: 1) to find a biophysical, biochemical or morphological signature of uEVs isolated from spot urine samples as an accessible and original monitoring for hypoxia-induced changes in urinary function, and 2) to find whether or not putative changes in uEVs are accompanied by a parallel dysfunction of urinary system with oxinflammatory burden.

11.3 Methods

11.3.1 Study design

As extensively reported elsewhere[17], the project "Monte rosa exploration & physiology" was carried out by trekking 4 days from Alagna Valsesia (1191 m a.s.l.) up to Capanna Regina Margherita (4556 m a.s.l.), thus encountering a range of temperature from 3.5 to 31.3 ◦ c and of relative humidity from to 36 to 95 %. Urine samples were collected twice, at the lowest and highest altitude, on the same days for all participants.

11.3.2 Participants

As a whole, the expedition involved 15 participants, of which 7 women and 8 men, whose age ranged from 24 to 63 years and BMI from 17.93 to 30.76 kg/m^2.

All of them took acetazolamide once daily 125 mg at 2370 m and 250 mg at both 3647 and 4556 m; 6 participants developed AMS as resulted from 2018 Lake Louise Acute Mountain Sickness Score; along with the massive reduction in peripheral saturation, on average heart rate and blood pressure both increased at high altitude[17].

11.3.3 Urine sampling and management

The pre-processing flow is reported following the recommendations of Urine Task Force of the Rigor and Standardization Subcommittee of the International Society for Extracellular Vesicles (ISEV)[18]:

1) Urine samples were collected in sterile containers as first void specimens in the early morning at lowest (Alagna Valsesia, 1191 m) and highest altitude (Capanna Regina Margherita, 4556 m), as a surrogate of 24-h collection achievable during field studies

2) At lowest altitude samples were stored in a freezer, at highest altitude samples were transported in boxes with ice packs down to lowest altitude in a few hours

3) All the samples were transported in boxes with ice packs to Chieti (duration of about half a day) for isothermal transport and before the night all the samples were inspected for integrity and then stored at 80° C

4) Once thawed at 37 ◦ C in water bath, a medium aliquote (9 ml) was allocated for EVs isolation and two small aliquots (1.5 ml each) were allocated for urinalysis and OxInflammation analysis.

When applicable, the analytical procedures of uEVs are reported following the last report on "Minimal information for studies of extracellular vesicles" (MISEV)[19].

Urynalisis Albumin and creatinin dosage was carried out with automated clinical chemistry assays on Architect Plus (Abbott Laboratories, USA) by using in particular the immunoturbidimetric process for albumin and the kinetic alcaline picrate process for creatinin.

Then, the values ob tained in mg/l for albumin and mg/dl for creatinin were adjusted to obtain the albumin-to-creatinin ratio (ACR) in mg/g. 2.5. OxInflammation Lipid peroxidation was detected by competitive immunoassay of 8- isoprostane concentration (8-isoPGF2 α ; Item No. 516360, Cayman Chemical, Ann Arbor, MI, USA). 8-isoPGF2 α concentrations were determined using a standard curve. Samples and standards were read at a wavelength of 512 nm.

This method has been previously described[12,20]. According to the manufacturer's instructions, IL-6 urinary levels were determined by an ELISA kit (Cayman Chemical, Ann Arbor, MI, USA, Item No. 501030), based on the double-antibody "sandwich" technique in accordance with the manufacturer's instruction[21,22]. NO derivatives, nitrate, and nitrite ($NO_2 + NO_3 = NO_x$) were measured in urine samples by a colorimetric method based on the Griess reaction (Cayman Chemical, Ann Arbor, MI, USA, Item No.780001). Samples were read at 545 nm, and a standard curve assessed the concentration[21,22].

All the above samples and standards were read by a microplate reader spectrophotometer (Infinite M200, Tecan Group Ltd., M¨ annedorf, Switzerland). The determinations were assessed in duplicate, and the inter-assay coefficient of variation was in the range indicated by the manufacturer.

11.3.4 Isolation of extracellular vesicles

The procedures was carried out as follows:

1) centrifugation at RCF 2000 xg, 20 min 4°C;

2) surnatant centrifugation at RCF 10,000 xg, 30 min 4°C;

3) addition of 1 ml of sucrose cushion 30 % (m/v PBS 1×) on fresh tube;

4) carefully addition of the collected surnatant;

5) centrifu gation at RCF 100,000 xg, 90 min 4°C;

6) surnatant remotion main taining cushion volume;

7) addition of PBS 1× to reach the final volume and mixing of sample by turning it upside down;

8) centrifugation at RCF 100,000 xg, 70 min 4°C;

9) Resuspension in ≅ 20–25 μ l of PBS 1× (Fig. 1). The use of sucrose density gradient allows to obtain highly pure EVs samples, although this method is time consuming, requires special equipment and results in low yield.

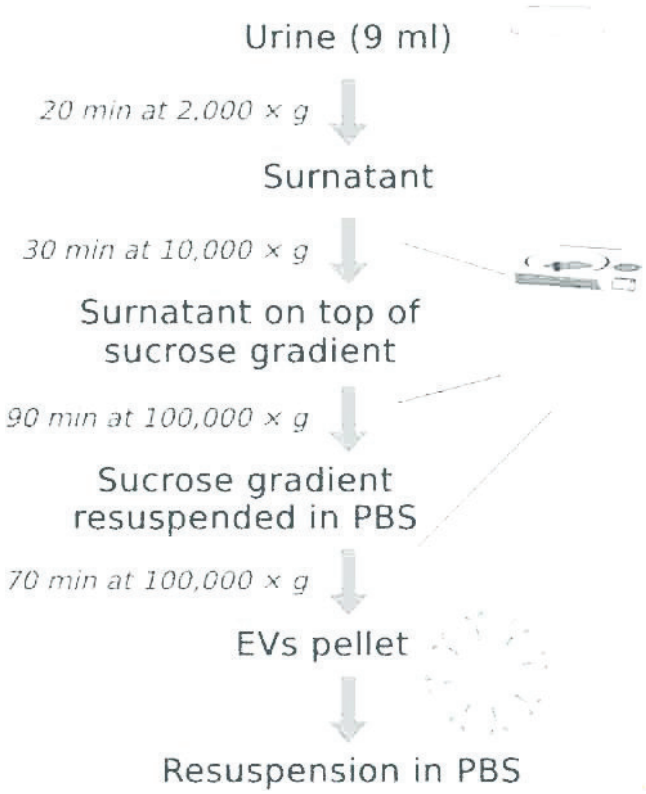

Fig. 22: Protocol of EVs isolation from urine samples. Image created with Bio

For the aim of this work, the use of a sucrose cushion represented the trade-off for limiting the disadvantages while maintaining those advantages that optimise further analyses. After resuspension, 1 µ l was immediately used for nucleic acid-to- protein ratio (NPr), estimated by UV absorbance at 260 nm and 280 nm, respectively, by UV–vis spectrophotometry in a Nanophotometer NP80 (Implen, Germany), calibrating the instrument using sample elution buffer Blank Control™ (Implen, Germany) before the test[23].

The samples were stored at 80°C until the further analyses.

11.3.5 Atomic force microscopy (AFM) investigation

Atomic force microscopy was used to study the size distribution and the morphology of EVs isolated from urine collected at low and high altitudes by using MultiMode 8 AFM microscope with Nanoscope V controller (Bruker, Billerica, Massachusetts, US).

To analyze the urinary EVs, the samples were properly diluted with MilliQ water and deposited onto a SiO_2 substrate followed by drying at 37°C for 2 h and then at room temperature overnight. The

obtained samples were scanned in air environment by the silicon ScanAsyst-Air probe (triangular geometry, cantilever resonance frequency 70 kHz and nominal spring constant 0.4 N/m) and information on dimensions and morphology of the vesicles were obtained from images of 512 × 512 pixels collected with different scan sizes and elaborated using the Nanoscope Analysis 1.8 software.

11.3.6 Raman spectroscopy analysis

Raman spectra of exosomes on SiO_2 substrate were collected using a confocal and high-performance Raman microscope (XploRA PLUS, HORIBA, Japan) with deep-cooled CCD detector technology.

LabSpec (Horiba, Japan) was employed to control the Raman spectroscopic system and optimise and process the acquired data. Samples were analysed through a 532 nm laser, and 10 s and 10 accumulations were chosen to optimise spectra acquisition.

Raman measurements were collected in a 550–3200 cm^{-1} range with 1800 line/mm grating. Furthermore, 10 mW of power was chosen, focusing on a 50× objective to avoid excessive surface heating. Eventually, data were manipulated using LabSpec (Horiba, Japan) to fit spectra through Lorentzian peak fitting. Thus, the data obtained are Lorentzian deconvolution of the obtained spectra.

11.3.7 Statistical comparisons

After assumption checks of normality of residuals and eventual remotion of outliers, a series of paired-sample t-test were carried out to compare low vs high altitude results. If assumption was violated, values were log-transformed before computing p values. Statistical analyses and graphs were made with GraphPad Prism (v. 10.1.1). Effect size was computed as Cohen's d for repeated mesures (dRM) that is effect size for within-subjects designs referred as Cohen's dz. controlled for the cor relation between the two sets of measurements[24], as. $d_{rm} = M_{diff} / \sqrt{(SD1^2 + SD2^2 - 2 \times r \times SD1 \times SD2)}$. Hedges' g for repeated measures (gRM) was also calculated through an online tool (Uanhoro, J. O. (2017). Effect size calculators. Available online at: https://effect-size-calculator.herokuapp.com/.), as it is corrected for both correlation and sample size.

11.4 Results

11.4.1 Urynalisis

We already reported that urine osmolality did not significantly change at high altitude (612 ± 320 to 595 ± 201; p = 0.879, d = 0.041), while urinary pH increased at altitude (from 6.15 ± 0.69 to 7.13 ± 0.32; p < 0.001, d = 1.502) [25].

Herein we report urinalysis results based on albumin and creatinin, as shown in Fig. 2. 12 out of 15 participants had increased values of albumin at high altitude (mean difference: 2.14 mg/ l, 95 % CI – 2.51 to 6.79 mg/l; p = 0.011, dRM = 0.255; gRM = 0.244). Creatinin changes were more heterogeneous across participants, although most of them experienced a reduction or a negligible increase and only one experienced a substantial increase (mean difference: 17.3 mg/dl, 95 % CI – 39.8 to 5.18 mg/dl; p = 0.121, dRM = 0.466; gRM = 0.595). As a result of creatinin and albumin changes, ACR sub stantially increased at high altitude (mean difference: 9.27 mg/g, 95 % CI 2.73 to 1.82; p = 0.009, dRM = 0.785; gRM = 0.700); at low altitude, only one participants had values over the clinical threshold of 30 mg/g and that participant remained over threshold at high altitude; instead, two participants that were under threshold at low altitude raised over the first threshold of microalbuminuria at high altitude. Spot osmolality/creatinin ratio (Uosm/Ucr) increased at altitude (mean difference: 37.3 mOsm/mmol, 95 % CI 17.6 to 57.1 mOsm/mmol; p = 0.001, dRM = 1.090; gRM = 1.026); obviously, the inverse index (Ucr/Uosm) decreased at high altitude (mean difference: 0.034 mmol/ mOsm, 95 % CI –0.056 to 0.013 mmol/mOsm; p = 0.004, dRM = 0.920; gRM = 1.013).

11.4.2 OxInflammation

As shown in Fig. 3, IL-6 consistently increased at high altitude (mean difference: 2.64 pg/ml, 95 % CI 1.56 to 3.72 pg/ml; p < 0.001, dRM = 1.554; gRM = 1.837), as did 8-isoprostane to a lower extent (mean difference: 155 pg/mg of creatinin, 95 % CI 22.6 to 287 pg/mg of cre atinin; p = 0.025, dRM = 0.678; gRM = 0.788). Instead, NOx did not change homogeneously across participants (mean difference: 101 95 % CI –93.3 to 295 μ μ M, M; p = 0.282, dRM = 0.300; gRM = 0.229).

11.4.3 Atomic force microscopy

AFM represents one of the main high-resolution imaging techniques to assess sample heterogeneity and morphological properties, as well as a useful method to confirm the efficiency of the isolation and purifica tion protocols of EVs. The urinary EVs collected at low altitude (LA) and high altitude (HA) were subjected to the same dilution treatment with MilliQ water and deposited onto SiO_2 substrates, characterized by high surface flatness. As shown in AFM micrographs reported in Fig. 4 and Figs. S1 and S2 in the Supplementary Material, the isolation protocol resulted very effective for the EVs extraction from all the samples, except for MR1-LA where no vesicular structures were detected. Indeed, the AFM probe tracked the morphology of only salt crystals and the absence of EVs was further confirmed by the disappearance of C H stretching deformation of lipid molecules in the region 2800–3200 cm^{-1} registered by Raman spectroscopy (see section Raman spectroscopy). At high scan sizes (10 μm ×10 μm), most samples were characterized by the presence of lots of sediments with micrometric dimensions in addition to smaller vesicular structures in isolated form.

Zooming into the clean areas, the vesicles showed a globular and flattened shape, due to alteration induced by the drying step. In some cases, such as for MR5 LA, MR7 HA, MR9 HA, MR12 HA, MR13 HA and MR15 HA (Figs. S1 and S2 in the Supplementary Material), the samples were characterized by a lot of contaminants and EVs lost their spherical shape as they resulted fused and incorporated into a sediment matrix.

Furthermore, the samples MR4, MR8 and MR10 showed the presence of flattened material spread over the surface which is consistent with the complete fusion of the vesicles with the consequent formation of bilayer films adhering onto the silicon substrate.

The Particle Analysis tool of the software was used to detect and measure the size of the vesicles and was applied to several AFM images to collect data from the analysis of tens of particles.

As reported in Table 1, the EVs populations showed a mean diameter in the range 70–250 nm, consistent with the presence of exosomes and small ectosomes. However, no correlation in mean diameters was detected for urinary EVs isolated at low and high altitude.

11.4.4 Raman spectroscopy

As a preliminary check before Raman spectroscopy, the 260/280 ratio from UV–vis spectrophotometry was registered immediately after the EV isolation, indicative of the relative composition of nucleic acid and protein, since phospholipids that mainly constitute vesicles' membranes are low-UV-absorbing molecules, thereby serving to evaluate the purity and relative protein or nucleic acid contamination.

We used it as quality control, resulting in values with an average of 1.055 (95 % confidence interval: 0.865 to 1.245), in line with expectations and compatible with the presence of proteins and nucleic acids[23].

The Raman spectra of EVs isolated from urine collected at low and high al titudes were compared to highlight differences in uEVs composition. Table S1 in the Supplementary Material indicates well recognized Raman bands that have been previously observed in samples of exosomes.

In Fig. 5, the most representative spectra obtained through Raman spectroscopy of EVs are reported. The regions between 1000 and 1500 cm^{-1} and between 2600 and 3200 cm^{-1} are mostly related, as described in Table S1 of the Supplementary Material, to alkyl chains (L) mainly of lipidic origin[26]. Meanwhile, the region between 1500 and 1800 cm^{-1} is typically assigned to protein and aminoacidic stretching (P)[27].

Furthermore, the peak at around 1650 cm^{-1} is the fingerprint of primary amide[27-29], while other peaks in the P region are related to Trp, Phe and Tyr[28]. Each spectrum is reported in the Fig. S3-S14 of the Sup plementary Material.

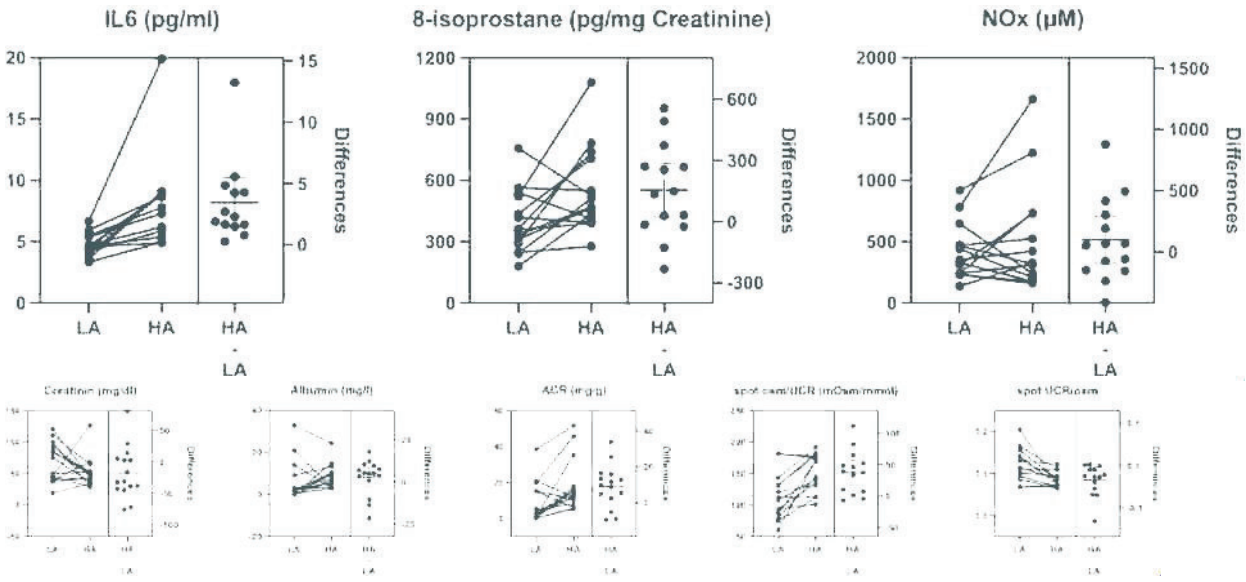

Fig. 2. Results of urinalysis; on each box, the left part represents the low vs high altitude individual comparison, while the right part represent individual high – low altitude differences

Fig. 3. Results of oxinflammatory biomarkers; on the left side of each box, the low vs high altitude individual comparison, while on the right side the individual high – low altitude differences.

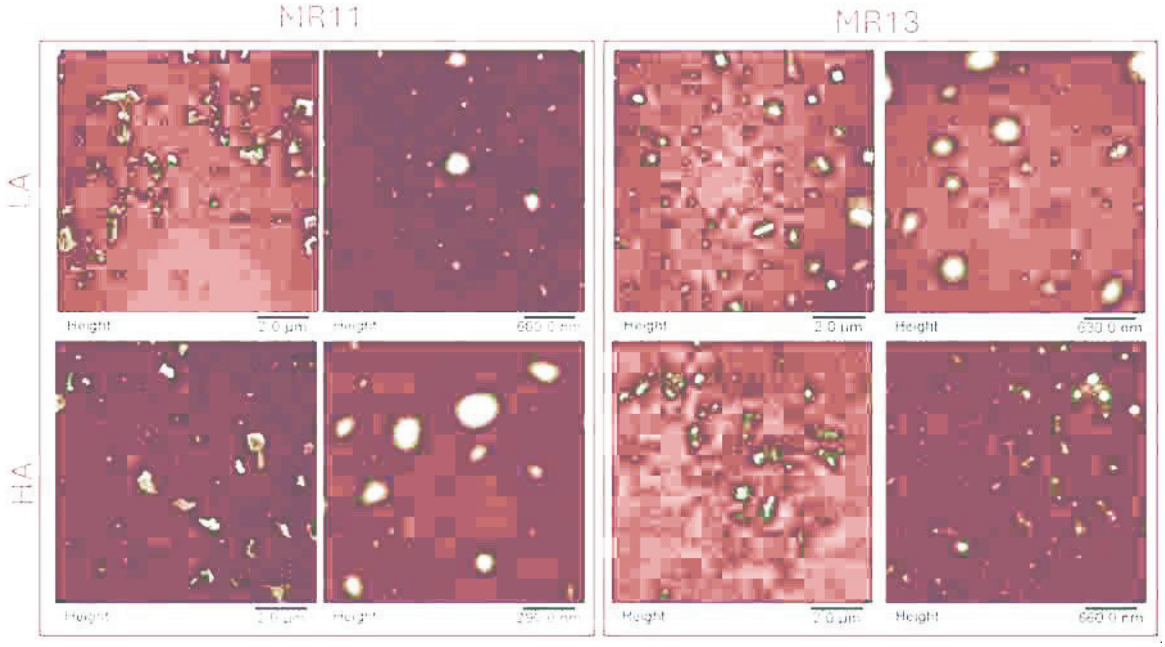

Fig. 4. AFM micrographs of topography of EVs isolated at low (LA) ad high altitude (HA) from the MR11 and MR13 urine samples collected during the Monte Rosa Expedition. For each condition two different micrographs were reported: an initial 10 µm × 10 µm scan size picture and a zoom into a smaller and particular area of the same region.

Table 1

Mean diameter (± standard deviation) values of urinary EVs isolated at low (LA) and high altitude (HA) measured by the particle analysis tool of the AFM Nanoscope Analysis software. Values are expressed in nm.

Sample	LA	HA	Sample	LA	HA	Sample	LA	HA
MR1	–	161.0 ± 70.0	**MR6**	122.3 ± 72.7	166.2 ± 103.4	**MR11**	107.2 ± 62.8	97.5 ± 59.1
MR2	103.2 ± 44.4	137.4 ± 61.7	**MR7**	221.5 ± 102.4	164.0 ± 64.9	**MR12**	96.5 ± 54.7	127.3 ± 45.9
MR3	–	71.9 ± 26.7	**MR8**	118.4 ± 59.3	252.6 ± 169.6	**MR13**	123.5 ± 96.1	111.6 ± 65.7
MR4	143.9 ± 40.5	134.2 ± 56.0	**MR9**	116.3 ± 67.4	91.0 ± 38.0	**MR14**	68.3 ± 55.2	123.9 ± 45.3
MR5	95.6 ± 43.8	100.4 ± 37.1	**MR10**	99.1 ± 42.3	143.3 ± 78.8	**MR15**	163.3 ± 91.5	82.7 ± 53.1

11.4.5 Summary report

A comprehensive account of the diverse issues pertaining to each sample, along with those encountered during the isolation of uEVs and subsequent analytical procedures, is provided in Table 2. Details of Raman spectroscopy are provided in the Supplementary Material.

11.5 Discussion

The topic of uEVs have attracted a massive interest in scholars and clinicians interested in kidney diseases. However, the possibility of using urine as a non-invasive sample has opened intriguing perspective beyond kidney pathophysiology only. For example, our group investigated uEVs to detect the effect of environmental exposure on metabolic pathways[30] and to identify the long-term effect of physical activity[31], and generally, this ever-expanding scientific field has added to technical and medical focuses an ancillary physiological focus[32]. Firstly, we explored urinary function through several biomarkers. Albumin concentration increased at high altitude, while creatinin con centration tended to decrease. As a result, albumin-to-creatinine ratio substantially increased at high altitude. The increase of this parameter usually indicates a damaged kidney, with higher risk for kidney and heart failure; however, alterations usually anticipate subsequent development of nephropathy. Rather than considering ACR values as a proxy of existing endothelial dysfunction that reflects underlying mac rovascular and microvascular disease as in clinic routine[33], we considered our results as transient sub-clinical kidney dysfunction. Uosm/Ucr serves as an estimation of renal concentrating function by normalizing urinary excretion of solutes to excretion of creatinin, assumed to be constant in non-

pathological states. Greater values can refer to acute kidney injury or dehydration status, although water loading can acutely rise values[34]. Since we did not observe substantial changes in bodily hydration status and the changes in creatinine were not homogeneous, we can interpret our results of greater spot Uosm/Ucr as an increased renal concentrating ability at high altitude. Usually, renal excretion function is estimated by serum creatinine, under the assumption that the urinary excretion rate of creatinine is steady. However, in situations where creatinine excretion changes, assuming daily renal load and urinary excretion of osmoles is stable, the Ucr/Uosm can serve as a plausible surrogate of urinary creatinine excretion rate. Indeed, neither spot urine creatinine nor osmolality per se adequately reflects urinary excretion function, while spot Ucr/Uosm, as the relative value of excreted creatinine to osmoles, is independent of actual urination intervals and volumes[35]. Diminished values should be considered negatively, and values lower than 0.08 account for the highest risk of acute accumulation of creatinine in the body, as resulting from the cross-sectional study on 3316 healthy adults[35]. Therefore, our results of lower Ucr/Uosm can be interpreted as negative changes at high altitude that remained non-pathological.

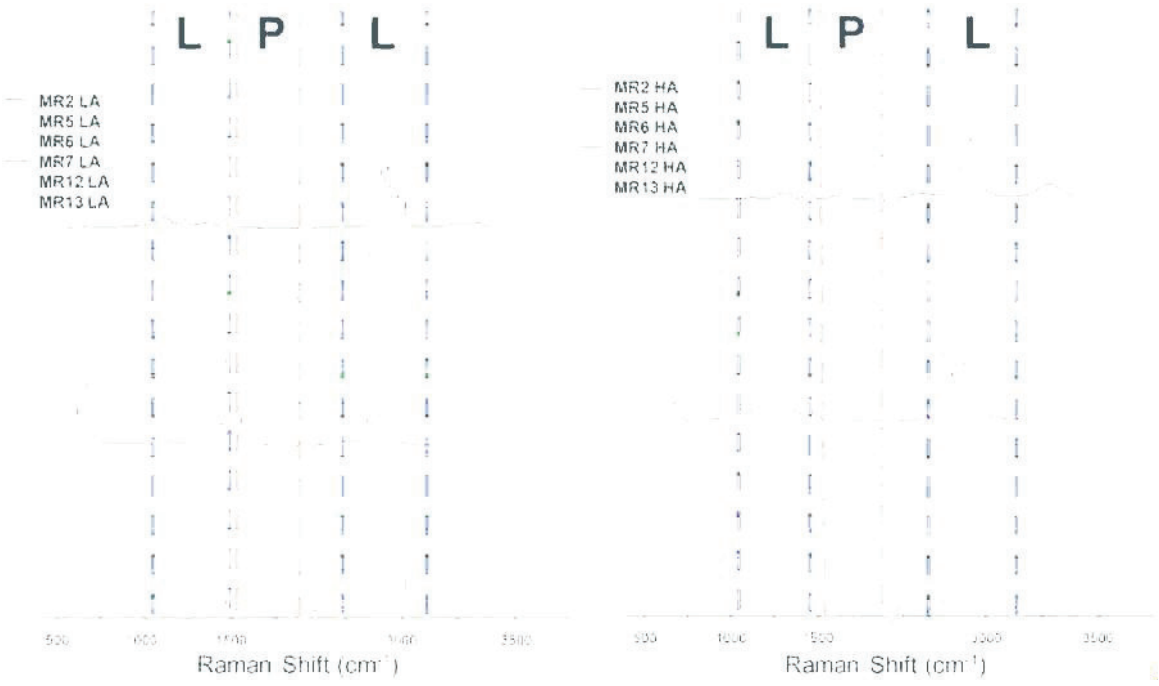

Fig. 5. Comparison between Raman spectra of some EVs isolated at low (LA, left panel) and high altitude (HA, right panel) from urine samples collected during the Monte Rosa Expedition. Orange lines highlight regions where aminoacidic and protein signals (P) are

present, while the phospholipidic regions (L) are highlighted between blue lines, as reported in Table 2. (For interpretation of the references to colour in this figure legend, the reader is referred to the web version of this article.)

11.5.1 OxInflammation

As is well known, the inflammatory state and ROS homeostasis are involved in the human hypoxic response, potentially also relevant to the mediation of diseases that induce a hypoxic state[20,36].

In particular, kidneys have an abundant blood supply: 20 %–25 % of cardiac output and high blood flow; thus, they are susceptible to the effects of hypoxia[37].

Our data once again confirm the synergy of hypoxic stress with inflammation and, in this case, with lipid damage. Despite IL-6 and 8-isoprostane increasing at high altitude, nitric oxides did not. These metabolites in spot urine have been demonstrated to be a surrogate of 24-h urine and representative of NO production[38].

Considering that NOx increased after a longer exposure to hypoxic trek[12], we may interpret our results as heterogeneous response of NO system to short-term alti tude hypoxia. Nitrites and nitrates become poorly indicative of NO production when renal function is altered[39]; however, in the present study, we found only sub-clinical alterations of renal function.

Therefore, further studies should clarify the time-dependent response of the NO system at hypoxia while specifying whether urinary NOx are altered when renal function is slightly affected.

Table 2

Summary report of urine quality and troubleshooting during the sequential processes.

ID	Sex	Age (y)	Quote	Urine inspection	Osmolality (mOsm/kg)	Isolation issues	AFM issues
MR1	m	31	LA	Dark yellow	829	No issue	No vesicles detected
			HA	No issue	568	No issue	Clean area full of spherical EVs
MR2	f	24	LA	Lots of sediment	795	No issue	Presence of contaminants with spherical EVs
			HA	No issue	538	No issue	Presence of contaminants with spherical EVs
MR3	m	36	LA	/	/	/	/
			HA	No issue	681	Possible contamination	Lots of spherical EVs with few crystals
MR4	m	34	LA	No issue	347	No issue	Presence of flattened material with few spherical and wrinkled EVs
			HA	Lots of sediment	1033	No issue	Presence of flattened material and crystals with few spherical EVs
MR5	f	25	LA	No issue	324	No issue	EVs embedded into a matrix of sediments and crystals
			HA	No issue	480	No issue	Lots of spherical and globular EVs
MR6	f	54	LA	No issue	523	No issue	EVs both in isolated and aggregated form with presence of debris
			HA	No issue	451	Not perfect sucrose level	Lots of spherical and well defined EVs
MR7	m	63	LA	Lots of sediment	1468	No issue	Lots of sediment with few large and spherical EVs
			HA	No issue	402	No issue	Presence of EVs fused and embedded into a matrix of sediments and crystals
MR8	f	29	LA		417	No issue	Lots of not spherical EVs in isolated form
			HA	Dark yellow	980	No issue	Presence of flattened material and debris with large EVs
MR9	m	29	LA	Lots of sediment, dark yellow	727	No issue	Lots of sediment with few spherical EVs
			HA	No issue	400	No issue	Lots of sediment with fused EVs
MR10	f	32	LA	Clear	93	No issue	Lots of sediments and crystals with few spherical EVs in isolated form
			HA	No issue	458	No issue	Presence of flattened material and debris with EVs in isolated form
MR11	m	24	LA	Lots of sediment	708	No issue	Lot of spherical EVs with debris
			HA	No issue	762	No issue	Presence of debris and spherical EVs
MR12	f	34	LA	Lots of sediment	649	No issue	Lots of sediments and crystals with spherical EVs in isolated form
			HA	No issue	510	No issue	Presence of EVs fused and embedded into a matrix of sediments and crystals
MR13	f	27	LA	No issue	588	No issue	Lots of spherical EVs in isolated form with some crystals
			HA	No issue	594	No issue	Presence of EVs fused and embedded into a matrix of sediments and crystals
MR14	m	51	LA	Lots of sediment	648	6 ml rather than 9 ml of volume	Lots of not spherical EVs in presence of crystals
			HA	No issue	671	No issue	Lots of globular EVs
MR15	m	26	LA	Lots of sediment	454	No issue	Lots of sediment with large EVs
			HA	No issue	477	No issue	Presence of EVs fused and embedded into a matrix of sediments and crystals

11.5.2 Insights and technical considerations from AFM and Raman spectroscopy

Despite the growing interest, the use of EVs in clinical applications is limited due to the lack of standardization in EVs isolation and analysis, especially when dealing with complex and highly heterogeneous biological samples. Different strategies for EVs characterization are currently available, including electron microscopy, atomic force microscopy (AFM), flow cytometry and various chemical/biological techniques which provide important information on vesicle morphology and composition. Furthermore, the technological advances in metabolomics provide a powerful approach to expand EVs research and the two main analytical techniques that have recently been applied to EVs metabolomics are nuclear magnetic resonance (NMR) and high-resolution mass spectrometry (MS)[40,41]. NMR is a highly reproducible spectroscopic method based on the energy absorption and re-emission of the atomic nuclei in an external magnetic field. 1H NMR is the most targeted nucleus for its natural abundance in biological samples[42,43].

One- dimensional NMR (1D-NMR) spectra using a single frequency axis is the most often applied method in metabolomics studies, even though to have a better peak resolution, the 2D-NMR method is sometimes applied to separate overlapping spectral peaks that cannot be identified with 1D- NMR, especially in the case of complex biological matrices[44,45].

Mass spectrometry (MS) acquires spectral data in the form of a mass- to-charge ratio and a relative abundance of the measured compounds, which has been extensively studied for metabolomics.

Compared to NMR, the MS method is considered to have higher specificity and sensitivity given a wide range of instrumental and technical variants that are currently available for metabolite characterization. On the other hand, recent studies have shown applications of Raman spectroscopy as a fast and alternative tool for characterization, compositional studies, and purity assessment of EVs derived from different tissues and biological fluids. Raman spectroscopy, based on anelastic scattering of light, is beneficial in being a label-free, chemical specific, and relatively non-destructive technique detecting molecular vibrations that can identify essential components present in EVs, such as

membrane lipids, proteins and nucleic acids, without the need to disrupt the EVs before the measurements.

Considering this background, the effects of high-altitude exposure on the parameters of extracellular vesicle (EVs) isolated from urine were studied with a combination of complementary techniques.

The EVs are important for physiological adaptations, also triggered by altitude hypoxia. The urinary EVs were obtained by a well standardized protocol of isolation by ultracentrifugation and characterized by AFM. As shown in AFM micrographs reported in Fig. 4 and S1-S2 of Supplementary Materials, the isolation protocol resulted very effective for the EVs extraction. Indeed, most of the samples revealed the presence of a high number of globular shaped extracellular vesicles present on the substrates. In the majority of the samples, the EVs collected at high altitude showed a higher concentration of contaminants and salts with respect to EVs collected at low altitude, resulting in EVs fused together and incorporated into a sediment matrix. Raman spectroscopy was also used to identify the presence of EVs molecular signatures or biomarkers in response to the exposure to high altitude. In line with AFM results, the isolation procedure resulted very effective for the EVs extraction, since most of the Raman spectra showed the typical phospholipidic pattern related to C H stretching deforma tion of lipid molecules in the region 2800–3200 cm 1 . As reported in Fig. 5, the most significant part of those spectra are clear, confirming that Raman spectroscopy is a suitable technique to analyze purity in EVs obtained through the sucrose gradient technique, which contrasts with the literature[46].

However, as shown in Fig. 5, the Raman spectra of several samples collected at high altitudes seem to be more disturbed than their low altitude counterparts. Indeed, as explained in more detail in Supplementary Materials, EVs obtained by urine collected after the body has been stressed by altitude seem to contain contaminants peaks (i.e. peaks connected with aminoacids or nucleic acids)[46,47], making the purification process less efficient. The presence of more salts and contaminants outside

the vesicles could be responsible of the distortion of the phospholipid CH_2 and CH_3 stretching bands recorded in some samples.

Furthermore, shifts of these bands and changes in the ratio of peaks are usually associated with different interactions of phospholipids and guest inserted in the vesicle bilayer, as already widely described in the literature.

Both changes refer to various packing and degrees of freedom of hydrocarbon chains of phospholipidic structures[48-52]. Fig. 6 reports the Raman spectra of the unique samples out of 15 pairs whose high-altitude sample spectrum appears less contaminated than the low altitude collected sample one.

Indeed, as shown in Fig. 6, both the spectra, the one referring to HA sample and that referring to the LA sample, seem contaminated, but the shape of the band indicative of the phospholipid alkyl chain of the LA sample is clearly more disturbed and almost unidentifiable.

This could be related, as in samples collected at high altitudes described broadly above, to a crown protein that shields EVs, reducing the contribution to the spectrum of the lipidic chain in favor of protein domain signals[53].

11.5.3 Limitations

We cannot exclude that changes in urinary pH affected uEV physi ology and isolation, as reported[14]. The rise in urinary pH was ex pected, since metabolic acidosis is a normal compensatory of humans at high altitude in response to respiratory alkalosis. Acetazolamide exac erbates this mechanism by inhibiting carbonic anhydrase in the kidneys, resulting in bicarbonaturia and generating metabolic acidosis thereby attenuating the effects of respiratory alkalosis due to the hypoxic- induced rise in ventilation. This drug also induces diuresis and natri uresis[2]. However, during this expedition dehydration did not occur, as evidenced by urine osmolality and by other analyses[25], likely because trained staff instructed all participants how to avoid dehydra tion. This drug could have potentially

influenced the results, by altering uEVs' release, cargo and subtype; however, all participants took the same amount of drug with the same time schedule, thus reducing the possible confounding effects.

We cannot rule out the possibility that the non-use of protease inhibitors altered the protein composition of the sample; however, all the samples were processed identically, and not all EV proteins are prone to proteolysis in urine[14].

The necessity to transport urine from high to low altitude may have possibly altered the samples; however, the difference on storage between the samples obtained at low vs high altitude consisted in a few hours, i.e., the transport from Capanna Margherita to Alagna Valsesia; all the rest of sample storage and transportation was identical.

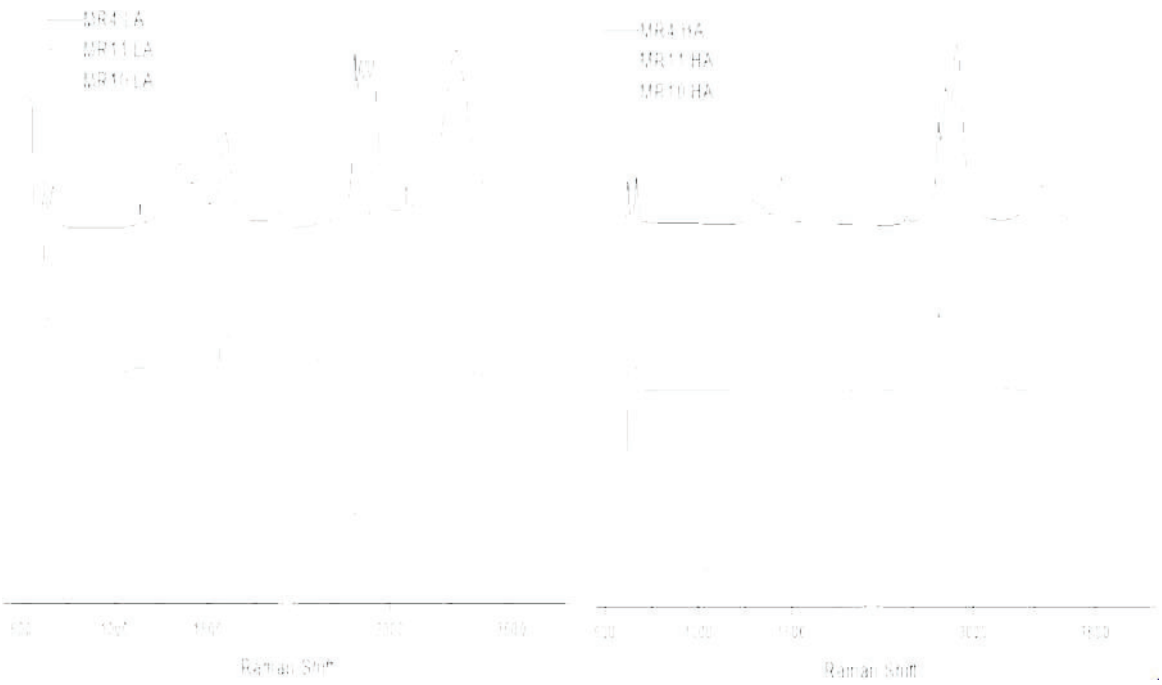

Fig. 6. Comparison between some samples collected at low altitude (LA) and high altitude (HA), on the left and on the right, respectively.

11.6 Conclusions

Under exposure to altitude hypoxia, the lower partial pressure of oxygen leads the body to implement a series of compensatory mecha nisms, collectively affecting human physiology.

After 4 days across from low to high altitude, a sub-clinical dysfunction occurred due to short- term stress on the kidneys; additionally, a synergy of hypoxic stress with inflammation and lipid damage was detected in urine samples.

The combination of AFM and Raman spectroscopy allowed to verify the effectiveness and purity of uEVs isolation. In the majority of the samples, the EVs collected at high altitude contained more contaminants andsalts, resulting in EVs fused together and incorporated into a sediment matrix, with Raman peaks connected with aminoacids or nucleic acids that altered the typical phospholipidic pattern.

The sub-clinical impairment of renal function at high altitude likely altered both the cargo of uEVs and the fluid in which uEVs were contained, thereby putatively altered crown protein that shields EVs. The high-altitude urineprint that includes clinical and oxinflammatory variable linked with EVs biology represents a promising avenue of research in the field of environmental physiology, with the potential for significant impli cations in the domain of translational medicine for hypoxia.

References

(1) A.T.K. Cockett, E. Bors, The influence of simulated altitude (18,000 feet) on uroflowmetry, UIN 18 (1964) 357–361, https://doi.org/10.1159/000279255.

(2) D.E. Leaf, D.S. Goldfarb, Mechanisms of action of acetazolamide in the prophylaxis and treatment of acute mountain sickness, J. Appl. Physiol. 102 (2007) 1313–1322, https://doi.org/10.1152/japplphysiol.01572.2005.

(3) G. Ohno, S. Otani, A. Ikeda, Human beings in Antarctica, in: M. Kanao, G. Toyokuni, M. Yamamoto (Eds.), Antarctica - A Key To Global Change, IntechOpen, 2018, https://doi.org/10.5772/intechopen.81974.

(4) V. Verratti, S. Mrakic-Sposta, M. Moriggi, A. Tonacci, S. Bhandari, D. Migliorelli, A. Bajracharya, D. Bondi, E.F. Agro, P. Cerretelli, Urinary physiology and hypoxia: ` a pilot study of moderate-altitude trekking effects on urodynamic indexes, Am. J. Physiol. Ren. Physiol. 317 (2019) F1081–F1086, https://doi.org/10.1152/ajprenal.00333.2019.

(5) V. Verratti, D. Bondi, A. Shakir, T. Pietrangelo, R. Piccinelli, V.M. Altieri, D. Migliorelli, A. Tafuri, Uroflowmetry and altitude hypoxia: a report from healthy Italian trekkers and nepali porters during himalayan expedition, Adv. Exp. Med. Biol. 1289 (2021) 99–105, https://doi.org/10.1007/5584_2020_543.

(6) A. Richardson, P. Watt, N. Maxwell, Hydration and the physiological responses to acute normobaric hypoxia, Wilderness Environ. Med. 20 (2009) 212–220, https:// doi.org/10.1580/09-WEME-OR-272R1.1.

(7) S.M. Zouboules, H.C. Lafave, K.D. O'Halloran, T.D. Brutsaert, H.E. Nysten, C. E. Nysten, C.D. Steinback, M.T. Sherpa, T.A. Day, Renal reactivity: acid-base compensation during incremental ascent to high altitude, J. Physiol. Lond. 596 (2018) 6191–6203, https://doi.org/10.1113/JP276973.

(8) Cristiano, F.; Posari, C.; d'Angelo, B.; Schiazza, A.; Gigante, A.; Caravelli, L.; Piano, A.; Fulle, S.; Cristiano, J.; Di Matteo, G.; Rosa Diez, G.; Verratti, V. *How to Assess the Glomerular Filtration Rate, and Which Method Is Deemed Most Reliable?* G. Ital. Nefrol. 2024, *41*, 2024–vol4. https://doi.org/10.69097/41-04-2024-02E.C.

(9) Witte, H.J. Lambers Heerspink, D. de Zeeuw, S.J.L. Bakker, P.E. de Jong, R. Gansevoort, First morning voids are more reliable than spot urine samples to assess microalbuminuria, J. Am. Soc. Nephrol. 20 (2009) 436–443, https://doi. org/10.1681/ASN.2008030292.

(10) P. Vart, L. Scheven, H.J. Lambers Heerspink, P.E. de Jong, D. de Zeeuw, R. T. Gansevoort, PREVEND Study Group and the RENAAL Investigators, Urine Albumin-Creatinine Ratio Versus Albumin Excretion for Albuminuria Staging: A Prospective Longitudinal Cohort Study, Am. J. Kidney Dis. 67 (2016) 70–78, https://doi.org/10.1053/j.ajkd.2015.05.025.

(11) H.M. Schenk, S.L. van Ockenburg, M.C. Nawijn, P. De Jonge, J.G.M. Rosmalen, Identification of inflammatory markers suitable for non-invasive, repeated measurement studies in biobehavioural research: A feasibility study, PLoS One 14 (2019) e0221993, https://doi.org/10.1371/journal.pone.0221993.

(12) S. Mrakic-Sposta, D. Biagini, D. Bondi, T. Pietrangelo, A. Vezzoli, T. Lomonaco, F. Di Francesco, V. Verratti, OxInflammation at high altitudes: a proof of concept from the Himalayas, Antioxidants 11 (2022) 368, https://doi.org/10.3390/ antiox11020368.

(13) D. Biagini, S. Mrakic-Sposta, D. Bondi, S. Ghimenti, A. Lenzi, F. Vivaldi, C. Santangelo, V. Verratti, T. Pietrangelo, A. Vezzoli, G. Giardini, C. Oger, J.- M. Galano, L. Balas, T. Durand, G. D'Angelo, T. Lomonaco, F. Di Francesco, A MEPS-UHPLC-MS/MS analytical platform to detect isoprostanoids and specialized pro-resolving mediators in the urinary extracellular vesicles of mountain ultramarathon runners, Talanta 279 (2024) 126619, https://doi.org/ 10.1016/j.talanta.2024.126619.

(14) U. Erdbrügger, C.J. Blijdorp, I.V. Bijnsdorp, F.E. Borras, D. Burger, B. Bussolati, J. `B. Byrd, A. Clayton, J.W. Dear, J.M. Falcon-Pérez, C. Grange, A.F. Hill, ´H. Holthofer, E.J. Hoorn, G. Jenster, C.R. Jimenez, K. Junker, J. Klein, M.A. Knepper, E.H. Koritzinsky, J.M. Luther, M. Lenassi, J. Leivo, I. Mertens, L. Musante, E. Oeyen, M. Puhka, M.E. Royen, C. Sanchez, C. Soekmadji, ´V. Thongboonkerd, V. Steijn, G. Verhaegh, J.P. Webber, K. Witwer, P.S.T. Yuen, L. Zheng, A. Llorente, E.S. Martens-Uzunova, Urinary extracellular vesicles: A position paper by the Urine Task Force of the International Society for Extracellular Vesicles, J. Extracellular Vesicles 10 (2021), https://doi.org/10.1002/jev2.12093.

(15) M. Logozzi, R. Di Raimo, D. Mizzoni, S. Fais, The potentiality of plant-derived nanovesicles in human health—a comparison with human exosomes and artificial nanoparticles, Int. J. Mol. Sci. 23 (2022) 4919, https://doi.org/10.3390/ ijms23094919.

(16) N. Bister, C. Pistono, B. Huremagic, J. Jolkkonen, R. Giugno, T. Malm, Hypoxia and extracellular vesicles: A review on methods, vesicular cargo and functions, J. Extracell Vesicles 10 (2020) e12002, https://doi.org/10.1002/jev2.12002.

(17) D. Bondi, L. Lobefalo, F. Ciampini, A. Rapagnani, C. Santangelo, P. Pignatelli, S. Bonan, V. Verratti, Clinical features and health-threatening conditions of the trek to Capanna Margherita, J. Sports Med. Phys. Fitness 63 (2023) 927–933, https:// doi.org/10.23736/S0022-4707.23.14859-6.

(18) M.E. van Royen, C. Soekmadji, C. Grange, J.P. Webber, T. Tertel, M. Droste, A. Buescher, B. Giebel, G.W. Jenster, A. Llorente, C.J. Blijdorp, D. Burger, U. Erdbrügger, E.S. Martens-Uzunova, The quick reference card “Storage of urinary EVs” – A practical guideline tool for research and clinical laboratories, J. Extracellular Vesicles 12 (2023) 12286, https://doi.org/10.1002/jev2.12286.

(19) J.A. Welsh, D.C.I. Goberdhan, L. O’Driscoll, E.I. Buzas, C. Blenkiron, B. Bussolati, H. Cai, D. Di Vizio, T.A.P. Driedonks, U. Erdbrügger, J.M. Falcon-Perez, Q.-L. Fu, A. F. Hill, M. Lenassi, S.K. Lim, M.G. Mahoney, S. Mohanty, A. Moller, R. Nieuwland, ¨T. Ochiya, S. Sahoo, A.C. Torrecilhas, L. Zheng, A. Zijlstra, S. Abuelreich, R. Bagabas, P. Bergese, E.M. Bridges, M. Brucale, D. Burger, R.P. Carney, E. Cocucci, R. Crescitelli, E. Hanser, A.L. Harris, N.J. Haughey, A. Hendrix, A. R. Ivanov, T. Jovanovic-Talisman, N.A. Kruh-Garcia, V. Ku’ulei-Lyn Faustino, D. Kyburz, C. Lasser, K.M. Lennon, J. Lotvall, A.L. Maddox, E.S. Martens-Uzunova, ¨R.R. Mizenko,L.A. Newman, A. Ridolfi, E. Rohde, T. Rojalin, A. Rowland, A. Saftics, U.S. Sandau, J.A. Saugstad, F. Shekari, S. Swift, D. Ter-Ovanesyan, J. P. Tosar, Z. Useckaite, F. Valle, Z. Varga, E. van der Pol, M.J.C. van Herwijnen, M. H.M. Wauben, A.M. Wehman, S. Williams, A. Zendrini, A.J. Zimmerman, MISEV Consortium, C. Thery, K.W. Witwer, Minimal information for studies of ´ extracellular vesicles (MISEV2023): From basic to advanced approaches, J. Extracell Vesicles 13 (2024) e12404, https://doi.org/10.1002/jev2.12404.

(20) S. Mrakic-Sposta, M. Gussoni, C. Dellanoce, M. Marzorati, M. Montorsi, L. Rasica, L. Pratali, G. D’Angelo, M. Martinelli, L. Bastiani, L. Di Natale, A. Vezzoli, Effects of acute and sub-acute hypobaric hypoxia on oxidative stress: a field study in the Alps, Eur. J. Appl. Physiol. 121 (2021) 297–306, https://doi.org/10.1007/s00421- 020-04527-x.

(21) S. Mrakic-Sposta, A. Vezzoli, F. D’Alessandro, M. Paganini, C. Dellanoce, D. Cialoni, G. Bosco, Change in oxidative stress biomarkers during 30 days in saturation dive: a pilot study, Int. J. Environ. Res. Public Health 17 (2020) E7118, https://doi.org/10.3390/ijerph17197118.

(22) A. Brizzolari, G. Bosco, A. Vezzoli, C. Dellanoce, A. Barassi, M. Paganini, D. Cialoni, S. Mrakic-Sposta, Seasonal oxy-inflammation and hydration status in non-elite freeskiing racer: a pilot study by non-invasive analytic method, Int. J. Environ. Res. Public Health 20 (2023) 3157, https://doi.org/10.3390/ijerph20043157.

(23) D. Sun, Z. Zhao, S. Spiegel, Y. Liu, J. Fan, P. Amrollahi, J. Hu, C.J. Lyon, M. Wan, T. Y. Hu, Dye-free spectrophotometric measurement of nucleic acid-to-protein ratio for cell-selective extracellular vesicle discrimination, Biosens. Bioelectron. 179 (2021) 113058, https://doi.org/10.1016/j.bios.2021.113058.

(24) D. Lakens, Calculating and reporting effect sizes to facilitate cumulative science: a practical primer for t-tests and ANOVAs, Front. Psychol. 4 (2013), https://doi.org/ 10.3389/fpsyg.2013.00863.

(25) C. Santangelo, V. Verratti, S. Mrakic-Sposta, F. Ciampini, S. Bonan, P. Pignatelli, T. Pietrangelo, S. Pilato, S. Moffa, A. Fontana, R. Piccinelli, C.L. Donne, L. Lobefalo, M. Beccatelli, P.L. Rizzini, D. Seletti, R. Mecca, T. Beccatelli, D. Bondi, Nutritional physiology and body composition changes during a rapid ascent to high altitude, Appl. Physiol. Nutr. Metab. (2024), https://doi.org/10.1139/apnm-2023-0338.

(26) J.R. Beattie, S.E.J. Bell, B.W. Moss, A critical evaluation of Raman spectroscopy for the analysis of lipids: fatty acid methyl esters, Lipids 39 (2004) 407–419, https:// doi.org/10.1007/s11745-004-1245-z.

(27) A. Rygula, K. Majzner, K.M. Marzec, A. Kaczor, M. Pilarczyk, M. Baranska, Raman spectroscopy of proteins: a review, J. Raman Spectrosc. 44 (2013) 1061–1076, https://doi.org/10.1002/jrs.4335.

(28) J.L. Lippert, D. Tyminski, P.J. Desmeules, Determination of the secondary structure of proteins by laser Raman spectroscopy, J. Am. Chem. Soc. 98 (1976) 7075–7080, https://doi.org/10.1021/ja00438a057.

(29) L.D. Barron, Z.Q. Wen, L. Hecht, Vibrational Raman optical activity of proteins, J. Am. Chem. Soc. 114 (1992) 784–786, https://doi.org/10.1021/ja00028a069.

(30) P. Cocci, D. Bondi, C. Santangelo, T. Pietrangelo, V. Verratti, A. Cichelli, G. Caprioli, F.K. Nzekoue, M.L.K. Nguefang, G. Sagratini, G. Mosconi, F. A. Palermo, Extracellular vesicles in environmental toxicological studies: association between urinary concentrations of phthalate metabolites and exosomal miRNA expression profiles, Int. J. Mol. Sci. 25 (2024) 4876, https://doi.org/ 10.3390/ijms25094876.

(31) T. Pietrangelo, C. Santangelo, D. Bondi, P. Cocci, R. Piccinelli, F. Piacenza, E. Rosato, S.N.A. Azman, E. Binetti, M. Farina, M. Locatelli, V. Brunetti, C. Le Donne, L. Marramiero, E.S. Di Filippo, V. Verratti, S. Fulle, V. Scollo, F. Palermo, Endurance-dependent urinary extracellular vesicle signature: shape, metabolic miRNAs, and purine content distinguish triathletes from inactive people, Pflugers Arch. - Eur. J. Physiol. (2023), https://doi.org/10.1007/s00424-023-02815-x.

(32) P. Svenningsen, R. Sabaratnam, B.L. Jensen, Urinary extracellular vesicles: Origin, role as intercellular messengers and biomarkers; efficient sorting and potential treatment options, Acta Physiol (Oxford) 228 (2020) e13346, https://doi.org/ 10.1111/apha.13346.

(33) H.C. Gerstein, J.F.E. Mann, Q. Yi, B. Zinman, S.F. Dinneen, B. Hoogwerf, J.P. Halle, ´ J. Young, A. Rashkow, C. Joyce, S. Nawaz, S. Yusuf, for the H.S.I. for the HOPE Study Investigators, Albuminuria and risk of cardiovascular events, death, and heart failure in diabetic and nondiabetic individuals, JAMA 286 (2001) 421–426, https://doi.org/10.1001/jama.286.4.421.

(34) S. Godevithanage, P.P. Kanankearachchi, M.P. Dissanayake, T.A. Jayalath, N. Chandrasiri, R.P. Jinasena, R.P.V. Kumarasiri, C.D.A. Goonasekera, Spot urine osmolality/creatinine ratio in healthy humans, KBR 33 (2010) 291–296, https:// doi.org/10.1159/000316509.

(35) S.-P. Hsu, C.-T. Chien, Reference intervals of spot urine creatinine-to-osmolality ratio as a surrogate of urinary creatinine excretion rate, Dis. Markers 2022 (2022) e3549047, https://doi.org/10.1155/2022/3549047.

(36) S. Malacrida, G. Strapazzon, S. Mrakic-Sposta, M. Pun, A. Cogo, Editorial: human molecular and physiological responses to hypoxia, Front. Physiol. 13 (2022) 888005, https://doi.org/10.3389/fphys.2022.888005.

(37) S.-Y. Wang, J. Gao, J.-H. Zhao, Effects of high altitude on renal physiology and kidney diseases, Front. Physiol. 13 (2022) 969456, https://doi.org/10.3389/ fphys.2022.969456.

(38) S. Kurioka, K. Koshimura, M. Sugitani, Y. Murakami, M. Nishiki, Y. Kato, Analysis of urinary nitric oxide metabolites in healthy subjects, Endocr. J. 46 (1999) 421–428, https://doi.org/10.1507/endocrj.46.421.

(39) J.K. Williams, M.J. Smallwood, N. Benjamin, R.J. D'Souza, A.C. Shore, P.
G. Winyard, M. Gilchrist, Renal nitrate clearance in chronic kidney disease, Nitric Oxide 97 (2020) 16–19, https://doi.org/10.1016/j.niox.2020.01.011.

(40) S. Kreimer, A.M. Belov, I. Ghiran, S.K. Murty, D.A. Frank, A.R. Ivanov, Mass- spectrometry-based molecular characterization of extracellular vescicle: lipidomics and proteomics, J. Proteome Res. 14 (2015) 2367–2384, https://doi.org/10.1021/ pr501279t.

(41) M. Agudiez, P.J. Martinez, M. Martin-Lorenzo, A. Heredero, A. Santiago- Hernandez, D. Molero, J.M. Garcia-Segura, G. Aldamiz-Echevarria, G. Alvarez- Llamas, Analysis of urinary exosomal metabolites identifies cardiovascular risk signatures with added value to urine analysis, BMC Biol. 18 (2020) 192, https:// doi.org/10.1186/s12915-020-00924-y.

(42) A. Emwas, R. Roy, R.T. McKay, L. Tenori, E. Saccenti, G.A. Nagana Gowda, D. Raftery, F. Alahmari, L. Jaremko, M. Jaremko, D.S. Wishart, NMR spectroscopy for metabolomics research, Metabolites 9 (2019) 123, https://doi.org/10.3390/ metabo9070123.

(43) K. Chandra, S. Al-Harthi, S. Sukumaran, F. Almulhim, A. Emwas, H.S. Atreya, L. Jaremko, M. Jaremko, NMR-based metabolomics with enhanced sensitivity, RSC Adv. 11 (2021) 8694–8700, https://doi.org/10.1039/d1ra01103k.

(44) U. Singh, S. Alsuhaymi, R. Al-Nemi, A. Emwas, M. Jaremko, Compound-specific 1D ^{1}H NMR pulse sequence selection for metabolomics analyses, ACS Omega 8 (2023) 23651–23663, https://doi.org/10.1021/acsomega.3c01688.

(45) U. Singh, A. Emwas, M. Jaremko, Enhancement of weak signals by applying a suppression method to high-intense methyl and methylene signals of lipids in NMR spectroscopy, RSC Adv. 14 (2024) 26873, https://doi.org/10.1039/d4ra03019b.

(46) A. Gualerzi, S.A.A. Kooijmans, S. Niada, S. Picciolini, A.T. Brini, G. Camussi, M. Bedoni, Raman spectroscopy as a quick tool to assess purity of extracellular vesicle preparations and predict their functionality, J. Extracellular Vesicles 8 (2019) 1568780, https://doi.org/10.1080/20013078.2019.1568780.

[47] J. Zini, H. Saari, P. Ciana, T. Viitala, A. Lohmus, J. Saarinen, M. Yliperttula, Infrared and Raman spectroscopy for purity assessment of extracellular vesicles, Eur. J. Pharm. Sci. 172 (2022) 106135, https://doi.org/10.1016/j.ejps.2022.106135.

[48] E. Kocisova, M. Prochazka, Drop-coating deposition Raman spectroscopy of liposomes, J. Raman Spectrosc. 42 (2011) 1606–1610, https://doi.org/10.1002/ jrs.2915.

[49] R. Zappacosta, M.D. Giulio, V. Ettorre, D. Bosco, C. Hadad, G. Siani, S. Bartolomeo, A. Cataldi, L. Cellini, A. Fontana, Liposome-induced exfoliation of graphite to few-layer graphene dispersion with antibacterial activity, J. Mater. Chem. B 3 (2015) 6520–6527, https://doi.org/10.1039/C5TB00798D.

[50] R. Gharib, S. Fourmentin, C. Charcosset, H. Greige-Gerges, Effect of hydroxypropyl-β–cyclodextrin on lipid membrane fluidity, stability and freeze- drying of liposomes, J. Drug Deliv. Sci. Technol. 44 (2018) 101–107, https://doi. org/10.1016/j.jddst.2017.12.009.

[51] J. Giancaspro, P. Scollan, J. Rosario, E. Miller, S. Braziel, S. Lee, Structural determination of model phospholipid membranes by Raman spectroscopy: Laboratory experiment, Biochem. Mol. Biol. Educ. 50 (2022) 181–192, https://doi. org/10.1002/bmb.21603.

[52] S. Moffa, S. Carradori, F. Melfi, A. Fontana, M. Ciulla, P. Di Profio, M. Aschi, R. Wolicki, S. Pilato, G. Siani, Fine-tuning of membrane permeability by reversible photoisomerization of aryl-azo derivatives of thymol

embedded in lipid nanoparticles, Colloids Surf. B: Biointerfaces 241 (2024) 114043, https://doi.org/10.1016/j.colsurfb.2024.114043.

[53] M. Heidarzadeh, A. Zarebkohan, R. Rahbarghazi, E. Sokullu, Protein corona and exosomes: new challenges and prospects, Cell Commun. Signal. 21 (2023) 64, https://doi.org/10.1186/s12964-023-01089-1.

12 Phenolic terpenes in liposomal bilayers: Unraveling physicochemical interactions and membrane perturbation via biophysical and computational approaches

DOI: https://doi.org/10.1016/j.jcis.2025.138358

12.1 Introduction

Understanding the interactions between small amphiphilic or hydrophobic molecules and lipid bilayers is a central topic in colloid and interface science, with broad implications ranging from drug delivery and nanocarrier design to antimicrobial agent development and membrane biophysics[1-5].

Lipid membranes are dynamic soft interfaces characterized by a delicate balance between hydrophobic and polar interactions, whose perturbation by molecular guests can induce changes in membrane fluidity, permeability, phase behaviour, and domain formation[2,6-10]. Elucidating the underlying mechanisms of guest-bilayer interactions is thus essential for a predictive understanding of colloidal stability, transport properties, and functional performance in biological and biomimetic systems.

Model lipid bilayers, particularly unilamellar liposomes, provide a well-controlled environment for studying these interactions. As simplified analogues of biological membranes, liposomes allow precise control over composition, curvature, and thermodynamic parameters, making them ideal for systematic investigations of structure-property relationships[3]. Their versatility has led to widespread use both as drug delivery carriers for hydrophobic and hydrophilic molecules[11-13], and as in vitro models to study mechanisms and kinetics of molecular transport[14-18].

Advanced biophysical techniques such as dynamic light scattering (DLS), differential scanning calorimetry (DSC), and Raman spectroscopy provide quantitative insights into how guest molecules influence bilayer organization, thermotropic transitions, and mechanical stability. When combined with molecular dynamics (MD) simulations, these tools offer a comprehensive framework for interpreting complex behaviour at multiple scales, including guest localization preferences, the nature of in teractions (e.g., hydrogen bonding or hydrophobic contacts), and the resulting impact on membrane organization and dynamics. In this context, we investigate the interaction of the phenolic monoterpenes thymol (2-isopropyl-5-methylphenol) and carvacrol (5- isopropyl-2-methylphenol), along with selected ether derivatives (Fig. 1), with model membranes composed of 1-palmitoyl-2-oleoyl-sn- glycero-3-phosphocholine (POPC). Thymol and carvacrol, major com ponents of essential oils from thyme (Thymus vulgaris L.) and oregano (Origanum vulgare L.), exhibit a wide range of biological activities, including antiseptic, anti-inflammatory, antifungal, and antimicrobial effects, largely attributed to their interaction with bacterial membranes[19–29]. The antimicrobial action is believed to involve insertion and accumulation within lipid bilayers, causing alterations in membrane f luidity, lipid order, and permeability[27–30]. The membrane-disruptive potential of thymol and carvacrol is thought to arise from a combination of hydrophobic partitioning and hydrogen bonding at the lipid-water interface, particularly via the phenolic -OH group[27,29,30]. Modifying this group by replacing it with ether -OR substituents, alters polarity, hydrogen bonding capacity, and lipophilicity, potentially affecting membrane interactions and antimicrobial efficacy. Some ether derivatives retain activity, although the precise impact depends on the nature of the substituent[31,32]. This study focuses on elucidating the molecular basis of terpene-lipid bilayer interactions by investigating how subtle chemical modifications, specifically, the replacement of the phenolic -OH group with ether -OR groups, affect the incorporation, localization, and membrane-perturbing effects of thymol, carvacrol, and their derivatives in POPC liposomes. We applied a multi-technique strategy involving DLS to determine vesicle size and colloidal stability, DSC to monitor thermotropic behaviour, Raman spectroscopy to probe bilayer organization and terpene-lipid interactions, and fluorescence leakage

assays to evaluate membrane permeability. By combining these experimental biophysical techniques with molecular dynamics simulations, we reveal that these monoterpenes preferentially interact with the polar headgroup region of the bilayer, inducing significant changes in membrane permeability and thermotropic behaviour without compromising vesicle integrity. Our key findings demonstrate that the presence of a free hydroxyl group strongly enhances membrane permeability through increased leakage in the initial burst phase, while ether derivatives modulate this effect primarily at higher terpene-to-lipid ratios. These results highlight the critical role of specific molecular features in governing guest-bilayer interactions and their consequences for membrane structure and stability. Notably, although POPC liposomes are widely used as model mem branes, their thermotropic behaviour in the presence of small amphi philic or hydrophobic molecules remains understudied by calorimetric methods. Our work represents one of the few comprehensive DSC ana lyses of POPC vesicles incorporating bioactive compounds, providing novel insights into the thermal stability and structural organization of these soft, self-assembled systems. By connecting chemical structure with molecular behaviour at lipid interfaces, this study not only advances fundamental understanding of membrane-active agents but also offers a framework that could inform the rational design of bioactive materials with tailored membrane in teractions for biomedical and antimicrobial applications.

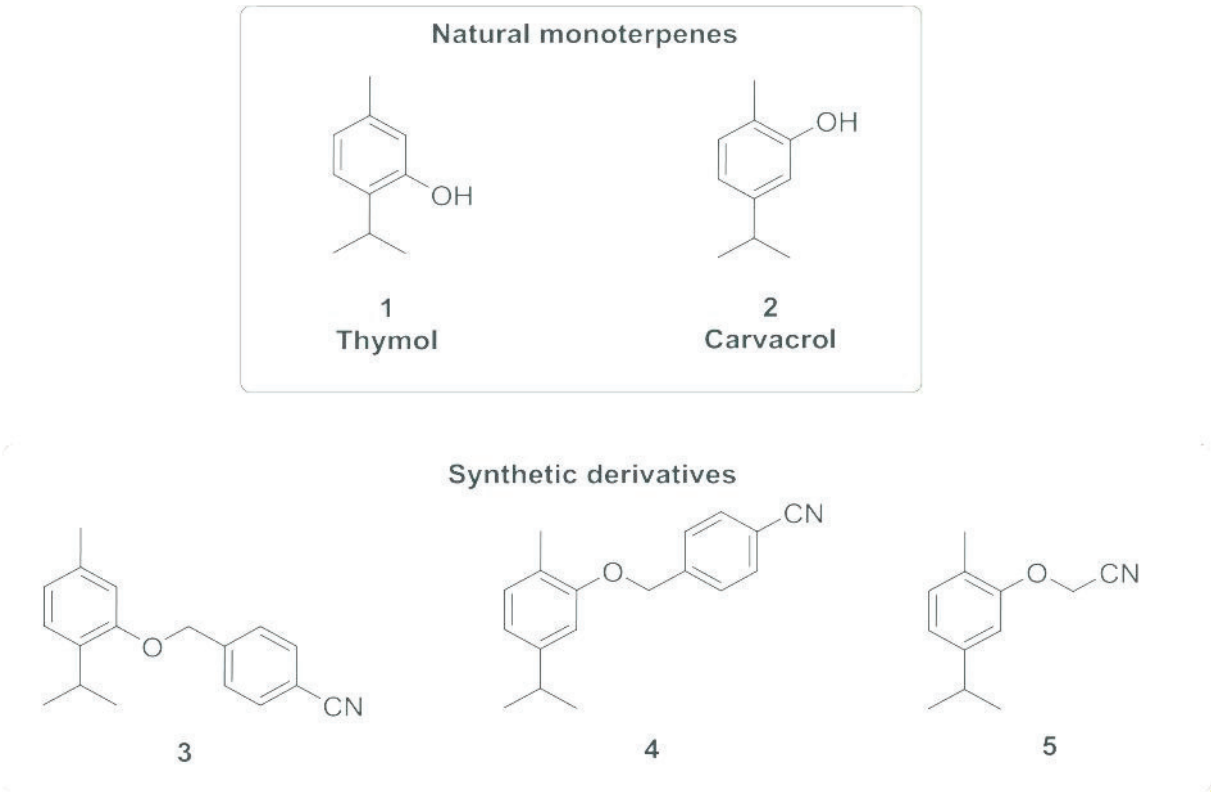

Fig. 1. Structures of the selected terpenes and derivatives.

12.2 Experimental

12.2.1 Chemicals and materials

1-Palmitoyl-2-oleoyl-sn-glycero-3-phosphocholine (POPC) was pur chased from Avanti Polar Lipids (Alabaster, AL). The fluorescent probes 5(6)-carboxyfluorescein (CF), pyrene, thymol, carvacrol, CHCl, CH_3, Sephadex G-25, ethylene glycol and the salts used for the preparation of buffers were purchased from Sigma Aldrich and used without further purification. All chemicals used were of analytical grade, water was doubly distilled deionized of HPLC grade, and all ex periments were conducted with freshly prepared solutions. Compounds 3–5 were synthesized and purified according

to pub lished procedures[31,32]. In particular, they were obtained through a nucleophilic substitution reaction, by using 4-cyanobenzyl bromide for 3 and 4, and 2-bromoacetonitrile for 5 [31,32].

12.2.2 Instruments

Fluorimetric measurements have been carried out on Jasco FP-6500 spectrofluorimeter. UV–vis spectra have been recorded by a Jasco V-550 UV/Vis spectrophotometer. The size and ζ potential values of liposomal systems were measured by using a 90Plus/BI-MAS ZetaPlus multiangle particle size analyzer (Brookhaven Instruments Corp., Holtsville, NY). DSC was conducted using an DSC25 (TA Instrument, New Castle, DE 19720, USA). Experiments were collected in the range of temperature from 15 ◦ C to 25 ◦ C, using a ramp of 1 ◦ C/min. All data collection and manipulation were carried out using TA Instrument TRIOS (version 5.6.0.87). Atomic Force Microscopy (AFM) measurements were carried out using a Multimode 8 system (Bruker, Billerica, MA, USA) equipped with a Nanoscope V controller, operating in ScanAsyst in air mode. Raman spectra were collected by confocal and high-performance Raman microscope (XploRA PLUS, HORIBA, Japan) with deep-cooled CCD detector technology. LabSpec 6.6.1.14 (Horiba, Japan) was employed to control, optimize, and process the acquired data.

12.2.3 Computational details

Molecular dynamics simulations were performed with the program Gromacs version 5.0.4.[33].

The POPC membrane and all the species inserted in the membrane were described using a force-field obtained from Automated Topology Builder[34]. Water molecules were described using the Single Point Charge (spc) model[35]. All the sim ulations were carried out in the canonical ensemble; the temperature was kept fixed at 25°C using the velocity-rescale algorithm[36]; the Particle Mesh Ewald was used for the electrostatics [37] and all the bond lengths were kept frozen using the LINCS algorithm[38].

For each system we performed two simulations: the first one with the solute initially located in the water membrane interface; the second one with the solute inserted in the central part of the membrane. This strategy, which could only provide us with qualitative information, was selected in order to minimize uncertainties derived from the (relatively) long relaxation times. The simulations were carried out according to the following protocol: (i) the system was first minimized; (ii) the system was then gradually heated from 10 K to 298 K using short (500 ps) trajectories. (iii) Finally, the productive run was propagated up to 100.0 ns.

For each system, 200 ns of simulation was utilized for the final results. The trajectories were analyzed through simple home-made routines in particular following, along the simulation time, the position of the solute along the membrane.

12.2.4. Preparation of liposomal systems

Large POPC unilamellar vesicles have been prepared by the thin film hydration method, following the procedure reported in the literature[17]. Briefly, the appropriate amount of a guest stock solution in $CHCl_3$ has been added to a 25 mg/mL stock solution of POPC in $CHCl_3$ to give the desired final guest/lipid ratio (0.5:100 or 1:100). The mixture was evaporated at 40° C under reduced pressure and

the obtained thin lipid f ilm formed on the wall of the flask was vacuum dried and rehydrated with MilliQ water or the appropriate aqueous buffer solution, depending on the type of measurement. After a hydration period of 30 min at room temperature, the lipid suspension was extruded at a nitrogen pressure of ~500 psi with 5 passes through polycarbonate membranes (pore size 200 nm, Nucleopore Track-Etched Membranes, Whatman, GE Health care, USA) mounted on an extruder (Lipex Biomembranes, Vancouver). The extrusion was performed at room temperature. Spectrophotometric measurements were carried out to confirm the incorporation of guests into the liposomal bilayer. The UV–vis spectra of guests in CH_3OH and the spectra of the related hybrid liposomal systems are reported in Supplementary Materials (Fig. S1) The amount of encapsulated guest was calculated as the difference between the total weighed amount of guest and the unincorporated fraction, which included the portion recovered from the polycarbonate membranes used during extrusion (washed with CH_3OH), as well as the fraction retained in the Sephadex during the gel-filtration step, subse quently eluted with CH_3OH. The recovered guest was quantified using a calibration curve. The encapsulation efficiency, EE, was calculated by Eq. 1: EE (%) = [(totalguest unincorporatedguest)/totalguest]x100 and was found to be ≥98 % for all guests.

12.2.5. Dynamic light scattering (DLS) analysis

For DLS measurements, the phospholipid thin film was rehydrated with MilliQ water. The mean hydrodynamic radius values and poly dispersity indexes were obtained by analysing the scattering intensity autocorrelation function, assuming a log Gaussian distribution of the liposome size. DLS was also used to assess ζ potential values which were calculated from the electrophoretic mobility.

12.2.6. Atomic force microscopy (AFM) analysis

AFM was employed to examine the surface morphology and size characteristics of the POPC-based liposomal systems incorporating different guest molecules. For sample preparation, a drop of diluted

liposome suspension (guest-to-lipid molar ratio of 1:100) was deposited onto SiO_2 substrates and subjected to controlled drying, initially at 303 K for 2 h in an oven, followed by overnight drying at room temperature.

Imaging was performed in air using a ScanAsyst-Air silicon probe (triangular shape, resonance frequency ~ 70 kHz, nominal spring con stant 0.4 N/m) operated in ScanAsyst mode. Topographic images (512 ×512 pixels) were recorded at a scan rate of 1 Hz with varying scan sizes and analyzed using Nanoscope Analysis 1.8 software.

12.2.7 Differential scanning calorimetry (DSC) experiments

Since the melting transition of ice overlap the gel-to-fluid phase transition temperature of POPC (Tm ~ 2 ◦C), the phospholipid thin film was rehydrated with an ethylene glycol/H2O 30:70 v/v mixture, with a freezing point of ~ 14 ◦C.

This protocol effectively prevented the interference caused by freezing water and revealed the phase transition of POPC.

Indeed, ethylene glycol-based water solutions are commonly used in heat-transfer applications where the temperature in the heat transfer fluid can occur below 0 °C[39,40].

Approx. 25 µL of the liposomal suspension were loaded in a pre- weighed, hermetically sealed DSC pan.

The reference pan was filled with the same components of the sample except the lipid phase. Samples were cooled from 25° C to 15° C and then warmed from 15 °C to 25 °C at a rate of 1 ◦C/min.

The entire procedure was repeated to ensure reproducibility. All data used for analysis were taken from the heating scans, while cooling scans were used to check for hysteresis of the transitions. The

thermal behaviour of liposomes was evaluated by determining the main transition temperature (Tm) and the enthalpy of the transition (ΔHm) expressed as J/g of liposomes in the sample.

12.2.8. Raman experiments

A drop of suspension of pure POPC liposomes or guest-doped lipo somes was deposited on a silicon wafer substrate. The Raman peaks were observed under a 532 nm laser with optical grating of 2400-line/mm. All spectra were collected in the spectral ranges 600–1600 cm1 and 2000–3500 cm1, with the same measurement parameters (10s integration time, 15 accumulations, ~10 mW laser power at the sample surface) focusing on the surface, at the edge of the drop, with a 100× objective, to avoid laser-induced heating.

12.2.9. Fluorimetric measurements

The change in the bilayer microviscosity induced by the incorpora tion of the guests into the liposomal membrane has been determined fluorimetrically by using the environmentally sensitive fluorophore pyrene as the probe. The fluorescent intensity ratio IE/IM, where IE is the fluorescent intensity of the excimer at λ =480 nm and IM is the fluorescent intensity of the monomer at λ =395 nm, was used to estimate the membrane viscosity. The final concentrations of guests were 1.32 × 10 6 M (guest/lipid ratio =0.5:100), and 2.64 ×10 6 M (guest/lipid ratio =1:100). Experiments were carried out following a previously reported procedure[17].

Briefly, 1 μL of a stock solution 2 $\times 10^{-3}$ M of pyrene in ethanol was added directly to the cuvette containing the liposomal suspension every 3 min for a period of 30 min until a final concentration of pyrene of 1 $\times 10^{-5}$ M was reached, which ensures an adequate fluorescence intensity in all the experiments.

The total amount of added ethanol never exceeds 0.5 % to avoid that high concentrations of ethanol could interfere with the organisation of the acyl chains of the phospholipids inside the membrane[41].

The fluorescence emission spectrum was recorded after each addition of pyrene, using an excitation wavelength of 335 nm. Content release experiments have been performed by using the fluorescent probe CF. The phospholipid thin film was rehydrated with a 50 mM CF solution in a buffer prepared from NaCl (121.5 mM), Na_2HPO_4 (25.2 mM) and KH_2PO_4 (4.8 mM).

The CF concentration was chosen in order to achieve a quenching concentration in the inner aqueous core.

The untrapped dye was removed by passing the lipo somal suspension through a Sephadex G-25 column at room temperature. The liposome suspension was then diluted with an isosmotic buffer (578 mOsm - pH 7.40) from NaCl (174 mM), Na_2HPO_4 (105 mM), and KH_2PO_4 (20 mM) to obtain a final POPC concentration of 1.32×10^{-5} M.

The increase in fluorescence emission intensity at λ =516 nm, using 490 nm as the excitation wavelength, due to the CF de-quenching which occurs after the leakage of the entrapped CF from the liposomes, was monitored over a period of 24 h.

12.3 Results and discussion

12.3.1. Computational analysis

As briefly described in the Computational Details section, we analyzed the position of the solute along the membrane for each system.

The results are reported in the Fig. 2. According to the reported values, Fig. 2 clearly shows that our simulation setup indicates that, essentially in all the investigated cases, the solute preferentially resides within the solvent-membrane interface. Interestingly the width of the distributions also suggests that, essentially in all the investigated cases, the solutes are rather mobile.

In one case (compound 4) the solute also appears as able to reach, with low but non-zero probability, the core of the membrane.

As already remarked in the Computational Details section, our results do not allow a fully quantitative picture and, hence, the small differences observed in the reported distributions are probably not significant. It follows that the only conclusion that can realistically and irrefutably be reached is that all the species appear to preferentially occupy the solvent-membrane interface.

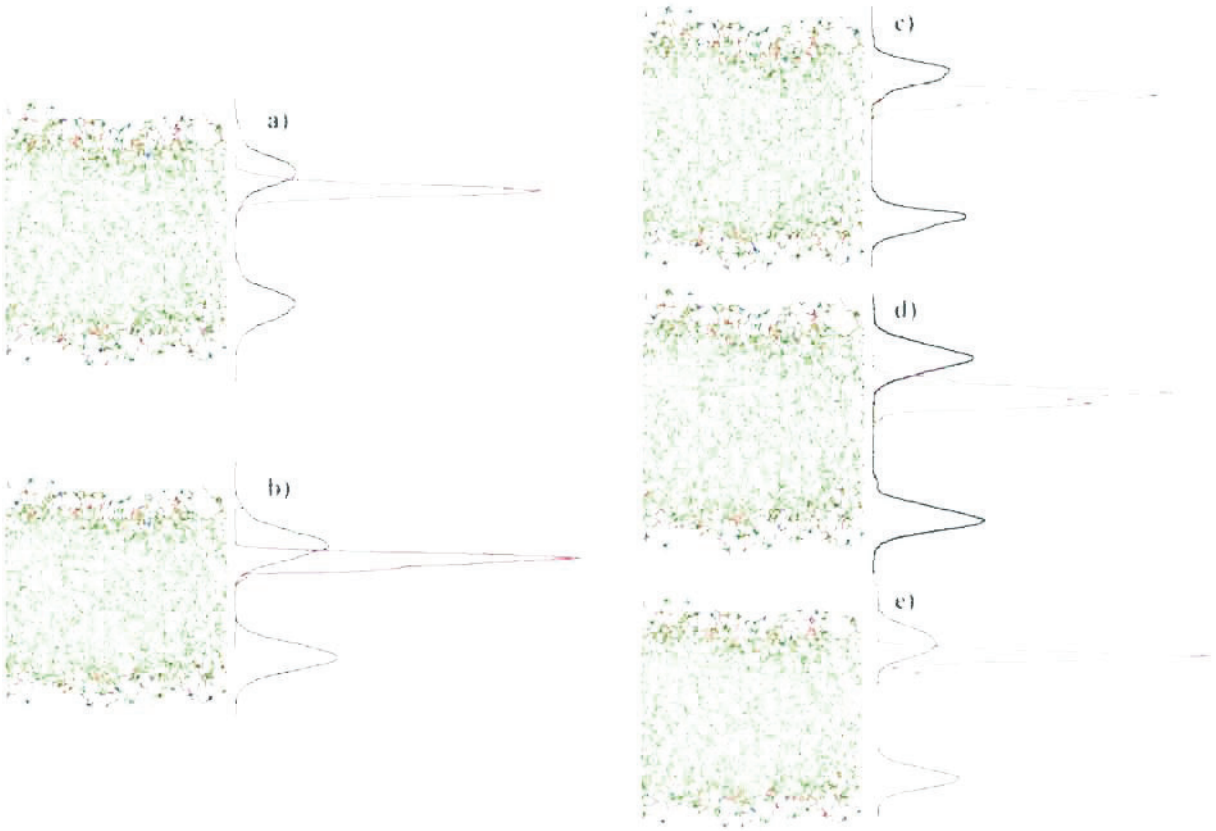

Fig. 2. Distributions of the solute centre-of-mass (red) and membrane polar heads (black) for a) **1**/POPC, b) **2**/POPC, c) **3**/POPC, d) **4**/POPC, e) **5**/POPC systems. Data are averaged over two trajectories with maximum deviations not exceeding 2.0 Å.

12.3.2. Particle size and zeta potential

Particle size and zeta potential are valuable sources of information on the physicochemical changes that occur in a lipid bilayer when a guest is incorporated into the membrane.

Indeed, the insertion of a guest molecules into the liposomal bilayer can promote phospholipid rearrangement by altering the morphology of liposomes as well as the physicochemical properties of the liposomal surface.

The effect of the insertion of the studied guests on the POPC liposome morphology was evaluated by DLS analysis in terms of mean hydrodynamic diameter, and the surface charge of the liposome was quantified by measuring the ζ potential.

The polydispersity index was also determined to assess the distribution of the liposome population, specifically the homogeneity of particle sizes. The results obtained for the hybrid liposomal systems, along with those for pure POPC liposomes for comparison, are reported in the Supplementary Material (Tables S1-S3).

DLS analysis confirmed the presence of particles whose diameters are consistent with the existence of liposomal aggregates, suggesting that the insertion of the guests did not affect substantially the structural integrity of liposomes, which is maintained after guest loading. The polydispersity index values indicate a relatively homogeneous size dis tribution.

However, the size of hybrid systems was found to change, compared to pure POPC liposomes, suggesting that, even if liposome structure is not disrupted, the presence of the guests influence the cur vature of the membrane. Measurements of ζ-potential provide a quan titative assessment of liposomal phosphate group surface exposure in the presence of guest molecules by analysing the

liposomal surface charge. The negative surface charge of the liposomes increases upon guest insertion (Table S3).

This result suggests that the guests predominantly localize near the polar head groups of the phospholipids, influencing their orientation and enhancing their exposure at the interface.

A similar shift in ζ-potential values has been observed in DPPC liposomal bilayers containing certain polyphenolic compounds[42], for which thermal analysis and 31 ^{P}NMR studies have confirmed their localization near the glycerol and C1-C10 region of the DPPC acyl chains. The same study suggested that molecules positioned closer to the bilayer center, from C10 onward, do not influence phosphate group exposure[42].

ζ potential values also quantify the degree of repulsion between charged particles in the dispersion. The high absolute values of the ζ potential obtained for the studied liposomes indicate a strong charge repulsion between the particles, that avoids their aggregation and pre cipitation, suggesting a high kinetic stability of the hybrid systems [43,44].

The stability of the liposomal formulations was evaluated at 0, 7, 14, and 21 days using dynamic light scattering (DLS) to monitor particle size and polydispersity index (PDI). The analysis was performed on samples stored at 4 ◦ C in the dark. Over the 21-day storage period, DLS mea surements revealed non-linear and fluctuating trends in both particle size and PDI across all liposomal systems, including pure POPC lipo somes (Tables S1-S2), showing no evidence of large-scale aggregation or fusion and no clear tendency toward narrowing or broadening of the size distribution.

Rather than indicating progressive destabilization, these f luctuations suggest a system in dynamic equilibrium and highlight the behaviour of the liposomal systems, which preserve their structural integrity despite minor, reversible changes in size and distribution.

12.3.3 AFM analysis

AFM imaging is well-suited for assessing the size and shape of het erogeneous systems such as liposome suspensions. Representative 2D height images of diluted pure POPC liposomes and POPC liposomes loaded with guest 1 are shown in Fig. 3.

Most vesicles exhibit a globular and somewhat flattened appearance, likely resulting from deformation during the drying process. It is worth noting that while AFM offers detailed morphological insights, particle size estimates may be influenced by tip convolution, sample preparation artifacts, and the smaller number of vesicles analyzed, making it more reliable for qualitative assessment of vesicle shape and surface characteristics.

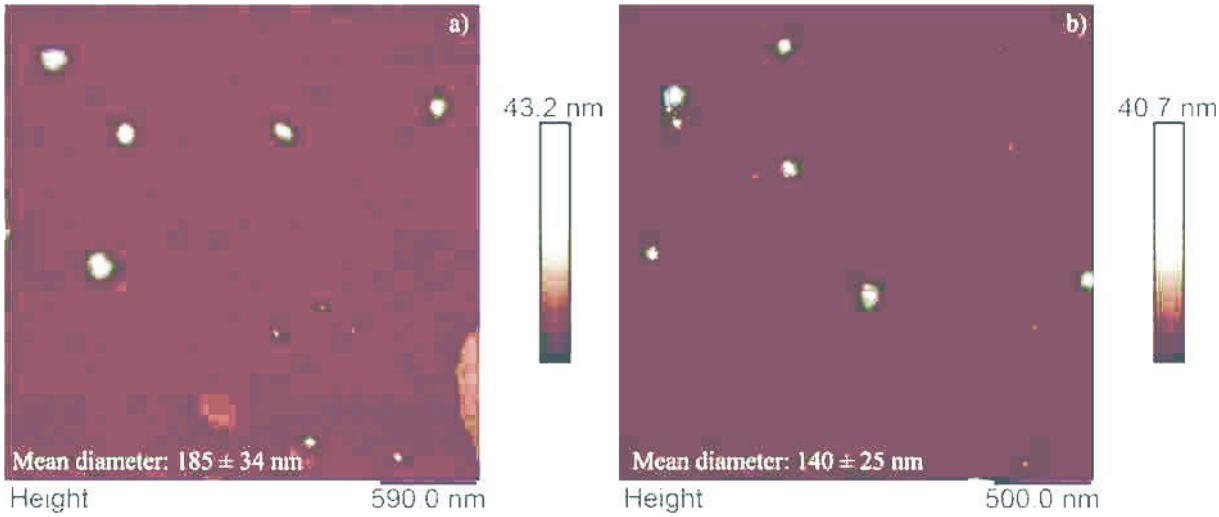

Fig. 3. AFM topography image of a) pure POPC liposomes and b) 1/POPC liposomes (guest-to-lipid molar ratio = 1:100). AFM images of the other liposomal systems are provided in the Supplementary Material.

12.3.4 Determining the microviscosity

Fluorescence spectroscopy is a valuable technique for obtaining in formation on the structural order and, consequently, the microviscosity of bilayers. This method is based on the motion characteristics of pyrene in the membrane, since the ratio between the fluorescence intensity of the excimer (I E) at

480 nm and the fluorescence intensity of the monomer (I M) at 395 nm is determined by the diffusion-controlled collision frequency between laterally diffusing monomers, which is sensitive to the viscosity changes in the phospholipid membrane[45]. When the environment limits lateral diffusion of pyrene molecules, fluorescence emission originates from pyrene monomers while, when lateral diffusion is unrestricted, the pyrene monomers collide to form excimer whose f luorescence prevails in the emission spectrum. As an example, the f luorescence spectra of pyrene in the 3/POPC liposomal system (guest/ lipid ratio = 0.5:100) are shown in Fig. 4. The parameter C'h, given by the equation. C ' h =(1/k) η where k is a constant accounting for both theoretical and instru mental factors and η represents viscosity, was determined as the inverse of the slope of the linear plot of the I_{480} /I_{395} ratio versus pyrene concentration (Fig. 4b) and is presented in Table 1as an indirect indi cator of bilayer microviscosity for all the studied liposomal systems. The data presented in Table 1 indicate that the incorporation of the different monoterpenes into POPC liposomes modifies the lipid mem brane dynamic properties, leading to an increased fluidity, compared to pure POPC liposomes.

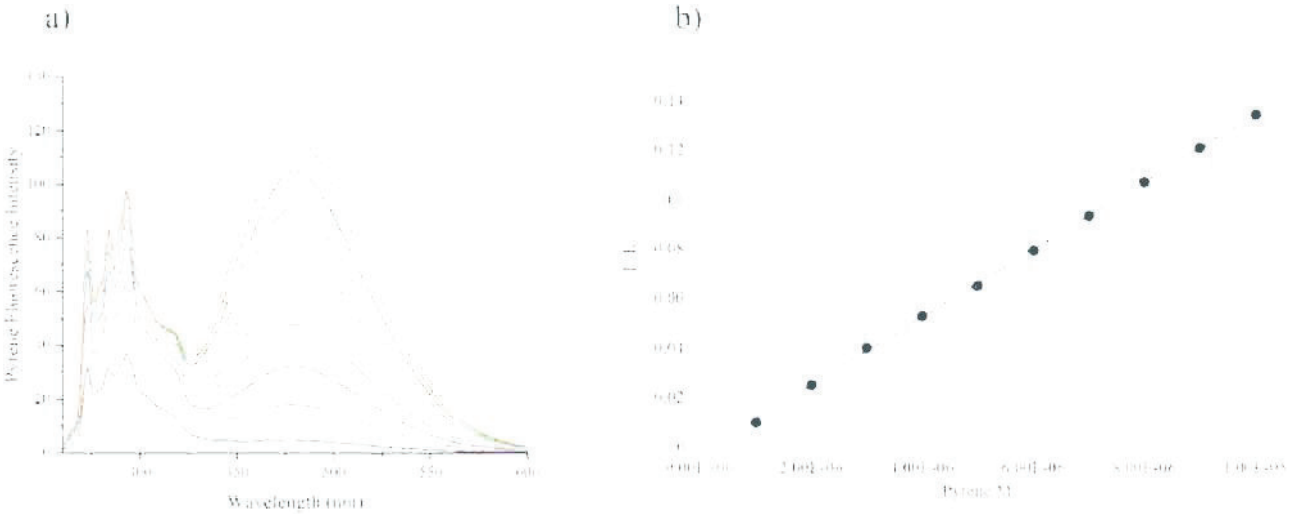

Fig. 4. a) Fluorescent emission spectra of pyrene in the liposomal system 3/POPC (guest/lipid ratio = 0.5:100) registered at 1 × 10 and b) plot of the I E(480) /I M(395) ratio versus pyrene concentration.

Table 1

C'h parameters calculated for pure POPC liposomes and hybrid liposomal systems.

	C'h (x 10^{-5})	
pure POPC [15]	15.9 (± 0.01)	
Liposomal system	Guest/POPC ratio 0.5:100	Guest/POPC ratio 1:100
1/POPC	6.93 ± 0.10	6.70 ± 0.43
2/POPC	8.00 ± 0.37	7.58 ± 0.34
3/POPC	7.50 ± 0.13	7.46 ± 0.01
4/POPC	8.05 ± 0.36	7.27 ± 0.21
5/POPC	8.61 ± 0.04	8.39 ± 0.02

12.3.5 DSC analysis

Phospholipid membranes exhibit lyotropic properties, meaning they can exist in different phases, gel and liquid crystal, depending on tem perature[46].

The transition between these phases, known as the gel-to- liquid crystal phase transition, is characterized by a transition temper ature (Tm) and an associated enthalpy change (ΔH_m) which is deter mined by integrating the area under the calorimetric curve. Below Tm, in the gel phase, phospholipid aliphatic chains are tightly packed, oriented parallel in the trans configuration, and exhibit limited mobility.

Above Tm, in the liquid crystalline phase, these chains adopt a more disordered state, increasing their mobility and shifting to a gauche conformation. The transition from an ordered to a disordered state requires heat ab sorption, which appears as an endothermic peak in the DSC curve. Representative DSC thermograms are presented in Fig. 5. As shown in Fig. 5, the liposomal bilayer of pure POPC liposomes displayed a typical peak at about 3.4 °C due to the transition from a gel to a liquid

crystalline phase. This value is consistent with those reported in the literature, which typically range between 2 and 5 °C [47–50].

Changes in DSC profiles were observed upon insertion of 1–5 into the liposomal bilayer, suggesting that guests modulate the organization and dynamics of the membrane and affect its overall thermodynamic behaviour. Guest insertion led to peak broadening and reduction in transition enthalpy compared to pure POPC control liposomes, while Tm showed a slight decrease, which became more pronounced at the highest concentrations of ether derivatives 3–5. All thermodynamic parameters are listed in Table 2. The broadening of the transition peak indicates that the guest molecule is situated in the C1 - C10 methylene region, where it interacts with the cooperative unit[42]. This interaction disrupts lipid packing and increases heterogeneity in the head group region, leading to a broader and less distinct endothermic peak due to a less cooperative phase transition which becomes less pronounced and occurs over a wider temperature range. In contrast, if a guest molecule is positioned closer to the bilayer center (C10 - C16 methylene region), the cooper ative unit remains unaffected, resulting in a sharper transition peak.

These findings correlate with the effect of guests on ζ-potential values which has been attributed to their localization in the C1 - C10 region of the POPC acyl chains. The slight change in Tm coupled with a decrease in enthalpy upon guest insertion into the liposomal bilayer can be explained by the location of the guest within the lipid structure.

Tm reflects the cooper ativity of the gel-to-liquid crystalline phase transition, which depends on the hydrophobic core's structural integrity. Guest molecules with limited ability to penetrate deeply into the hydrophobic core of the bi layers have a limited influence on Tm[51].

However, the interaction of the guest molecule with the polar head groups could weaken the cohe sive forces between lipid molecules, leading to a less thermal energy required to shift from an ordered lipid packing to a more disordered state. As a result, despite their preferential location near the

bilayer's polar head groups, guests may induce a shift to a more fluid state in the hydrophobic region of the bilayer. This interpretation aligns with ζ-potential measurements and computational analysis. At guest/POPC ratio 1:100, ether derivatives 3–5 demonstrated a greater effect on Tm.

At this concentration, these guests, which lack a free OH group, likely disrupt the packing of the lipid chains more effectively.

The relevance of the DSC results obtained in this study is further underscored by the limited availability of calorimetric investigations on fully hydrated POPC liposomes interacting with small molecules. We identified only one study in which POPC vesicles were analyzed in the presence of a lipophilic guest, α-tocopherol, at physiological concen tration (0.3 mol%)[52].

In that case, a slight reduction in both the main phase transition temperature (from 4.8 °C to 5.2 °C) and transition enthalpy was observed, suggesting perturbations at the interfacial level of the bilayer. Similarly, our data suggest that the terpene derivatives interact mainly with the polar headgroup region, as supported by complementary techniques and molecular dynamics simulations.

This congruence further reinforces the robustness of our experimental setup. In contrast, other studies reporting calorimetric analysis of guest-lipid interactions typically involve dehydrated or partially hydrated POPC membranes, conditions not directly comparable to our fully hydrated systems[53,54].

In this context, our results further extend current knowledge by providing a detailed comparative analysis of different terpene structures, an aspect still largely unexplored for POPC in the hydrated state.

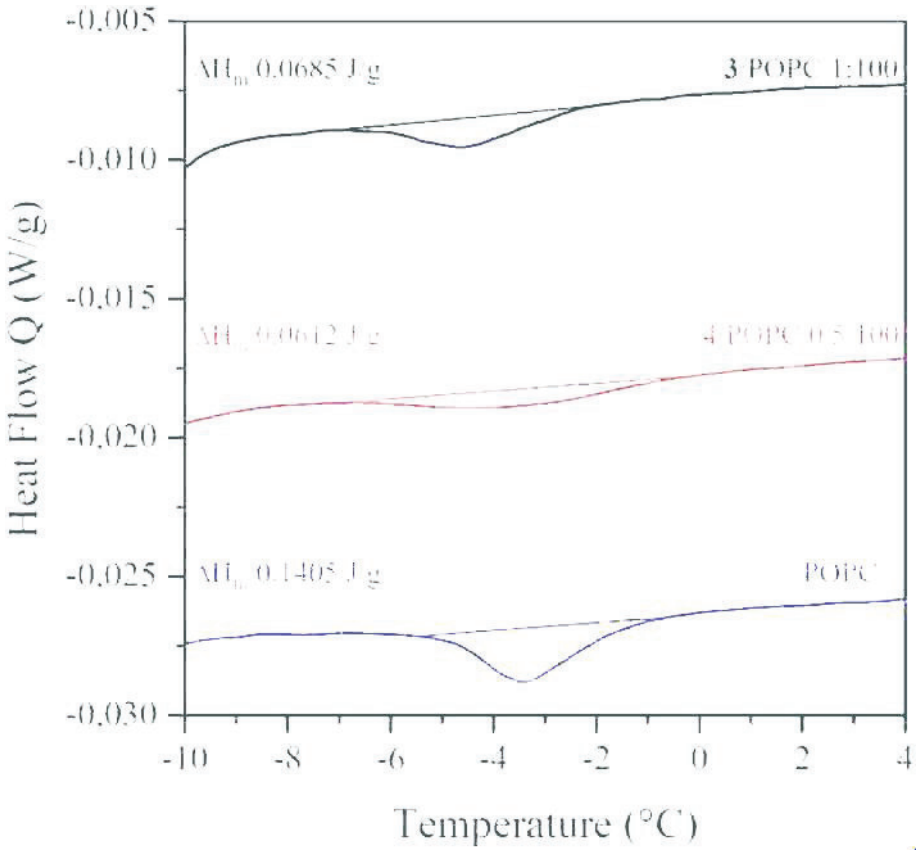

Fig. 5. DSC profiles of the gel-to-fluid state transition of pure POPC liposomes (blue line), **4**/POPC liposomal system 0.5:100 (red line) and **3**/POPC liposomal system 1:100 (black line). (For interpretation of the references to colour in this figure legend, the reader is referred to the web version of this article.)

Table 2

Thermotropic parameters obtained from the DSC profiles of pure POPC liposomes and guest/POPC liposomal systems.

Liposomal system	T_m (°C)	ΔH_m (J/g)
POPC	− 3.42 ± 0.04	0.1390 ± 0.0116
1/POPC 0.5:100	− 3.42 ± 0.05	0.0934 ± 0.0478
2/POPC 0.5:100	− 3.76 ± 0.09	0.1130 ± 0.0105
3/POPC 0.5:100	− 3.56 ± 0.17	0.0729 ± 0.0088
4/POPC 0.5:100	− 3.67 ± 0.16	0.0614 ± 0.0066
5/POPC 0.5:100	− 3.64 ± 0.11	0.0617 ± 0.0095
1/POPC 1:100	− 3.71 ± 0.11	0.1008 ± 0.0140
2/POPC 1:100	− 3.39 ± 0.07	0.1109 ± 0.0099
3/POPC 1:100	− 4.54 ± 0.06	0.0717 ± 0.0082
4/POPC 1:100	− 4.04 ± 0.13	0.0829 ± 0.0148

5/POPC 1:100	− 4.17 ± 0.18	0.0920 ± 0.0130

12.3.6 Raman analysis

Raman spectroscopy is a powerful analytical spectroscopic technique for obtaining molecular-level information on the structural organization and dynamics of lipid membranes.

It is particularly useful for determining the localization of guest molecules within liposomal membranes[55].

By analysing specific spectral regions, Raman spectroscopy helps identify molecular interactions and structural perturbations induced by the incorporation of these molecules into the bilayer.

The spectral region between 2800 cm^{-1} and 3050 cm^{-1} is crucial for assessing the structural and dynamic properties of phospholipid acyl chains inside the bilayer.

This region contains three well-defined peaks that correspond to different vibrational modes of C–H bonds in the lipid tails: a peak at 2850 cm^{-1} assigned to the symmetric stretching of C–H bonds in methylene ($-CH_2$) groups, a peak at 2880 cm^{-1} assigned to the asym metric stretching of C–H bonds in methylene ($-CH_2$) groups, and a peak at 2930 cm^{-1} assigned to the symmetric stretching of terminal C–H bonds in methyl ($-CH_3$) groups[56]. If a guest molecule is located in the hydrophobic domain of the membrane, it can alter the conformation and organization of lipid tails, leading to measurable changes in this spectral region[57].

The intensity ratios I_{2930}/I_{2850} and I_{2930}/I_{2880} are particularly informative because they are sensitive to the lateral packing den sity of the acyl chains.

Changes in these ratios provide insight into how tightly the lipids are packed and whether the lipid tails adopt an ordered or disordered conformation[58].

Increase in I_{2930}/I_{2850} and I_{2930}/I_{2880} suggests a more disordered and fluid membrane, indicative of reduced lipid packing. Another key Raman spectral marker is the absorption band at 715 cm^{-1}, which

is assigned to the symmetric stretching of the C–N bond in the choline moiety of the POPC head group. This vibrational mode is highly sensitive to molecular interactions occurring at the polar interface of the membrane: variations in the intensity or frequency of this peak serve as direct indicators of molecular interactions at the membrane interface, providing crucial information on whether a compound prefers to locate near the polar headgroups or to be embedded deeply within the bilayer[59].

Reduced choline C–N vibrational in tensity may indicate disruption of lipid headgroup organization, possibly due to guest intercalation or competition with lipid-lipid in teractions. It may also suggest increased membrane fluidity or destabilization.

By combining the analysis of both spectral regions (2800–3050 cm^{-1} for acyl chains and 715 cm^{-1} for head groups), the preferred localization of a guest molecule within the liposomal membrane can be determined. The Raman spectrum of POPC and of the hybrid liposomal systems were recorded and processed using Origin 2024, applying a 2nd derivative baseline correction. Deconvolution of the 2800–3050 cm^{-1} and 715 cm^{-1} regions in the Raman spectra was performed using Lorentzian peak fitting to resolve overlapping peaks into individual components and provide more precise information on the interactions between guest molecules and membrane phospholipids[60]

The interchain lateral ordering of the lipid molecules were characterized by the height in tensity ratios I_{2930}/I_{2850} and I_{2930}/I_{2880}. As the integrated intensity of the CH_2 bending vibration peak near 1440 cm^{-1} is considered to be independent of the conformational change in the polar head[61], the intensity ratio I_{715}/I_{1440} was used to quantify changes in the C–N symmetric stretching vibration of the liposomal head choline group. A complete listing of peak intensity ratios is provided in Table 3, showing that changes occurred in both spectral regions.

The increase in I_{2930}/I_{2850} ratio and the decrease in I_{715}/I_{1440} ratio suggest that guest molecules, preferentially localized within the inter facial domain, simultaneously interact with phospholipid headgroups and the adjacent segments of hydrophobic tails.

This interpretation aligns with ζ-potential measurements, DSC data and computational re sults. Additional evidence of guest interactions at the bilayer's polar head region is provided by a 2–4.4 cm^{-1} shift to a higher wavenumber in the C–N stretching peak of the Raman spectra for guest-loaded liposomes compared to pure POPC liposomes.

The limited impact on the I_{2930}/I_{2880} intensity ratio, particularly observed for guests 1 and 2, and more generally for all guests at the lowest guest/lipid ratio, is more difficult to interpret. It could be inferred that, in these cases, the effect on packing primarily arises from an in crease in rotational disorder and freedom of motion, which is reflected in the I_{2930}/I_{2850} ratio, rather than from a decrease in both intra molecular and intermolecular interactions, which are captured by the I_{2930}/I_{2880} ratio[62].

Consistent with the DSC results, guests 3–5, at the highest concentration, showed the greatest effect on the interchain lateral ordering of lipid molecules.

Table 3

Peak intensity ratios calculated from Raman spectra of the investigated hybrid liposomal systems and pure POPC liposomes.

Liposomal system	I_{2930}/I_{2850}	I_{2930}/I_{2880}	I_{714}/I_{1440}
POPC	0.74 ± 0.06	0.89 ± 0.02	0.53 ± 0.01
1/POPC 0.5:100	0.81 ± 0.01	0.83 ± 0.04	0.49 ± 0.01
2/POPC 0.5:100	0.74 ± 0.03	0.86 ± 0.07	0.45 ± 0.01
3/POPC 0.5:100	0.87 ± 0.04	0.95 ± 0.02	0.43 ± 0.01
4/POPC 0.5:100	0.83 ± 0.02	0.88 ± 0.01	0.47 ± 0.03
5/POPC 0.5:100	0.89 ± 0.01	0.89 ± 0.05	0.45 ± 0.01
1/POPC 1:100	0.86 ± 0.01	0.83 ± 0.03	0.36 ± 0.02
2/POPC 1:100	0.75 ± 0.06	0.86 ± 0.01	0.35 ± 0.03

3/POPC 1:100	1.16 ± 0.01	1.01 ± 0.09	0.43 ± 0.01
4/POPC 1:100	1.08 ± 0.01	0.97 ± 0.01	0.39 ± 0.02
5/POPC 1:100	0.85 ± 0.01	0.97 ± 0.01	0.49 ± 0.01

12.3.7 Release experiments

Liposomal membrane permeability was assessed by monitoring the spontaneous release of the fluorescent probe CF from the aqueous core of the aggregates. The release of CF, likely caused by pore formation and defects in the phospholipid bilayer[63], was tracked by measuring fluorescence intensity.

CF fluorescence is quenched at high concentra tions in the inner core of liposomes but increases (de-quenches) upon dilution in the external solution. Representative kinetic profiles of CF release from select liposomal systems are presented in Fig. 6.

The release behaviour follows a biphasic kinetic model with high accuracy, as indicated by correlation coefficients (R2) ≥ 0.998, demonstrating excellent fit quality.

This model describes liposomal content release as occurring in two distinct phases, each characterized by different rate constants. It captures heterogeneous release mecha nisms, typically consisting of an initial rapid phase followed by a slower, sustained release. The general equation for biphasic release is:

$$[CF]_{eq} - [CF]_t = Ae^{-t/k1} + Be^{-t/k2}$$

where $[CF]_{eq}$ and $[CF]_t$ are the total concentrations of CF released at equilibrium and at time t, respectively, and k_1 and k_2 are the rate con stants for the first and the second release step, respectively. The fast release step represents the initial burst release of liposome content, possibly due to transient pore formation and/or defects in the lipid bilayer.

The slow-release phase corresponds to the gradual diffu sion of encapsulated content from the liposome core, potentially influenced by bilayer integrity or membrane restructuring.

Kinetic data presented in Table 4 indicate that thymol (1) and carvacrol (2) accelerate CF release during the initial “burst” phase. A similar effect is observed for derivatives 3–5 at the highest guest/lipid ratio.

However, for derivatives 3–5 at the lowest guest/POPC ratio, the burst phase disappears, profiles display a more regular trait, and the first-order kinetic model provides the best fit for CF release (see Fig. 4).

Overall, the ability of the guest molecule to enhance membrane permeability appears to depend primarily on the presence of a free OH group and, to a lesser extent, on their concentration in the bilayer.

This may be due to the stronger interaction of the free hydroxyl groups in compounds 1 and 2 with the membrane’s polar region compared to the ether groups in compounds 3–5, which disrupts the polar head organi zation and promotes pore or channel formation, thereby increasing permeability.

Table 4

Rate constant values for the biphasic (k_1 and k_2) and first-order (k_{obs}) release of CF from the investigated liposomal systems.

Lyposomal system	$10^{-4} k_1$ (s^{-1})	$10^{-4} k_2$ (s^{-1})	$10^{-4} k_{obs}$ (s^{-1})
POPC	1.87 ± 0.03	0.257 ± 0.005	
1/POPC 0.5:100	4.39 ± 0.12	0.0725 ± 0.1323	
2/POPC 0.5:100	6.72 ± 0.39	0.0525 ± 0.0015	
3/POPC 0.5:100	–	–	0.426 ± 0.009
4/POPC 0.5:100	–	–	0.489 ± 0.001

5/POPC 0.5:100	–	–	0.356 ± 0.005
1/POPC 1:100	5.24 ± 0.13	0.0549 ± 0.0692	
2/POPC 1:100	9.33 ± 0.11	0.0735 ± 0.0007	
3/POPC 1:100	3.52 ± 0.96	0.183 ± 0.080	
4/POPC 1:100	3.08 ± 0.02	0.145 ± 0.002	
5/POPC 1:100	5.92 ± 0.01	0.240 ± 0.029	

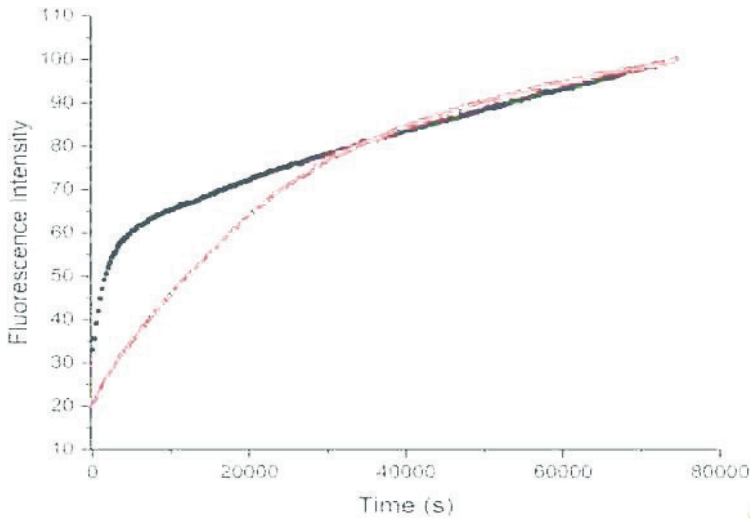

Fig. 6. Normalized kinetic profiles of the spontaneous CF release at 25 °C from **1**/POPC 0.5:100 (black line) and **5**/POPC 0.5:100 (red line) liposomal systems. (For interpretation of the references to colour in this figure legend, the reader is referred to the web version of this article.)

12.3.8 Comparative discussion of the applied techniques

The combined use of DLS, ζ-potential, fluorescence spectroscopy, DSC, and Raman spectroscopy provides a consistent picture of how guest molecules modulate liposomal structure and dynamics. DLS and ζ-po tential measurements suggest that guest insertion does not compromise liposome integrity but alters surface charge and curvature, pointing to preferential localization near the polar

headgroups. This is supported by Raman spectral shifts and reduced intensity of the C–N choline vibra tion, indicating disruption at the membrane interface.

Microviscosity data and Raman intensity ratios (I_{2930}/I_{2850}, I_{2930}/I_{2880}) reveal increased membrane fluidity and reduced lipid packing, especially for compounds with free hydroxyl groups (1 and 2).

These findings corre late with DSC thermograms, where broadened transitions and decreased enthalpy reflect reduced cooperativity and increased bilayer disorder. The thermal and spectroscopic evidence consistently place guest molecules within the C1-C10 region of the acyl chains. Release experi ments confirm these structural effects functionally, with compounds 1 and 2 markedly enhancing membrane permeability. Overall, the inte grated results from all techniques highlight a shared mechanism in which guest-membrane interactions occur primarily at the interface, leading to altered surface charge, packing, and bilayer fluidity.

12.3.9 Conclusions

This study provides a comprehensive and multi-scale analysis of the interactions between thymol, carvacrol, and their ether derivatives with biomimetic POPC liposomal membranes, aiming to unveil the molecular basis governing terpene–lipid interplay.

All compounds were success fully incorporated into the bilayer with high encapsulation efficiency and without compromising liposome integrity, as confirmed by DLS and AFM. The absence of vesicle disruption suggests that these small hydrophobic guests are compatible with the lipid architecture at the con centrations tested.

A combination of biophysical techniques, including fluorescence leakage assays, differential scanning calorimetry, and Raman spectras copy, revealed that the monoterpenes interact predominantly with the polar headgroup region of the bilayer, rather than penetrating deeply into the hydrophobic core.

Notably, DSC studies on POPC liposomes remain limited in the literature; therefore, our thermotropic analysis offers novel insights into how these fluid-phase membranes respond to small guest molecules. These interactions led to measurable changes in membrane permeability and thermotropic behaviour. The presence of a free hydroxyl group in thymol and carvacrol significantly enhanced membrane permeability, as evidenced by increased CF release during the initial burst phase. In contrast, ether derivatives produced pro nounced effects on the fast release step only at higher terpene-to-lipid ratios.

Molecular dynamics simulations supported these experimental f indings by confirming the preferential terpene localization beneath the polar interface. By elucidating how minor chemical modifications in small guest molecules translate into distinct functional outcomes at the membrane level, this work advances our fundamental understanding of guest-–bilayer interactions in soft matter systems. Beyond model membranes, our insights hold translational relevance for the rational engineering of liposomal drug delivery platforms, particularly in the design of systems with tunable permeability, stability, and release kinetics.

As such, this study not only deepens the mechanistic knowledge of terpene-lipid dy namics but also contributes meaningfully to the development of more effective and predictable nanocarrier systems in biomedical applications.

References

(1) C. Peetla, A. Stine, V. Labhasetwar, Biophysical interactions with model lipid membranes: applications in drug discovery and drug delivery, Mol. Pharm. 6 (2009) 1264–1276, https://doi.org/10.1021/mp9000662.

(2) D. Lombardo, P. Calandra, D. Barreca, S. Magazù, M.A. Kiselev, Soft interaction in liposome Nanocarriers for therapeutic drug delivery, Nanomaterials 6 (2016) 125, https://doi.org/10.3390/nano6070125.

(3) S. Andrade, M.J. Ramalho, J.A. Loureiro, M. Carmo Pereira, Liposomes as biomembrane models: biophysical techniques for drug-membrane interaction studies, J. Mol. Liq. 334 (2021) 116141, https://doi.org/10.1016/j.molliq.2021.116141.

(4) S. Sekowski, N. Naziris, M. Chountoulesi, E. Olchowik-Grabarek, K. Czerkas, A. Veiko, N. Abdulladjanova, C. Demetzos, M. Zamaraeva, Interaction of *Rhus typhina* tannin with lipid nanoparticles: Implication for the formulation of a tannin–liposome hybrid biomaterial with antibacterial activity, J. Funct. Biomater. 14 (2023) 296, https://doi.org/10.3390/jfb14060296.

(5) O. Yu Selyutina, E.A. Shelepova, E.D. Paramonova, L.A. Kichigina, S.S. Khalikov, N. E. Polyakov, Glycyrrhizin-induced changes in phospholipid dynamics studied by 1H NMR and MD simulation, Arch. Biochem. Biophys. 686 (2020) 108368, https:// doi.org/10.1016/j.abb.2020.108368.

(6) K. Sofinska, D. Lupa, A. Chachaj-Brekiesz, M. Czaja, J. Kobierski, S. Seweryn, ´ K. Skirlinska-Nosek, M. Szymonski, N. Wilkosz, A. Wn´ ętrzak, E. Lipiec, Revealing local molecular distribution, orientation, phase separation, and formation of domains in artificial lipid layers: towards comprehensive characterization of biological membranes, Adv. Colloid Interf. Sci. 301 (2022) 102614, https://doi.org/10.1016/j.cis.2022.102614.

(7) V.K. Sharma, E. Mamontov, Multiscale lipid membrane dynamics as revealed by neutron spectroscopy, Prog. Lipid Res. 87 (2022) 101179, https://doi.org/ 10.1016/j.plipres.2022.101179.

(8) K. Przykaza, M. Jurak, A.E. Wiącek, Effect of naproxen on the model lipid membrane formed on the water-chitosan subphase, BBA-Biomembranes 1865 (2023) 184099, https://doi.org/10.1016/j.bbamem.2022.184099.

(9) R. Wang, J. Peng, X. Shi, S. Cao, Y. Xu, G. Xiao, C. Li, BBA-Biomembranes 1864 (2022) 184015, https://doi.org/10.1016/j.bbamem.2022.184015.

(10) J. Gudyka, J. Ceja-Vega, K. Ivanchenko, W. Perla, C. Poust, A. Gamez Hernandez, C. Clarke, S. Silverberg, E. Perez, S. Lee, J. Phys. Chem. B 128 (2024) 2412–2424, https://doi.org/10.1021/acs.jpcb.3c08390.

(11) R. Kesharwani, P. Jaiswal, D.K. Patel, P.K. Yadav, Lipid-based drug delivery system (LBDDS): an emerging paradigm to enhance Oral bioavailability of poorly soluble drugs, Biomed. Mater. Devices 1 (2023) 648–663, https://doi.org/10.1007/ s44174-022-00041-0.

(12) S. Losada-Barreiro, S. Celik, Z. Sezgin-Bayindir, S. Bravo-Fernandez, C. Bravo-Díaz, ´ Carrier Systems for Advanced Drug Delivery: improving drug solubility/ bioavailability and administration routes, Pharmaceutics 16 (2024) 852, https:// doi.org/10.3390/pharmaceutics16070852.

(13) B. Rocha, L.A. de Morais, M.C. Viana, G. Carneiro, Promising strategies for improving oral bioavailability of poor water-soluble drugs, Expert Opin. Drug Discov. 18 (2023) 615–627, https://doi.org/10.1080/17460441.2023.2211801.

(14) R. Zappacosta, G. Siani, S. Silvi, A. Credi, A. Fontana, Light-driven directed proton transport across the liposomal membrane, Langmuir 30 (2014) 13667–13672, https://doi.org/10.1021/la503604e.

(15) S. Pilato, M. Aschi, M. Bazzoni, F. Cester Bonati, G. Cera, S. Moffa, V. Canale, M. Ciulla, A. Secchi, A. Arduini, A. Fontana, G. Siani, Calixarene-based artificial ionophores for chloride transport across natural liposomal bilayer: synthesis, structure-function relationships, and computational study, BBA-Biomembranes 2021 (1863) 183667, https://doi.org/10.1016/j.bbamem.2021.183667.

(16) S. Moffa, S. Carradori, F. Melfi, A. Fontana, M. Ciulla, P. Di Profio, M. Aschi, R. Wolicki, S. Pilato, G. Siani, Fine-tuning of membrane permeability by reversible photoisomerization of aryl-azo derivatives of thymol embedded in lipid nanoparticles, Colloids Surf. B: Biointerfaces 241 (2024) 114043, https://doi.org/ 10.1016/j.colsurfb.2024.114043.

(17) R. Zappacosta, M. Aschi, A. Ammazzalorso, P. Di Profio, A. Fontana, G. Siani, Embedding calix[4]resorcinarenes in liposomes: experimental and computational investigation of the effect of resorcinarene inclusion on liposome properties and stability, BBA-Biomembranes 1861 (2019) 1252–1259, https://doi.org/10.1016/j. bbamem.2019.04.010.

(18) M. Orlikowska, A. Wyciszkiewicz, K. Węgrzyn, J. Mehringer, D. de Souza Paiva, P. Jurczak, Methods for monitoring protein-membrane binding. Comparison based on the interactions between amyloidogenic protein human cystatin C and phospholipid liposomes, Int. J. Biol. Macromol. 278 (2024) 134889, https://doi.org/10.1016/j.ijbiomac.2024.134889.

(19) O. Kosakowska, Z. Węglarz, S. Styczynska, A. Synowiec, M. Gniewosz, K. B ´ączek, Activity of common thyme (*Thymus vulgaris* L.), greek oregano (*Origanum vulgare* L. ssp. hirtum), and common oregano (*Origanum*

vulgare L. ssp. vulgare) essential oils against selected phytopathogens, Molecules *29* (**2024**) 4617, https://doi.org/ 10.3390/molecules29194617.

(20) R. Nurzynska-Wierdak, M. Walasek-Janusz, Chemical composition, biological ´ activity, and potential uses of oregano (*Origanum vulgare* L.) and oregano essential oil, Pharmaceuticals 18 (2025) 267, https://doi.org/10.3390/ph18020267.

(21) L.A. Sampaio, L. Tairiny Santos Pina, M. Russo Serafini, D. dos Santos Tavares, A. Gibara Guimaraes, Antitumor effects of Carvacrol and thymol: a systematic review, ˜ Front. Pharmacol. 12 (2021) 702487, https://doi.org/10.3389/ fphar.2021.702487.

(22) Y. Chang, W. Boukari, S.S. Riley, P.F. Harmon, A. Sarkhosh, J.K. Brecht, In vitro antifungal activity of white thyme, oregano, and savory oils against five *Monilinia fructicola* isolates from the southeastern United States, Plant Health Prog. 25 (2024) 262–269, https://doi.org/10.1094/PHP-12-23-0111-RS.

(23) E. Vassiliou, O. Awoleye, A. Davis, S. Mishra, Anti-inflammatory and antimicrobial properties of thyme oil and its Main constituents, Int. J. Mol. Sci. 24 (2023) 6936, https://doi.org/10.3390/ijms24086936.

(24) Y. Hao, J. Li, L. Shi, A Carvacrol-rich essential oil extracted from oregano (*Origanum vulgare* "hot & Spicy") exerts potent antibacterial effects against *Staphylococcus aur*eus, Front. Microbiol. 12 (2021) 741861, https://doi.org/ 10.3389/fmicb.2021.741861.

(25) S. Mechmechani, A. Gharsallaoui, A. Fadel, K. El Omari, S. Khelissa, M. Hamze, N.- E. Chihib, Microencapsulation of carvacrol as an efficient tool to fight *Pseudomonas aeruginosa* and *Enterococcus faecalis* biofilms, PLoS One 17 (2022) e0270200, https://doi.org/10.1371/journal.pone.0270200.

(26) J.-H. Lee, Y.-G. Kim, J. Lee, Carvacrol-rich oregano oil and thymol-rich thyme red oil inhibit biofilm formation and the virulence of uropathogenic *Escherichia coli*, J. Appl. Microbiol. 123 (2017) 1420–1428, https://doi.org/10.1111/jam.13602.

(27) K. Kachur, Z. Suntres, The antibacterial properties of phenolic isomers, carvacrol and thymol, Crit. Rev. Food Sci. Nutr. 60 (2020) 3042–3053, https://doi.org/ 10.1080/10408398.2019.1675585.

(28) J. Xu, F. Zhou, B.-P. Ji, R.-S. Pei, N. Xu, The antibacterial mechanism of carvacrol and thymol against *Escherichia coli*, Lett. Appl. Microbiol. 47 (2008) 174–179, https://doi.org/10.1111/j.1472-765X.2008.02407.x.

(29) N.M. Wijesundara, S.F. Lee, Z. Cheng, R. Davidson, D.N. Langelaan, H.P. Vasantha Rupasinghe, Bactericidal activity of Carvacrol against *Streptococcus pyogenes* involves alteration of membrane fluidity and integrity

through interaction with membrane phospholipids, Pharmaceutics 14 (2022) 1992, https://doi.org/10.3390/pharmaceutics14101992.

(30) A. Ultee, M.H.J. Bennik, R. Moezelaar, The phenolic hydroxyl group of carvacrol is essential for action against the food-borne pathogen *Bacillus cereus*, Appl. Environ. Microbiol. 68 (2002) 1561–1568, https://doi.org/10.1128/AEM.68.4.1561- 1568.2002.

(31) F. Sisto, S. Carradori, P. Guglielmi, C.B. Traversi, M. Spano, A.P. Sobolev, D. Secci, M.C. Di Marcantonio, E. Haloci, R. Grande, G. Mincione, Synthesis and biological evaluation of carvacrol-based derivatives as dual inhibitors of *H. pylori* strains and AGS cell proliferation, Pharmaceuticals 13 (2020) 405, https://doi.org/10.3390/ ph13110405.

(32) F. Sisto, S. Carradori, P. Guglielmi, M. Spano, D. Secci, A. Granese, A.P. Sobolev, R. Grande, C. Campestre, M.C. Di Marcantonio, G. Mincione, Synthesis and evaluation of thymol-based synthetic derivatives as dual-action inhibitors against different strains of *H. pylori* and AGS cell line, Molecules 26 (2021) 1829, https://doi.org/10.3390/molecules26071829.

(33) M.J. Abraham, D. van der Spoel, E. Lindahl, B. Hess, the GROMACS development team, GROMACS User Manual version 5.0.4. www.gromacs.org, 2014.

(34) A.K. Malde, L. Zuo, M. Breeze, M. Stroet, D. Poger, P.C. Nair, C. Oostenbrink, A. Mark, An automated force field topology builder (ATB) and repository: version 1.0, J. Chem. Theory Comput. 7 (2011) 4026–4037, https://doi.org/10.1021/ ct200196m.

(35) H.J.C. Berendsen, J.P.M. Postma, W.F. van Gunsteren, J. Hermans, in: B. Pullman (Ed.), Intermolecular Forces, Reidel, Dordrecht, 1981, p. 331.

(36) G. Bussi, D. Donadio, M. Parrinello, Canonical sampling through velocity rescale, J. Chem. Phys. 126 (2007) 014101, https://doi.org/10.1063/1.2408420.

(37) T. Darden, D. York, L. Pedersen, Particle mesh Ewald: an N ·log(N) method for Ewald sums in large systems, J. Chem. Phys. 98 (1993) 10089–10092, https://doi. org/10.1063/1.464397.

(38) B. Hess, H. Bekker, H.J.C. Berendsen, J.G.E.M. Fraaije, LINCS: a linear constraint solver for molecular simulations, J. Comput. Chem. 18 (1997) 1463–1472, https:// doi.org/10.1002/jcc.540181207.

(39) P.J. Davis, K.M.W. Keough, Phase diagrams of bilayers of dimyristoyl lecithin plus heteroacid lecithins, Chem. Phys. Lipids 35 (1984) 299–308, https://doi.org/ 10.1016/0009 https://www.engineeringtoolbox.com/ethylene-glycol-d_146.html.

(40) Xia, S.; Tan, C.; Zhang, Y.; Abbas, S.; Feng, B.; Zhang, X.; Qin, F. *Modulating Effect of Lipid Bilayer–Carotenoid Interactions on the Property of Liposome Encapsulation*. *Colloids Surf. B: Biointerfaces* 2015, *128*, 172–180. https://doi.org/10.1016/j.colsurfb.2015.02.004

(41) Giancaspro, J.; Scollan, P.; Rosario, J.; Miller, E.; Braziel, S.; Lee, S. *Structural Determination of Model Phospholipid Membranes by Raman Spectroscopy: Laboratory Experiment*. *Biochem. Mol. Biol. Educ.* 2022, *50* (2), 181–192. https://doi.org/10.1002/bmb.21603.

(42) Kashchiev, D.; Exerova, D. *Bilayer Lipid Membrane Permeation and Rupture Due to Hole Formation*. *Biochim. Biophys. Acta, Biomembr.* 1983, *732*, 133–145. https://doi.org/10.1016/0005-2736(83)90196-7.

(43) H.A. Pillman, G.J. Blanchard, Effects of ethanol on the organization of phosphocholine lipid bilayers, J. Phys. Chem. B 114 (2010) 3840–3846, https:// doi.org/10.1021/jp910897t.

(44) S.A. Malekar, A.L. Sarode, A.C. Bach II, D.R. Worthen, The localization of phenolic compounds in liposomal bilayers and their effects on surface characteristics and colloidal stability, AAPS PharmSciTech 17 (2016) 1468–1476, https://doi.org/ 10.1208/s12249-016-0483-5.

(45) A. Wiącek, E. Chibowski, Zeta potential, effective diameter and multimodal size distribution in oil/water emulsion, Colloids Surf. A Physicochem. Eng. Asp. 159 (1999) 253–261, https://doi.org/10.1016/S0927-7757(99)00281-2.

(46) S. Moffa, M. Aschi, M. Bazzoni, F. Cester Bonati, A. Secchi, P. Bruni, P. Di Profio, A. Fontana, S. Pilato, G. Siani, Synthesis, characterization, and computational study of aggregates from amphiphilic calix[6]arenes. Effect of encapsulation on degradation kinetics of curcumin, J. Mol. Liq. 368 (2022) 120731, https://doi.org/ 10.1016/j.molliq.2022.120731.

(47) J. Vanderkooi, J. Callis, B. Chance, Use of the fluorescent dye, pyrene, to study the dynamic aspects of membrane structure, Histochem. J. 6 (1974) 301–310, https:// doi.org/10.1007/BF01312248.

(48) D. Marsh, General features of phospholipid phase transitions, Chem. Phys. Lipids 57 (1991) 109–120, https://doi.org/10.1016/0009-3084(91)90071-I.

(49) W. Curatolo, B. Sears, L.J. Neuringer, A calorimetry and deuterium NMR study of mixed model membranes of l-palmitoyl-2-oleylphosphatidylcholine and saturated phosphatidylcholines, Biochim. Biophys. Acta Biomembr. 817 (1985) 261–270, https://doi.org/10.1016/0005-2736(85)90027-6.

(50) M. Fidorra, T. Heimburg, L.A. Bagatolli, Direct visualization of the lateral structure of porcine brain Cerebrosides/POPC mixtures in presence and absence of cholesterol, Biophys. J. 97 (2009) 142–154, https://doi.org/10.1016/j. bpj.2009.03.060.

(51) P.J. Davis, B.D. Fleming, K.P. Coolbear, K.M.W. Keough, Gel to liquid-crystalline transition temperatures of water dispersions of two pairs of positional isomers of unsaturated mixed-acid phosphatidylcholines, Biochem 20 (1981) 3633–3636, https://doi.org/10.1021/bi00515a051.

(52) J.A. Svetlovics, S.A. Wheaten, P.F. Almeida, Phase separation and fluctuations in mixtures of a saturated and an unsaturated phospholipid, Biophys. J. 102 (2012) 2526–2535, https://doi.org/10.1016/j.bpj.2012.04.017.

(53) P. Zambrano, M. Manrique-Moreno, K. Petit, J.R. Colina, M. Jemiola-Rzeminska, M. Suwalsky, K. Strzalka, Differential scanning calorimetry in drug-membrane interactions, Biochem. Biophys. Res. Commun. 709 (2024) 149806, https://doi. org/10.1016/j.bbrc.2024.149806.

(54) D. Marquardt, N. Kuˇcerka, J. Katsaras, T.A. Harroun, α-Tocopherol's location in membranes is not affected by their composition, Langmuir 31 (2015) 4464–4472, https://doi.org/10.1021/la502605c.

(55) K.L. Koster, M.S. Webb, G. Bryant, D.V. Lynch, Interactions between soluble sugars and POPC (1-palmitoyl-2-oleoylphosphatidylcholine) during dehydration: vitrification of sugars alters the phase behavior of the phospholipid, Biochim. Biophys. Acta Biomembr. 1193 (1994) 143–150, https://doi.org/10.1016/0005-2736(94)90343-3.

(56) W.C. Mobley, H. Schreier, Phase transition temperature reduction and glass formation in dehydroprotected lyophilized liposomes, J. Control. Release 31 (1994) 73–87, https://doi.org/10.1016/0168-3659(94)90082-5.

(57) K. Czamara, K. Majzner, M.Z. Pacia, K. Kochan, A. Kaczor, M. Baranska, Raman spectroscopy of lipids: a review, J. Raman Spectrosc. 46 (2015) 4–20, https://doi. org/10.1002/jrs.4607.

(58) C.J. Orendorff, M.W. Ducey Jr., J.E. Pemberton, Quantitative correlation of Raman spectral indicators in determining conformational order in alkyl chains, J. Phys. Chem. A 106 (2002) 6991–6998, https://doi.org/10.1021/jp014311n.

(59) F.N.R. Petersen, C.H. Nielsen, Raman spectroscopy as a tool for investigating lipid protein interactions, Spectroscopy 24 (2009) 26–35.

(60) R. Gharib, L. Auezova, C. Charcosset, H. Greige-Gerges, Effect of a series of essential oil molecules on DPPC membrane fluidity: a biophysical study, J. Iran. Chem. Soc. 15 (2018) 75–84, https://doi.org/10.1007/s13738-017-1210-1.

(61) K. Gardikis, S. Hatziantoniou, K. Viras, M. Wagner, C. Demetzos, A DSC and Raman spectroscopy study on the effect of PAMAM dendrimer on DPPC model lipid membranes, Int. J. Pharm. 318 (2006) 118–123, https://doi.org/10.1016/j. ijpharm.2006.03.023.

(62) R.K. Singh, S.N. Singh, B.P. Asthana, C.M. Pathak, Deconvolution of lorentzian Raman linewidth: techniques of polynomial fitting and extrapolation, J. Raman Spectrosc. 25 (1994) 423–428, https://doi.org/10.1002/jrs.1250250608.

(63) S. Xia, C. Tan, Y. Zhang, S. Abbas, B. Feng, X. Zhang, F. Qin, Modulating effect of lipid bilayer–carotenoid interactions on the property of liposome encapsulation,

13 Reutilisation of the waste

Within our work, the material was separated to be valorised individually or using scrap as is to optimise its valorisation. Beyond paragraph 11, where the waste graphite was obtained from Carbotech Srl., other project was done and/or started using waste graphite. To delve it better, it should be important to remind the composition of the waste. Indeed, the available waste is made up of approximately 25% copper, and the remaining 75% is a mixture of epoxy or phenolic resins, amines (up to 10-20%), which is then carbonised, used by the company for the curing process of the material and finally by graphite for the vast majority[1]. In summary, the waste is composed of epoxy and phenolic resins, with amines, as well as copper graphite, since the resins with the amines, once heated at high T in N_2, undergo the hardening and carbonisation process, increasing stability and conductivity. Taken individually, the graphitic part has been used for the synthesis of graphene and graphene derivatives. The scrap was used for CN cross-coupling and for the Ullmann reaction and for the electroreduction of CO_2. Nitrogen-containing compounds are of great importance due to their interesting and varied biological activities. Despite significant advances in this field, the creation of the C–N bond still represents a significant challenge for organic chemists, due to the often-difficult reaction conditions or the use of catalysts that are often expensive[2]. The mitigation of global climate change has become a critical priority as atmospheric carbon dioxide CO_2 levels continue to reach unprecedented heights. In 2023, global CO_2 emissions from fossil fuels and cement increased by 1.1% compared to 2022, reaching a record high of 36.8 billion tons[3]. This growth represents a 1.4% increase over pre-COVID-19 levels, as reported by the Global Carbon Project[4]. Atmospheric concentrations have surged from 315 ppm in 1959 to 422 ppm in 2023, contributing to 2023 being the warmest year on record with temperatures approximately 1.45°C above pre-industrial levels[5]. Developing a sustainable recycling system to convert CO_2 into useful materials is a primary strategy for decreasing climate risks[6].

While the electrochemical reduction of CO_2 (eCO_2RR) offers a sophisticated route to high-value products, its large-scale implementation is inherently tied to the efficiency of Carbon Capture technologies. The mitigation of atmospheric CO_2 cannot rely solely on conversion; it requires an integrated Capture and Utilize framework. Currently, the most mature technology involves amine-based liquid scrubbing; however, this process is plagued by high energy penalties during solvent regeneration and the corrosive nature of the chemicals used.

In this context, Solid Adsorbents have emerged as a more sustainable alternative. Specifically, porous carbon-based materials, like the graphene derivatives synthesized from the Carbotech Srl. waste brushes, offer high chemical stability, large surface areas, and the potential for low-energy regeneration. By functionalizing these waste-derived carbons with nitrogen-rich groups, we can create a "circular" material life cycle.

The recycling and "upcycling" of industrial waste into CO_2 sorbents serves a dual purpose in green chemistry:

1. Waste Valorization: Transforming carbon brush scraps (which contain graphite, copper, and resins) into high-performance sorbents avoids landfilling and reduces the carbon footprint of the material production itself;
2. Closing the Carbon Loop: By using a waste-derived sorbent to capture CO_2, which is then converted via eCO_2RR using a catalyst derived from the same waste source.

This integrated approach addresses the dilution problem: since CO_2 in flue gas or air is relatively dilute, capturing and concentrating it via adsorption is a thermodynamic necessity before it can be effectively fed into the electrochemical cells described in the following sections. Thus, CO_2 capture is not merely a disposal method, but the essential first step in a sustainable recycling refinery.

Due to its thermodynamic stability and inertness, CO_2 conversion typically requires extreme conditions, such as high pressures, high temperatures, and high overvoltages[7,8]. Various processes have been explored for this conversion, including chemical reforming[9,10] biological processes, mineralization, and photochemical methods[11,12]. Among these, the aqueous electrochemical reduction of CO_2 (eCO_2RR) is particularly promising because it operates under mild conditions 20°C-25°C, 1 atm, and utilizes water as an abundant, inexpensive proton source[13,14].

Metallic catalysts for CO_2RR are generally classified based on their binding energies for key reaction intermediates such as CO*, H*, OCHO*, and COOH*[15]:

- Group I (Cd, Sn, Tl, Bi, Hg, Pb): These metals exhibit high performance in the production of formate[16].
- Group II (Ga, Ag, Zn, Au, Pd): These are most suitable for the production of carbon monoxide (CO)[17-19].
- Group III (Ni, Fe, Pt, Ti): These metals predominantly facilitate the hydrogen evolution reaction (HER) rather than CO_2RR.
- Group IV (Copper): Copper (Cu) is uniquely superior as it is the only known high-performance metal catalyst capable of producing a wide range of hydrocarbons and fuels[20].

The efficiency of the eCO_2RR process is defined by several key parameters[21]:

- Faradaic Efficiency (FE): The fraction of electrons used to form a specific product, which is directly related to catalyst selectivity and depends on the catalyst's composition and structure.
- Energetic Efficiency (EE): A measure of energy consumed for a specific product, optimized by achieving high FE and low overpotentials
- Current Density (j): An indicator of the reaction rate per unit of electrode surface area.

Despite these advances, eCO_2RR faces significant kinetic challenges. For example, forming C-H bonds via H transfer is often more kinetically desirable than forming C-C bonds, which leads to lower selectivity for the desired C_{2+} products. Higher overpotentials are generally required to overcome the large kinetic barriers associated with hydrocarbon formation.

The electrocatalytic CO_2 reduction reaction (CO_2RR) is an effective and promising technology for reusing CO_2 and converting it into high-value-added products, offering a viable route to achieving carbon neutrality.

Due to the affinity of copper (Cu) for key CO_2RR intermediates, copper-based electrocatalysts are emerging as highly promising catalysts to produce multi-carbon ($C_2/_{2+}$) products through CO2RR[22,23].

14 Waste-Derived Nanoporous Graphene Oxide–TEPA Sorbents for High-Pressure CO_2 Capture

14.1 Introduction

Atmospheric CO_2 concentrations are continuing to rise rapidly in response to the increased combustion of fossil fuels, particularly coal, to meet the world's growing energy demand. As CO_2 is a major greenhouse gas contributing to global climate change, a swift transition toward a sustainable, low-carbon energy system has become an urgent global priority. Technologies such as biogas or hydrogen production are good candidates for producing energy in a cleaner and more sustainable way, although they are still associated with CO_2 production. The successful deployment of carbon capture, utilisation, and storage (CCUS) value chains depends critically on the availability of CO_2 capture technologies that are both efficient and economically feasible. Over the past decades, a broad range of CO_2 capture approaches has been developed, including absorption[1–3], adsorption[4,5], membrane separation[6,7], biological methods[8,9], mineralization[10,11], and other emerging techniques.

Among these, absorption - particularly using chemical solvents, such as amines - remains the most mature and widely implemented method for large-scale CO_2 capture. The performance of such processes is highly influenced by the characteristics of the sorbent material employed[12]. Effective adsorbents must exhibit high CO_2 capacity and selectivity, fast kinetics, ease of regeneration, and scalability at low cost[13]. Despite its widespread use, amine-based scrubbing systems face challenges including corrosivity and significant energy requirements for regeneration. Ongoing research aims to address these limitations by optimizing amine formulations and exploring alternative solutions with improved efficiency.

Porous solid sorbents, characterised by high specific surface area and tunable pore architectures, have emerged as possible candidates for CO_2 capture such as zeolites[14–16], metal-organic frameworks[17–19], mesoporous silicas[20–22], carbon-based adsorbents[23–26] and polymer foams[27–30]. These materials offer

potential solutions to the common drawbacks associated with amine-based solvents, such as equipment corrosion, solvent degradation, and high regeneration costs[31].

During the past decade graphene oxide (GO), which consists of single to few-layer graphene modified with oxygen functional groups, has emerged as a promising material for CO_2 adsorption owing to its large surface area, tuneable porosity, compatibility with wet chemistry and easy functionalization route, and a natural affinity towards CO_2 due to the presence of carboxyl, hydroxyl, and epoxy groups in its basal plane and edges of its 2D structure[32–35].

The electron deficiency on the carbon atom of CO_2 is the defining factor in the classification of this compound as a Lewis acid. It is therefore expected that the introduction of basic adsorption sites, will increase the adsorption capacity and selectivity towards CO_2. In that sense, amino-functionalized solid adsorbents have attracted considerable attention due to their simple synthesis, high concentration of amino groups, effective CO_2 capture capabilities, and low energy demands during adsorbent regeneration[36–39].

Numerous studies have explored the utilisation of different carbon precursors and biomass sources, such oil palm leaves[40], pine leaves[41], rice straw[42] and industrial scraps such as tyres[43], bio-soot[44] and Zn-C batteries[45] for synthesising GO. However, recycling industrial graphite waste offers a pathway to high-quality carbon precursors. Carbon brushes are critical electromechanical components used to conduct electrical current between stationary and rotating parts in motors and generators, with a global market constantly driven by the automotive and industrial manufacturing sectors. However, the production of these high-purity graphite components involves subtractive manufacturing processes, like cutting, grinding, and machining, that generate significant amounts of graphite waste in the form of dust and off-cuts.

This issue is particularly pressing in the European Union, where natural graphite is classified as a strategic resource under the Critical Raw Materials Act, owing to the region's high import reliance and the material's economic importance for the battery and energy transition sectors

Nevertheless, the use of scraps from carbon brush manufacturing remains unexplored compared to other wastes like tyres or batteries. The strategic necessity to valorise industrial scrap and the environmental imperative to develop cost-effective capture solutions brought us to synthesise Graphene Oxide (GO) directly from graphite recovered from production waste obtained during carbon brushes production.

In this study, GO was synthesised from industrial scrap, specifically carbon brushes, and subsequently engineered for carbon capture.

To combine the affinity of functional groups containing heteroatoms, particularly nitrogen and oxygen, for CO_2 via either dipole-quadrupole or hydrogen-bonding interactions[46], with the physical absorption properties of porous materials, we prepared two porous graphene systems derivatised with TEPA (cpGO-TEPA and wpGO-TEPA) as solid sorbents for CO_2. In this study, GO was synthesised from industrial waste through a modified Hummers method and its performance as CO_2 sorbent was tested and compared with commercial GO. Two synthetic steps were suggested to improve both the adsorption capacity and selectivity of the GO-based adsorbents. The first regards the formation of nanopores in the GO sheets by oxidation treatment. The second consists in the introduction of amine fruops by grafting Tetraethylenepentamine (TEPA) onto the surface of the porous GO. Both modification processes were carried out concurrently using a commercial GO and a recycled GO. To the best of our knowledge, this is the first report of a graphene-based sorbent synthesised from waste sources.

14.2 Experimental

14.2.1 Materials

Graphene oxide (GO) was purchased from Graphenea (San Sebastian, Spain). Waste graphite was obtained from a carbon brush company called “Carbotech S.r.L” (Martinsicuro, Italy). Nitric acid (HNO_3), 1-ethyl-3-(3-dimethylaminopropyl) carbodiimide hydrochloride (EDCl), and N-

hydroxysuccinimide (NHS) were obtained from Merck (Germany). Sulphuric acid 95%, hydrogen peroxide 30% and hydrochloric acid 1N were purchased form VWR CHEMICALS. Potassium permanganate was acquired from Carlo Erba Reagents. Ultrapure water (Milli-Q) was used in all procedures.

14.2.2 Synthesis procedures

Graphite from industrial waste was separated from epoxy resin through several washing with ethanol aimed to remove resin excess and isolate graphite that subsequently will be converted into GO.

14.2.3 Preparation of wGO

Waste derived graphite was obtained washing scraps obtained during carbon brushes production. More precisely, after the addition of epoxy resin, so we washed graphite several times using ethanol through centrifugation. As obtained graphite was also characterised by Raman spectroscopy (supplementary). Waste-derived graphene oxide (wGO) was produced via modified Hummers' method. 5 g of graphite powder were dispersed in 150 mL of 95% H_2SO_4 and stirred overnight. After a cooling process to 5°C, the as-prepared solution was carefully treated with 20 g of $KMnO_4$. To promote an efficient oxidation of graphite, the temperature was then raised to 100°C while magnetic stirring was maintained for 6 hours. After that time, 400 mL of DI water was slowly added, setting the temperature at 90 °C. Ultimately, the suspension was treated with 30 mL of 30% H_2O_2 to fully reduce the oxidant excess. The product was then filtered, washed both with deionized water and HCl solution (1 M), obtaining the wGO.

14.2.4 Preparation of porous GO

Commercial GO (cGO) and waste-derived GO (wGO) were both processed using a modified oxidative protocol. A 100 mL aqueous dispersion (1 $mg \cdot mL^{-1}$) of each GO was sonicated for 1 h. An equal volume of 65% HNO_3 was added, and the mixture was maintained at 100°C for 4 h under

magnetic stirring. After cooling, dispersions were filtered, washed with distilled water to neutrality, and freeze-dried, yielding cnGO (from commercial precursor) and wpGO (from waste precursor)[47].

14.2.5 TEPA functionalization of porous GO

For TEPA modification, 100 mg of either cpGO or wpGO was dispersed in 15 mL water by sonication. EDCl (0.81 mmol, 124 mg) and NHS (0.81 mmol, 93 mg) were then added, with stirring at 40°C for 30 min. An aqueous TEPA solution (10 mg·mL^{-1}, TEPA:pGO ratio 5:1, w/w) was prepared and added to the reaction mixture, which was stirred at 35°C for 24 h. The products were separated by centrifugation (14,500 rpm, 2 h, 15°C), repeatedly washed (sonication–centrifugation cycles), and freeze-dried.

Characterization

14.2.6 Thermogravimetric analysis (TGA)

TGA was performed using a TA SDT650 (TA Instruments, USA) in a nitrogen atmosphere (100 mL·min^{-1}), from 100°C to 800°C, at a rate of 10°C·min^{-1} following a 15 min isothermal step at 100°C.

14.2.7 X-ray photoelectron spectroscopy (XPS)

XPS was conducted under UHV with a Thermo Scientific K-Alpha spectrometer (Al Kα source, hν = 1486.6 eV), using 200 eV for survey scans and 50 eV for high-resolution spectra.

14.2.8 Scanning electron microscopy (SEM)

Morphology was assessed by drop-casting aqueous suspensions onto holey copper grids, air-dried, and observed with a ZEISS Gemini 2 microscope at 30 kV.

Gas sorption experiments

14.2.9 Sample preparation

250 mg of each powder (cGO, wGO, cnGO, wnGO, cGO-TEPA, wnGO-TEPA) was ground and sieved to select a 200–600 µm particle size, sealed in PET–nylon bags, and used for testing.

14.2.10 Experimental setup

The reactor was a 10 mL AISI 316L stainless steel vessel (max 60 bar), thermostated by a 1000 W chiller (Figure 5). Gas flow was controlled via a thermal mass flow meter (Bronkhorst F131 M, 1–100 $NmL \cdot min^{-1}$, 200 bar max) and a micrometering valve (Tescom CC). Reactor and feed line pressures were monitored (Gems Sensors & Controls); temperature via PT100 RTDs (Omega Engineering). Data was acquired with an ELCO Top 7 PLC[59–61].

14.2.11 Sorption procedure

Each sample was evacuated (0.2 bar), then loaded with CO_2 up to the required pressure setpoint (3, 7, 10, 20, 40 bar) at the target temperature (5, 20, 40°C, as relevant). For TEPA-modified samples, 40°C and higher pressures were included. After adsorption, CO_2 uptake was calculated arithmetically by subtracting gas volumes measured in runs with inert fill materials. Densities were determined by helium pycnometry. Samples were regenerated between cycles under vacuum (0.2 bar, 15 min).

DTA gas sorption test were done:

1. 15 minutes of N_2 flow 100 mL/min;
2. 15 minutes of N_2 saturated environement with no flow;
3. 15 minutes of CO_2 flow 100 mL/min;

4. 15 minutes of CO_2 saturated environment with no flow;

Each cycle was reproduced 5 times for each sample.

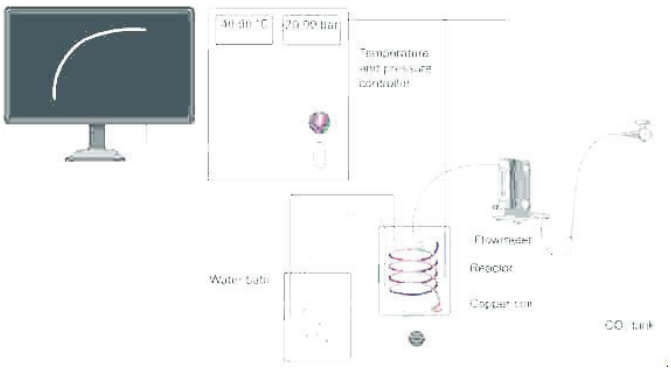

Figure 6: *experimental setup for in-pressure CO2 capture*

14.2.12 Kinetics and validation

Adsorption profiles were fitted to a first-order rate law:

$$\frac{d[CO_2]}{dt} = k_{obs}[CO_2]$$

A least-squares approach was used to determine k_{obs}. Gravimetric validation confirmed error <0.5 wt% compared to volumetric analysis, across full P/T range.

Spectroscopic and structural characterization

14.2.13 Raman spectroscopy

Raman analysis was conducted on an XploRA PLUS (HORIBA, Japan) with a 532 nm laser (10 mW, 100× objective), acquiring 10 spectra (10 s each). Data from 1000–2000 cm^{-1} was smoothed

(Savitzky-Golay), fitted (Origin pro 2024, 2 Gaussian and 3 Voigt peaks: D*, D, D", G, D'), and disorder evaluated via intensity ratios (I_D/I_G, I_{D^*}/I_G, $I_{D'}/I_G$).

14.2.14 X-ray diffraction (XRD)

XRD diffractograms were processed with GSAS-II, background subtracted (Chebyshev-1, n=10), and peaks fitted to determine crystallite size by the Scherrer equation:

$$\boldsymbol{D = \frac{K\lambda}{\beta \cos\ \theta}}$$

($\boldsymbol{K = 0.89}$, $\boldsymbol{\lambda = 0.154}$ nm, CuK$\boldsymbol{\alpha}$), with lattice spacing extracted by Bragg's law:

$$\boldsymbol{n\lambda = 2dsin\theta}$$

14.3 Results and Discussion

To produce GO-based adsorbent platforms endowed with capacity and selectivity in CO_2 capture process, two synthetic modifications were performed on GO starting materials (Fig 1a). To promote material reciclability, waste-derived GO (wGO) was synthesised from industrial waste using the Hummer method. Concurrently, the same modifications were performed on commercial GO (cGO). The first modification involved the porization of GO (wpGO/cpGO) by oxidative treatment with nitric acid under heating conditions (Fig 1a)[47]. This process increases the surface area of GO, thereby enhancing its adsorption capacity. Subsequently, a coupling reaction with tetraethylenepentamine (TEPA) was conducted to introduce amino groups onto the surface of the porous GO (wpGO-TEPA, cpGO-TEPA) (Fig. 1a), which are well known for their affinity towards CO_2 molecules.

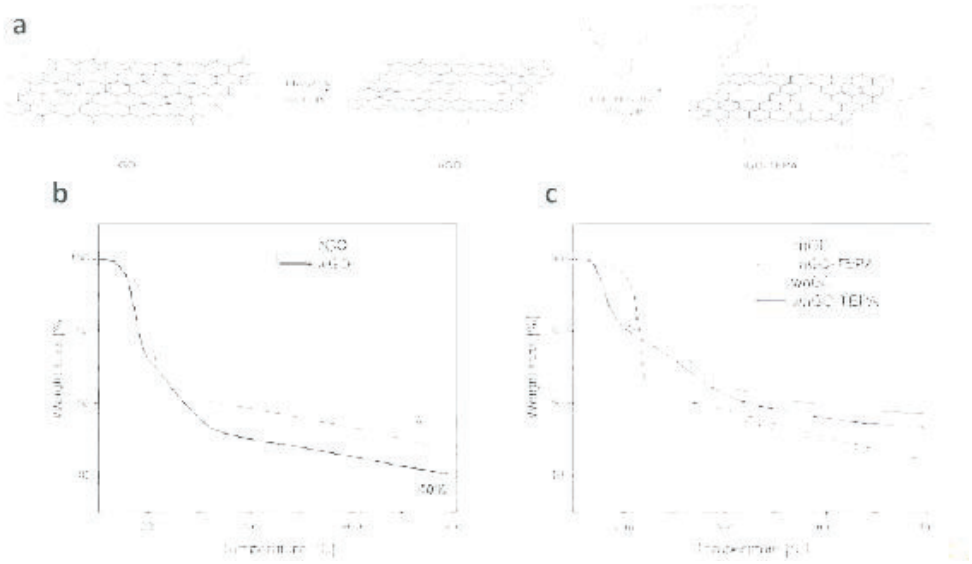

Figure 1. a) Schematic representation of the synthesis of porous graphene (pGO) and TEPA-modified porous graphene. b) TGA profiles of cGO (red line), wGO (black line). c) TGA profiles of cpGO (dashed red line), cpGO-TEPA (red line), wpGO (dashed blue line) wpGO-TEPA (blue line). All the TGA analyses were performed under a nitrogen atmosphere.

The modified GO platforms were characterised by several techniques, including TGA, XPS and SEM analyses. The success of preparing GO from industrial waste was demonstrated by TGA analysis. It can be observed that cGO and wGO show similar thermal degradation trend characterised by two steps of thermal decomposition between 180 and 350°C (Fig. 1b). The first decomposition is associated with less thermally stable groups, such as hydroxyl moieties, while the second one pertains to more stable moieties such as carboxylic and lactone groups[48]. However, wGO exhibited less thermal stability compared to cGO (47 vs 40 residual mass %), probably due to a slightly higher amount of oxygen functional groups (Fig. 1b).

Even if cGO and wGO differ in TG profiles, the TGA of nanoporous graphene (cpGO, wpGO) and TEPA-modified graphene (cpGO-TEPA, wpGO-TEPA) exhibited the same thermal behaviour (Fig. 1c).

Both cpGO and wpGO exhibited enhanced thermal stability compared to the starting materials (Table S1). This improvement is attributed to the oxidation of hydroxyl groups into carboxylic groups during the acid treatment.

Regarding TEPA-modified porous graphenes (cpGO-TEPA and wpGO-TEPA) the success of the synthesis was confirmed by TGA. Both cpGO-TEPA and wpGO-TEPA showed an additional third step of weight loss

between 280 and 400°C, in comparison to cpGO and wpGO precursors, which is related to the decomposition of amine groups (Fig. 1c). The residual mass was higher compared to the starting GO in both cases, and this is consistent with the thermal behaviour of TEPA-modified graphene oxide reported previously[36,48,49]. Even if the thermal behaviour is similar, slight differences in the residual mass were observed between cpGO-TEPA and wpGO-TEPA (Table S1). These differences could be correlated to a higher degree of functionalization cpGO-TEPA compared to wpGO-TEPA.

A further confirmation of GO derivatisation was provided by XPS analysis. Both porous samples (cpGO and wpGO) exhibited an increased oxygen content, reflected in enhanced OH–C=O, C=O and C-O contributions (Fig. 2, Tables S2, S3) compared to the starting materials GO and wGO, respectively. This indicates a higher content of oxygen functional groups because of the acidic treatment employed in the nanoporous graphene synthesis protocol. Additionally, the significant increase in N content from 0.82% to 12.4% for cpGO-TEPA and from 0.71% to 6.99% for wpGO-TEPA, resulting in a higher contribution of C–N bonds (Fig. 2, Tables S2, S3), and the concurrent decrease in oxygen content from 35.57% to 25.21% (cpGO-TEPA) and from 33.11% to 25.08% (wpGO-TEPA), further confirm the successful functionalization of the porous graphene surfaces with TEPA.

SEM analysis showed a completely different morphology between the two starting materials (Fig. S1). cGO appears as a series of well-defined agglomerated structures, whereas wGO seems to be a single amorphous block. The acid treatment induces the formation of a rough surface, while the linkage of TEPA seems to exfoliate the structure, particularly in cnGO–TEPA (Fig. S1).

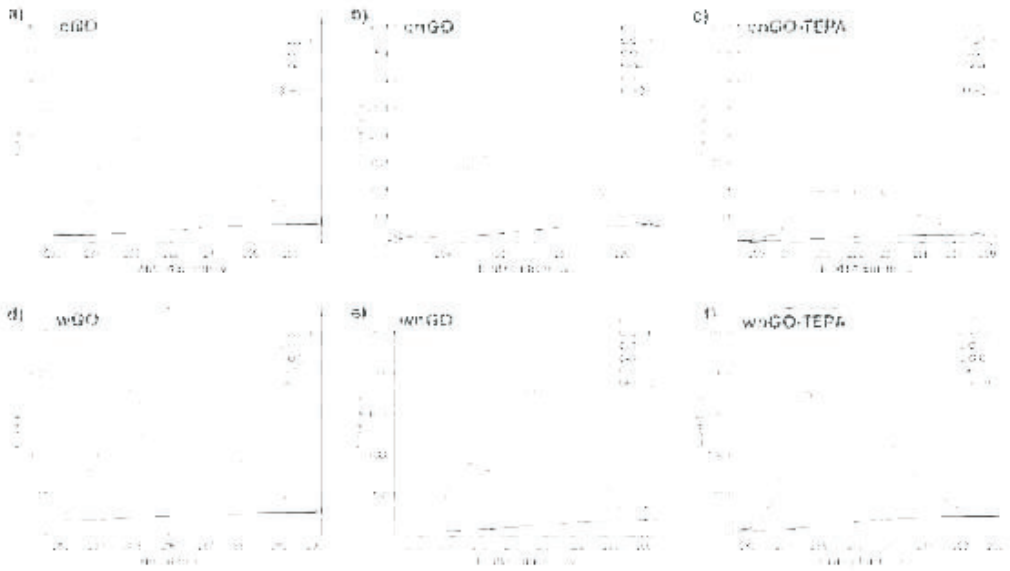

Figure 2. High-resolution C 1s deconvoluted profiles of cGO(a), cpGO (b), cpGO-TEPA (c), wGO (d), wpGO (e) and wpGO-TEPA (f).

Graphene oxide XRD is a useful tool to directly evaluate interlayer distance, crystallite dimension and number of layers. Typical XRD signals of graphene oxide are the (001) and the (100) reflection peaks[50]. Through Bragg's and Scherrer's laws it is possible to evaluate the interlayer distance (d-spacing) and the crystallite dimensions, respectively. The ratio between these values allows for evaluating the number of stacking layers.

Table 1 summarises crystallographic information from the investigated samples. The (001) reflection peak of GO shifts depending on the interlayer distance. It is interesting to note that the nanoporation process reduces both the interlayer distance and the crystallite dimensions, confirming an increase in defects in the samples. In particular, the d-spacing of wGO decreases from 7.92 Å to 7.7 Å and that of cGO from 8.27 Å to 7.87 Å, in agreement with a partial oxygen removal and pore formation that promotes interlayer distance compression. Furthermore, in the case of cGO, a shrinkage of the crystallite dimension occurs with interlayer distance passing from 6.39 nm to 4.75 nm in the porated sample (cpGO), indicating pore formation and an increase of defects. This effect is far more limited in the wGO sample.

The functionalization with TEPA creates a different pattern.

The presence of the peak at $2\theta \approx 8\text{-}10°$ for the TEPA functionalized materials indicates that the interlayer distance in TEPA functionalized GO resembles the stacking structure of GO rather than that of graphite, the

only difference being a slight shift in the peak position to lower angles as well as the appearance of low intensity peaks at 2θ = 18°, a diffraction peak typical of graphitic materials. The former shift is indicative of an increase of the distance between two stacked graphene sheets due to amine group insertions between the layers and/or to inter-lamellar water trapped between the hydrophilic GO sheets, whereas the latter modification may suggest a partial reduction of the GO structures, due to the decrease of oxygen-containing groups and the presence of intercalated TEPA at the interlayer spaces. The reduction of GO is also confirmed by the great reduction in crystallite size in both samples, which implies more lateral defects[51].

Indeed, the crystallite dimension from 4.75 Å in cpGO dropped to 3.66 Å in cpGO-TEPA. The same effect is monitored in the wpGO-TEPA sample, where shrinkage from 7.26 Å to 5.16 Å is monitored.

***Table 1**: XRD summary of samples.*

Sample	Interlayer Distance [001] (Å)	Crystallite Dimension [001] (nm)	Crystallite Dimension [100] (nm)	Interlayer Distance [100] (Å)	Number of Layers [001]	GO Features [002] (nm)
wGO	7.92	7.34	9.19	2.14	9	/
cGO	8.27	6.39	9.57	2.14	7–8	/
wpGO	7.7	7.26	9.56	2.13	9	/
cpGO	7.87	4.75	6.83	2.14	6	/
wpGO-TEPA	9.81	5.16	1.54	2.12	5	1.19 (4.79 Å)
cpGO-TEPA	9.81	3.66	3.1	2.13	3	1.71 (4.49 Å)

Raman spectra are one of the most powerful tools for graphene derivatives characterisation. Briefly, GO spectra in the range of 1000-2000 cm^{-1} are characterised by 2 peaks obtained through 3 Voigt peak fitting deconvolution and 2 Gaussian. The D* peak, located at around 1200 cm^{-1}, is related to sp^3 orbitals[52] and disordered graphite lattice[53] and allows for indirect evaluation of the oxidation degree[54] of graphene oxide. The D peak originates from breathing modes of the six-atom rings and therefore implies the presence of defects, while the G peak represents the in-plane vibration of sp^2

hybridised carbon atoms[55]. The D" band, at 1500–1550 cm^{-1}, originates from the amorphous phase and it has an inversely proportional intensity with the crystallinity of the sample, whereas the D' peak originates from the presence of defects and is also strictly connected with N-doping[56].

As reported in Figure 3, following A. Young Lee et al.[54], Different peak ratios have been considered and discussed (Table 1).

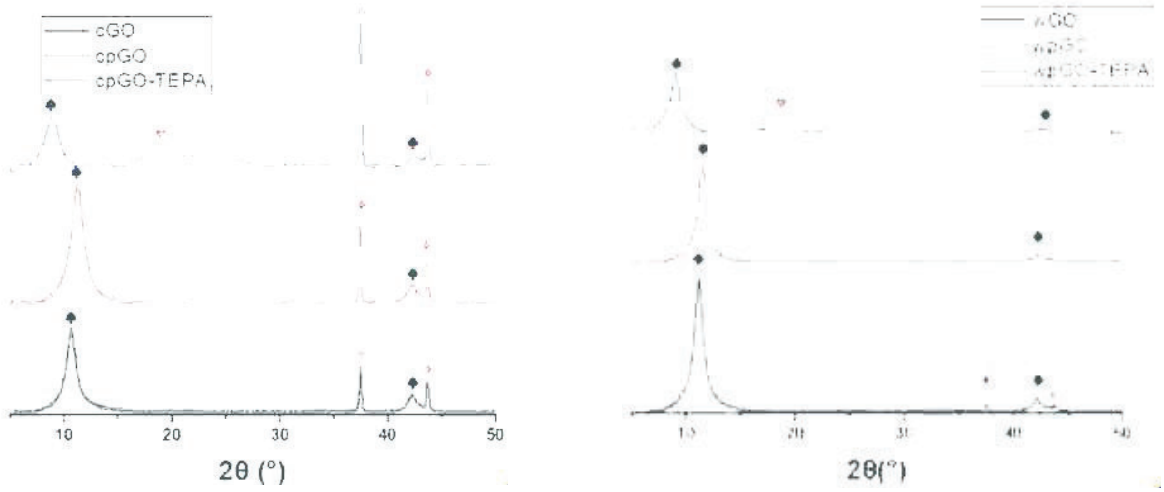

Figure 3*: X-ray diffraction (XRD) patterns of different graphene oxide (GO) samples before and after modification. The black spades indicate peaks associated with bare graphene oxide, the red diamonds correspond to the XRD support, and the red hearts highlight features of reduced graphene oxide (rGO).*

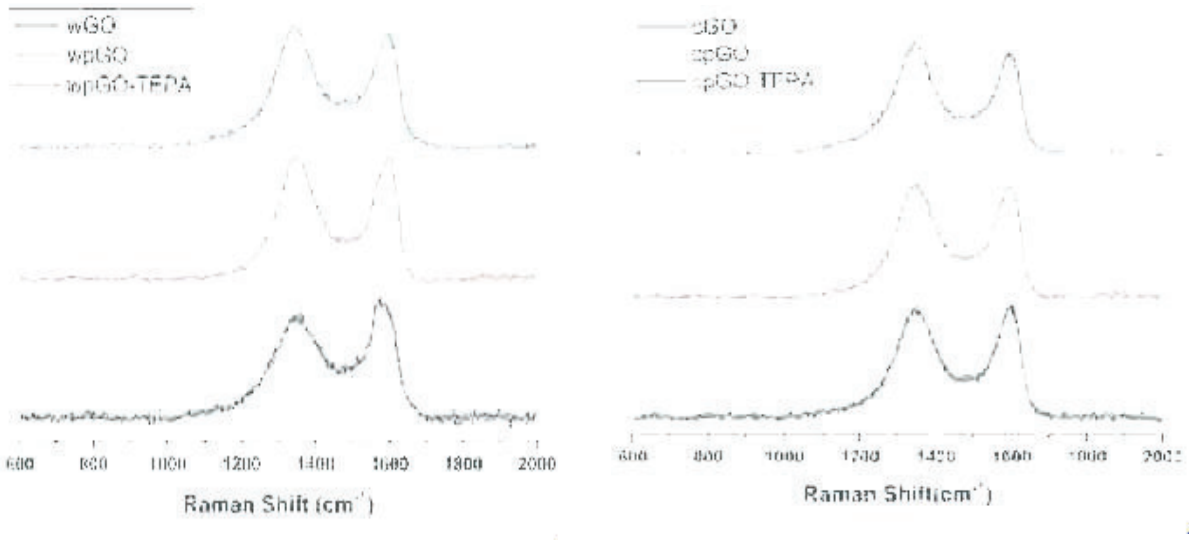

Figure 4*: Overlapped spectra of wGO, wpGO and wpGO-TEPA on the left and the commercial counterpart on the right.*

As shown in Fig. 4, an increase in the intensity of the D peak of graphene can be clearly observed, so there are more defects after the functionalisation. This is consistent with the XRD results, which indicate a reduction in crystallite size.

Furthermore, the deconvolution done as reported in literature by Lee at al.[54] and Yoo et al.[57] , it was possible to deconvolute the raman spectra in 5 different peak, through fitting 3 voigt and 2 gaussians. As reported, there are 5 peaks, D*, D, D'', G and D'. D* is related to sp^3 carbon, more precisely to sp^3 C-OH carbons, so it is reported that a reduction of the ratio between I_D^*/I_G occurs with the oxidation. This was evaluated even in this case; indeed, cGO shows an I_D*/I_G of 0.11, cpGO:0.05, and cpGO-TEPA:0.17.[58] So, the Raman confirms with the XPS that shows an oxidation during the poration and a drop of oxygen-containing group after the functionalisation with TEPA.

Eventually, this trend is confirmed even in wGO, where the I_{D*}/I_G ratio increases from 0.07 to 0.21 after nanoporation and treatment.

14.3.1 Gas sorption experiments

As shown in Table 2, poration seems to dramatically increase the carbon capture in both series of samples, according to DFT studies, due to increased C=O and O-C=O groups and increased edge defects as highlighted through XRD and Raman spectroscopy. This effect is particularly evident for derivatives obtained from a commercial sample. Similarly, N_2 uptake increased after nanoporation. Nevertheless, it is worth noting a different selectivity between the samples with the waste-derived samples being more selective towards CO_2 than commercial samples. Indeed, wpGO selectivity is 2.8, whereas cpGO selectivity is 1.84, and the same pattern holds for non-porous samples. After TEPA functionalization, a drop in CO_2 uptake occurs. It appears as if TEPA functionalization, which increases the number of C=C bonds of the samples as confirmed by XPS data, reduces the

adsorption sites generated by nanoporation or the capacity of the material to adsorb gas. The absorption pattern is the same in the cGO and its derivatives, but in this case, cpGO-TEPA shows a higher CO_2 uptake than the bare cGO maybe due to the higher similarity with the not non-functionalized sample in terms of C=O and O-C=O groups.

In conclusion, the CO_2 adsorption measured under flow conditions, in agreement with XPS data, seems correlated to the presence of carbonylic and carboxylic groups.

Table 2*: % mass of each gas adsorption and the total amount of both gases.*

SAMPLE	CO_2 (% mass)	N_2 (% mass)	TOTAL GAS (% mass)
cGO	1%	0,6%	1,6%
cpGO	4,04%	2,2%	6,2%
cpGO-TEPA	1,8%	0,7%	2,5%
wGO	2,15%	0,23%	2,38%
wpGO	3,62%	1,3%	3,92%
wnGO-TEPA	/	0,3%	0,3%

14.3.2 In pressure adsorption measurement

The adsorption performances are shown in Fig. 5.

As reported in this work, we avoided carrying out adsorption at low temperatures and pressures in the TEPA-functionalised sample because these conditions are unfavourable for chemisorption. In commercial and waste graphene oxide and porous counterparts, it was done from an opposite point

of view because, in those conditions, the physisorption processes are favoured at low temperature and pressure.

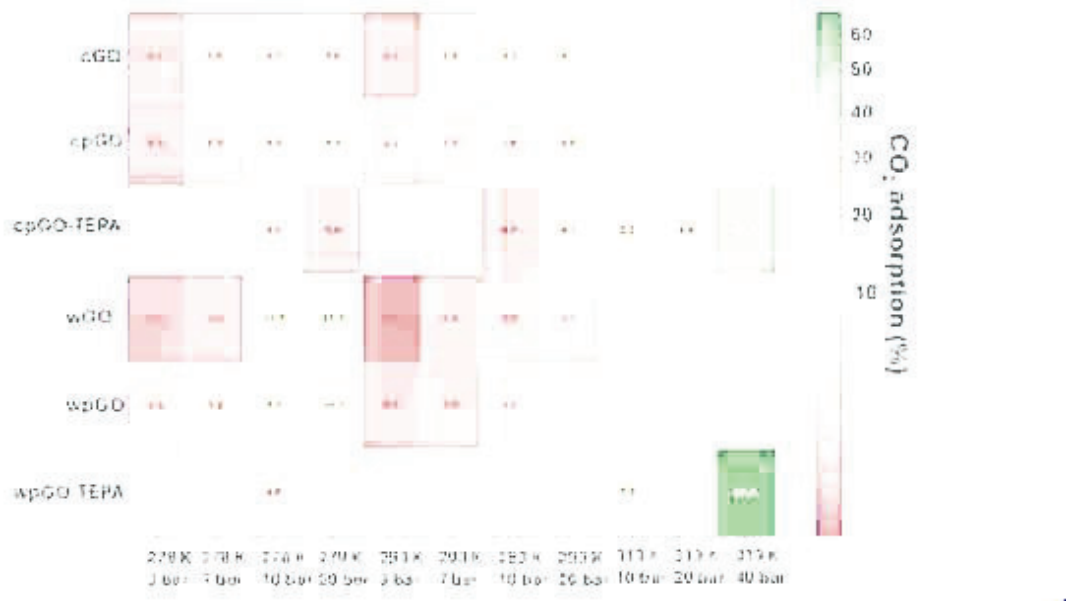

***Figure 5**: heatmap related CO_2 adsorption of each material at each T and each P.*

14.3.3 Structure-Performance Correlations

To elucidate the relationship between material structure and CO_2 adsorption performance, we correlated the spectroscopic and structural data (XPS, XRD, Raman) with the pressure-temperature adsorption results (Figure 5).

The most significant correlation observed is between nitrogen content and CO_2 capture capacity. TEPA functionalization dramatically increased N content from 0.82% to 12.4% for cpGO-TEPA and from 0.71% to 6.99% for wpGO-TEPA. Remarkably, wpGO-TEPA achieves superior CO_2 uptake (67 wt% at 40°C/40 bar) despite having nearly half the nitrogen content of cpGO-TEPA (43.6 wt% under identical conditions).

This counterintuitive result suggests that the distribution and accessibility of amine sites, rather than absolute nitrogen content, governs performance. The waste-derived platform may provide superior dispersion of TEPA molecules due to its inherently higher defect density and more disordered structure, explainable by XRD rGO features with smaller crystallite dimension and higher interlayer distance(Table 1)

XRD analysis revealed systematic decreases in crystallite size following poration and TEPA functionalization: cGO (6.39 nm) → cpGO (4.75 nm) → cpGO-TEPA (3.66 nm), and wGO (7.34 nm) → wpGO (7.26 nm) → wpGO-TEPA (5.16 nm). Smaller crystallites indicate higher defect density, confirmed even by raman spectroscopy Fig.4) and more exposed edge sites, which serve as secondary CO_2 adsorption centres.

The observation that wpGO and cpGO (porous, non-functionalized materials) achieve respectable CO_2 uptakes of 23.3% and 4.0%, respectively, at moderate conditions (20°C/20 bar) can be attributed to physisorption at these defect sites, even in the absence of amine functionality.

TEPA functionalization increased interlayer d-spacing from 7.87 Å to 9.81 Å in cpGO-TEPA and from 7.70 Å to 9.81 Å in wpGO-TEPA, as determined by XRD. This expansion facilitates the intercalation of CO_2 molecules between graphene sheets and improves accessibility to interior amine sites. The larger interlayer distance in TEPA-modified materials correlates with their enhanced performance at elevated pressures, where multilayer adsorption and interlayer penetration become significant.

Raman spectroscopy provided insights into oxidation state changes through the I_{D*}/I_G ratio, which tracks sp^3 C-OH content. Poration decreased this ratio (cGO: 0.11 → cpGO: 0.05; wGO: 0.07 → wpGO: 0.21),

consistent with oxidative conversion of hydroxyl groups to carboxylic acids. Conversely, TEPA functionalization increased the ratio (cpGO: 0.05 → cpGO-TEPA: 0.17), indicating partial reduction and replacement of oxygen functionalities with amine groups. XPS data confirm this trend, showing oxygen content decreases from 35.57% to 25.21% in cpGO-TEPA and from 33.11% to 25.08% in wpGO-TEPA upon TEPA grafting. The residual oxygen groups (C=O, O-C=O) identified by XPS contribute to CO_2 capture through dipole-quadrupole interactions, London forces etccc.. complementing the primary amine-CO_2 chemisorption mechanism.

The heatmap analysis (Figure 5) reveals distinct optimal conditions for each material class. Non-functionalized porous materials (cpGO, wpGO) show maximum uptake at low-to-moderate temperatures (5-20°C) and moderate pressures (10-20 bar), consistent with physisorption-

dominated mechanisms that are thermodynamically favoured at lower temperatures. In contrast, TEPA-functionalized materials require elevated temperatures (40°C) and pressures (40 bar) to achieve maximum performance, reflecting the thermally activated nature of

amine-CO_2 chemisorption. At 40°C, increased molecular mobility and reaction kinetics facilitate carbamate formation ($R\text{-}NH_2 + CO_2 \rightarrow R\text{-}NHCOO^-$), while high pressure provides the thermodynamic driving force for multilayer loading. Indeed, as reported in the Supplementary Fig. 4, in the second cycle, there is a dramatic drop in performance from 47% to 26% maybe due to the interaction itself.

The remarkable increase in cpGO-TEPA performance (from 0.8% to 43.6%) and in wpGO-TEPA (from 4.0% to 67.0%) from low to high T/P conditions demonstrates the critical importance of process optimisation for amine-functionalized sorbents.

14.4 Conclusions

Across all conditions tested, waste-derived materials consistently outperformed commercial analogues: wpGO vs. cpGO and wpGO-TEPA vs. cpGO-TEPA (Fig.5). This superiority, despite

lower absolute nitrogen content in wpGO-TEPA, can be attributed to the structural characteristics imparted by the industrial graphite precursor. The waste-derived materials likely possess inherently higher concentrations of structural defects, edge sites, and a more disordered interlayer structure that promotes better TEPA dispersion and CO_2 accessibility. This finding validates the circular economy approach and demonstrates that waste valorisation can yield materials with superior functional properties compared to commercial alternatives.

References

(1) Chai, S. Y. W., Ngu, L. H. & How, B. S. Review of carbon capture absorbents for CO2 utilization. *Greenhouse Gases: Science and Technology* vol. 12 394–427 Preprint at https://doi.org/10.1002/ghg.2151 (2022)

(2) Lin, Q.; Zhang, X.; Wang, T.; Zheng, C.; Gao, X. *Technical Perspective of Carbon Capture, Utilization, and Storage*. **Engineering 2022**, *14* (7), 27–32. https://doi.org/10.1016/j.eng.2021.12.013

(3) Zhao, F., Cui, C., Dong, S., Xu, X. & Liu, H. An overview on the corrosion mechanisms and inhibition techniques for amine-based post-combustion carbon capture process. *Sep Purif Technol* 304, (2023).

(4) Yao, X., Cordova, K. E. & Zhang, Y. B. Flexible Metal–Organic Frameworks as CO2 Adsorbents en Route to Energy-Efficient Carbon Capture. *Small Structures* vol. 3 Preprint at https://doi.org/10.1002/sstr.202100209 (2022).

(5) Rajendran, A., Shimizu, G. K. H. & Woo, T. K. The Challenge of Water Competition in Physical Adsorption of CO2 by Porous Solids for Carbon Capture Applications – A Short Perspective. *Advanced Materials* 36, (2024).

(6) Chen, G., Wang, T., Zhang, G., Liu, G. & Jin, W. Membrane materials targeting carbon capture and utilization. *Advanced Membranes* 2, 100025 (2022).

(7) Hou, R., Fong, C., Freeman, B. D., Hill, M. R. & Xie, Z. Current status and advances in membrane technology for carbon capture. *Sep Purif Technol* 300, 121863 (2022).

(8) Daneshvar, E., Wicker, R. J., Show, P. L. & Bhatnagar, A. Biologically-mediated carbon capture and utilization by microalgae towards sustainable CO2 biofixation and biomass valorization – A review. *Chemical Engineering Journal* 427, 130884 (2022).

(9) Rosa, L. & Mazzotti, M. Potential for hydrogen production from sustainable biomass with carbon capture and storage. *Renewable and Sustainable Energy Reviews* 157, 112123 (2022).

(10) Rosa, L., Becattini, V., Gabrielli, P., Andreotti, A. & Mazzotti, M. Carbon dioxide mineralization in recycled concrete aggregates can contribute immediately to carbon-neutrality. *Resour Conserv Recycl* 184, 106436 (2022).

(11) Zhao, H. *et al*. On the role of system integration of carbon capture and mineralization in achieving net-negative emissions in industrial sectors. *Energy Environ Sci* 16, 4356–4372 (2023).

(12) Sun, M. *et al*. Customizing high-performance molten salt biochar from wood waste for CO2/N2 separation. *Fuel Processing Technology* 234, 107319 (2022).

(13) Hanif, A. *et al*. CO2 Adsorption on Pore-Engineered Carbons Derived from Jute Sticks. *Chem Asian J* 18, e202300481 (2023).

(14) Lozinska, M. M., Miller, D. N., Brandani, S. & Wright, P. A. Hiding extra-framework cations in zeolites L and Y by internal ion exchange and its effect on CO2 adsorption. *J Mater Chem A Mater* 8, 3280–3292 (2020).

(15) Jiang, Q. *et al*. Synthesis of T-type zeolite nanoparticles for the separation of CO2/N2 and CO2/CH4 by adsorption process. *Chemical Engineering Journal* 230, 380–388 (2013).

(16) Chen, C., Park, D. W. & Ahn, W. S. CO2 capture using zeolite 13X prepared from bentonite. *Appl Surf Sci* 292, 63–67 (2014).

(17) Gaikwad, S., Kim, Y., Gaikwad, R. & Han, S. Enhanced CO2 capture capacity of amine-functionalized MOF-177 metal organic framework. *J Environ Chem Eng* 9, 105523 (2021).

(18) Chen, C., Jiang, Q., Xu, H. & Lin, Z. Highly Efficient Synthesis of a Moisture-Stable Nitrogen-Abundant Metal-Organic Framework (MOF) for Large-Scale CO 2 Capture. *Ind Eng Chem Res* 58, 1773–1777 (2019)

(19) Raganati, F., Gargiulo, V., Ammendola, P., Alfe, M. & Chirone, R. CO2 capture performance of HKUST-1 in a sound assisted fluidized bed. *Chemical Engineering Journal* 239, 75–86 (2014).

(20) Sanz-Pérez, E. S. *et al*. Reuse and recycling of amine-functionalized silica materials for CO2 adsorption. *Chemical Engineering Journal* 308, 1021–1033 (2017).

(21) Kong, Y., Shen, X., Fan, M., Yang, M. & Cui, S. Dynamic capture of low-concentration CO2 on amine hybrid silsesquioxane aerogel. *Chemical Engineering Journal* 283, 1059–1068 (2016).

(22) Wang, X., Chen, L. & Guo, Q. Development of hybrid amine-functionalized MCM-41 sorbents for CO2 capture. *Chemical Engineering Journal* 260, 573–581 (2015).

(23) Tiwari, D., Bhunia, H. & Bajpai, P. K. Urea-formaldehyde derived porous carbons for adsorption of CO2. *RSC Adv* 6, 111842–111855 (2016).

(24) Zhang, Y. *et al*. Multi-walled carbon nanotubes/carbon foam nanocomposites derived from biomass for CO2 capture and supercapacitor applications. *Fuel* 305, 121622 (2021).

(25) Tiwari, D., Goel, C., Bhunia, H. & Bajpai, P. K. Novel nanostructured carbons derived from epoxy resin and their adsorption characteristics for CO2 capture. *RSC Adv* 6, 97728–97738 (2016).

(26) Zhang, C. *et al*. Enhancement of CO2 Capture on Biomass-Based Carbon from Black Locust by KOH Activation and Ammonia Modification. *Energy and Fuels* 30, 4181–4190 (2016).

(27) Deng, M. & Park, H. G. Spacer-Assisted Amine-Coiled Carbon Nanotubes for CO2 Capture. *Langmuir* 35, 4453–4459 (2019).

(28) Chen, Y., Lin, G. & Chen, S. Preparation of a Solid Amine Microspherical Adsorbent with High CO2Adsorption Capacity. *Langmuir* 36, 7715–7723 (2020).

(29) Garibay, S. J. *et al*. Accessing functionalized porous aromatic frameworks (PAFs) through a de novo approach. *CrystEngComm* 15, 1515–1519 (2013).

(30) Gao, Q. *et al*. Covalent Organic Framework with Frustrated Bonding Network for Enhanced Carbon Dioxide Storage. *Chemistry of Materials* 30, 1762–1768 (2018).

(31) Yu, C. H., Huang, C. H. & Tan, C. S. A Review of CO2 Capture by Absorption and Adsorption. *Aerosol Air Qual Res* 12, 745–769 (2012).

(32) Chowdhury, S. & Balasubramanian, R. Recent advances in the use of graphene-family nanoadsorbents for removal of toxic pollutants from wastewater. *Adv Colloid Interface Sci* 204, 35–56 (2014).

(33) Chen, D., Feng, H. & Li, J. Graphene oxide: Preparation, functionalization, and electrochemical applications. *Chem Rev* 112, 6027–6053 (2012).

(34) Zhao, G., Li, J., Ren, X., Chen, C. & Wang, X. Few-layered graphene oxide nanosheets as superior sorbents for heavy metal ion pollution management. *Environ Sci Technol* 45, 10454–10462 (2011).

(35) Pavagadhi, S., Tang, A. L. L., Sathishkumar, M., Loh, K. P. & Balasubramanian, R. Removal of microcystin-LR and microcystin-RR by graphene oxide: Adsorption and kinetic experiments. *Water Res* 47, 4621–4629 (2013).

(36) Liu, Y., Sajjadi, B., Chen, W. Y. & Chatterjee, R. Ultrasound-assisted amine functionalized graphene oxide for enhanced CO2 adsorption. *Fuel* 247, 10–18 (2019).

(37) Song, Y. *et al*. Amino-functionalized graphene oxide blend with monoethanolamine for efficient carbon dioxide capture. *J Alloys Compd* 704, 245–253 (2017).

(38) Hong, S. M. & Lee, K. B. Solvent-assisted amine modification of graphite oxide for CO2 adsorption. *RSC Adv* 4, 56707–56712 (2014).

(39) Li, X. *et al*. Interlayer functionalization of vermiculite derived silica with hierarchical layered porous structure for stable CO2 adsorption. *Chemical Engineering Journal* 435, 134875 (2022).

(40) Fathy, M., Hosny, · R, Keshawy, · Mohamed & Gaffer, · Amany. Green synthesis of graphene oxide from oil palm leaves as novel adsorbent for removal of Cu(II) ions from synthetic wastewater. *Graphene Technology 2019 4:1* 4, 33–40 (2019).

(41) Singhal, K., Mehtab, S., Pandey, M. & Zaidi, M. G. H. Sustainable development of graphene oxide from pine leaves for electrochemical energy storage and corrosion protection. *Current Research in Green and Sustainable Chemistry* 5, 100266 (2022).

(42) Goswami, S., Banerjee, P., Datta, S., Mukhopadhayay, A. & Das, P. Graphene oxide nanoplatelets synthesized with carbonized agro-waste biomass as green precursor and its application for the treatment of dye rich wastewater. *Process Safety and Environmental Protection* 106, 163–172 (2017).

(43) Anuar, A. U., Bonnia, N. N., Jamil, N. M. & Affandi, N. D. N. Graphene oxide based regenerated carbon waste tyre (rCB): Synthesis by modified Hummers method and characterization. *Mater Today Proc* https://doi.org/10.1016/J.MATPR.2023.02.280 (2023) doi:10.1016/J.MATPR.2023.02.280.

(44) Kumar Sahoo, S. *et al*. Preparation of graphene oxide from Bio-soot wastes: As an efficient adsorbent for highly noxious Congo red dye. *FlatChem* 24, 100198 (2020).

(45) Hassanin, M. A. *et al*. Sustainable Remedy Waste to Generate SiO2 Functionalized on Graphene Oxide for Removal of U(VI) Ions. *Sustainability 2022, Vol. 14, Page 2699* 14, 2699 (2022).

(46) Meconi, G. M., Tomovska, R. & Zangi, R. Adsorption of CO2 gas on graphene–polymer composites. *Journal of CO2 Utilization* 32, 92–105 (2019).

(47) Qie, F. *et al*. β-Cyclodextrin Functionalized Nanoporous Graphene Oxides for Efficient Resolution of Asparagine Enantiomers. *Chem Asian J* 13, 2812–2817 (2018).

(48) Hosseini, Y., Najafi, M., Khalili, S., Jahanshahi, M. & Peyravi, M. Assembly of amine-functionalized graphene oxide for efficient and selective adsorption of CO_2. *Mater Chem Phys* 270, 124788 (2021).

(49) Chen, Y., Li, D., Yang, W., Xiao, C. & Wei, M. Effects of different amine-functionalized graphene on the mechanical, thermal, and tribological properties of polyimide nanocomposites synthesized by in situ polymerization. *Polymer (Guildf)* 140, 56–72 (2018).

(50) Stobinski, L. *et al*. Graphene oxide and reduced graphene oxide studied by the XRD, TEM and electron spectroscopy methods. *J Electron Spectros Relat Phenomena* 195, 145–154 (2014).

(51) Kaushal, A., Dhawan, S. K. & Singh, V. Determination of crystallite size, number of graphene layers and defect density of graphene oxide (GO) and reduced graphene oxide (RGO). *AIP Conf Proc* 2115, (2019).

(52) Ferrari, A. C. & Robertson, J. Origin of the 1150 − cm−1 Raman mode in nanocrystalline diamond. *Phys Rev B Condens Matter Mater Phys* 63, (2001).

(53) Al-Jishi, R. & Dresselhaus, G. Lattice-dynamical model for graphite. *Phys Rev B* 26, 4514 (1982).

(54) Lee, A. Y. *et al.* Raman study of D* band in graphene oxide and its correlation with reduction. *Appl Surf Sci* 536, 147990 (2021).

(55) Ferrari, A. C. & Basko, D. M. Raman spectroscopy as a versatile tool for studying the properties of graphene. *Nature Nanotechnology 2013 8:4* 8, 235–246 (2013).

(56) Zafar, Z. *et al.* Evolution of Raman spectra in nitrogen doped graphene. *Carbon N Y* 61, 57–62 (2013).

(57) Yoo, J. *et al.* Unraveling the role of Raman modes in evaluating the degree of reduction in graphene oxide via explainable artificial intelligence. *Nano Today* 57, 102366 (2024).

(58) Yoo, J. *et al.* Unraveling the role of Raman modes in evaluating the degree of reduction in graphene oxide via explainable artificial intelligence. *Nano Today* 57, (2024).

(59) Di Profio, P. *et al.* Separation of CO_2 and CH_4 from biogas by formation of clathrate hydrates: Importance of the driving force and kinetic promoters. *ACS Sustain Chem Eng* 5, 1990–1997 (2017).

(60) Canale, V., Fontana, A., Siani, G. & Di Profio, P. Hydrate Induction Time with Temperature Steps: A Novel Method for the Determination of Kinetic Parameters. *Energy and Fuels* 33, 6113–6118 (2019).

(61) Apparatus for preparing and studying clathrate hydrate. (2006).

15 Nanocarb Project→ Photoelectrochemical O_2 evolution.

15.1 Substrate preparation

FTO substrates were sequentially sonicated in three solvents: water, acetone, isopropyl alcohol (IPA). Following sonication, substrates underwent UV/Ozone treatment for 30 minutes to enhance surface cleanliness, wettability and reactivity.

15.2 Graphene oxide synthesis

Graphene oxide was synthetized starting from graphite. Briefly, 5 g of graphite were added to 150 mL of H_2SO_4 followed by the addition of 20 g of $KMnO_4$ and avoiding the rise of temperature above 25 °C using an ice bath. Afterwards, the temperature increased to 80°C. After 6h, the reaction mixture was cooled to room temperature and 400 mL of water were added to neutralize the solution. Finally, the addition of H_2O_2 (50 mL) was intended to neutralise excess $KMnO_4$. The brown suspension was filtered and rinsed with water and dried.

15.3 Graphene oxide electrophoretic deposition (EPD)

100 mL of a 1 mg/mL solution of graphene oxide in water was sonicated for 15 minutes. Two FTO substrates were used as the cathode and anode, while GO was used as the electrolyte. A potential of 15 V was applied (Figure 1) for 1, 2, and 3 minutes, respectively, to obtain 3 different GO films on the FTO surface. After the coating, the obtained substrates were dried at 60°C overnight.



Figure 1. *DC supplier used for the EPD.*

15.4 Thermal annealing

Each sample was thermally annealed in a tubular furnace in nitrogen atmosphere using a 5 mL/min flow. A ramp of 10°C/min was selected and followed by a 2 h isothermal treatment to reduce the obtained GO-layered FTO. An additional GO-layered FTO (time of deposition 2 min) was annealed in the presence of urea (1:10 GO-Urea w/W) (Figure), to achieve the N-doping of the carbon skeleton of graphene.

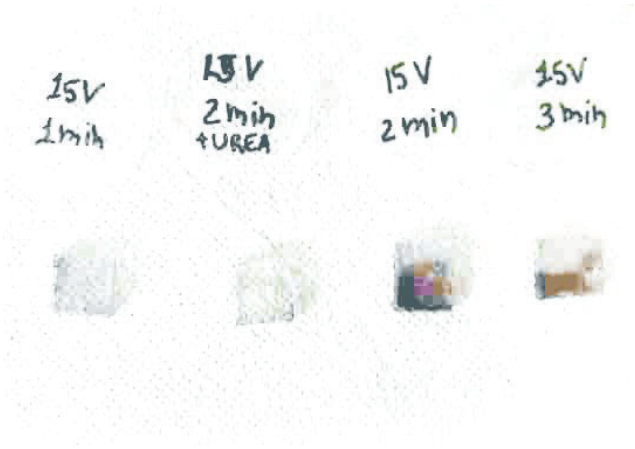

Figure 2. *As-obtained FTO-EPD-rGO after thermal annealing.*

15.5 Raman Analysis

The Raman spectra of GO EPD and annealed 1-min-EPD, 2-min-EPD and 3-min-EPD coated FTO substrates were obtained by confocal and high-performance Raman microscope (XploRA PLUS, HORIBA, Japan) with deep-cooled CCD detector technology. LabSpec (Horiba, Japan) was employed to control the Raman spectroscopic system and for the optimization and processing of the acquired data.

All Raman spectroscopic measurements were performed in the range of 600–3300 cm^{-1} and with a 1800-line/mm grating. The samples were detected with a 532 nm laser, with a time of 1 s and 1 accumulation for each spectrum. Moderate power irradiation at the sample surface was used (∼10 mW), focusing onto the sample surface with a 50× objective to avoid laser-induced heating. For the Raman mapping of the G band intensity, an area of 400 μm^2 was chosen by using a 50× objective and scanned with an excitation laser of 532 nm with 2.2 μm between each point.

15.6 KuQuinone Spin Coating

A solution of KuQEt (0.36 mg/mL in methanol) was spin-coated onto the substrate. For each coating cycle, 100 μL of the solution was deposited and spin coated. This process was repeated three times, with a 90-second interval between each coating step to enhance π–π stacking interactions

15.7 Results and Discussion

As shown in

Figure 3 a smooth and homogenously distributed GO film after a minute of EPD in GO (1 mg/mL) solution.

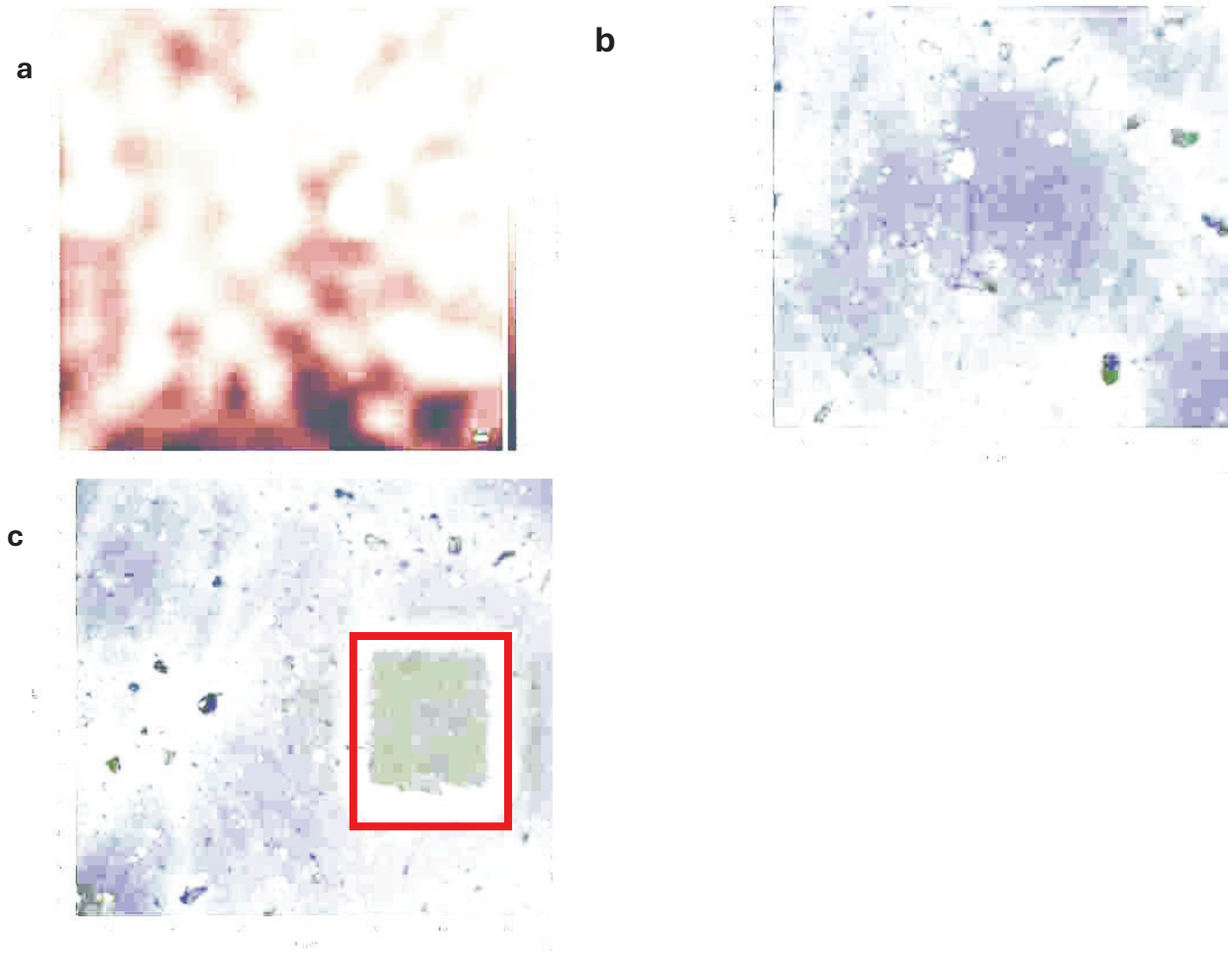

Figure 3. *a)GO Raman mapping of the sample obtained by monitoring the concentration through the G peak at ca. 1600 cm^{-1}, that could be evaluated on the scale bar on the right from 95 up to 165 counts ; b) FTO-EPD-1min-GO sample c) Optical image of FTO after the EPD process; c) Optical image of FTO after the Raman mapping that caused the burn of the GO film (highlighted in red).*

The Raman spectrum of the sample after the thermal treatment shows many differences with respect to the GO-EPD sample. Indeed, there is a drop in terms of I_D/I_G ratio from 0.81 to 0.65 (Figure 4) that highlights a partial restoration of sp^2 system. Furthermore, even the film colour changes from light blue to a grey(-ish) region, as shown in Figure6-A,6-B.

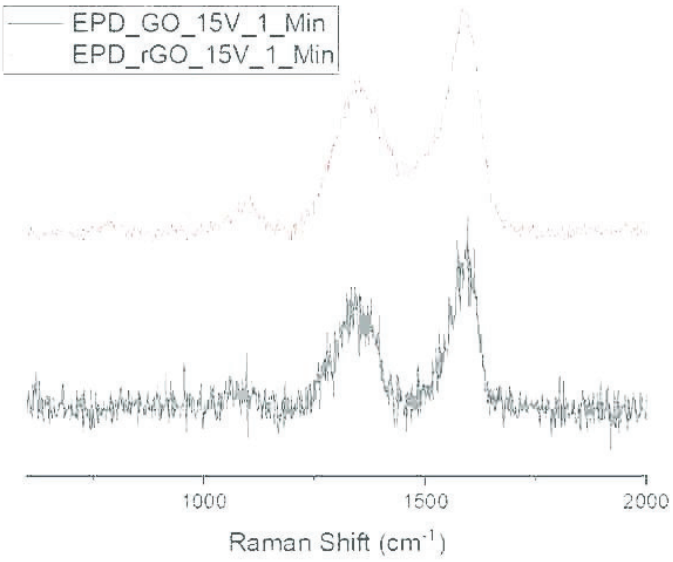

Figure 4. *Comparison of the 1 min EPD-GO-deposited FTO before and after thermal treatment.*

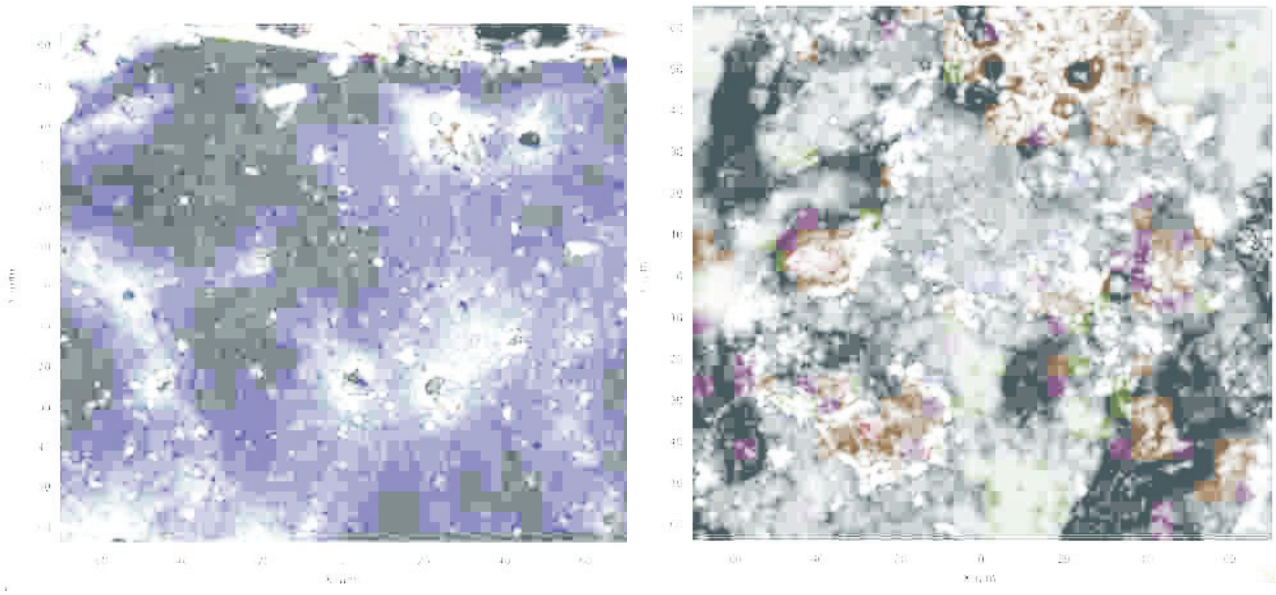

Figure 5. Optical microscope image of graphene oxide before (left image) and after (right image) thermal annealing.

The N-doped-1-minutes, the 2 minutes and 3 minutes EPD deposited FTO show a significantly higher homogeneity of the film on the surfaces than the 1-minute-EPD-sample (Figure).

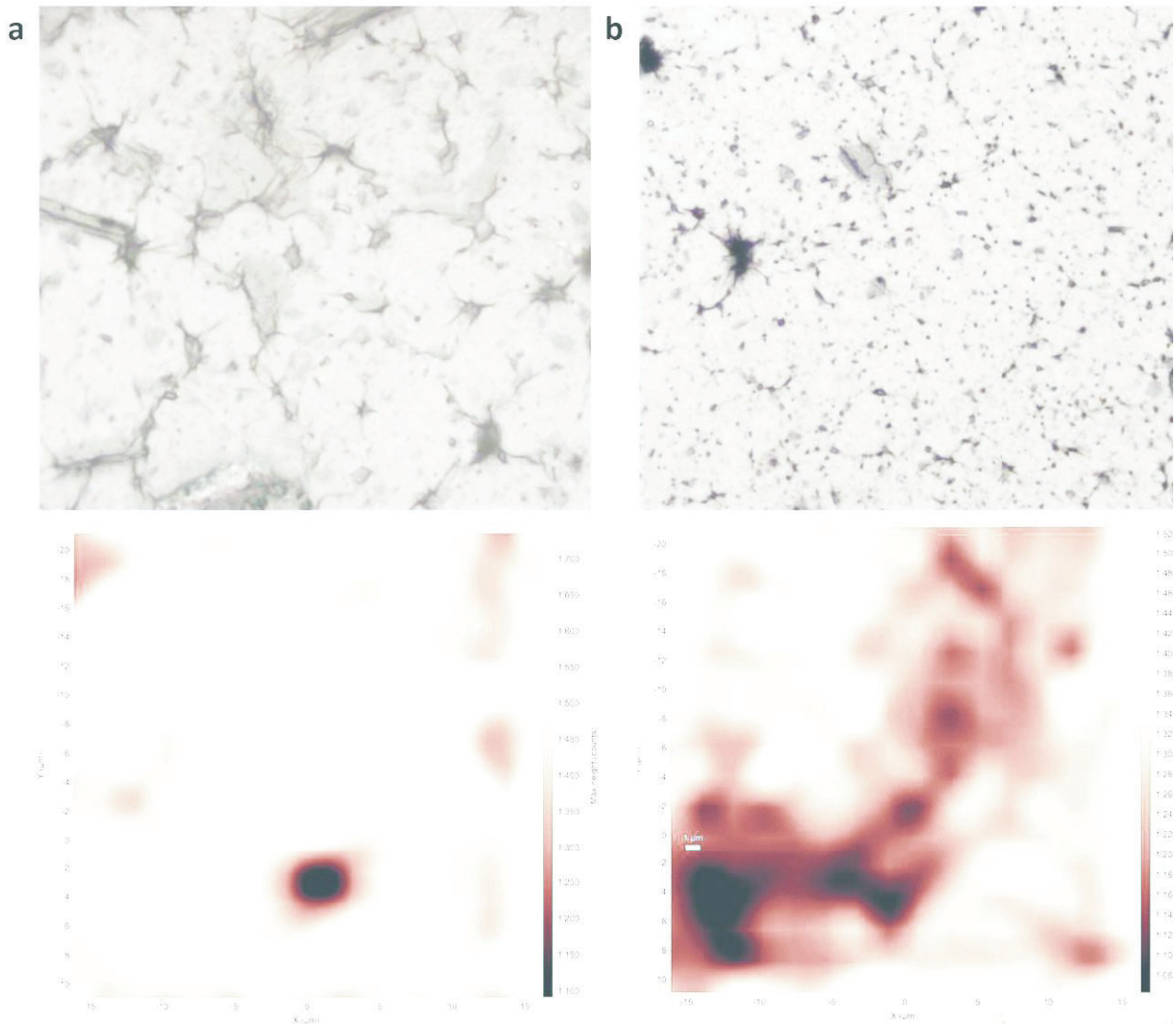

Figure 6 *Optical microscopy photographs (above Figures) and related Raman mapping (Figures below) of (A) 2 min EPD-GO after the annealing process (100x). B) 3 min EPD-GO after the annealing process (50x).*

Even after annealing at 400°C, the surface of the sample appears remarkably smooth, and reduced GO shows a well-dispersed film, as highlighted by Raman spectroscopy on an area of 900 μm^2.

It is worth noting how the treatment with urea changes the shape and colour of the film. Indeed, the 2 min EPD-GO annealed in the presence of urea shows a different film, as shown in Figure .

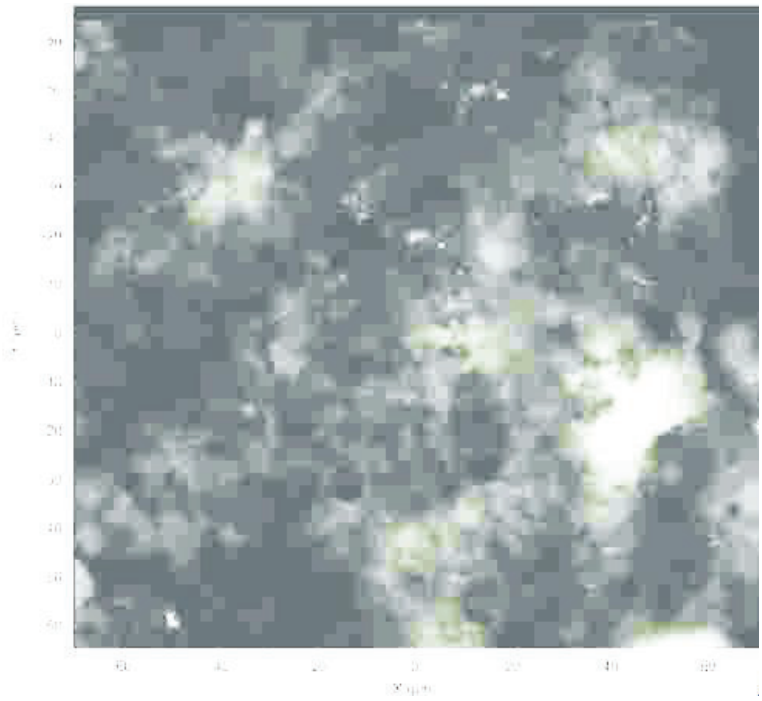

Figure 7. *Optical microscopy of 2-min EPD-GO annealed in the presence of urea.*

15.8 Raman characterisation of spin-coated samples

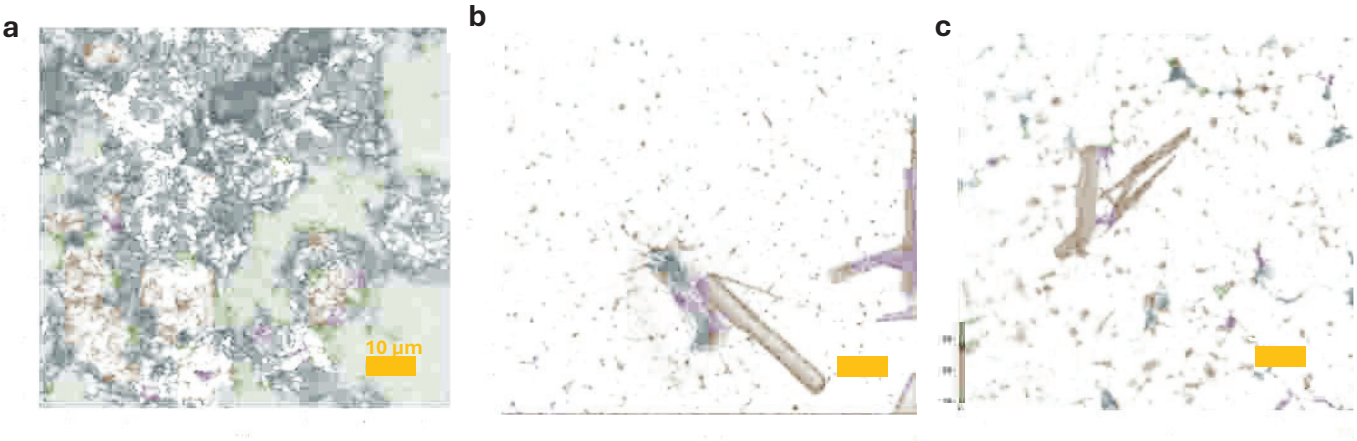

Figure 8. *Optical microscopy image of 1 (a), 2 (b), or 3 (c) minutes-EPD-rGO after spin coating KuQuinone.*

The texture of the sample after KuQuinone spin coating appears largely unchanged, the only difference being the presence of some KuQuinone crystals on the surface (Fig. 8-B, Fig.8-C). However, Raman mapping reveals that although the concentration of KuQuinone is high enough to

induce crystal formation, KuQuinone is well-dispersed across the entire surface of the FTO-rGO, as demonstrated from Raman mapping in Figure 9.

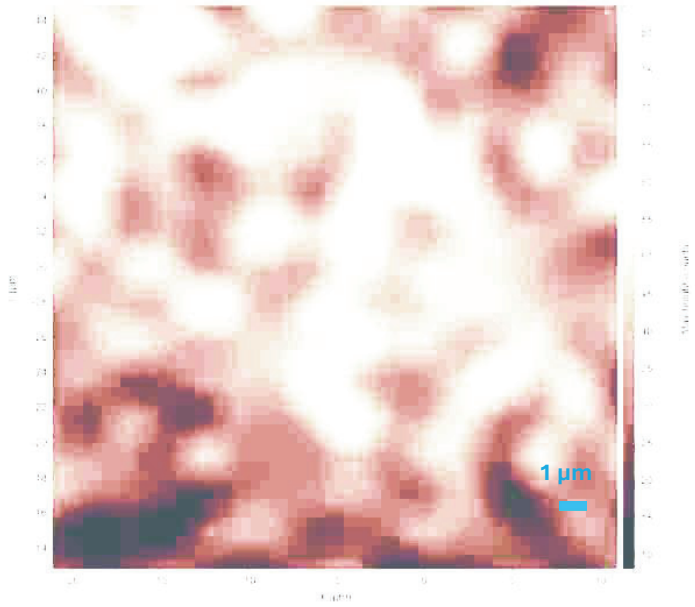

Figure 9. *2 minutes- EPD-rGO Raman mapping after KuQuinone spin coating. The scale bar refers to the KuQuinone peak intensity at 1450 cm^{-1}.*

The Raman spectrum shows a change in shape due to the presence of KuQuinone. Indeed, between the D and G peak appears a peak due to KuQuinone as reported in Figure in both 2 and 3 minutes EPD-rGO-Antenna composites.

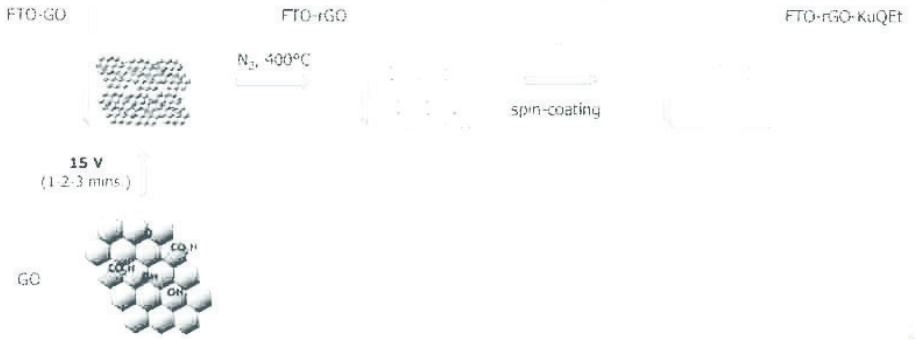

Figura 10: Photoelectrocatalyst preparation procedures.

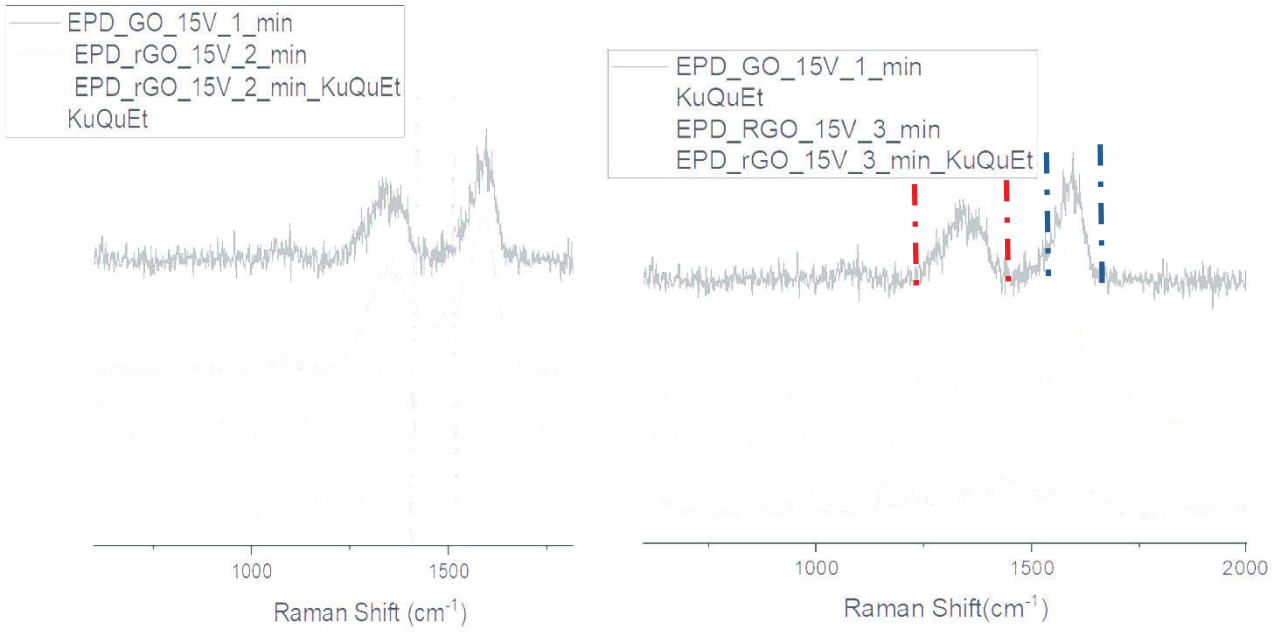

Figure 11. *Raman spectra recorded after each step of the preparation protocol of 2 min-EPD-rGO-KuQuin (on the left) and 3 min-EPD-rGO-KuQuin (on the right).*

After the thermal treatment, a noticeable reduction in the I_D/I_G ratio is observed, indicating a decrease in the structural disorder of the graphene layer. Additionally, the observed red shift of the G peak could be attributed to the partial restoration of the sp^2 carbon network. Another significant feature is the pronounced band in the region between the D (1350 cm^{-1}) and G (1580 cm^{-1}) peaks, (that are delimited by red and blue lines respectively in Fig.11-right) along with the presence of additional peaks ascribed to KuQEt (in between the purple lines of Fig.11-left). These spectral changes confirm the successful spin-coating of KuQEt onto the surface, as previously shown in the referenced image (Fig.10), and further validated by Raman mapping.

15.9 X-ray diffraction

Due to experimental constraints, the X-Ray analysis (Figure 13) was carried out on bare powder to simulate what happens on the support. The interlayer distance decreases, as calculated from Bragg's law, equation 1, from 0.79 nm to 0.422 nm, confirming that the reduction process has taken place.

$$n\lambda = 2dsin\theta$$

Equation 1 Bragg's Law for calculation of interlayer distance through the Bragg angle. Where n = order of reflection, (usually 1); λ= wavelength of the incident X-rays, it depends by the source (0,15406 nm for copper source); d = interplanar spacing between the crystal planes; θ = angle of incidence (Bragg angle), measured from the crystal plane.

The crystallite size decreases significantly due to the loss of long-range order in the out-of-plane stacking that occurs with the increase in temperature. This suggests that temperature induces out-of-plane exfoliation and in-plane structural healing.

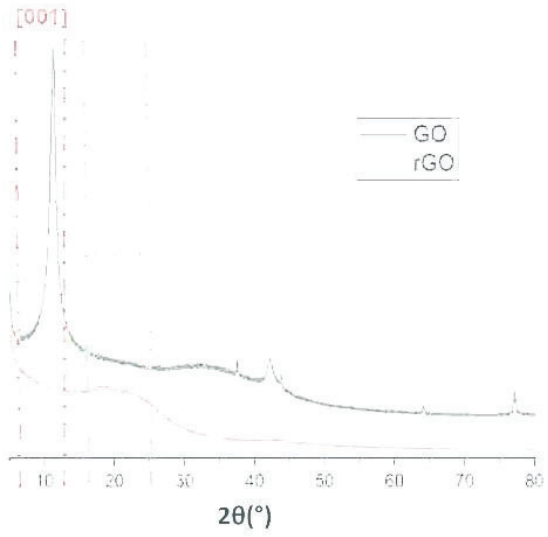

Figure 13. *XRD data of graphene oxide and graphene oxide after thermal annealing.*

15.10 Photoelectrochemical measurements

Photoelectrochemical measurements were performed in an aqueous solution of 0.1 M Na_2SO_4 as a supporting electrolyte. The cell was composed by the functionalized FTO/rGO/KuQEt as working electrodes, a platinum counter electrode and SCE reference electrode, applying a bias potential of 0.3 V (3). Bare FTO electrode gave a flat signal. Conversely, irradiation of the FTO/rGO/KuQEt electrodes with a green LED (10 W) resulted in the generation of anodic photocurrent. After switching off the illumination, the photocurrent immediately dropped.

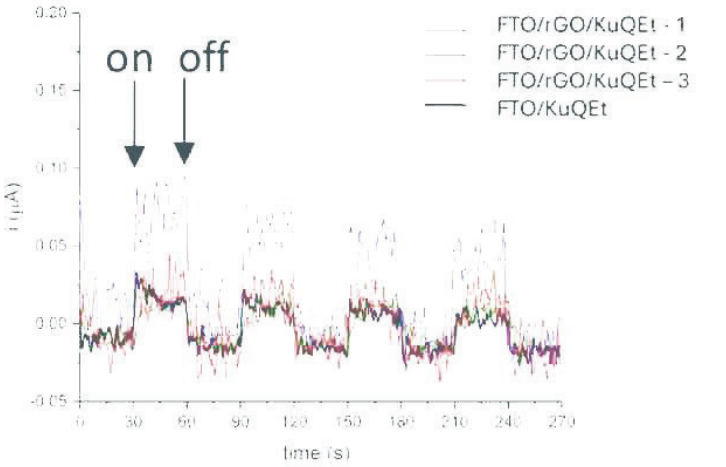

Figure 14: *Photoelectrochemical response of FTO/KuQEt (black trace), FTO/rGO/KuQEt - 1 (purple trace), FTO/rGO/KuQEt - 2 (green trace), FTO/rGO/KuQEt - 1 (red trace) in H_2O/0.1 M Na_2SO_4 at 0.3 V vs. SCE, upon irradiation with a green LED at room temperature; 30 seconds of irradiation were alternated with 30 seconds of dark.*

15.11 Conclusions

Electrophoretic deposition (EPD) and spin coating techniques were successfully employed to fabricate and functionalize graphene oxide (GO) films on FTO substrates. Through careful thermal annealing under nitrogen atmosphere, a significant reduction of GO was achieved, as evidenced by Raman spectroscopy and XRD analysis. The decrease in the I_D/I_G ratio and the shift in the G band confirmed the partial restoration of the sp^2 carbon network, while the reduction in interlayer distance from 0.79 nm to 0.422 nm validated the effective removal of oxygen-containing groups. Furthermore, thermal treatment induced a noticeable loss of long-range order in the out-of-plane stacking, highlighting a mechanism of exfoliation and structural reorganisation.

Finally, spin coating of KuQEt onto the thermally reduced GO layers yielded uniform and well-dispersed hybrid materials. Raman mapping revealed both the presence and effective distribution of the KuQEt compound, as well as distinctive spectral features related to its interaction with the rGO matrix. These results demonstrate the potential of the combined EPD and spin coating approach for developing tailored GO-based hybrid materials with tunable properties for future electronics and catalysis applications.

Eventually, photoelectrochemical tests demonstrated enhanced photocurrent responses upon visible-light irradiation, confirming the stabilising role of GO in the hybrid system.

16 Nanocarb Project→ CO_2 electroreduction

16.1 Introduction

In this part of the project, we developed electrodes for CO_2RR. More precisely, the industrial waste was compressed and threatened as it is a carbon brushes, even though its application was the reduction of CO_2.

This was aimed to the demonstration of the reduction of carbon dioxide by an electrode already scalable with an in-house technology.

16.2 Materials and methods

16.2.1 Electrode production

More precisely, the powder was mixed and compressed at 3 ton/cm^2, followed by a curing process at 3°C/min until 450°C, followed by 1h isotherm.

16.2.2 Electrochemical processes

All electrochemical experiments, including Cyclic Voltammetry (CV) and Chronoamperometry (CA), were carried out using a Metrohm Autolab PGSTAT302N potentiostat. Data acquisition and instrumental control were managed via Autolab NOVA software. The potential was referenced against a saturated Ag/AgCl reference electrode in an H-cell, with a nafion separation membrane.

16.2.3 Chronoamperometry

A bias of -1.4 V vs Ag/AgCl was applied for 3 hours to estimate the stability of the electrode. After 3 h, the sampling was done.

16.2.4 Product quantification by ^{1}H-NMR spectroscopy

The liquid products obtained from the electrochemical CO_2 reduction reaction (CO_2RR) were identified and quantified by ^{1}H-NMR spectroscopy. At the end of each electrolysis experiment, an aliquot of the electrolyte was collected from the cathodic compartment.

For NMR analysis, the samples were prepared following a standard protocol. Specifically, 400 µL of the reaction electrolyte were mixed with 40 µL of a deuterated solution consisting of deuterium oxide (D_2O) containing a known concentration of an internal standard (DMSO 4 mM). The internal standard was used both for chemical shift calibration and for quantitative analysis.

The concentration of each liquid product was calculated using the following equation, commonly reported in the literature:

$$C_a = \frac{I_a}{I_{st}} \cdot \frac{N_{st}}{N_a} \cdot C_{st} \cdot \frac{V_{st}}{V_a}$$

where $C_a$and $C_{st}$are the concentrations of the analyte and the internal standard, respectively; $I_a$and $I_{st}$are the integrated areas of the corresponding NMR signals; $N_a$and N_{st}represent the number of protons contributing to the selected resonance peaks; and $V_a$and $V_{st}$are the volumes of the electrolyte sample (400 µL) and the internal standard solution (40 µL), respectively.

All ^{1}H-NMR spectra were acquired at Bruker 300 MHz and processed using Mestrenova software. Water signal suppression was applied using a standard presaturation pulse sequence in order to minimize the solvent signal and enhance the resolution of the product resonances.

16.3 Results and Discussion



Figure 1: *electrochemical setup used for CO_2 reduction reaction using waste based electrodes provided from Carbotech Srl.*

In Fig. 1, the setup used for the CO2 reduction reaction is shown. The electrodes used are obtained through the comprising of waste graphite(for the anode) and copper graphite or copper, molybdenum disulfide, graphite as cathodes, that appears as in Fig.2.



Figure 2: *electrode obtained from waste materials used for CO_2RR.*

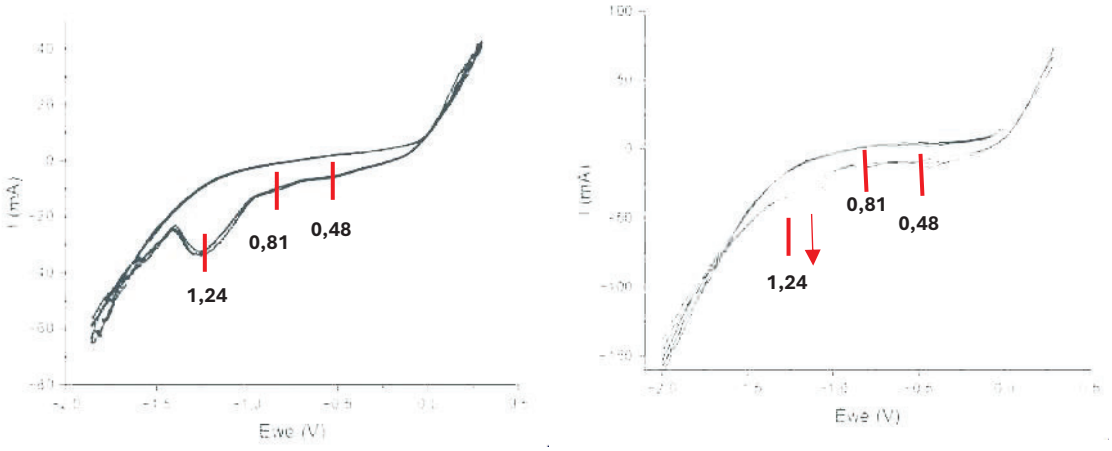

Figure 3: CV of copper-graphite electrode and copper-Molybdenum disulfide-graphite electrodes, on the left and the right, respectively.

Fig.3 reports copper reduction peaks. It is interesting to note that during the CV (10 mV/s, from +0.3 to -2V vs Ag/AgCl electrode) the concentration of the species that pass from Cu^{2+} to Cu^{0} decreased cycle after cycle, in the case of Cu_MoS_2@graphite, while only copper containing-electrode remain the same cycle after cycle. This may be due to the conversion of insulating layers into electrochemically accessible Cu^{2+} sites, then subsequent cycles increase the intensity of the conversion to the metallic form. Alternatively, the electrode may become more catalytically active cycle after cycle (e.g., through surface roughening or in situ generation of catalytic sites), enhancing the reaction rate.

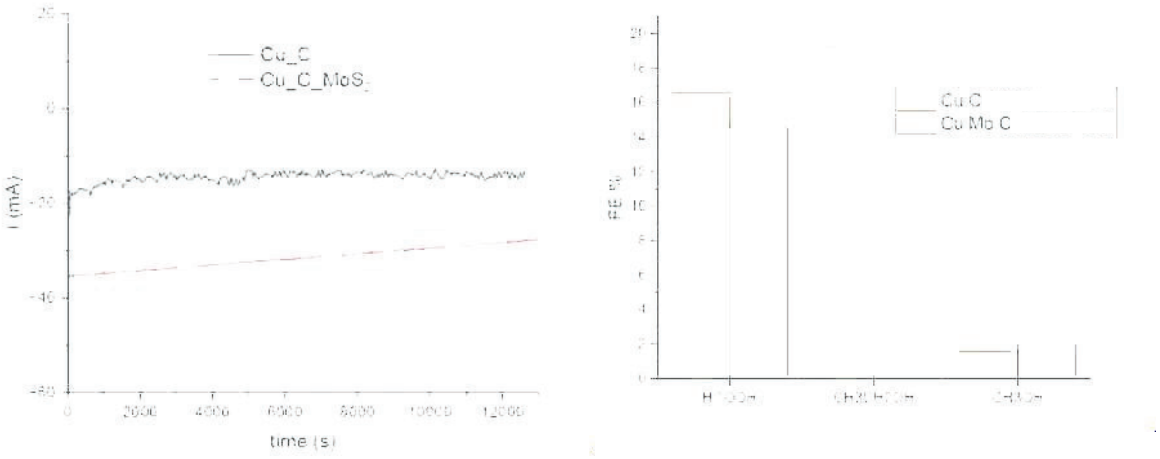

Figure 4: *Chronoamperometry and faradaic efficiency related graph, on the left and right respectively.*

Fig.4 reports the current and FE of the electrodes. None of the electrode is completely selective because both of them do form more than one product. Indeed, a certain degree of selectivity towards formate, as shown in the figure 4, is observed for thr Cu_C electrode, since the amount of methanol produced is very low. Furthermore, the current is pretty stable for both electrodes. As a matter of fact the surface area of the Cu_C_MoS_2 electrode is higher than that of the Cu_C electrode and the current density obtained *J* is ca. 10 mA/cm^2. Eventually, both materials show a higher selectivity towards formate, so a different buffer and condition will be explored.

16.4 Conclusion

We demonstrated the possibility of a large scale production of electrodes exploiting the well-known technology of carbon brushes production. Optimization is possible through the processes already described, specifically by accelerating the ramp-up or adjusting the compression stage pressure. The stability, as shown through the cronoamperometry data highlights a pretty constant stability but other conditions and time endurance should be explored and optimised. The use of flow could also increase the current density *j*.

17 Ullmann Reaction

17.1 Materials and Methods

In order to optimize waste recovery, using it in its original waste form is definitely the best option. In fact, reducing the number of steps involved in recovery reduces the amount of energy used and is therefore both energy-efficient and cost-effective, meeting sustainability objectives.

The waste as such was used for an Ullmann reaction, specifically a C-N cross coupling between indole and iodobenzene. More specifically, 4.5 mmol of indole was reacted with 4.0 mmol of iodobenzene using 458 mg of KOH as a base, in different solvents, including NMP (N-methylpyrrolidone), DMSO, toluene, and ethylene glycol. The amount of catalyst used, the environment (inert or not), the time, and the temperature were varied. The reaction, whose reaction scheme is shown in Figure 1, was conducted at reflux for 24 hours. The resulting suspension was transferred to a separatory funnel and extracted with a chloroform/ethyl acetate mixture. The organic phases were combined, washed sequentially with water and brine to remove residual inorganic salts and polar impurities, then dried over anhydrous sodium sulfate. After filtration, the solvent was removed under reduced pressure using a rotary evaporator to afford a crude yellowish oil. The residue was further dried under high vacuum to remove traces of high-boiling solvents (notably DMSO), yielding the crude product, which was directly analyzed by NMR spectroscopy without further purification.

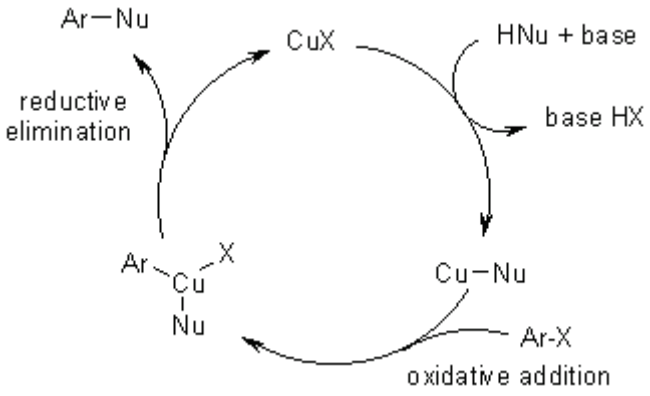

Figure 1: Ullmann reaction catalytic cycle.

17.2 Results and Discussion

Table 1 shows a summary of the results obtained from the Ullmann reaction as well as the amount of catalyst, solvent, and reaction environment varied. DMSO appears to be the best solvent for conducting the reaction. An inert environment is necessary because Cu(I) is the catalytic species, and air induces copper oxidation, causing a drastic drop in yield.

Table 1: *Summary table of yields as conditions vary. a) An excess of iodobenzene was used: 5.6 mmol of iodobenzene rather than 4.0 mmol of iodobenzene.*

Experiment	m_{cat}	T	t	Solvent	Environement	Yield
1	40 mg	110°C	24 h	DMSO	N_2	12%
2	80 mg	110°C	24 h	DMSO	N_2	27%
3	80 mg	110°C	24 h	DMSO	Air	14%
4	160 mg	110°C	24 h	DMSO	N_2	50%
5	160 mg	110°C	24 h	Toluene	N_2	8%
6	160 mg	110°C	24 h	EG	N_2	Traces
7	160 mg	110°C	24 h	DMSO	N_2	74%[a]

The crude reaction mixture obtained from the Ullmann copper-catalyzed C–N cross-coupling between indole and iodobenzene was analyzed by ^{1}H-NMR spectroscopy (400 MHz, $CDCl_3$) in order to confirm product formation and assess the extent of conversion. The spectrum clearly demonstrates the formation of 1-phenyl-1H-indole as the predominant organic species.

The most diagnostic resonance confirming successful N-arylation is observed at δ = 6.94 ppm(-ish), appearing as a doublet of doublets and assigned to the H-3 proton of the indole ring. This signal is particularly informative: the resolved vicinal coupling to H-4 and the detectable long-range allylic coupling to H-5 are characteristic of N-substituted indoles.

In contrast, unsubstituted indole typically exhibits the H-3 proton as a singlet or poorly resolved multiplet, indicating that the observed splitting pattern provides unambiguous evidence of N-phenylation.

Further confirmation is provided by the H-4 indole proton, which appears as the most deshielded resonance of the indole core at δ = 7.76–7.80 ppm. This pronounced downfield shift is consistent with its ortho position relative to the nitrogen atom and reflects the combined electron-withdrawing and anisotropic effects associated with N-substitution. The remaining indole protons resonate in the expected aromatic region: H-5 and H-6 appear as overlapping multiplets between δ = 7.18 and 7.32 ppm, H-7 appears as a doublet at δ = 7.55–7.62 ppm, and H-2 is observed as a multiplet at δ = 7.35–7.42 ppm. The overall deshielding pattern across the indole framework follows the expected electronic gradient for an N-arylated indole system.

The N-phenyl substituent contributes five aromatic protons, observed as overlapping multiplets between δ = 7.08 and 7.48 ppm, with the ortho protons appearing at slightly higher chemical shift than the meta and para protons, in agreement with an N-attached phenyl ring.

Signals attributable to unreacted indole are also present, in some case, in spectra reported below, indicating incomplete conversion.

In particular, the broad N–H resonance at δ = 8.2–8.5 ppm and the H-3 signal of indole at δ ≈ 7.03 ppm are clearly distinguishable from the corresponding product resonances. The relative integration of the product and starting material H-3 signals provides a qualitative estimate of conversion, consistent with literature-reported isolated yields for this transformation.

Spectral calibration is ensured by the residual $CHCl_3$ signal at δ = 7.26 ppm, confirming correct chemical shift referencing. Additional resonances corresponding to residual DMSO, ethyl acetate, and trace water are observed outside the diagnostic aromatic region and do not interfere with product assignment.

Overall, the ^{1}H-NMR data are in excellent agreement with reported literature values for authentic 1-phenyl-1H-indole, conclusively confirming successful N-arylation under the applied Ullmann coupling conditions.

***Table 2**: Complete ^{1}H-NMR Assignment Summary for Crude Ullmann C-N Cross Coupling Product (Indole + Iodobenzene → 1-Phenyl-1H-Indole)*

Compound/Component	Proton Assignment	Chemical Shift δ (ppm)	Multiplicity	Integration (nH)	Notes / Structural Significance
1-PHENYL-1H-INDOLE (MAIN PRODUCT)					Yellowish oil; $C_{14}H_{11}N$; MW 193.24 g/mol
	H-3 (β-indole)	6.94	dd	1H	**DIAGNOSTIC SIGNAL** for N-arylation; resolved allylic
	H-4 (ortho to N)	7.76–7.80	d	1H	Highly deshielded by ortho nitrogen; most downfield indole proton
	H-5 (benzenoid)	7.18–7.32	t	1H	Coupling to H-4 and H-6 (ortho pairs); benzenoid coupling pattern
	H-6 (benzenoid)	7.18–7.32	t	1H	Coupling to H-5 and H-7 (ortho pairs); benzenoid coupling pattern
	H-7 (ortho to ring fusion)	7.55–7.62	d	1H	Secondary deshielding from ring fusion; couples only to H-6
	H-2 (on N-bearing carbon)	7.35–7.42	m	1H	N-bearing carbon; intermediate deshielding; partially compensated by C3=C2 double bond
	N-Phenyl ortho (relative to N)	7.40–7.48	m	2H	Directly attached to electron-withdrawing N; most deshielded phenyl protons
	N-Phenyl meta (relative to N)	7.24–7.32	m	2H	Intermediate deshielding; standard aromatic coupling to ortho protons
	N-Phenyl para (relative to N)	7.08–7.16	m	1H	Farthest from N; maximally shielded N-phenyl protons
UNREACTED INDOLE (STARTING MATERIAL)					Residual indicates partial conversion
	N-H	8.2–8.5	br s	~0.5H	Broad singlet; unambiguous indicator of free indole
	H-3	~7.03	d	~0.5H	Distinguished from product H-3 by simpler multiplet structure

Compound/Component	Proton Assignment	Chemical Shift δ (ppm)	Multiplicity	Integration (nH)	Notes / Structural Significance
	H-4	~7.58	d	~0.5H	Sharp doublet
	H-5 to H-	7.10–7.35	m	~1.5H	Overlapping multiplets;
IODOBENZENE (UNREACTED ARYL HALIDE)					Residual aryl halide; signals overlap with N-phenyl aromatic region
	Aromatic (ortho to I)	7.65–7.75	m	~2H	Ortho to electron-donating I (via π-donation); slightly shielded relative to N-phenyl ortho
	Aromatic (meta to I)	7.20–7.35	m	~2H	Meta coupling to ortho protons; overlaps with N-phenyl meta signals
	Aromatic (para to I)	7.00–7.10	m	~1H	Most shielded due to distance from I and resonance electron donation
CALIBRATION & INTERNAL STANDARDS					
	$CHCl_3$ (solvent reference)	7.26	s	—	IUPAC universal ^{1}H-NMR reference
	p-dinitrobenzene (qNMR standard)	~8.40	s	1H	Quantitative internal standard; permits absolute yield calculation;
RESIDUAL SOLVENTS & IMPURITIES					
	Ethyl acetate ($-OCH_2-$)	4.15	q	2H	From aqueous extraction workup;
	Ethyl acetate ($-CH_3$)	1.25	t	3H	2:3 integration ratio (quartet:triplet) confirms EtOAc identification
	DMSO (reaction solvent)	2.70	s	All equivalent	Boiling point 189 °C; hygroscopic; incompletely removed by standard workup

Interpretation and Quantitative Analysis

The ^{1}H-NMR analysis provides unambiguous spectroscopic confirmation of successful N-arylation to afford 1-phenyl-1H-indole. The diagnostic doublet of doublets for H-3 at δ = 6.94 ppm, is a chemical fingerprint of the product and is definitively absent in free indole.

The presence of residual indole N-H singlet (δ = 8.2–8.5 ppm) and unreacted indole aromatic signals provides quantitative evidence of partial conversion, with the integration ratio of product H-3 to unreacted indole H-3 yielding a preliminary conversion estimate. Integration of the product H-3 signal relative to the *p*-dinitrobenzene internal standard (δ ≈ 8.40 ppm, ^{1}H singlet) enables calculation of absolute product mass via quantitative NMR without requiring product isolation or purification:



N_P: Number of protons contributing to the product signal (usually 1 for the product CH peaks).

I_S: Integration of the standard peak (e.g., the signal at 8.42 ppm).

N_S: Number of protons contributing to the standard signal (see note below).

m_S: Mass of internal standard added to the sample (in mg).

P_S: Purity of the standard (9.99% was used.)

MW_S: Molecular weight of the standard (1,4-dinitrobenzene: 168.11 g/mol)

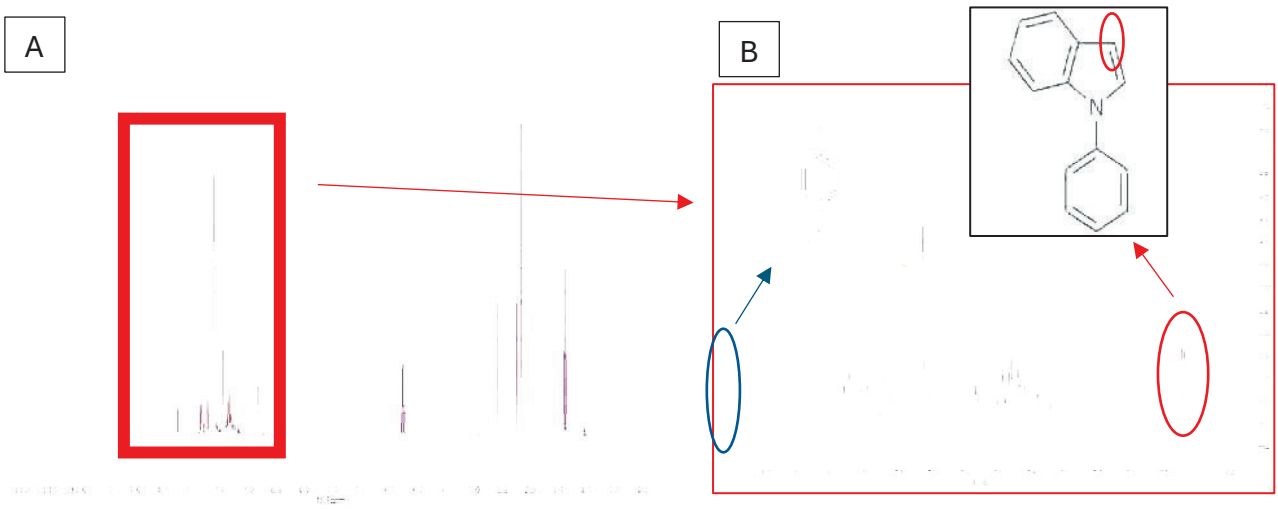

***Figure 2**: Experiment n. 7 of Table 1, ^{1}H NMR spectrum of the reaction mixture: (A) full spectrum with the region of interest, zoomed in figure B [red rectangular]; (B) expanded view of the region of interest (zoomed-in) highlighting the diagnostic signals used for product confirmation of experiment n. 7, Table 1.*



***Figure 3**: Experiment n. 2, Table 1, expanded view of the region of interest (zoomed-in).*

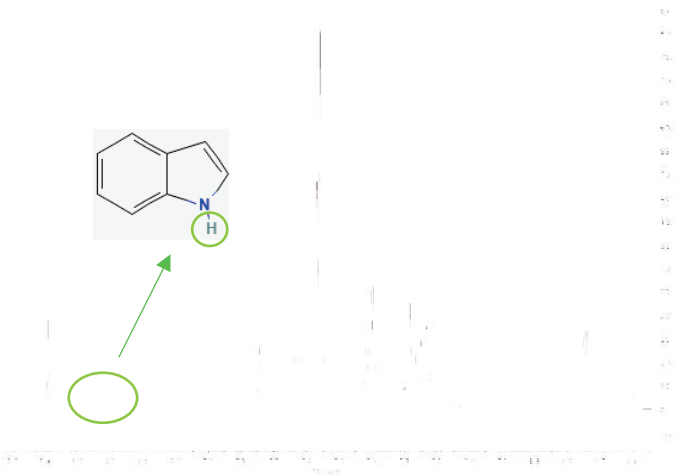

***Figure 4:** Experiment n. 3, Table 1, expanded view of the region of interest (zoomed-in) . The signal of N-H of indole is highlighted in green.*

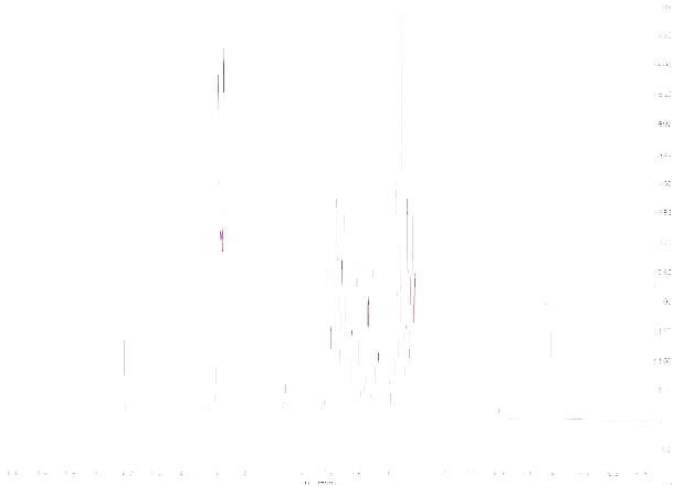

Figure 5:*Experiment n. 5, Table 1, expanded view of the region of interest (zoomed-in).*

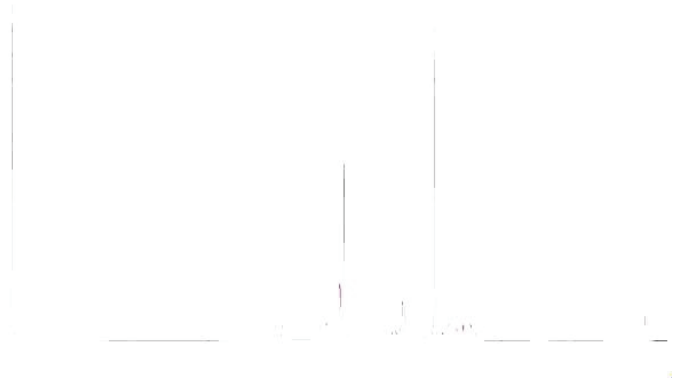

Figure 6:*Experiment n. 6, Table 1, expanded view of the region of interest (zoomed-in).*

17.3 Conclusions

The results clearly demonstrate that the direct use of the recovered waste as a catalyst is an effective and sustainable strategy for promoting the Ullmann C–N cross-coupling reaction between indole and iodobenzene. Minimizing post-treatment and purification steps not only reduces energy consumption and operational costs but also aligns well with the principles of green chemistry and waste valorization.

Among the solvents investigated, DMSO proved to be the most suitable medium, consistently affording higher yields compared to toluene and ethylene glycol, which resulted in low yields or only trace product formation. Catalyst loading has a strong influence on reaction efficiency, with a clear

increase in yield observed as the amount of catalyst is raised, reaching optimal performance at 160 mg catalyst. Under these conditions, a maximum yield of up to 74% was achieved with excess of iodobenzene.

The reaction atmosphere also played a critical role since the reaction performed under nitrogen atmosphere preserves the catalytically active Cu(I) species. Exposure to air led to copper oxidation and a significant decrease in yield, confirming the sensitivity of the catalytic system to oxidative conditions.

Overall, this study confirms that waste-derived copper catalysts can be efficiently reused “as it is” for Ullmann-type C–N coupling reactions, provided that appropriate solvent choice and inert conditions are employed. This approach offers a promising, low-cost, and environmentally friendly route for waste recovery and reuse in synthetic organic chemistry.